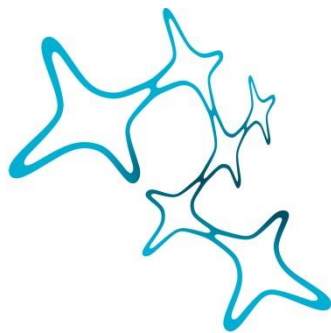

Neural Basis of Visual Motion Perception: An Illusory Perspective

Yunmin Wu



Graduate School of
Systemic Neurosciences

LMU Munich



Dissertation at the
Graduate School of Systemic Neurosciences
Ludwig-Maximilians-Universität München

October 2019

Supervisor
Prof. Dr. Herwig Baier
Dr. Fumi Kubo
Max Planck Institute of Neurobiology

First Reviewer: Prof. Dr. Herwig Baier
Second Reviewer: Prof. Dr. Alexander Borst
External Reviewer: Jun.-Prof. Dr. Aristides Arrenberg

Date of Submission: 1st Oct 2019
Date of Defense : 2nd Dec 2019

“Reality is merely an illusion, albeit a very persistent one.”

Albert Einstein

SUMMARY

Motion is one of the fundamental features of the visual scene. Most animals process visual motion signals effortlessly and generate proper motor reactions almost simultaneously. How the brain efficiently extracts relevant motion information from the physical world remains a persistent question in the field of visual neuroscience. This dissertation seeks to further dissect the neural circuit underlying visual motion processing in larval zebrafish, which renders unprecedented access to the brain given its rich genetic toolkit and easy optical access.

In the first study, I closely examined the retinal ganglion cells (RGCs), the output neurons of the eye. I found that some RGCs responded to motion in a direction-selective manner. Careful anatomical analysis revealed that these direction-selective RGCs not only innervate the optic tectum but also a local pretectal neuropil. Together with my colleagues, we identified a local circuit in the pretectum that can transform global motion signals from the retina into neural commands that can drive optomotor behavior.

In the second study, I employed an optical illusion as a circuit breaking tool. The chosen illusion is called the motion aftereffect (MAE), which offers a unique scenario of seeing motion in the absence of visual motion after prolonged exposure to continuous motion. Using eye movements as a readout for motion perception, first, I confirmed that larval zebrafish, like humans, were also susceptible to MAE. Next, with functional imaging, I identified the neural correlates of MAE in a subpopulation of direction-selective neurons across the brain. Among the many brain areas that harbored MAE-correlated neurons, optogenetic silencing highlighted the indispensable role of the pretectum in inducing MAE. Finally, focusing on the MAE-correlated neurons in the pretectum, I homed in on individual neurons essential to global motion perception through optogenetic activation and photoablation. My study of MAE in larval zebrafish not only revealed the neural processing of this illusion at cellular resolution, but it also shed light on key components in the motion processing circuit as well as their underlying computational mechanisms.

Taken together, this dissertation harnessed the advanced genetic and optical methods in larval zebrafish and provided a cellular roadmap to the neural circuit underlying visual motion processing. This roadmap lays the foundation for the future investigation of network connectivity and neural computations.

CONTENTS

1. Introduction	1
1.1 Visual illusions.....	1
1.2 Motion aftereffect.....	2
1.2.1 Psychophysics	4
1.2.1.1 Setups and measurements.....	4
1.2.1.2 MAE features.....	6
1.2.2 Theoretical models.....	7
1.2.3 Neural substrates.....	8
1.2.3.1 Retinal ganglion cells.....	8
1.2.3.2 Primary visual cortex.....	9
1.2.3.3 Middle temporal visual area	10
1.2.3.4 Other cortical areas	11
1.3 Zebrafish as a model system	11
1.3.1 Global motion induced behaviors.....	12
1.3.1.1 Optokinetic response.....	12
1.3.1.2 Optomotor response	13
1.3.2 Neural circuit underlying global motion perception	14
1.3.2.1 Retinal ganglion cells.....	14
1.3.2.2 Tectum.....	15
1.3.2.3 Pretectum.....	17
1.3.3 Genetic and optical methods	18
1.3.3.1 Transgenic lines.....	18
1.3.3.2 Functional imaging.....	20
1.3.3.3 Laser ablation	21
1.3.3.4 Optogenetic manipulation	22

1.4. Aims of this thesis.....	24
2. Manuscripts.....	26
2.1 Neuronal Architecture of a Visual Center that Processes Optic Flow	26
2.2 An Essential Circuit Node for Motion-Induced Behavior Identified by an Optical Illusion	66
3. Discussion	105
3.1 Direction selectivity in zebrafish RGCs.....	105
3.2 MAE in an animal without a cortex.....	106
3.3 Neural mechanism of MAE.....	107
3.3.1 CMT neurons	107
3.3.2 OMT neurons.....	108
3.3.1 Neural implementation of the “opponent process” model.....	110
3.4 Role of the pretectum in OKR	111
3.5 Role of the tectum in OKR	112
3.6 Dedicated motion processing pathways.....	113
3.7 Conclusions and outlook.....	114
4. References.....	116
Acknowledgment	133
Appendix	135

1. INTRODUCTION

1.1 Visual illusions

Visual illusions are unique stimuli, of which our perception deviates from the physical reality. With their immediate impact on the observers, these illusions have fascinated many people, especially neuroscientists. They remind us that our vision is not simply a camera taking snapshots of the world. Instead, without conscious awareness, elaborate interpretations are seamlessly weaved into our perception by the intricate neural networks in the brain.

The brain actively interprets the visual scenes for good reasons. On one hand, the input to the brain is first encoded by millions of photoreceptors in the retina, each looking at a particular point in space. Given the ever-changing visual scenes faced by awake animals, this poses a potential problem of information overflow. The visual system must swiftly extract relevant information so as to make prompt decisions and generate immediate motor responses. On the other hand, the input to the brain, namely the retinal image, is two-dimensional (2D). In order to gain three-dimensional (3D) information, the brain has to reconstruct a 3D world from 2D inputs.

To efficiently interpret and reconstruct the visual world, the brain has to make some assumptions. Although it works flawlessly most of the time, an assumption can be proven wrong in edge cases. This is when an illusion arises (Hoffman, 2005). In other words, visual illusions are not the result of weaknesses or mistakes in the design of our visual system, but rather they reflect the dynamic process in the brain that powers our visual system. Interestingly, this notion is supported by a study in computer vision, in which a convolutional neural network (CNNs) trained to recognize natural images also reproduced human's response to some illusions, suggesting that visual illusions emerge as a byproduct of efficient processing (Gomez-Villa et al., 2019).

In fact, some principles of neural processing have been distilled from the study of illusions. For instance, the Hermann grid illusion (Figure 1A), in which illusory dots were perceived at intersections, contributed to our understanding of lateral interaction between neighboring neurons (Schiller and Carvey, 2005); the Ponzo illusion (Figure 1B), which describes the misperception of two lines of equal length in the background of

converging lines, revealed our innate default interpretation of space according to linear perspective (Gandhi et al., 2015; Schiffman and Thompson, 1977); the Ebbinghaus illusion (Figure 1C), which causes strong effect in perception but weak effect in the act of grasping, provided evidence for the hypothesis that different processing pathways underlie vision-to-perception and vision-to-action transformations (Haffenden et al., 2001). Plausible theories have been formed for many illusions like the above-mentioned, however, for many of them, the exact neural implementation still remains elusive.

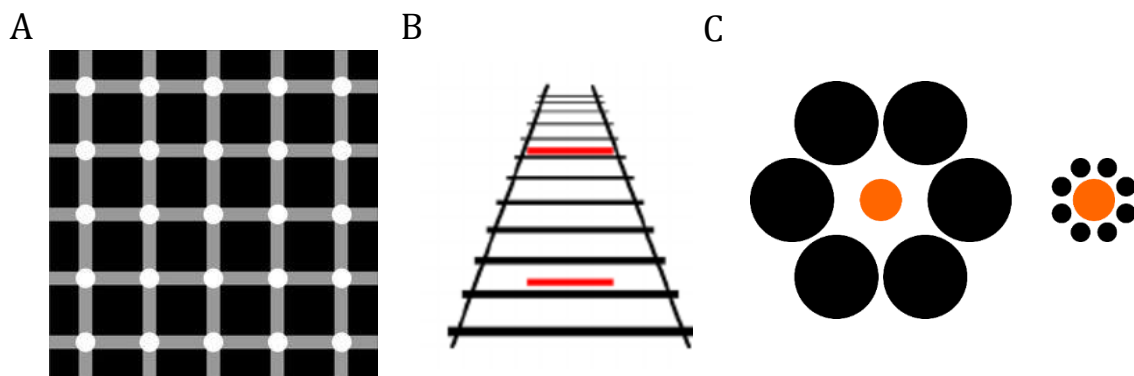


Figure 1. Illusions reveal features of visual processing. A. The Hermann grid illusion, in which illusory grey spots are seen at the intersections. B. The Ponzio illusion, in which the horizontal line closer to where the vertical lines converge appears to be further away and longer. C. The Ebbinghaus illusion, in which the dot surrounded by bigger dots appears to be smaller than the dot surrounded by smaller dots.

Visual illusions open up a powerful window into the neurobiology of vision (Eagleman, 2001). Understanding how visual illusions work will not only add on to our knowledge of the visual system, but it can also provide novel ideas for the algorithm design of computer vision that can one day approximate or even surpass the biological visual systems (Mély et al., 2018; Watanabe et al., 2018). This provides strong incentives to further examine the rich repertoire of visual illusions, especially the ones whose neural underpinnings and their biological values are yet to be found out.

1.2 Motion aftereffect

Motion aftereffect (MAE), also known as the waterfall illusion, is a classical visual illusion that describes the phenomenon of motion perception in the absence of visual motion after prolonged viewing of motion in one direction. For instance, if one fixates on a waterfall for some time, and then shift the gaze away to the rocks nearby, these stationary rocks would appear to be moving upwards. MAE was first described by Aristotle more than two thousand years ago (Aristotle, 350B.C.). Later, it was rediscovered independently by Purkinje (Purkinje, 1820) and Addams (Addams, 1834) based on

similar visual experience at the sight of flowing water in nature. The scientific research on MAE did not take off until the 1960s. From then, the publication on MAE grew exponentially (Figure 2). Even today MAE is still a popular topic in vision science.

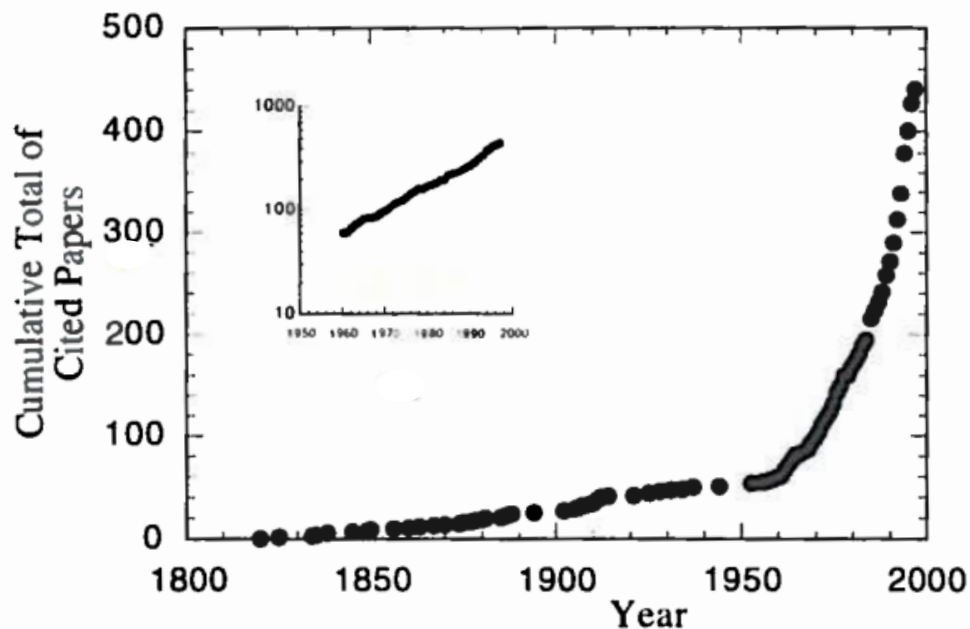


Figure 2. Cumulative plot of the number of publications on MAE by year. The number of MAE publications grew linearly before 1960, and exponentially (as show in the inset log-scale plot) since then (From Mather et al., 1998).

There are two interesting features of MAE. First, the observers see motion in objects that display no physical change in position. This indicates that the perception of the illusory motion originates from the brain. Second, the direction of the illusory motion is always opposite to the previously observed motion (first described by Lucretius, 56B.C.). This suggests that the mechanism underlying MAE is direction specific. Before it was possible to peep inside the brain by means of electrophysiology or functional imaging, these interesting features of MAE provided additional information for the curious minds to postulate potential computations under the hood that transform sensory inputs into perception or actions.

Past studies showed that MAE not only affects humans (Wohlgemuth, 1911), but also a wide range of other vertebrates and invertebrates. These include mice (Samonds et al., 2018), monkeys (Scott and Milligan, 1970), pigeons (Xiao and Güntürkün, 2008), zebrafish (Najafian et al., 2014; Pérez-Schuster et al., 2016), and insects (Srinivasan and Dvorak, 1979). The cross-species impact of MAE suggests that it is tapping on some fundamental mechanisms in visual processing, which are conserved through evolution.

In fact, perceptual aftereffect is not limited to motion. Phenomena of the same concept have been reported in other visual features, e.g. orientation (Gibson and Radner, 1937), and shape (O'leary and McMahon, 1991). One striking example is the color aftereffect, which refers to the emergence of an illusory contour in complementary color upon prolonged stimulation with a certain hue (Loomis, 1972; Zaidi et al., 2012). In addition, aftereffects also exist in other sensory modalities and seem to have a cross-modal effect. For instance, visual MAE can not only be induced by visual motion, but also by directional auditory and tactile stimuli (Berger and Ehrsson, 2016; Konkle et al., 2009). This suggests that MAE can be transferred between sensory modalities. The vast variety of aftereffects implies that their underlying mechanism could be a universal principle adopted across sensory systems.

1.2.1 Psychophysics

Early studies on MAE aimed to unravel the characteristics of illusory motion and the stimulus determinants to induce the illusory perception. Typically, an MAE experiment consists of two phases: a conditioning phase (also called adaptation phase) of continuous motion in one direction to induce MAE and a test phase of a stationary scene or test motion to measure the occurrence or the strength of MAE. Some studies in the 1900s extended to clinical applications, e.g. use MAE to evaluate personality traits and psychological conditions, although no causal relationship was ever shown between MAE and psychological features. The majority of the test subjects for MAE psychophysical studies were primates.

1.2.1.1 *Setups and measurements*

The knowledge of MAE grew with the evolution of experiment setup and measurement procedure. Classical setups to study MAE include hand-operated moving gratings (Bowditch, 1881) (Figure 3A) and S.P. Thompson's spiral (Figure 3, B and C). In most experiments done with these setups, the moving stimuli came to a halt in the test phase, mimicking MAE in natural viewing conditions. This is referred to as the static MAE (SMAE). From the twentieth century, computer-generated dynamic stimuli came into play, which allowed more diverse stimulus types (e.g. second-order motion) and wider range of motion stimuli (e.g. spatial and temporal frequencies). One widely adopted dynamic stimulus is the random dot kinematogram (Curran and Benton, 2006) (Figure 3D), which consists of short-lived dots appearing in random position moving in directions

of various coherence. With dynamic stimuli, moving objects instead of stationary objects are displayed in the test phase, and hence they are named the dynamic MAE (DMAE). Interestingly, adaptation with the second-order motion, which bears no point-to-point correspondence over time, could elicit a DMAE but not an SMAE (Nishida and Sato, 1995; Nishida et al., 1994). This suggests that the two types of MAE might have different causes.

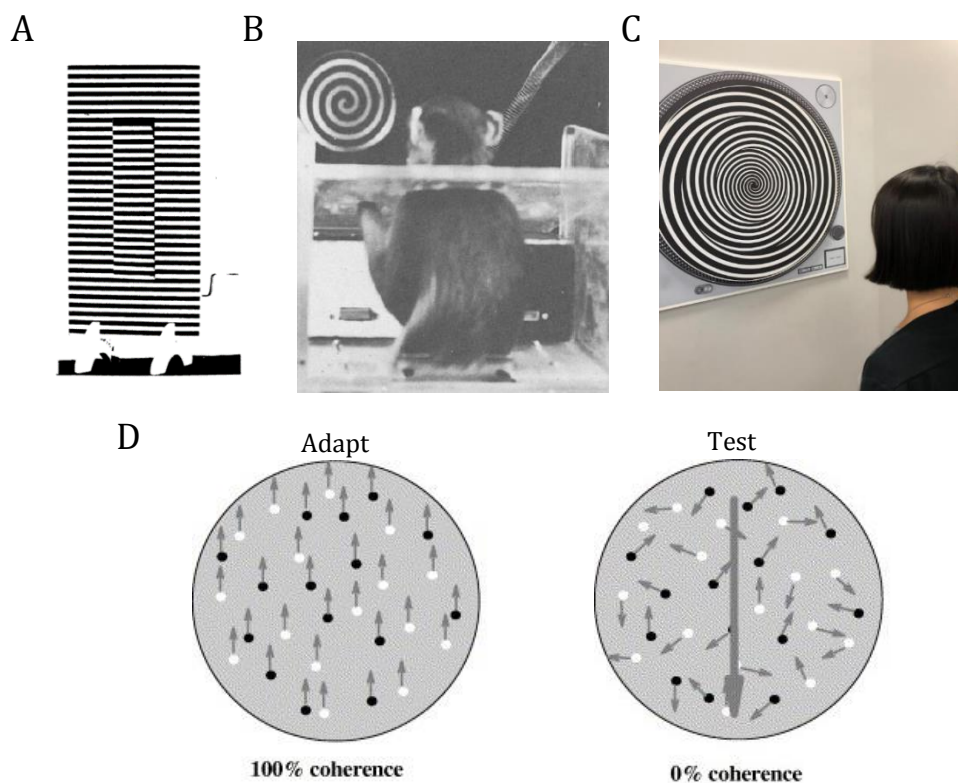


Figure 3. Typical setups for psychophysics experiments of MAE. A. Hand operated apparatus to induce MAE (From Bowditch and Hall, 1881). B-C. S.P. Thompson's spiral with Rhesus monkey subject (From Scott and Miligan, 1970) and human subject (Photo taken by author at Museum der Illusionen Hamburg, Germany). D. Dynamic random dot kinematograms displayed on LCD screens (From Curran and Benton, 2006).

In terms of measurement, early measurements were based on the verbal report of experiment subjects, which includes occurrence, duration, and vividness of the illusory motion perception. Although such experiments were easy to carry out, the results were rather subjective and qualitative. More quantitative measurements were made possible by computer generated stimuli. A common measurement is the nulling method, which attempts to estimate the speed or the strength of MAE by identifying real motion in the opposite direction that can effectively cancel the illusory perception. Another recently developed measurement of MAE is based on eye movements. During MAE, it has been shown that smooth pursuit eye movements in the opposite direction to the conditioning

motion was elicited (Braun et al., 2006; Gardner et al., 2004). This particular MAE-induced behavior is termed the oculomotor MAE as opposed to the self-report based perceptual MAE.

1.2.1.2 MAE features

Careful psychophysical studies revealed interesting features of MAE. Generally, MAE can be generated after the viewing of continuous motion of a wide range of speeds and duration (Glasser et al., 2011; Mather et al., 1998; Wohlgenuth, 1911). MAE was the strongest when the stimulus pattern in the test phase resembled that in the conditioning phase, and a lack of contour in the test phase reduced illusory perception (Spiegel 1962). Rotating radial patterns in the conditioning phase produced a stronger MAE than straight moving translational patterns (Bex et al., 1999). Additionally, the MAE also has the following unique features:

Storage period: in human subjects, the perception of MAE can be delayed by closing the eyes right after the conditioning phase. The subjects do not perceive MAE until the subsequent viewing of the test pattern. This phenomenon is known as the storage of the MAE (Spiegel, 1962; Wohlgenuth, 1911). In addition to closed eyes, a blank screen, as well as test patterns dissimilar to the adaptation pattern at the beginning of the test phase, could all lead to the storage of MAE (Thompson and Wright, 1994). The storage effect not only exists in the perceptual MAE but also in the oculomotor MAE (Watamaniuk and Heinen, 2007).

Interocular transfer: after monocular presentation of the conditioning motion to one eye, the perception of MAE persisted if the test pattern was only presented to the other non-adapted eye (a black screen for the adapted eye). This so-called interocular transfer (IOT) of MAE was first described in detail by Dvorak in 1870 (translated in Broerse et al., 1994). Since the conditioning motion and the test pattern were presented to different eyes, the IOT was believed to originate from the adaptation of binocular neurons (Coltheart, 1971; Mitchell and Ware, 1974; Movshon et al., 1972). The IOT rate was about 30-50% for SMAE, but almost 100% for DMAE, suggesting that the neural computation underlying SMAE and DMAE might take place on different levels of visual motion processing that involve different degrees of binocularity (Nishida et al., 1994; Raymond, 1993; Wade et al., 1993).

Link to diseases: it has been shown that MAE was altered in individuals with certain neurological diseases. For example, MAE was prolonged in patients with migraine and schizophrenia (Harris, 1994; Singh and Shepherd, 2016). However, it is unclear what neurological changes underlie the prolonged MAE effect.

1.2.2 Theoretical models

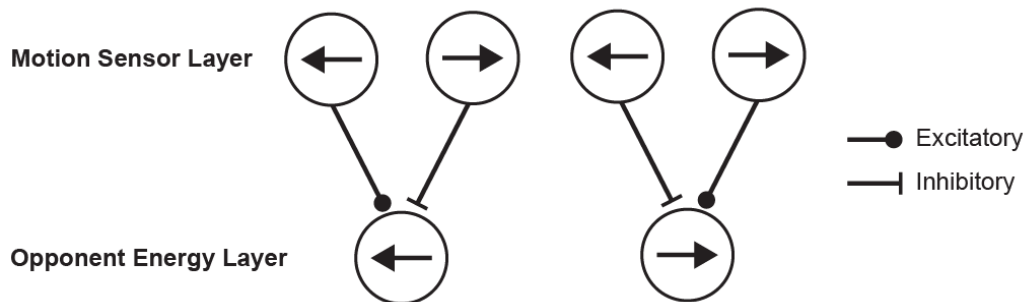


Figure 4. Opponent process model of MAE. Oppositely tuned cells (leftward and rightward tuned cells in this example) in the motion sensor layer provide paired excitatory and inhibitory inputs to the comparator cells in the opponent energy layer. The comparator cell on the left is tuned to leftward motion, and the one on the right is tuned to rightward motion (Based on Barlow and Hill, 1963a).

The theoretical models of MAE evolved over time. Early explanations of MAE concerned eye movement and muscle fatigue (Purkinje, 1820). However, most of them were disproved by psychophysics experiments (Drysdale, 1975; Seidman et al., 1992; Sekuler and Ganz, 1963). Modern theories of MAE took shape based on the inspiration of the physiology of cortical neurons. One of the most plausible hypothesis was the ratio model, which was put forward by Sutherland in 1961 after the discovery of direction-selective (DS) neurons (Hubel and Wiesel, 1959). He proposed that the perception of motion could be based on the ratio of firing neurons tuned to different directions. After prolonged viewing of motion, cells that have just been stimulated fire less compared to the others. This imbalance leads to the perception of apparent movement in the opposite direction (Sutherland, 1961). This idea was further developed in the “opponent process” model (Figure 4), which includes two layers of processing: the motion sensor layer and the opponent energy layer (Barlow and Hill, 1963a). Comparator cells in the opponent energy layer receive paired inputs from direction-selective cells in the motion sensor layer that are tuned to opposite directions. One of the inputs is excitatory and the other inhibitory. As such, the output of the opponent energy layer is based on the difference in activity between oppositely tuned motion sensors. With this organization, a suppressed firing in motion sensors caused by adaptation can be transformed into an activation of

the comparator cells tuned to the opposite direction of the conditioning motion. To account for the two-dimensional effect of the MAE, a third layer, the integrator layer was added to the “opponent-process” model. The integrator cells receive excitatory and inhibitory inputs from comparator cells tuned to various directions (Wilson et al., 1992).

1.2.3 Neural substrates

Psychophysics studies indicated that different neural populations could contribute to MAE. To find out where these populations are located in the brain, scientists took advantage of techniques like microelectrode recording (Ling and Gerard, 1949) and functional magnetic resonance imaging (fMRI)(Lauterbur, 1973). Accumulating evidence suggests that MAE taps on multiple sites in the brain on different levels of the motion processing pathway (Bavelier et al., 2001).

1.2.3.1 Retinal ganglion cells

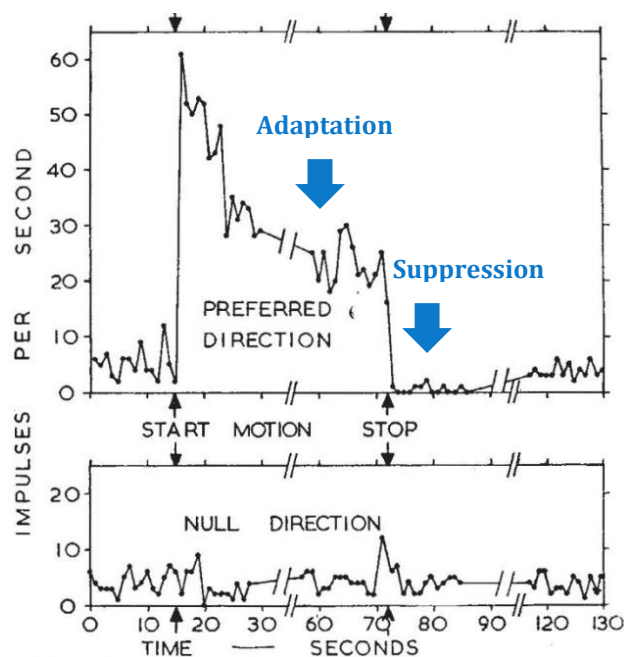


Figure 5. Example response of rabbit direction-selective RGCs in response to prolonged motion stimulation. Top, an RGC adapted in its preferred direction; bottom, an RGC adapted in its null direction (Adapted from Barlow and Hill 1963).

Retinal ganglion cells (RGCs) are the output neurons of the retina, which relay information from the eyes to the brain. DS RGCs have been found in many species, including rabbit (Barlow et al., 1964), mouse (Elstrott et al., 2008; Sun et al., 2006; Weng et al., 2005), and zebrafish (Gabriel et al., 2012; Hunter et al., 2013; Lowe et al., 2013; Nikolaou et al., 2012), although the existence of DS RGCs in primate still remains to be

definitively established. The single-unit recordings of DS RGCs in the rabbit retina were the first experimental evidence for the neural substrates of MAE (Barlow and Hill, 1963a). They showed that motion adaptation in a neuron's preferred direction led to a gradual decrease in firing rate during motion presentation and subsequently a suppression in spontaneous activity when the motion ended. In contrast, motion adaptation in a neuron's null direction (the direction opposite to the preferred direction) resulted in no significant change in firing rate (Figure 5). Barlow and Hill regarded the reduction in spontaneous activity in the DS population adapted in their preferred direction as the neural substrate of MAE. However, this is just the tip of the iceberg. Further computations take place downstream of RGCs, which is necessary to explain other features of MAE (e.g. interocular transfer).

1.2.3.2 Primary visual cortex

The visual area 1 (V1) is often referred to as the primary visual cortex or the striate cortex. Neurons with orientation and direction selectivity can be reliably found in V1. V1 receives input from the lateral geniculate nucleus (LGN) of the thalamus and relays processed visual information to higher visual areas, including V2, V3, MT/V5. There are two distinct cell types in V1: simple cells and complex cells (Hubel and Wiesel, 1962). Simple cells have defined antagonistic receptive fields so that their response can be predicted solely based on the stimulus location in the receptive field. On the contrary, complex cells have invariance in their receptive fields. A certain visual feature like orientation would make them fire whenever it is located in their receptive fields.

Single-cell recordings in cat V1 showed that DS neurons conditioned in their preferred direction decreased their firing rate in the course of continuous motion stimulation (Giaschi et al., 1993; Hammond et al., 1985, 1988; von der Heydt et al., 1978; Maffei and Fiorentini, 1973; Marlin et al., 1988). Some studies reported different time courses of adaptation between simple cells and complex cells (Giaschi et al., 1993; Hammond et al., 1988; Maffei and Fiorentini, 1973; Marlin et al., 1988), while others reported no difference (Vautin and Berkley, 1977). On the other hand, for neurons conditioned in their null direction, while some studies reported a slightly enhanced response in the test phase (von der Heydt et al., 1978; Marlin et al., 1988), others reported no change or even suppressed spontaneous activity (Giaschi et al., 1993). Notably, the enhanced response in the test phase was only found in simple cells but not in complex cells (von der Heydt et

al., 1978). In summary, although it seems certain that all V1 DS neurons adapt to prolonged motion stimulation, there still exist many open questions, in particular regarding 1) the response of V1 neurons in the test phase, 2) their temporal dynamics, and 3) the difference between simple and complex cells. The early single-cell studies failed to reach consensus, mostly due to the limited sampling and the vastly different visual stimulus protocols used in each study.

Recent functional magnetic resonance imaging (fMRI) studies, limited by the method's low temporal and spatial resolution, were not able to resolve these open questions in V1. Instead, they found that V1 might not play a major role in MAE after all. One fMRI study showed that the MAE-specific modulation of the population response was only observed in area MT (see 1.2.3.3), but not in V1 (Hogendoorn and Verstraten, 2013). Moreover, repetitive transcranial magnetic stimulation (rTMS) on V1 right before or during MAE did not affect the illusory motion perception (Théoret et al., 2002). These results suggest that there are likely further computations of MAE beyond or independent of V1.

1.2.3.3 Middle temporal visual area

MT or V5 refers to the middle temporal area of extrastriate cortex, which contains a big proportion of DS neurons (Maunsell and Van Essen, 1983; Zeki, 1974). It receives feedforward input from early visual areas, and it projects to areas implicated in the analysis of optic flow (e.g., MST) and the generation of eye movements (e.g., LIP) (Born and Bradley, 2005). fMRI study in human showed increase in activity in MT during MAE illusory perception, and the time course of this activity matched psychophysical MAE (Figure 6) (He et al., 1998; Tootell et al., 1995). Moreover, single-unit recordings of DS neurons in macaque MT identified neural correlates of MAE, which after adaptation in its null direction showed enhanced response to a stationary scene (Van Wezel and Britten, 2002) and a zero-motion counter-phase flickering grating (Kohn and Movshon, 2004).

On the other hand, the duration of MAE in human subjects was shortened, when MT was perturbed by transcranial magnetic stimulation (TMS) during a storage period before the test phase or during MAE (Antal et al., 2004; Stewart et al., 1999; Théoret et al., 2002). In contrast, the same stimulation on early visual area V1 and non-motion area dorsolateral prefrontal cortex (DLPFC) produced a negligible effect (Antal et al., 2004; Théoret et al.,

2002). Together with the imaging studies, these results suggest a crucial role of MT for MAE.

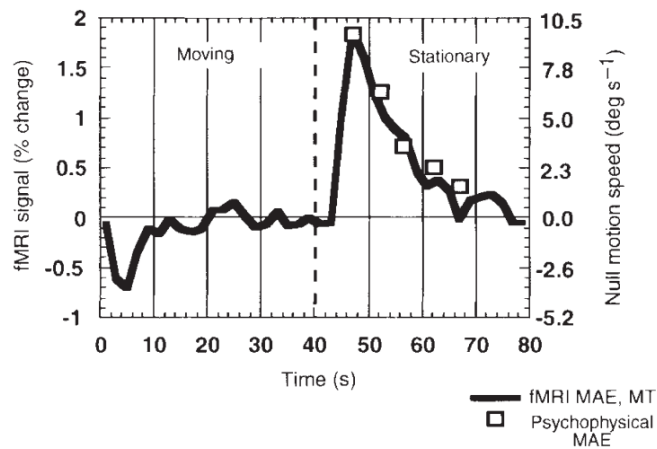


Figure 6. Temporal dynamics of MT activity matched psychophysical MAE
(From Tootell et al. 1995).

1.2.3.4 Other cortical areas

In addition to MT, several other brain areas were also activated during MAE. These areas include V2, V3a, BA37 (fusiform gyrus), BA40 (supramarginal gyrus), BA44 (pars opercularis of inferior frontal gyrus), BA46 (dorsolateral prefrontal cortex), BA47 (orbital part of inferior frontal gyrus), and the anterior cingulate gyrus (CG) (Hautzel et al., 2001; Huk et al., 2001; Taylor et al., 2000). Medial superior temporal area (MST) is particularly implicated in phantom MAE, in which MAE is observed outside the adapted visual field (Meng et al., 2006). Together, these physiological experiments in primates suggest that MAE involves multiple neural levels of motion processing, most likely with adaptation as a universal feature and opponent processing as a unique feature in higher levels specific to global motion processing.

1.3 Zebrafish as a model system

Zebrafish (*Danio rerio*) has been established as a model system well-suited for studying visual behaviors and neural circuits (Baier, 2000; Orger, 2016; Portugues and Engert, 2009). The visual system in zebrafish develops rapidly. It is well developed by 5 days post fertilization (dpf) in terms of morphology, electrophysiology, and behavior (Bilotta and Saszik, 2001; Rinner et al., 2005). It is a highly functional system that can give rise to a variety of visually induced behaviors, although it is made up of much fewer neurons and synaptic connections in comparison to the mammalian visual system. On the other hand, zebrafish, as a genetic model, has accumulated a rich collection of transgenic lines, which

can express useful tools like neural activity indicators and optogenetic tools in specific groups of neurons. The expression of these tools in the translucent larval zebrafish allows all-optical interrogation of the brain. Using only light, neural activity can be monitored and manipulated, while the behavior of the fish is tracked. With all these advantages, zebrafish is without doubt an unprecedented vertebrate platform to decipher the neural mechanism underlying visual behaviors.

1.3.1 Global motion induced behaviors

Global motion on the retina occurs during active or passive movement. In response, larval zebrafish actively move their eyes and tails to compensate for self-motion or drift in the environment. These motion-induced innate behaviors emerge at early life stages (as larvae), and they can serve as a useful readout of motion perception in larval zebrafish, which cannot disclose perceived motion by self-report.

1.3.1.1 Optokinetic response

The presence of rotational motion elicits stereotypic eye movements, called the optokinetic response (OKR), which consists of slow phase eye movements in the direction of visual motion followed by rapid saccades in the opposite direction to reset the eye position (Figure 6B). This reflexive behavior for gaze stabilization not only exists in foveate animals like human and monkeys (Pasik et al., 1972; Tarnutzer and Straumann, 2018), but also in afoveate animals like mice and zebrafish (Brockerhoff et al., 1995; Iwashita et al., 2001). Remarkably, the OKR behavior in zebrafish can be observed as early as 3dpf (Beck et al., 2004; Easter and Nicola, 1996, 1997). Moreover, it is highly consistent and robust across individuals (Brockerhoff et al., 1995).

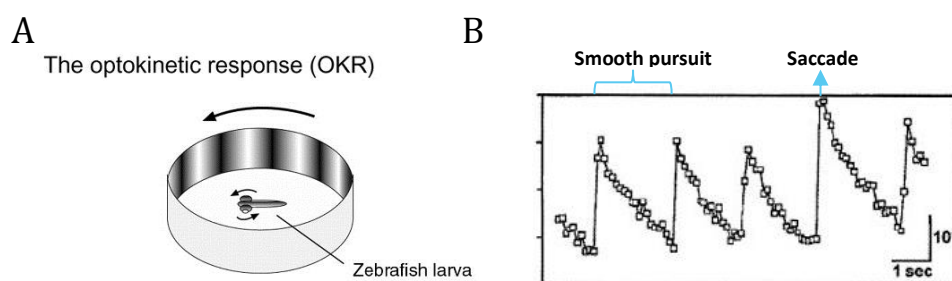


Figure 7. Optokinetic response in larval zebrafish. A. Typical setup of rotating sinusoidal gratings to induce OKR (From Roeser and Baier, 2000). B. Example eye movement traces of a zebrafish larva during OKR (Adapted from Neuhauss et al., 1999).

Experimentally, it is easy to induce OKR in eye-fixed restrained larval zebrafish with a rotating drum of sinusoidal gratings (Figure 7A) (Neuhauss et al., 1999). Psychophysics studies have discovered that the OKR behavior in larval zebrafish was dependent on stimulus velocity and spatial frequency (Rinner et al., 2005). In fact, the initial eye velocity during the slow phase almost matched the stimulus velocity within a certain range (Beck et al., 2004). On the contrary, the OKR behavior in larval zebrafish was largely independent of stimulus brightness if it was beyond the detection threshold (Rinner et al., 2005).

In mammals, the OKR is mediated by a subcortical neural pathway including two heavily interconnected areas, the accessory optic systems (AOS) (Simpson, 1984), and the nucleus of the optic tract (NOT) (Wallman, 1993). AOS and NOT receive input of motion information from RGCs and cortical areas, and they send output to premotor areas in the brain stem that drive eye movements (Giolli et al., 2006; Sun et al., 2015; Yakushin et al., 2000). In teleost, the pretectal area or area pretectalis (APT), part of which is a homologous structure to the mammalian AOS/NOT, is implicated in the OKR behavior (Masseck and Hoffmann, 2008, 2009a, 2009b).

1.3.1.2 Optomotor response

The presence of translational motion elicits another reflexive behavior, called the optomotor response (OMR), in which the fish swim in the direction of perceived motion in order to stabilize their position in flowing water (Neuhauss et al., 1999). Like OKR, OMR is also an innate behavior that is widely observed in the animal kingdom. E.g. in mice (Abdeljalil et al., 2005), crabs (Tomsic, 2016), flies (Reichardt, 1969), and etc. In zebrafish, OMR is normally fully mature by 6dpf (Neuhauss, 2003).

OMR can be elicited in free swimming larvae exposed to moving sinusoidal gratings (Figure 8A). The free swimming assay is usually used to measure population response, in which the average position of a group of fish is determined (Muto et al., 2005). On the other hand, OMR can also be induced in a head restrained preparation with the tail of the fish freed. The actual tail movement or its proxy, namely the activity in the peripheral motor nerve (fictive swims), can be measured to reflect the OMR behavior in larval zebrafish (Figure 8B) (Naumann et al., 2016; Pérez-Schuster et al., 2016; Vladimirov et al., 2018).

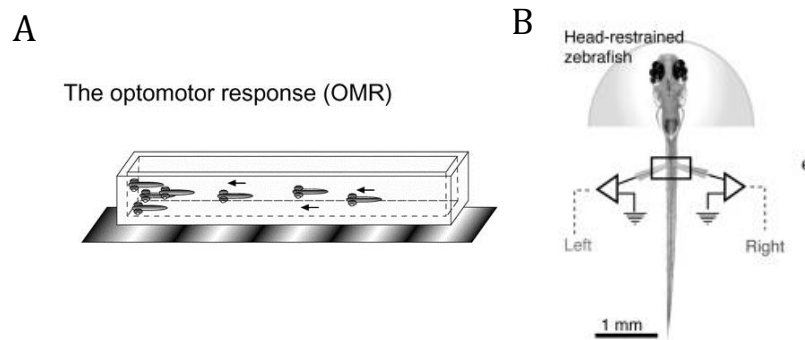


Figure 8. Optomotor response in larval zebrafish. A. Free swimming assay with moving sinusoidal gratings to induce OMR (From Roeser and Baier, 2000). B. Head-restrained preparation of paralyzed fish. The tail movement is approximated by the activity of the peripheral motor nerve measured by electrophysiology. (From Naumann et al. 2016).

In mammals, like OKR, OMR is also mediated by AOS and NOT (Simpson, 1984). In goldfish, the tectum has been shown to play an indispensable role for OMR behavior (Springer et al., 1977). However, larval zebrafish with tectal ablation could still perform OMR (Roeser and Baier, 2003). A recent study proposed that the OMR behavior in larval zebrafish was mediated by a circuit broadly distributed in the brain, which could explain why tectal ablation alone did not abolish OMR (Naumann et al., 2016).

1.3.2 Neural circuit underlying global motion perception

Like in many other animals, the processing of motion stimuli in larval zebrafish begins in the retina. RGCs, the output neurons of the retina, relay motion information to the retinorecipient areas in the brain. Upon further processing, the motion information is then sent to the motor/premotor areas in the midbrain and the hindbrain, which drive appropriate motor responses. Since MAE involves a reversal of perceived direction, we are particularly interested in the DS neurons.

1.3.2.1 Retinal ganglion cells

In larval zebrafish, all RGCs project to the contralateral hemisphere. Their axons terminate in 10 distinct areas called arborization fields (AFs) (Burrill and Easter, 1994). AF 1-9 span the region of the preoptic area/hypothalamus, the thalamus, and the pretectum, whereas AF 10 is the neuropil of the optic tectum (Figure 9A) (Burrill and Easter, 1994; Robles et al., 2014). Each AF is innervated by a unique combination of RGCs of distinct dendritic morphologies and functional response types (Robles et al., 2014). A highly plausible hypothesis is that different AFs function as parallel processing channels

for behavioral functions (Baier, 2000), e.g. prey detection (small, mobile objects), collision avoidance (fast expanding, high contrast stimuli), and phototaxis (ambient luminance increments) (Semmelhack et al., 2014; Temizer et al., 2015; Zhang et al., 2017). Motion response, in particular DS response, was found in the superficial layer of AF10, namely the *stratum fibrosum et griseum superficiale* (SFGS), and they have three preferred directions that are roughly 120° apart (Figure 9B)(Nikolaou et al., 2012). In the SFGS, DS RGC axons innervate the most superficial layer (Figure 9B)(Nikolaou et al., 2012). RGCs that innervate the superficial SFGS also form axon collaterals in AF5 (Robles et al., 2014). Thus, we hypothesized AF5 to be the pretectal AF carrying directional motion information(see 1.3.2.3 Pretectum). Contradictory to our hypothesis, Naumann et al. reported DS response in a neighboring AF, AF6 (Figure 9C) (Naumann et al., 2016). One goal of my thesis was to resolve this discrepancy.

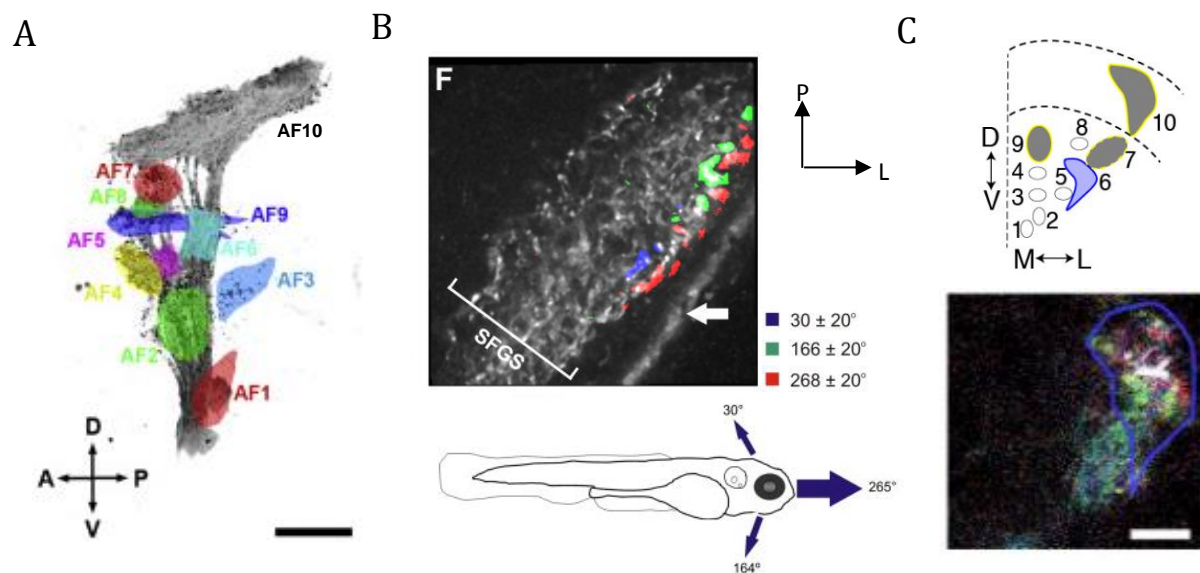


Figure 9. Functionally and morphologically distinct RGC axons terminate in different AFs. A. Lateral view of AFs (From Robels et al. 2014) B. Direction-selective response in the SFGS layer of AF10 (From Nikolaou et al. 2012) C. Direction-selective response in AF6 (From Naumann et al. 2016).

1.3.2.2 Tectum

The tectum is the largest retinal recipient area in larval zebrafish and has a highly laminated structure (Figure 10)(Baier, 2013). The tectal neurons can be categorized into periventricular neurons (PVNs), superficial interneurons (SINs), and neuropil neurons (NPNs) based on the location of their cell bodies (Kinoshita and Ito, 2006; Nevin et al., 2010; D. Förster, pers. communication). The former resides in the *stratum*

periventriculare (SPV), while the latter two resides in the tectal neuropil. The tectal neurons can also be classified into interneurons and projection neurons based on their neurite projections. While interneurons transmit information within the tectum, projection neurons send their axons to premotor areas in the forebrain, the midbrain and the hindbrain. In particular, these areas include the pretectum, the reticular formation, and the medulla oblongata (Scott and Baier, 2009). Most PVNs (70%) are projection neurons (Scott and Baier, 2009). Interestingly, there exists not only retinotopy but also a motor map in the tectum (Helmbrecht et al., 2018; Robles et al., 2014). In other words, the tectum not only encodes the precise location of the visual stimuli, but it is also capable of initiating different types of directional motor responses. This unique organization may underlie the essential role of the tectum in sensorimotor transformation for behaviors like approach and escape (Barker and Baier, 2015; Bianco and Engert, 2015; Dunn et al., 2016; Filosa et al., 2016; Heap et al., 2018).

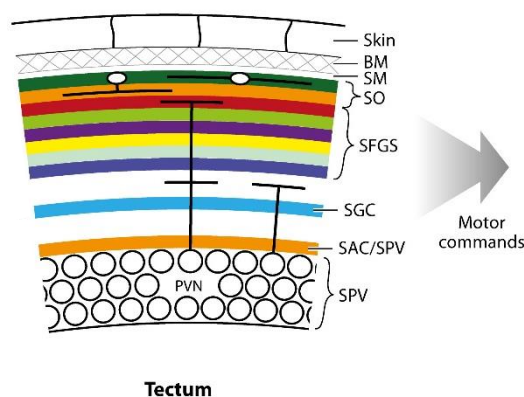


Figure 10. Laminated structure of the tectum in larval zebrafish. Abbreviations: BM, basement membrane; SAC, *stratum album centrale*; SAC/SPV, boundary between SAC and SPV; SFGS, *stratum fibrosum et griseum superficiale*; SGC, *stratum griseum centrale*; SM, *stratum marginale*; SO, *stratum opticum*; SPV, *stratum periventriculare* (From Baier, 2013).

A substantial amount of tectal neurons are direction-selective, and these include both PVNs (~44 % of the active cells)(Gabriel et al., 2012; Gebhardt et al., 2013; Grama and Engert, 2012) and SINS (~20%)(Yin et al., 2019). Monocular DS neurons in the tectum had four preferred directions, corresponding to the cardinal coordinates (Abbas et al., 2017; Hunter et al., 2013; Wang et al., 2019). The emerging tuning to the rostral-caudal direction, which is not present in the RGCs, is most likely due to a *de novo* computation in the tectum. However, despite the presence of DS neurons in the tectum, zebrafish larvae, whose RGC axons projecting to the tectum were ablated, could still perform OKR and OMR

(Roeser and Baier, 2003). This suggests that the tectum does not play a leading role in global motion processing.

1.3.2.3 Pretectum

The pretectum in adult zebrafish resides in the caudal diencephalon (Figure 11). It comprises of multiple interconnected pretectal nuclei, of which some are retinorecipient (parvocellular superficial, central, intercalated, paracommissural, and periventricular) and some non-retinorecipient (magnocellular superficial, posterior, and accessory) (Yáñez et al., 2018). The pretectum in larval zebrafish is located ventral to the tectum. Just like the tectum, the pretectum also receives visual information from direct RGC input (Burrill and Easter, 1994). It sends output to areas including the tectum, the hypothalamus, the oculomotor nuclei, the medial longitudinal fasciculus (nMLF), the cerebellum, and the reticular formation (Antinucci et al., 2019; Muto et al., 2017; Semmelhack et al., 2014). Pretectal activity can be modulated by efferents from the nucleus isthmi (NI) (Henriques et al., 2019).

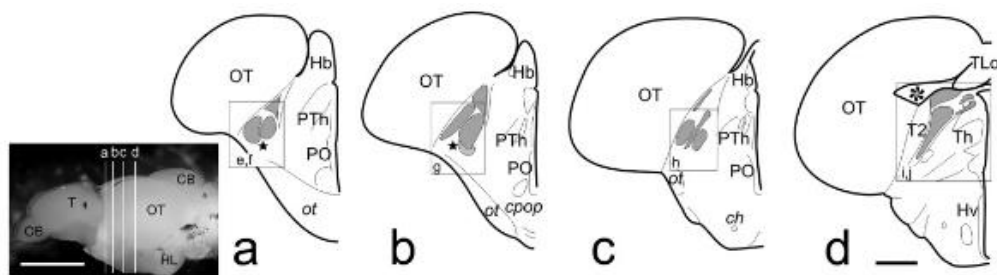


Figure 11. Schematics of the pretectal nuclei in adult zebrafish. Pretectal nuclei are labeled in gray. Abbreviations: ch, horizontal commissure; cpop, postoptic commissure; Hb, habenula; ot, optic tract; OT, optic tectum; PTh, prethalamus; PO, posterior pretectal nucleus; TLo, torus longitudinalis; Th, thalamus (From Yáñez et al., 2018).

Functionally, the pretectum is engaged in a variety of visually guided behaviors. Some pretectal neurons, which are located in the vicinity of AF7 and potentially receive input from it, serve as prey detectors. The ablation of these pretectal neurons or AF7 significantly impaired the prey capture (Antinucci et al., 2019; Muto et al., 2017; Semmelhack et al., 2014). Moreover, a recent study reported that the optogenetic activation of single cells in the pretectum was sufficient to initiate hunting behavior (Antinucci et al., 2019). This highlights the function of the pretectum as a command center for predatory behavior.

In terms of motion processing, the pretectum seems to assume the role of a command center as well. The pretectum is prevalently populated by both monocular and binocular DS neurons (Kubo et al., 2014; Naumann et al., 2016; Portugues et al., 2014; Wang et al., 2019). Similar to the tectal neurons, the pretectal monocular DS neurons are also tuned to the four cardinal directions (Wang et al., 2019). Notably, the binocular DS neurons encoded specific binocular optic flow patterns, including rotation and translation in all three body axes (Wang et al., 2019). This full coverage of response types suggests that the neural computation at the level of the pretectum could be sufficient to elicit appropriate global motion induced behaviors. In fact, with broad optogenetic activation and inhibition, the pretectum has been shown to be both required and sufficient for the OKR behavior in larval zebrafish (Kubo et al., 2014). In my thesis, I addressed the question of which exact neurons, out of the large pretectal DS population, drive a specific global motion induced behavior like OKR.

1.3.3 Genetic and optical methods

To crack a neural circuit, a common experimental strategy is to first figure out which neurons are involved by monitoring brain activity during normal behavior. Then, based on how different neurons respond, hypotheses of the circuit mechanism can be formed. Finally, by perturbing individual circuit components and measuring its behavioral consequences, these hypotheses can be either confirmed or rejected. Larval zebrafish, with its full collection of circuit breaking tools, is well-suited to implement this workflow.

1.3.3.1 Transgenic lines

To specifically and non-invasively express circuit breaking tools in target cell populations, a binary system of expression, namely the Gal4/UAS system, was established in zebrafish. Originated from yeast, Gal4 is an 881 amino acid transcription factor, which binds to a specific recognition sequence called UAS (upstream activating sequence), and thereby activates the transcription of downstream target genes (Guarente et al., 1982). It not only functions in yeast, but also in many other organisms including flies (Fischer et al., 1988), zebrafish (Scheer and Campos-Ortega, 1999), frogs (Hartley et al., 2002), and mice (Ornitz et al., 1991). The binary nature of this system enables the mix and match of different circuit breaking tools with various genetically defined expression patterns, simply by crossing animals expressing different reporters and Gal4 drivers (Figure 12). Gal4 was later on replaced by Gal4-VP16, a fusion protein with the DNA-binding domain

from Gal4 and the transcriptional activation domain from the herpes simplex virus VP16 protein. Compared to the original Gal4, Gal4-VP16 showed a stronger induction of UAS gene expression (Köster and Fraser, 2001; Sadowski et al., 1988). Gal4-VP16 was further genetically engineered to generate Gal4FF, which is less toxic in embryonic stages (Asakawa et al., 2008).

The transgenesis efficiency in zebrafish was vastly increased with the development of the Tol2 transposon system, which was first discovered in the medaka fish (*Oryzias latipes*), a small freshwater teleost from East Asia. (Kawakami and Shima, 1999; Kawakami et al., 1998, 2000). The Tol2 element encodes an active transposase, which can facilitate the excision and the reintegration of a foreign gene into the host genome without causing any gross rearrangement in the surrounding genomic DNA (Figure 12)(Kawakami, 2005). Compared to DNA microinjection alone, the germline transmission efficiency increases fourfold using the Tol2 system, meaning that much fewer animals have to be injected and screened in order to identify a founder (Kawakami et al., 2004).

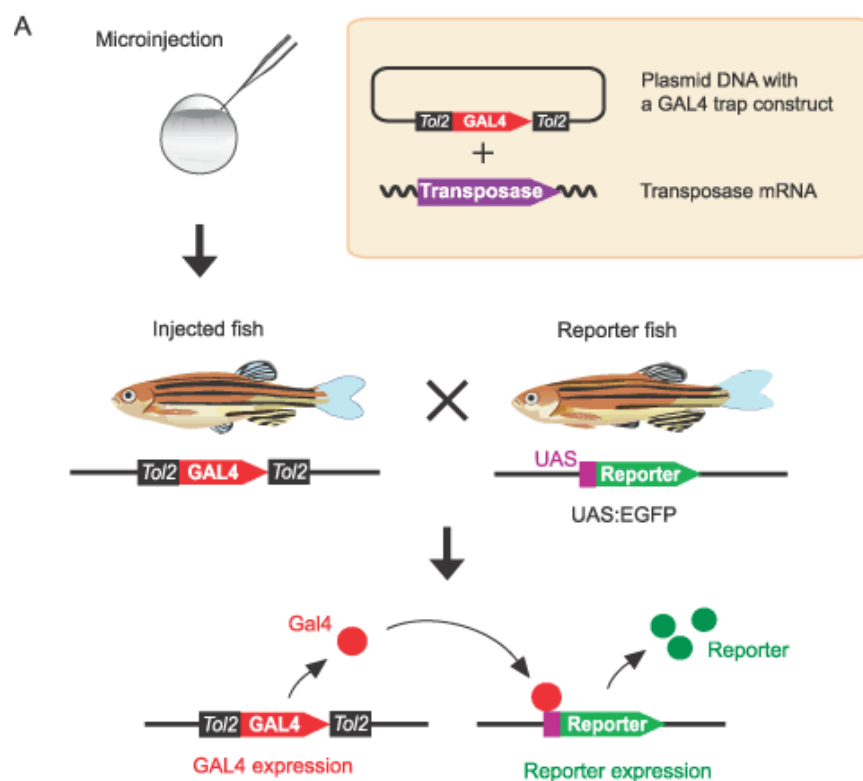


Figure 12. Tol2 mediated Gal4 enhancer trap or gene trap screens. A transposon donor plasmid containing a GAL4 trap construct is injected into fertilized eggs together with the transposase mRNA. The GAL4 trap construct is excised from the donor plasmid and integrated into the fish genome. The transgene pattern can be visualized by crossing identified founders with transgenic fish expressing a reporter gene, e.g. enhanced green fluorescence protein (EGFP) (Adapted from Asakawa et al., 2008).

Facilitated by the high efficiency of the Tol2 system, a large number of transgenic lines with distinct expression patterns have been generated by enhancer trapping (Asakawa et al., 2008; Balciunas et al., 2004; Ellingsen et al., 2005; Marquart et al., 2015; Ogura et al., 2009; Parinov et al., 2004; Scott et al., 2007) and gene trapping (Asakawa et al., 2008; Davison et al., 2007; Kawakami et al., 2004). To achieve transgenesis, a transgene like *GAL4* is placed after a basal promoter for enhancer trapping or a splice acceptor sequence for gene trapping. The entire cassette is inserted between two Tol2 arms. As such, the transgene will only be expressed if the cassette flanked by the Tol2 arms is integrated near an endogenous enhancer or into an endogenous gene with a splice donor, respectively. Both strategies, upon successful integrations, allow the expression of transgenes in a pattern similar to the endogenous gene (Asakawa et al., 2008). The hundreds of Gal4 lines generated by enhancer and gene trapping provide genetic access to different cell types and tissues within the zebrafish nervous system, which lays the foundation for circuit neuroscience in zebrafish (Scott and Baier, 2009).

1.3.3.2 Functional imaging

In larval zebrafish, it is possible to monitor neural activity noninvasively with optical methods. This is thanks to the genetically encoded calcium indicators (GECIs). A widely used GECI is a fusion protein called GCaMP, which is made up of green fluorescence protein (GFP), calmodulin, and a peptide sequence from myosin light chain kinase. Its fluorescence intensity fluctuates with intracellular calcium concentration, and thereby serves as a proxy of neural activity (Nakai et al., 2001). The GECIs vary in their temporal dynamics and excitation wavelength, making them suitable for different experiments (Lin and Schnitzer, 2016). With the Gal4/UAS system, GECIs like GCaMP can be used to monitor the activity of different genetically defined neural populations. Furthermore, given the transparency of larval zebrafish, they can be imaged directly after immobilization in the agarose without any prior surgery (Vanwalleggem et al., 2018).

Thanks to the development in imaging techniques, it became possible to image more than one z plane almost simultaneously. To gain access to multiple z planes, one strategy is to use an electrically tunable lens (ETL), which remotely shifts the focus without moving the specimen or the objective (Grewe et al., 2011). This way, a flexible volume can be imaged at a relatively high speed (Dal Maschio et al., 2017). More recently developed volumetric imaging techniques have faster imaging rate and improved 3D coverage. Techniques like

light-sheet microscopy (Ahrens et al., 2013; Dunn et al., 2016; Naumann et al., 2016; Portugues et al., 2014; Quirin et al., 2016), scanned oblique plane illumination microscopy (Kumar et al., 2018), and seeded iterative demixing microscopy (Nöbauer et al., 2017) have been implemented for functional imaging in larval zebrafish. Given the small brain size of larval zebrafish, whole-brain coverage can be achieved with single cell resolution.

To combine and compare the functional responses within and across individual fish, techniques have been developed to register the results of different functional imaging sessions from different fish to a common anatomical framework. Using algorithms like ANTs (Avants et al., 2011) and CMTK (Rohlfing and Maurer, 2003), a test brain could be registered to a target brain by linear and non-linear transformations. Once registered, the transformation matrix could also be used to register auxiliary information, e.g. other fluorescence channels, neuron tracings, and functional information (Chen et al., 2018; Helmbrecht et al., 2018). A common framework allows direct comparison of data from different experimental animals, and moreover, it enables a combinatorial usage of different databases, including anatomical annotations, single-cell tracings, transgenic lines, and histochemical staining (Kunst et al., 2019; Marquart et al., 2017; Randlett et al., 2015). With these databases, further virtual anatomical, functional, and histochemical analyses could be carried out post hoc. In a nutshell, brain image registration is a powerful approach to uncover hidden relationships from the functional imaging data.

1.3.3.3 Laser ablation

Functional imaging is informative, but it only shows correlation between neural activities and external stimuli or animal's behaviors. One way to test causality is to remove certain circuit components by killing the corresponding neurons. For a small number of neurons, this is typically done by two-photon-laser plasma ablation (laser ablation in short) (Muto et al., 2017; Vladimirov et al., 2018). This method, given its two-photon nature, exerts minimal impact outside the focal volume (Tsai and Kleinfeld, 2009). This enables us to specifically ablate targeted cells while leaving adjacent cells or neurites intact.

Compared to chemogenetic ablation or gross lesion, laser ablation is more flexible and specific. It can target not only single cells (Antinucci et al., 2019; Kawashima et al., 2016; Muto et al., 2017), but also commissures and neuropils (Naumann et al., 2016; Semmelhack et al., 2014). It is particularly suited for functionally identified neurons,

which may not be defined genetically (Vladimirov et al., 2018). However, laser ablation also has its limitations. It is irreversible, and furthermore, the effect of laser ablation on behavior or neural readout may not directly reflect the actual function of targeted neurons in the circuit (e.g. due to cellular redundancy in neural circuits).

1.3.3.4 Optogenetic manipulation

Optogenetics is another widely adopted method to probe the causal relationship between activities of specific neurons and behaviors in larval zebrafish. It represents a variety of genetically encoded light-gated ion channels, which, upon light stimulation, can be opened or closed in order to modulate the excitability of neurons (Mutter et al., 2014). These channels are naturally occurring microbial or animal opsins, although many of them have been further genetically engineered for higher efficiency, bidirectional control, or shifted activation wavelength to be compatible with calcium imaging.

Compared to invertebrate model organisms like drosophila, zebrafish has the advantage of having endogenous storage of all-trans retinal, which means no external supply of retinal is necessary for the rhodopsin-based optogenetic tools to function (Boyden et al., 2005; Nagel et al., 2003). In addition, given the transparency of larval zebrafish, the light stimulus can be easily delivered via external optic fibers or whole field illumination to restrained or free-swimming animals without any implants (Portugues et al., 2013). These features make optogenetics a convenient tool in larval zebrafish.

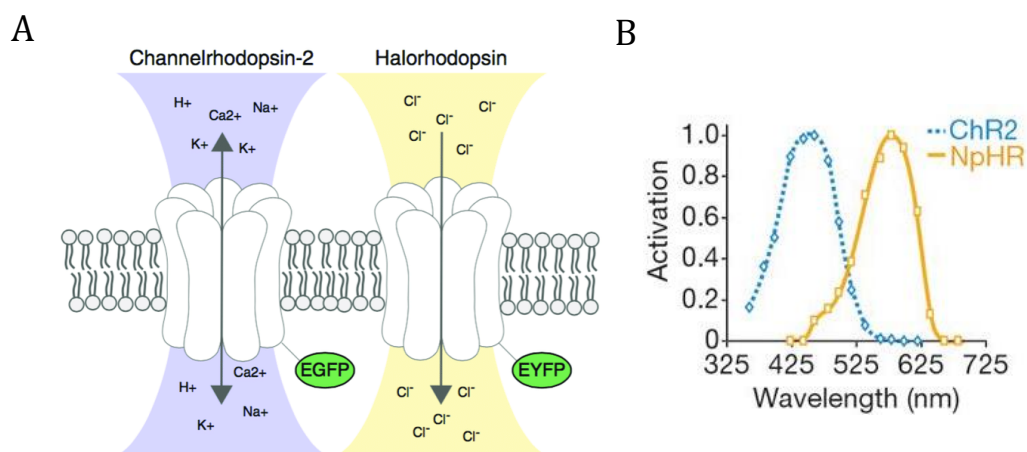


Figure 13. Optogenetic tools for activation and inhibition of neural activity. A. Schematic drawing of two example optogenetic tools, channelrhodopsin-2 (ChR2) and halorhodopsin (NpHR). They differ in their activation spectrum, ion selectivity, and kinetics (From Mutter et al. 2014). B. Activation spectrum for ChR2 (peak sensitivity 470 nm) and NpHR (peak sensitivity 580 nm) (From Zhang et al. 2017).

To activate neurons, channelrhodopsin-2 (ChR2) from the green alga *Chlamydomonas reinhardtii*, is commonly used (Nagel et al., 2003). It is a light-gated cation-selective channel, which, upon blue light stimulation, allows nonspecific cations to permeate (Nagel et al., 2003). ChR2 has been applied in larval zebrafish to dissect spinal circuits (Kimura et al., 2013; Umeda et al., 2016), to disentangle potential connectivity (Blumhagen et al., 2011; Bundschuh et al., 2012; Cheng et al., 2017), and to test sufficiency for various behaviors (Antinucci et al., 2019; Arrenberg et al., 2009; Barker and Baier, 2015; Cheng et al., 2016; Douglass et al., 2008; Gonçalves et al., 2014; Kubo et al., 2014; Monesson-Olson et al., 2014; Schoonheim et al., 2010).

To silence neurons, halorhodopsin from *Natronomonas pharaonis* (NpHR) has been the favorite choice in the past (Boyden et al., 2005; Gradinaru et al., 2008; Zhang et al., 2007). NpHR is a light-driven chloride pump, which actively transports chloride ion into the cytoplasm and hence hyperpolarizes the cell (Zhang et al., 2007). It can be used in conjunction with ChR2 to achieve bidirectional control of membrane voltage with two colors of light (Han and Boyden, 2007). The combination of these two tools, either in conjunction or in separate animals, enabled gain-of-function and loss-of-function experiments in vivo, which was proven a powerful way to dissect neural circuits in larval zebrafish (Antinucci et al., 2019; Arrenberg et al., 2009; Cheng et al., 2016; Kubo et al., 2014; Schoonheim et al., 2010). Recently, a family of light-gated anion channels named anion channel rhodopsins (ACRs) was discovered in cryptophyte algae *Guillardia theta* (Govorunova et al., 2015). Compared to NpHR, the ACRs are more efficient, because they are anion channels with no limited capacity like a pump (Govorunova et al., 2015). GtACR1 and GtACR2 have been used to effectively inhibit spinal neurons and reduce spontaneous movements in zebrafish embryos (Mohamed et al., 2017). The ACRs are no doubt one of the most potent optogenetic silencers so far. However, the ACRs also have limitations. Depending on targeted cell types and subcellular site of optogenetic stimulation, the ACRs could have both hyperpolarizing and depolarizing effects (Malyshev et al., 2017; Wiegert et al., 2017).

Compared to laser targeted ablation, optogenetics offers the possibility of reversible manipulation on neurons with precise temporal and spatial control (Tan et al., 2015). The light stimulation can be time-locked to external sensory stimuli, or to a certain behavior of the fish. In addition, the expression of optogenetic tools can be restricted to a small

desired population using the extensive collection of Gal4 lines available in zebrafish, and the specificity can be further improved with optical targeting. It has been shown that ChR2 could also be activated by two-photon lasers, which provided better spatial specificity (Papagiakoumou et al., 2010; Rickgauer and Tank, 2009). With recently developed computer generated holography, it became possible to optogenetically manipulate any group of individual neurons located at different locations in the brain with the capacity of concurrent two-photon functional imaging (Dal Maschio et al., 2017; Hernandez et al., 2016). Taken together, optogenetics is an invaluable tool in larval zebrafish to reveal how neural circuits generate behavior.

1.4. Aims of this thesis

This thesis is devoted to gain a better cellular understanding of the neural basis of visual motion processing in larval zebrafish, and how it can give rise to motion illusions. Specifically, the aim of the thesis is two-fold: first, by harnessing the remarkable optical and genetic access to the brain in larval zebrafish, I sought to identify the neural substrates of MAE in this model organism; second, using MAE as an extension to the conventional stimulus space, I intended to identify the DS neurons that bear causal significance in the motion processing circuit that evokes OKR behavior.

As a groundwork to study MAE, which involves a reversal in perceived motion direction, first I searched the brain for neurons with DS response. With two-photon microscopy, I systematically imaged the activity of different neural populations, while presenting the fish with moving gratings in a variety of directions. For the RGCs in particular, I, together with my colleagues, used an axon-terminal-specific transgenic line as well as an image-registration strategy to more accurately map out the AF(s) that encodes the directional information of motion. The results clarified a previous confusion in the field, and it became an important part of the first publication (Kramer et al., 2019) in this cumulative-style thesis.

To study MAE in larval zebrafish, first I looked for the visual stimuli that could robustly induce the perception of illusory motion. I systematically varied the parameters of the conditioning motion and monitored the eye movements of the fish as a readout of motion perception. With the best stimulus condition identified, I carried out volumetric calcium imaging followed by a clustering analysis to identify the neural correlates of MAE. I

further examined these MAE-correlated neurons in terms of their neurotransmitter identity, ocular input, optic flow selectivity, and location. Finally, by optogenetic perturbation, I determined the brain regions, which played an indispensable role to evoke MAE illusory perception.

On the other hand, to look for the DS neurons that are essential for driving OKR behavior, I hypothesized that the MAE-correlated neurons would be a more likely candidate because of their correlation to the OKR behavior with and without visual motion stimuli. I focused on a spatial hotspot of the MAE-correlated neurons in the pretectum. By laser targeted ablation and focal optogenetic activation, I pinpointed an essential node in the motion processing circuit, which was not only required but also sufficient for OKR behavior. Together, my study of MAE in larval zebrafish led to the second manuscript (Wu et al., 2019) in this cumulative-style thesis.

2. MANUSCRIPTS

2.1 Neuronal Architecture of a Visual Center that Processes Optic Flow

Anna Kramer, **Yunmin Wu**, Herwig Baier, Fumi Kubo

The article “Neuronal Architecture of a Visual Center that Processes Optic Flow” (DOI: [10.1016/j.neuron.2019.04.018](https://doi.org/10.1016/j.neuron.2019.04.018)) was published in Neuron in July 2019.

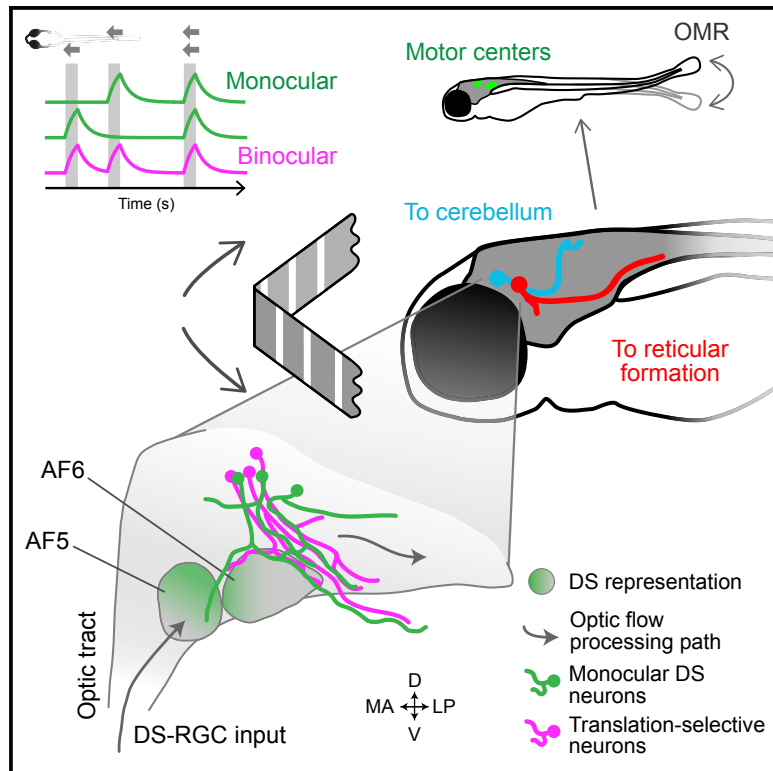
Author contributions:

H.B. and F.K. conceived the project. A.K. performed FuGIMA experiments, generated the UAS:FuGIMA and UAS:FuGIMA-C3PA transgenic lines, and performed anatomical registrations and complementation analyses. **Y.W.** performed the imaging on RGC terminal responses and analyzed the direction-selective responses in RGCs. F.K. generated the UAS:syGCaMP6s transgenic line. A.K., **Y.W.**, and F.K. annotated arborization fields. A.K., **Y.W.**, H.B., and F.K. wrote the manuscript.

Neuron

Neuronal Architecture of a Visual Center that Processes Optic Flow

Graphical Abstract



Authors

Anna Kramer, Yunmin Wu,
Herwig Baier, Fumi Kubo

Correspondence

fumikubo@nig.ac.jp

In Brief

Based on the projection patterns of functionally identified neurons in zebrafish pretectum, Kramer et al. propose that monocular direction-selective neurons combine retinal inputs to generate binocular optic flow responses. Single-neuron tracings highlight two downstream pathways to hindbrain motor centers.

Highlights

- Function-guided inducible morphological analysis (FuGIMA) in pretectum
- Functionally identified, optic-flow-responsive neurons show distinct morphologies
- Direction-selective retinal ganglion cell axons innervate a local pretectal neuropil
- Single-neuron atlas highlights putative optomotor outputs of the pretectal circuit



Kramer et al., 2019, *Neuron* 103, 118–132
July 3, 2019 © 2019 Elsevier Inc.
<https://doi.org/10.1016/j.neuron.2019.04.018>

CellPress

Neuronal Architecture of a Visual Center that Processes Optic Flow

Anna Kramer,¹ Yunmin Wu,¹ Herwig Baier,¹ and Fumi Kubo^{1,2,3,*}

¹Department Genes – Circuits – Behavior, Max Planck Institute of Neurobiology, Am Klopferspitz 18, 82152 Martinsried, Germany

²Center for Frontier Research, National Institute of Genetics, 1111 Yata, Mishima, Shizuoka 411-8540, Japan

³Lead Contact

*Correspondence: fumikubo@nig.ac.jp

<https://doi.org/10.1016/j.neuron.2019.04.018>

SUMMARY

Animals use global image motion cues to actively stabilize their position by compensatory movements. Neurons in the zebrafish pretectum distinguish different optic flow patterns, e.g., rotation and translation, to drive appropriate behaviors. Combining functional imaging and morphological reconstruction of single cells, we revealed critical neuroanatomical features of this sensorimotor transformation. Terminals of direction-selective retinal ganglion cells (DS-RGCs) are located within the pretectal retinal arborization field 5 (AF5), where they meet dendrites of pretectal neurons with simple tuning to monocular optic flow. Translation-selective neurons, which respond selectively to optic flow in the same direction for both eyes, are intermingled with these simple cells but do not receive inputs from DS-RGCs. Mutually exclusive populations of pretectal projection neurons innervate either the reticular formation or the cerebellum, which in turn control motor responses. We posit that local computations in a defined pretectal circuit transform optic flow signals into neural commands driving optomotor behavior.

INTRODUCTION

When animals actively move, or are passively carried through the environment, their visual systems experience continuous movement of stationary features in the visual scene. Neuronal circuits use the drifting retinal images to compute global image motion (optic flow) in order to adjust the animal's body posture and position and stabilize the direction of gaze. In teleost fish and other vertebrates, the optokinetic response (OKR) and the optomotor response (OMR) are typical optic-flow-driven behaviors that compensate for self-motion (Masseck and Hoffmann, 2009a). Eye movements accompanying the OKR consist of slow following phases, which minimize retinal slip, interspersed by quick reset phases. The OMR is characterized by locomotion in the direction of the perceived motion. This ensures that the animal does not drift away from its location, for instance, in a flowing water stream. Zebrafish larvae older than 5 days post-

fertilization (>5 dpf) exhibit both robust OKR and OMR (Neuhauss et al., 1999; Orger et al., 2000, 2004, 2008; Portugues and Engert, 2009; Rinner et al., 2005).

Retinal ganglion cells (RGCs) are the sole output neuron class of the retina. In zebrafish larvae, all RGC axons cross the midline and terminate in nine arborization fields (AFs) (numbered AF1–AF9) in the preoptic area and/or hypothalamus, the thalamus, and the pretectum, in addition to the optic tectum, which is AF10 (Burrill and Easter, 1994; Robles et al., 2014). Each AF and each of the ten layers of the tectum receive input from a distinct combination of morphologically and functionally identifiable RGC types, which form parallel processing channels for specific visual features, such as prey-like objects, looming stimuli, and decreasing or increasing ambient light levels (Robles et al., 2014; Semmelhack et al., 2014; Temizer et al., 2015; Zhang et al., 2017). A unifying hypothesis posits that behaviorally relevant information is packaged in spatially segregated information channels (Dhande and Huberman, 2014), which in turn evoke distinct adaptive behaviors (Baier, 2000; Helmbrecht et al., 2018). Therefore, knowledge of AF tuning provides a productive entry point to decipher the “division of labor” among the different visual and visuomotor processing streams.

Broad activation of the pretectum (accessory optic system) is sufficient to evoke OKR in mammals and zebrafish, and lesions or experimental inactivation suppress this behavior (Cazin et al., 1980; Kubo et al., 2014; Schiff et al., 1988). This observation led to the prediction that the subset of RGCs that encodes the direction of movement, namely the direction-selective (DS-) RGCs (Barlow and Hill, 1963; Dhande and Huberman, 2014), carries information about image motion to the pretectal area. Previous anatomical work in zebrafish had shown that the RGCs that project to the DS sublayer of the optic tectum, the *stratum fibrosum et griseum superficiale 1* (SFGS1) (Gabriel et al., 2012; Gebhardt et al., 2013; Nikolaou et al., 2012), also form collateral branches in AF5 (Robles et al., 2014). This observation made AF5 a prime candidate for the pretectal neuropil region that receives DS-RGC inputs. Until now, however, DS-RGC responses had not been detected in AF5. Rather, a recent study annotated the neighboring area AF6 as the DS-RGC recipient area (Naumann et al., 2016). One goal of the current study was to precisely map DS-RGC inputs within the pretectum to resolve this discrepancy.

In lateral-eyed animals, such as zebrafish, each eye samples roughly one hemisphere of the visual world. Therefore, integrating visual inputs from both eyes is an obvious strategy for

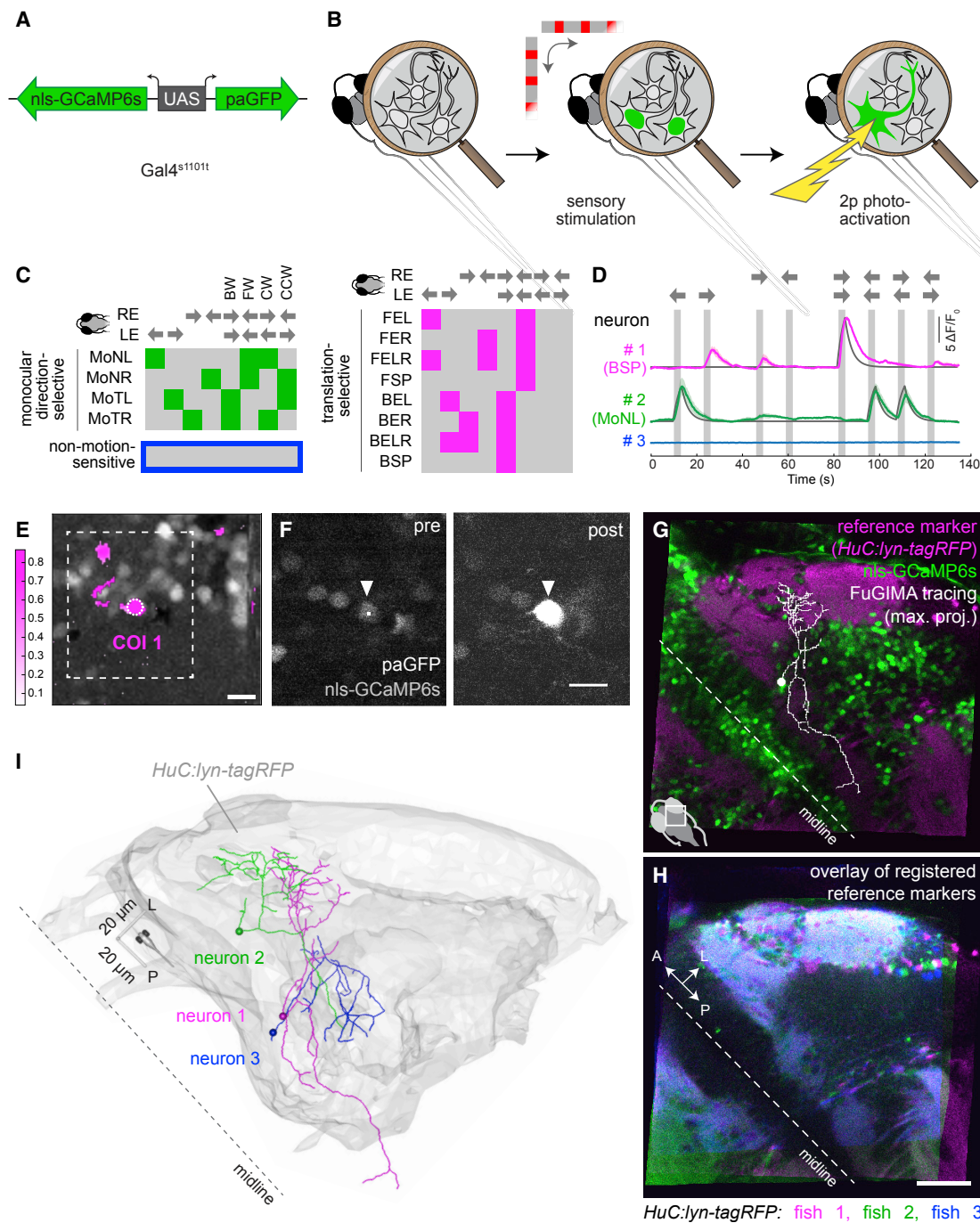


Figure 1. FuGIMA Enables Morphological Reconstructions of Functionally Characterized Pretectal Neurons

(A) The bidirectional genetic construct *UAS:FuGIMA* enables co-expression of nls-GCaMP6s and paGFP using the Gal4-UAS system.

(B) FuGIMA workflow: inactive nls-GCaMP6s and paGFP show little or no fluorescence. During stimulation with horizontally moving gratings, neuronal activity is recorded to determine a cell of interest. PaGFP is focally photoactivated with a two-photon (2p) laser ($\lambda = 750$ nm) and subsequently labels the cell of interest's morphology by diffusion.

(C) (Top) The presented visual stimulus consists of eight motion phases, i.e., four monocular (nasalward left, temporalward left, temporalward right, and nasalward right) and four binocular (BW, backward; FW, forward; CW, clockwise; CCW, counter-clockwise) phases (see also Figure S2A). (Below) Of 2^8 possible regressors, the following response types were investigated (barcode visualization): four monocular direction-selective types (green square); eight translation-selective response types (magenta square); and the non-motion-sensitive type (blue outline). Response type names are adapted from Kubo et al. (2014). Filled squares symbolize neuronal activity during the stimulation phase. The color code applies to other panels of this figure. B, backward translation; E, excited by; F, forward translation; L, to the left eye; Mo, monocular; N, nasalward; R, to the right eye; SP, specific; T, temporalward.

(legend continued on next page)

discriminating translational versus rotational optic flow (i.e., movement in the same or in the opposite directions for left and right eye; Masseck and Hoffmann, 2009a, 2009b; Sabbah et al., 2017; Wang et al., 2019; Wylie et al., 1998). Functional imaging had shown that most pretectal neurons in zebrafish fall into one of two broad categories: (1) “simple” optic-flow-responsive cells, which are driven by DS inputs from one eye and (2) “complex” cells that respond to translational optic flow and are suppressed by rotational optic flow (Kubo et al., 2014). In a parsimonious wiring diagram, simple monocular pretectal cells might combine their DS tuning across hemispheres to generate the responses of complex translation-selective neurons (Kubo et al., 2014). The latter cells might then convey the processed information to premotor centers in the hindbrain, which in turn initiate the OMR.

To test the anatomical predictions of this wiring diagram, we set out to determine the cellular composition of the pretectal optic-flow-processing circuit and test predictions of its input and output pathways. We found that the majority of DS-RGCs terminate in AF5, consistent with earlier anatomical findings (Robles et al., 2014). Morphological reconstructions of optic-flow-responsive pretectal cells showed that the putative dendrites of simple monocular cells overlap with DS-RGC presynaptic terminals in AF5. Complex translation-selective cells have different morphologies and project neurites into a neuropil region abutting, and overlapping with, AF6. Long-range projections connect the optic-flow-sensitive pretectal area to the cerebellum, the reticular formation, and other motor-related centers. Together, our work integrating diverse functional and anatomical datasets traces a universally important visual pathway with cellular resolution from the retina to the hindbrain.

RESULTS

FuGIMA Approach Allows Reconstruction and Visualization of Functionally Identified Pretectal Neurons

We asked how optic flow information is represented by cell types of the pretectum. The pretectum is an anatomically complex region comprised of retinorecipient and non-retinorecipient cells (Yáñez et al., 2018). Pretectal cells with different functional properties are intermingled (Kubo et al., 2014; Naumann et al., 2016). To reveal the morphologies of optic-flow-responsive pretectal neurons, we employed the all-optical method FuGIMA (function-guided inducible morphological analysis) (Förster et al., 2018). FuGIMA is based on the co-expression of nuclear local-

ized GCaMP6s (nls-GCaMP6s) and cytoplasmic photoactivatable GFP (paGFP) under the control of a bidirectional upstream activating sequence (UAS) (Janus-UAS; Distel et al., 2010; Paquet et al., 2009; Figure 1A). Although both nls-GCaMP6s and photoactivated paGFP emit green fluorescence, signals from the two proteins are separated by way of their nuclear versus cytoplasmic localization, thus allowing their combination in the same cell.

We used zebrafish larvae expressing the FuGIMA components in all neurons by crossing the panneuronal driver *Gal4s1101t* with *UAS:FuGIMA* (see STAR Methods). Neuronal activity in the pretectum was recorded by imaging of nls-GCaMP6s signals upon stimulation with whole-field motion (Figure 1B). The visual stimulus protocol consisted of monocular and binocular optic flow patterns (horizontally moving gratings) in a sequence of eight phases: four monocular phases with gratings shown to the left or right side of the fish, moving either nasally or temporally, and four binocular phases, namely backward, forward, clockwise, and counter-clockwise motions (Figure S2A). Responses to each of the eight phases were used to assign to each cell a barcode, which represents the stimulus combination to which the cell is tuned (Kubo et al., 2014; Figure 1C). A cell of interest was then chosen for photoactivation, based on its response to optic flow, and labeled by focusing 750-nm laser light in two-photon (2p) mode onto the soma (Figures 1D–1F). Photoactivated paGFP diffuses into the neurites and, after several hours, reveals the morphology of the cell (Förster et al., 2018; Figure 1G). The maximum distance over which neurites can be traced is dependent on the diffusion properties of paGFP and was empirically determined to be around 200 μm (Figures S1A and S1B; see STAR Methods).

Pretectal Neurons with Optic Flow Tuning Differ in Their Morphologies from Non-Motion-Sensitive Neurons

Out of the 256 (2^8) theoretically possible barcodes, we focused on the following three response classes (Kubo et al., 2014): simple monocular DS (comprising four response types); complex translation-selective (eight response types); and non-motion-sensitive as controls (activity not locked to any motion phase; Figure 1C). We used a regressor-based analysis to semi-automatically identify response types of interest in a near-online fashion (see three exemplary GCaMP6s fluorescent traces in Figure 1D). Among these cells, we selected one cell of interest for photoactivation (correlation map of regressor 1; Figures 1E and 1F). After allowing for diffusion of GFP fluorescence, cells of interest were manually traced (Figure 1G) and registered to a

(D) nls-GCaMP6s fluorescence time series of example neurons of distinct response types identified by regressor-based analysis (overlaid on the respective regressor, gray). Solid colored line, average of three repetitions; shaded area, SEM; gray bars, stimulation periods.

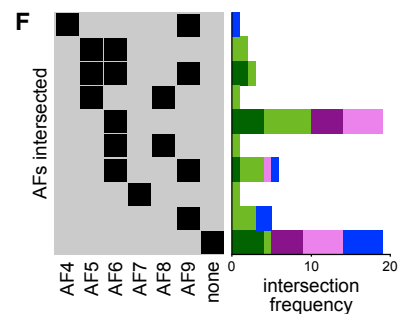
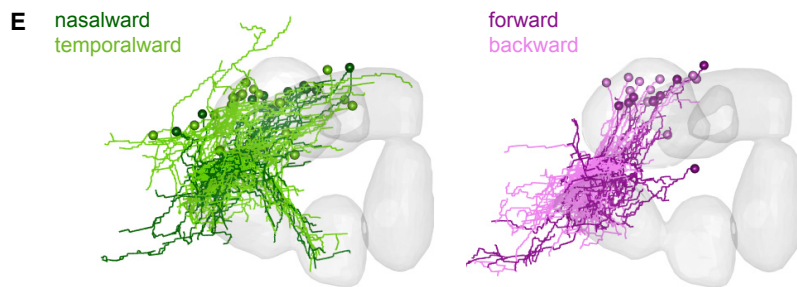
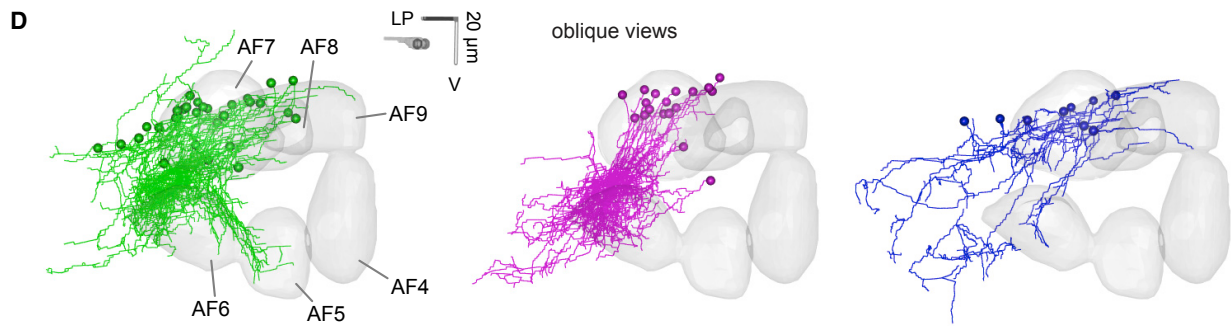
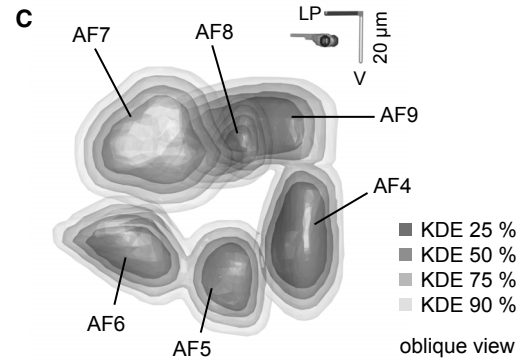
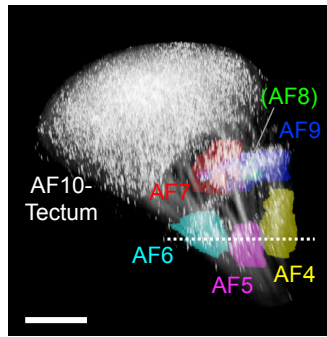
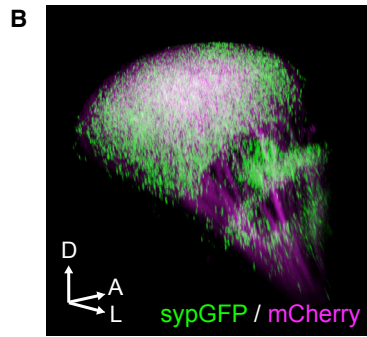
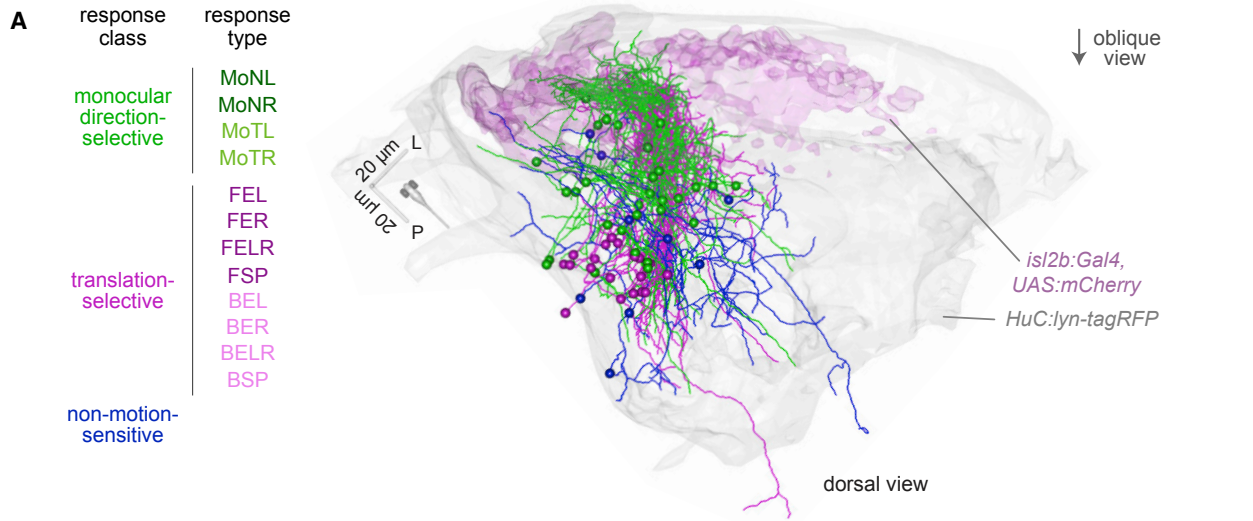
(E) Overlay of field-of-view (mean $\Delta F/F_0$) and pixel-wise regressor-based analysis (color bar: Pearson's correlation coefficient), highlighting two neurons best correlated with the regressor 1 shown in (D) (top trace). The white dotted circle indicates example neuron 1 (COI1, cell of interest 1); white dashed square indicates field of view used in (F).

(F) Photoactivation of neuron 1. Before photoactivation, most nuclei exhibit dim nls-GCaMP6s fluorescence. After photoactivation of the soma, neuron 1 exhibits bright paGFP fluorescence (white arrowhead, neuron 1; small white square, approximate photoactivation region).

(G) Tracing of photoactivated neuron 1 (white, maximum intensity projection) superimposed on one plane of the registered experimental z stack (green, nls-GCaMP6s/paGFP; magenta, *HuC:lyn-tagRFP*).

(H) Overlay of the reference marker (*HuC:lyn-tagRFP*) derived from three experimental fish that have been registered to the standard brain.

(I) 3D rendering of the standard brain surface (gray) with three registered tracings (dorsal view). The color of the three tracings corresponds to that used in (D). Scale bars represent 10 μm in (E) and (F) and 50 μm in (H). See also Figure S1.



(legend on next page)

standard brain for interindividual comparisons via a reference marker (*HuC:lyn-tagRFP*; Figures 1H, 1I, S1D, and S1E; see STAR Methods).

We reconstructed the morphologies of 58 pretectal neurons from 46 fish (30 monocular DS neurons, 19 translation-selective neurons, and 9 non-motion-sensitive neurons; for individual calcium traces, see Figures S2B and S2C). The respective frequencies of response types detected in our FuGIMA dataset was overall similar to Kubo et al. (2014); however, monocular DS neurons responding to nasalward motion (i.e., MoNR and MoNL) located in the brain ipsilateral to the visually stimulated eye were not identified in this limited dataset (Figures S2D and S2E).

Motion-sensitive neurons in our FuGIMA dataset showed overall similar morphologies; their stem neurite pointed in a lateral-anterior-ventral direction (Figure 2A; Video S1). The neurites of non-motion-sensitive neurons, on the other hand, typically branched and extended in the anterior and posterior directions, suggesting that the morphologies of optic-flow-sensitive cells differ fundamentally from those of the non-motion-sensitive control neurons (Figure 2A). Cell bodies of monocular DS neurons were widely distributed in an anterior-lateral domain, whereas the translation-selective neurons were located in a more confined, posterior-medial domain (Figure S4B).

Neurons with Monocular DS versus Binocular Translational Optic Flow Tuning Differ in Their AF Projection Patterns

To examine which FuGIMA neurons are potentially retinorecipient, we registered RGC axon projections (Figure 2B) to the standard brain (Figures S3A and S3B; see STAR Methods). Guided by known anatomical features (Burrill and Easter, 1994; Robles et al., 2014), the volumes of AFs 4–10 could be reliably annotated (see STAR Methods; Video S2). We found that the majority of optic-flow-responsive cells (35 of 49; 71%) overlapped with one or more of the AFs. We noticed that monocular DS cells (6 of 30; 20%) extended neurites into AF5, regardless of their preferred direction (Figures 2D, left, 2E, left, and 2F; individual tracings in Figure S4A; Video S1), and translation-selective neurons did not receive inputs from the AF5 region. On the other hand, both monocular DS and translation-selective classes densely branch in a region that is abutting, and overlapping with, the dorsal part of AF6. In fact, all translation-selective cells project ventrally in the direction of AF6, regardless of whether

they are responsive to forward or backward motion (Figures 2D, middle, and 2E, right).

The analysis of intersections of all FuGIMA tracings with AF boundaries (defined by kernel density estimate [KDE] = 50%) revealed that many FuGIMA cells (25 of 58; 43%) intersected with one AF: 19 with AF6; 5 with AF9; and 1 with AF7. About a quarter of FuGIMA-traced cells (14 of 58; 24%) intersected with more than one AF in varying combinations (Figure 2F). The total number of intersections per AF changed with the applied threshold for KDE. However, as we varied KDE from 25% to 75%, the number of cells overlapping with AFs 5, 7, and 8 remained constant ($n = 6, 1, \text{ and } 2$, respectively), suggesting that overall intersection patterns of response classes do not depend on the stringency with which these AFs are annotated (Figure S3C).

DS-RGCs Project to Pretectal Neuropil Area AF5

Monocular DS-responsive pretectal neurons may inherit their tuning from DS-RGCs that project to AF5. To test this prediction, we measured responses to moving gratings in RGC axon terminals and aligned the functional responses from multiple fish in a second standard brain, “RGC standard brain,” which we constructed based on the *isl2b:Gal4* × *UAS:mCherry* labeling pattern (Figure S5A). The *isl2b* promoter allows targeting of the vast majority of RGCs (Pittman et al., 2008), and Dil injection confirmed that the *isl2b:Gal4* line labels most of the RGCs terminating in the ventrally located AF4–AF6 (Figure S5E). For imaging of axon terminals of DS-RGCs in the pretectum, we expressed synaptophysin-tagged GCaMP6s (syGCaMP6s) in RGCs (*isl2b:Gal4*; *UAS:syGCaMP6s*; Figures S5B–S5D). Fusion to synaptophysin targets the calcium indicator to presynaptic terminals (Dreosti et al., 2009; Dunn et al., 2016; Nikolaou et al., 2012). Recorded syGCaMP6s signals were then mapped onto the RGC standard brain (see STAR Methods), and accuracy of the mapping was confirmed by overlay of multiple brains with the RGC standard brain (Figures S5F–S5K).

We examined visual motion-induced activity in RGC terminals by presenting monocular moving gratings to the contralateral eye of the fish. Visual stimuli were presented from the side of the fish, and recorded brain areas included most of the tectal neuropil (AF10) and more ventral AFs in the pretectum and thalamus, including AF4–AF6 (Figures 2B and 3A). Response profiles of AF4 and AF6 were largely consistent with previous studies, with AF4 being activated by ON and AF6 by OFF whole-field luminance changes (Temizer et al., 2015; Zhang et al., 2017;

Figure 2. Monocular DS and Translation-Selective Neurons Show Different Morphologies

(A) 3D rendering of all FuGIMA tracings ($n = 58$ tracings) with the standard brain (*HuC:lyn-tagRFP*) and RGC terminals as labeled with *isl2b:Gal4*, *UAS:mCherry*. The tracings are color coded according to the neurons' response class (dorsal view). See also Video S1.
 (B) Anatomical representation of AFs. (Left) SypGFP signal driven by *atoh7:Gal4* driver reveals distinct AFs at 6 dpf (compound of three fish). (Right) Annotation of AFs in the same 3D volume is shown. Dotted line corresponds to the optical planes for imaging AF4, AF5, and AF6. See also Video S2.
 (C) Boundaries of AFs (from the RGC standard brain) after registration to the FuGIMA standard brain. 3D rendering of a thresholded kernel-density estimation (KDE) of co-registered AF masks from (B) (thresholded to 25%, 50%, 75%, and 90%; $n = 7$ bridging z stacks, from 4 fish). See also Figure S3.
 (D) 3D rendering of FuGIMA tracings grouped by response class together with AF masks (oblique views; AFs 4–9; KDE = 50%).
 (E) Further classification of FuGIMA neurons by direction selectivity (left: light green, monocular temporalward; dark green, monocular nasalward. right: light magenta, backward; dark magenta: forward).
 (F) Analysis of morphological types of all FuGIMA neurons. Intersections of individual tracings with AFs 4–9 reveals widespread intersections between FuGIMA tracings and the AFs (black squares symbolize the intersection with the indicated AF). (Right) Intersection frequency according to response class is shown. Scale bar represents 50 μm in (B). See also Figures S2, S3, and S4.

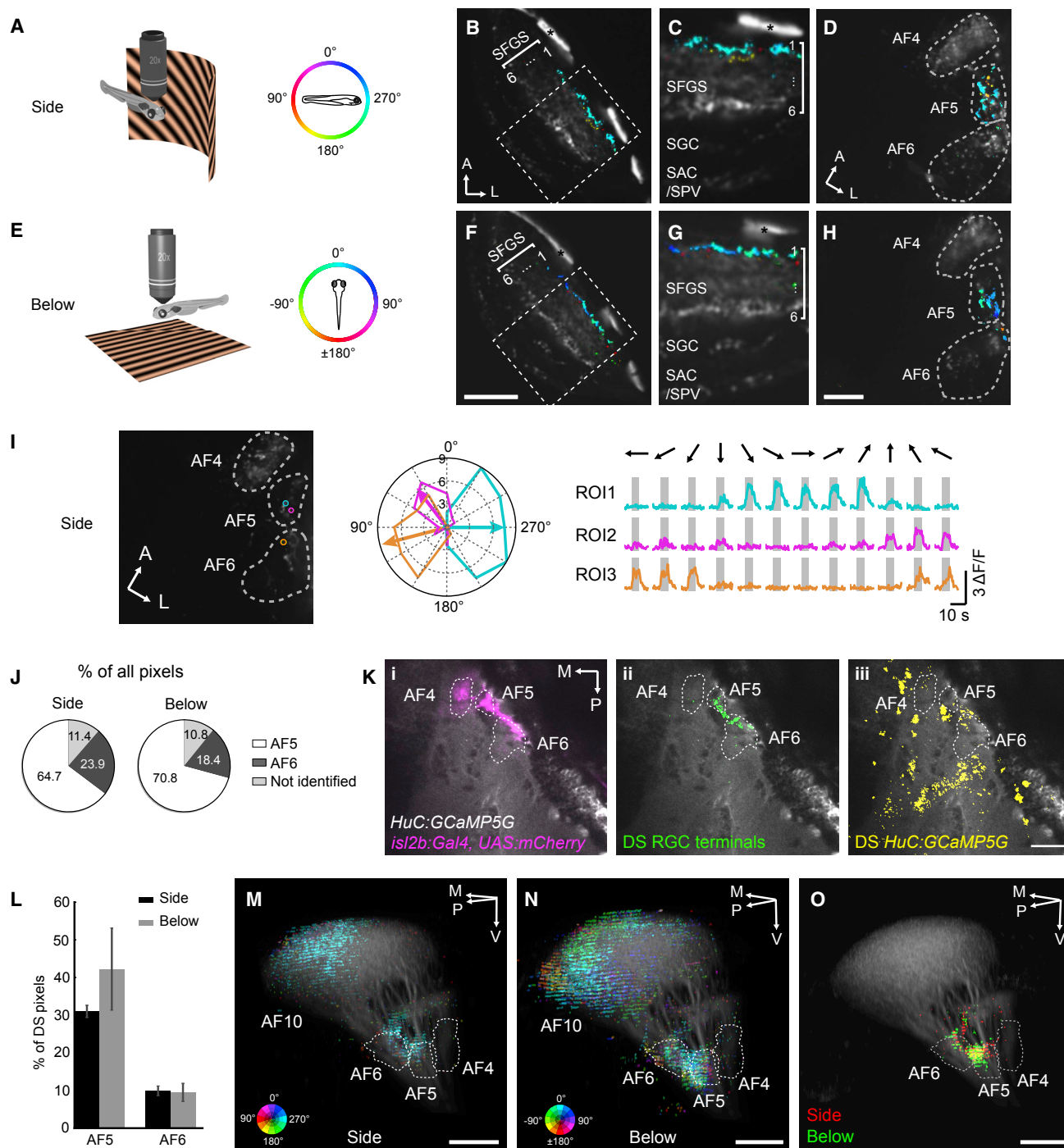


Figure 3. Direction-Selective RGCs Largely Terminate in Arborization Fields AF5 and Tectum (AF10)

(A) Schematic of the experimental setup for visual stimulation with moving gratings presented from the side. Color indicates direction of motion. (B–D) DS pixels in AF10 (B and C) and AF4, AF5, and AF6 (D). (E) Schematic of the experimental setup for visual stimulation with moving gratings presented below. (F–H) DS pixels in AF10 (F and G) and AF4, 5, and 6 (H). In (B)–(D) and (F)–(H), DS pixels are plotted on top of the mean image of syGCaMP6s (gray). (I) Representative responses of DS-RGC terminals in AF5 and AF6. Visual stimuli were presented from the side. ROIs correspond to synaptic puncta marked in the left image. Polar plot (middle) is derived from the $\Delta F/F$ traces shown on the right. (J) Distribution of DS pixels identified in ventral AFs. The pie charts show the percentage of DS pixels residing in AF5, AF6, and a region neither AF5 nor 6 ("not identified"), summed from 6 and 7 fish for side and below stimulus presentation, respectively.

(legend continued on next page)

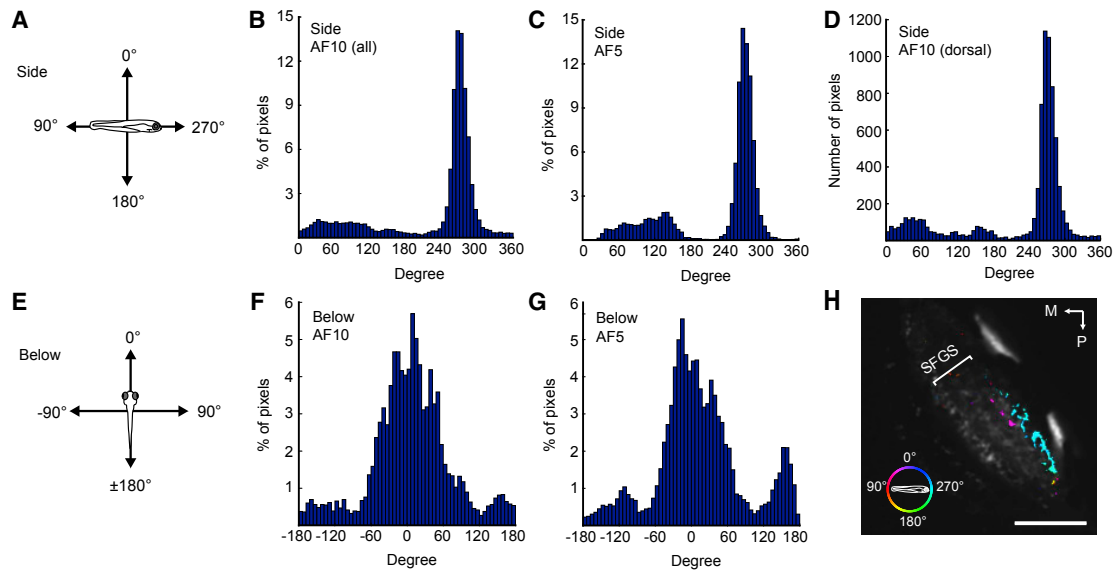


Figure 4. Distribution of Preferred Directions of DS-RGCs Reveals Shared Inputs in AF5 and Tectum

(A) Direction space of motion stimulus presented from the side.

(B and C) Distributions of preferred directions of DS-RGC terminals in AF10 (B; N = 6 fish) and AF5 (C; N = 6 fish). Motion was presented from the side.

(D) Distribution of preferred direction of DS-RGC terminals in the dorsal AF10. In contrast to (B), where the entire AF10 was sampled, only 3 planes (separated by 4 μm) in AF10 were selected in this histogram, as was reported previously (Nikolaou et al., 2012).

(E) Direction space of motion stimulus presented from below.

(F and G) Distributions of preferred directions of DS-RGC terminals in AF10 (F; N = 7 fish) and AF5 (G; N = 7 fish). Motion was presented from below.

(H) DS response map of a single representative optical plane in the dorsal AF10 analyzed in (D). Scale bar: 30 μm .

Figures S6A–S6C). We then identified pixels that exhibited DS signals (“DS pixels”; see STAR Methods). Within the tectum, DS pixels localized to the posterior half of the SFGS1 (Figures 3B, 3C, S6D, and S6E), as described previously (Nikolaou et al., 2012). In a more ventral optical plane, DS pixels were found predominantly in AF5 (64.7%), with fewer DS pixels in AF6 (23.9%; N = 6; Figures 3D and 3J). This difference was further augmented when the relatively larger number of synaptic puncta within AF6 were considered. DS pixels represented about 30%–40% of the total pixels in AF5, whereas in AF6, the DS pixels comprised about 10% of the total pixels (Figure 3L). The responses localized to AF6 by our anatomical mask were observed in terminals close to the boundary to AF5, suggesting that the corresponding terminals might sit on branches of AF5-projecting

RGCs (Figures 3D and 3I). In addition, a sparse subset of RGC terminals in AF6 was orientation selective (OS) (Figures S6F–S6J). In conclusion, the majority of the DS-RGC inputs are sent to AF5.

AF5 (and SFGS1) Receive Retinal DS Responses Regardless of RGC Soma Position within the Retina

In a previous study (Naumann et al., 2016), motion stimuli were presented from below, which activates predominantly the dorsal part of the retina (Robles et al., 2014; Stuermer, 1988). It is conceivable that dorsally positioned DS-RGCs project to different AFs than those that were activated by motion shown from the side. To test this possibility, we repeated above imaging experiments while displaying moving gratings from below

(K) Overlay of a registered *HuC:GCaMP5G* image (gray) with RGC axons (i, *isl2b:Gal4, UAS:mCherry*), DS-RGC terminals (ii, identified from below projection; sum of 6 fish), and DS neuropil of *HuC:GCaMP5G* fish (iii, identified from below projection; sum of 5 fish) in an optical plane that contains AF4, AF5, and AF6. DS-RGCs and DS neuropil represent all DS populations tuned to any direction of motion.

(L) Percentage of DS pixels relative to the entire pixel counts in AF5 and 6. Average pixel counts in each AF were quantified using anatomical stacks of *isl2b:Gal4, UAS:sypGFP* fish (see STAR Methods for details). N = 6 fish (side) and 7 fish (below) for each AF. Error bars represent SEM.

(M and N) 3D representations of DS-RGC terminals. For side-presented 3D map (M), both AF10 and AF4, AF5, and AF6 volumes are pooled from 6 imaged volumes. For below-presented 3D map (N), both AF10 and AF4, AF5, and AF6 volumes are pooled from 7 imaged volumes. Color wheels represent the preferred directions of DS pixels. The intensity of DS pixels corresponds to the probability of a particular pixel to be DS across all imaged fish (the maximum intensity corresponds to the frequency of 0.67 and 0.57 for M and N, respectively). See also Videos S3 and S4.

(O) Comparison of DS-RGC terminals responsive to side versus below presentations. Composite 3D map of a single fish that underwent both side and below presentations. Note that DS-RGC terminals identified by side (red) and below (green) presentations co-localize in AF5. A, anterior; L, lateral; M, medial; P, posterior; SAC, *stratum album centrale*; SFGS, *stratum fibrosum et griseum superficiale*; SGC, *stratum griseum centrale*; SPV, *stratum periventriculare*; V, ventral; *, skin auto-fluorescence.

Scale bars represent 20 μm (F), 10 μm (H), 30 μm (K), and 50 μm (M–O). See also Figures S5 and S6.

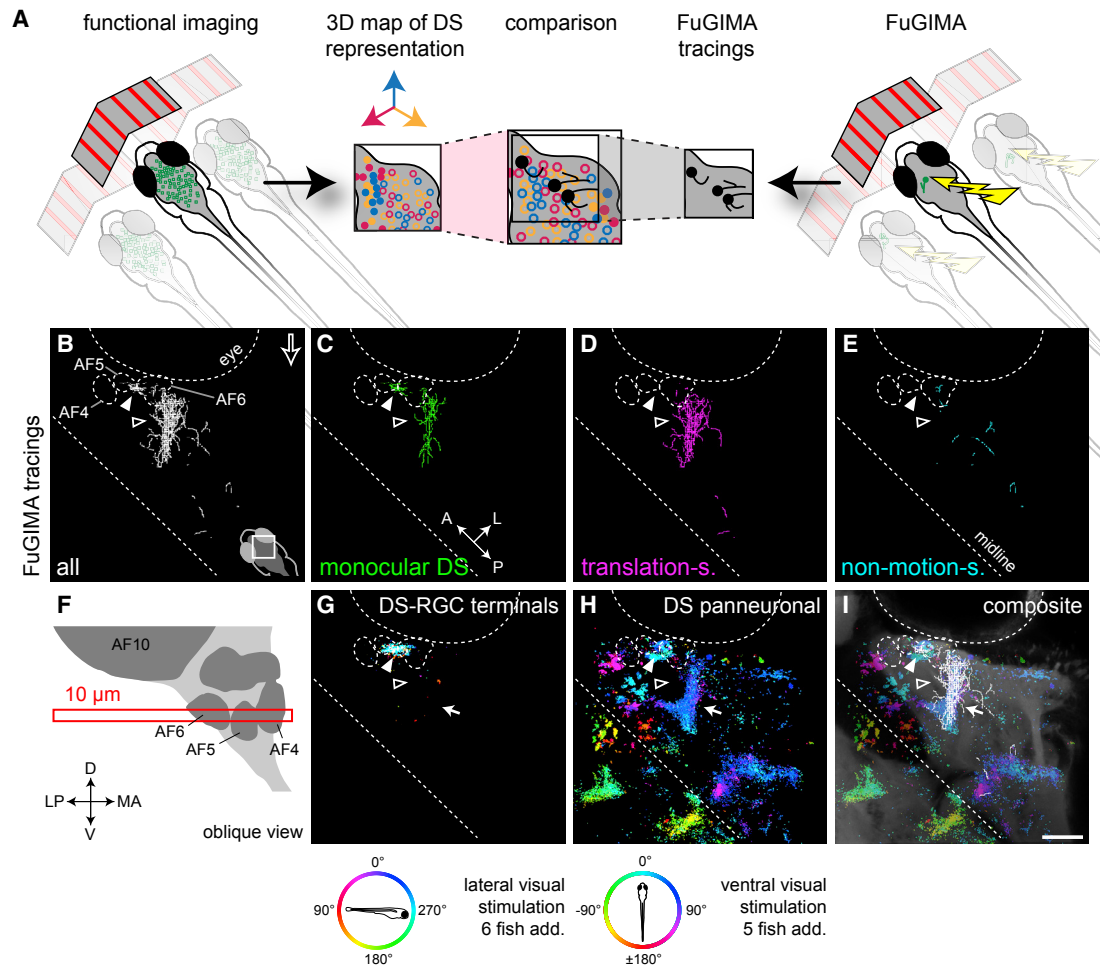


Figure 5. Co-registration of FuGIMA with Two Functional Imaging Datasets Shows Overlap of DS-RGC Input with Monocular DS, but Not with Translation-Selective, Neurons

(A) Schematic illustrating acquisition and integration of the functional maps and the FuGIMA dataset.

(B–I) A slice of the co-registered volume at the level of the AFs 4–6 with FuGIMA tracings and functional maps of DS-RGC terminals and DS neurons (right hemisphere, maximum intensity projection over $z = 10 \mu\text{m}$; see schematic in F; of 58 FuGIMA tracings, 42 of the following classes extend into the slice: 19 monocular DS; 17 translation-selective; 6 not motion-sensitive).

(B–E) FuGIMA tracings (open white arrowhead, FuGIMA tracing bundle; filled white arrowhead, small tracing patch at the border between AFs 5 and 6; open arrow, direction of oblique view): (B) all (white); (C) monocular DS (green); (D) translation-selective (magenta); and (E) non-motion-sensitive (blue).

(F) Schematic of z stack slicing (oblique view used to visualize optic tract [light gray] and AFs [dark gray]).

(G) Registered 3D map of DS-RGC terminals (*isl2b:Gal4, UAS:syGCaMP6s*; see color wheel below for direction of moving gratings presented from side; composite of 6 fish).

(H) Registered 3D map of DS-panneuronal (*HuC:GCaMP5G*; white arrow, broad band of DS pixels; see color wheel below for direction of moving gratings presented from below; composite of 5 fish).

(I) Composite of DS-panneuronal with all FuGIMA tracings and standard brain reference marker (*HuC:lyn-tagRFP* in gray).

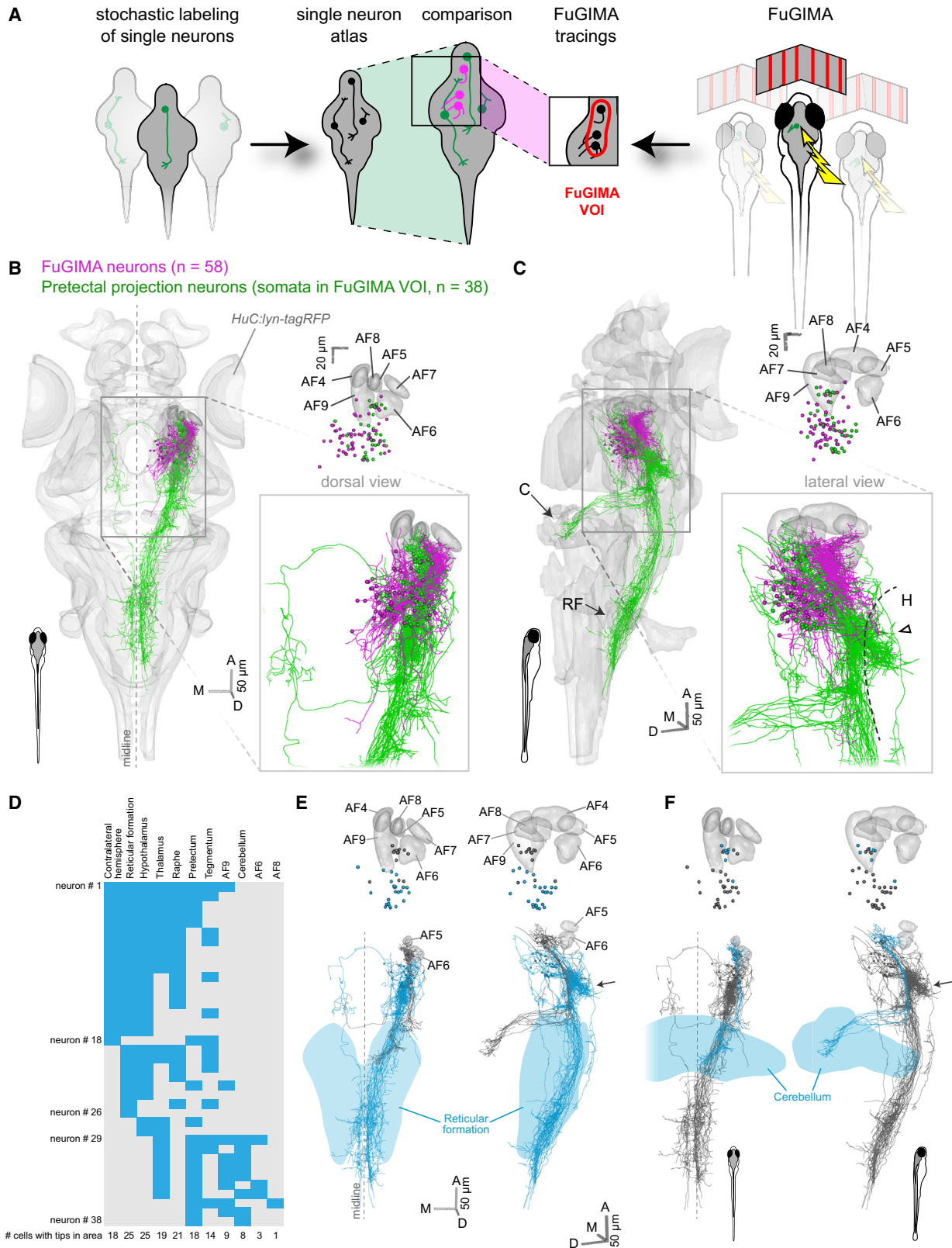
For (G)–(I), imaging artifact DS pixels located in the eye were removed with a mask. Scale bar represents $50 \mu\text{m}$ (I).

(Figures 3E–3H). Similar to the presentation from the side, the majority of DS-RGC inputs were found in AF5 (70.8%), and fewer were found in AF6 (18.4%; $N = 7$ fish; Figure 3J). DS-RGC inputs from dorsal retina were also observed in SFGS1 (Figures 3F, 3G, S6D, and S6E). This indicates that DS-RGCs project to AF5 and SFGS1, regardless of their soma positions along the dorsoventral axis of the retina.

To localize DS-RGC pixels within the larger neuropil volume surrounding the AFs, we registered an image stack from the

HuC:GCaMP5G line to our RGC standard brain. As expected, RGC axons occupied only a small subvolume of the pretectal neuropil labeled in *HuC:GCaMP5G* (Figure 3Ki). Registration of visual responses to whole-field motion in the RGC standard brain revealed that DS responses in the panneuronal *HuC:GCaMP5G* neuropil extended outside of the AFs (Figures 3Kii and 3Kiii).

To establish a 3D map of DS representations in RGC terminals, we mapped DS pixels identified in multiple fish onto the RGC standard brain. In the tectum, DS pixels occupied the posterior



(legend on next page)

half of the neuropil volume when the stimulus was presented from the side (Figure 3M; Video S3). When the stimulus was projected from below, DS pixels were preferentially identified in the ventral tectum (Figure 3N; Video S4). This location is consistent with the topographic organization of the retinotectal projection (Robles et al., 2014; Stuermer, 1988). Notably, in the pretectum, a co-registration of DS pixels obtained from a single fish, which was stimulated both from the side and from below, shows that the identified DS pixels were co-localized in a similar volume, corresponding to AF5 (Figure 3O). In summary, our results demonstrate that RGC terminals exhibiting DS responses in the pretectal neuropil are situated predominantly in AF5 and that this is independent of the position of the visual stimulus.

AF5- and SFGS1-Projecting DS-RGCs Show Very Similar DS Tuning, Consistent with Collateral Branching from the Same Axon

We hypothesized that the DS-RGC axon terminals in AF5 are collateral branches of RGCs projecting to SFGS1. If so, preferred directions of RGC axons in AF5 should be identical to those in SFGS1. When the visual stimuli were presented from the side (Figures 4A–4D and 4H), the majority of the DS pixels were tuned to forward stimulus motion ($\sim 270^\circ$) in both the tectum (Figure 4B) and AF5 (Figure 4C), with a much smaller population of DS pixels with broadly distributed preferred directions between 30° and 180° . In the dorsal part of the tectum, we observed three populations of DS-RGCs, tuned to whole-field motion in a forward (270°), oblique-backward (around 45°), and downward (around 160°) direction, respectively, as reported previously (Lowe et al., 2013; Nikolaou et al., 2012; Figures 4D and 4H). When the visual stimuli were presented from below, the majority of DS pixels in SFGS1 and AF5 preferred the forward direction ($\sim 0^\circ$) as well (Figures 4E–4G). These results are in agreement with a direction-of-motion-sensitive visual pathway composed of three differently tuned classes of DS-RGCs, whose axons branch in AF5 on their way to SFGS1.

DS-RGC Terminals Spatially Overlap with Dendrites of Monocular DS-Pretectal Cells in AF5

We next tested the prediction that the neurites of monocular DS pretectal neurons coincided in space with DS-RGC terminals. In FuGIMA experiments, calcium responses in the neuropil are invisible due to nuclear localized GCaMP. Therefore, we registered two sets of functional imaging data to the FuGIMA standard brain: DS signals recorded in RGC terminals

(*isl2b:Gal4, UAS:syGCaMP6s*) and DS signals from all neurons (*HuC:GCaMP5G*; Figure 5A). In this overlay, DS-RGC pixels overlapped with dendrites from monocular DS cells, but not with those of translation-selective neurons (Figure 5G). Neurites of both monocular DS and translation-selective cells were also seen outside the RGC neuropil, caudal to AF6 (Figures 5B–5D). This region was contained in the broader pretectal DS neuropil revealed by *HuC:GCaMP5G* imaging (Figures 5H and 5I). Tracings of control neurons (non-motion-sensitive) did not overlap with DS-RGC pixels (Figure 5E). Taken together, registration of two 3D maps of functional data to the FuGIMA dataset suggests that monocular DS neurons receive direct input from DS-RGCs in AF5 and that additional DS responses in the pretectum emanate from branches of pretectal optic-flow-responsive neurons.

Distinct Classes of Pretectal Neurons from the Optic-Flow-Processing Region Project to Premotor Centers

We hypothesized that translation-selective neurons might project to premotor centers that drive the OMR. The FuGIMA method relies on relatively slow, distance-dependent diffusion of paGFP and is therefore unsuited to label long-range projections. To investigate the connections of the DS pretectal area, we employed “virtual tract tracing” by interrogating the cellular-resolution brain atlas of Kunst et al. (2019) [this issue of *Neuron*]. At the time of analysis, this dataset contained the morphologies of 1,743 single-cell tracings, all co-registered within a standard brain. Specifically, we focused on pretectal projection neurons (PPNs) whose cell bodies reside in immediate vicinity of FuGIMA neurons (Figure 6A).

38 PPNs were found to reside within the cloud-shaped “FuGIMA volume of interest” (FuGIMA VOI) (offset between cell body center and edge of volume $\sim 10 \mu\text{m}$; Figure S7A). Cell bodies of these neurons (Figure S7B) tend to be located laterally compared to those of the FuGIMA neurons (Figure 6B). Axons of PPNs terminate in the hindbrain reticular formation (25 “pre-pecto-reticular” PPNs; 18 = 72% thereof in the contralateral hemisphere) or the cerebellum (8 “pre-pecto-cerebellar” PPNs) in a mutually exclusive pattern (Video S5). A large fraction of neurons also terminate in the hypothalamus (25 of 38), the thalamus (19 of 38), the raphe (21 of 38), the pretectum (18 of 38), and tegmentum (14 of 38; including the nucleus of the medial longitudinal fascicle, the oculomotor nucleus, and the nucleus isthmi), in various combinations. AFs encompassing PPN termini are AF9 (9 of 38), AF6 (3 of 38), and AF6 (1 of 38). The cell bodies

Figure 6. Pretectal Projection Neurons Target the Cerebellum and Ventral Hindbrain

- (A) Schematic illustrating the strategy to combine the single-neuron atlas of Kunst et al. (2019) and the FuGIMA dataset.
 (B and C) 3D representation of the standard brain (*HuC:lyn-tagRFP*) together with all FuGIMA neurons (magenta, $n = 58$) as well as pretectal projection neurons (PPNs) (green, $n = 38$), chosen based on their soma location within the FuGIMA “volume-of-interest” (FuGIMA VOI) (Figure S7).
 (B) (Left, dorsal view, top right) Dorsal view of cell bodies with AFs 4–9; (bottom right) detail of tracings.
 (C) As (B) but lateral view (C, cerebellum; H, hypothalamus; RF, reticular formation; dashed line, dorsal border of hypothalamus; open arrowhead, dense branching of PPNs).
 (D) Intersection analysis of PPNs with annotated brain areas, i.e., contralateral hemisphere, reticular formation, hypothalamus, thalamus, raphe, pretectum, tegmentum, AF9, cerebellum, AF6, and AF8. Each row represents one neuron; blue filled rectangles symbolize intersection with the annotated brain area.
 (E) 3D rendering of intersection of PPNs with the reticular formation (blue, intersecting tracings [$n = 25$ of 38 PPNs]; gray, not intersecting PPNs; light blue, reticular formation; top, somata and AFs 4–9; bottom, tracings and AFs 5 and 6; left, dorsal view; right, lateral view; arrow, dense branching area in dorsal hypothalamus).
 (F) As (E) but intersection of PPNs with the cerebellum (blue, intersecting tracings [$n = 8$ of 38 PPNs]; light blue, cerebellum).
 See also Figure S7 and Video S5.

of pretecto-reticular PPNs reside in the posterior-lateral part of the FuGIMA VOI (Figure 6E). Their axons heavily branch in an area directly posterior and about 20 μm ventral to the main branching area of FuGIMA cells, partially crossing the dorsal border of the hypothalamus (Figures 6C and 6E). Most of them (18 of 25) project bilaterally (Figures 6D and 6E). In contrast, cell bodies of the pretecto-cerebellar PPNs were mainly found in an anterior cluster lateral to AF9 (Figure 6F). Their neurites branch in the vicinity of the cell body, contacting AF6 ($n = 2$), or AF9 ($n = 5$), again in varied combinations, and terminate in two patches of the medial cerebellum (Figures 6D and 6F). The traced set of PPNs did not intersect with AF4, AF5, or AF7. In conclusion, two mutually exclusive groups of PPNs connect the optic-flow-sensitive region to the reticular formation (often with collaterals in the hypothalamus) and to the cerebellum (often with collaterals in thalamus and pretectum).

DISCUSSION

This study has revealed the cellular composition, as well as the afferent and efferent pathways, of the optic-flow-processing center in the zebrafish pretectum. We demonstrate that signals from DS-RGCs are transmitted primarily to retinal arborization field AF5 in the pretectal neuropil. DS-RGC axon terminals spatially overlap with putative dendrites of simple, monocular DS pretectal neurons in AF5, but not with those of complex, translation-selective neurons. Complementation of the FuGIMA dataset with tracings from a single-neuron atlas has revealed projection targets of pretectal neurons, i.e., the reticular formation, the tegmentum, the hypothalamus, and the cerebellum. Based on our findings, we propose a model of processing stages in the optic-flow-responsive pathway (Figure 7). Direction selectivity, transmitted by RGC axons to AF5, is inherited by simple, monocular DS neurons and is then combined across the two eyes, likely in the densely innervated neuropil dorso-posterior to AF6, to generate translation-selective tuning in complex cells. The behaviorally relevant binocular optic flow information, computed in the pretectum, is then further relayed to premotor areas in the hindbrain to ultimately drive optomotor behavior.

We demonstrate that DS-RGCs project mainly to AF5. A smaller fraction of DS-responsive RGC terminals was also found in AF6. It is noteworthy that, to generate the consensus anatomical mask, AF boundaries were drawn by outlining the silhouettes of neuropil shapes in multiple fish. Functional data were not taken into consideration in these AF annotations, and it is conceivable that axon collaterals do not respect our annotated anatomical boundaries. It is plausible that the DS responses detectable in AF6 originate from branches of RGC axons that are primarily targeting AF5. This interpretation is in contrast to a previous study (Naumann et al., 2016), which implicated AF6 in pretectal DS-RGC processing. Naumann et al. (2016) identified a conglomerate of neuropil areas exhibiting DS responses as “AF6.” The fish they imaged carried the *HuC:GCaMP5G* transgene, in which GCaMP is expressed in almost all neurons. Because GCaMP expression was therefore not limited to RGCs, this approach does not differentiate AFs or disambiguate RGC terminals from axons or dendrites that arise from other neurons. When we registered our two imaging datasets per-

formed in *HuC:GCaMP5G* transgenic fish and RGC terminals into the FuGIMA dataset, the DS neuropil area detected in *HuC:GCaMP5G* transgenic fish overlaps with both RGC terminals and neurites of motion-responsive pretectal neurons. This result suggests that Naumann et al.’s AF6 is likely a mix of AF5, AF6, and additional neuropil formed by pretectal neurons; it is certainly not exclusively AF6.

A previous comprehensive analysis of projection patterns of RGC axons revealed that AF5-projecting RGCs do not form collaterals in AF6 and vice versa (Robles et al., 2014). Furthermore, all AF5- and AF6-projecting RGCs in addition innervate specific layers of the tectum. AF6-projecting RGCs innervate the deepest layer of the SFGS (SFGS6) and the *stratum griseum centrale* (SGC) (Robles et al., 2014), which do not show DS responses (Gabriel et al., 2012; Nikolaou et al., 2012). AF5-projecting RGCs, on the other hand, innervate the most superficial layer of the SFGS layer (SFGS1), which receives DS-RGC input (Gabriel et al., 2012; Nikolaou et al., 2012; this study). Assuming that multiple axonal branches of single DS-RGCs share the same tuning, our functional imaging result is therefore consistent with the anatomical organization of RGC projection patterns, further supporting AF5 as a center for DS motion processing.

We applied the FuGIMA technique (Förster et al., 2018) to tie tuning properties of individual neurons to their morphologies. This method is based on diffusion of the fluorescent paGFP and is therefore well suited to label local neurites, particularly dendrites, whose calibers are generally bigger than those of axons (Vishwanathan et al., 2017) but cannot be used to trace axons over long (>200 μm) distances. We focused on monocular DS neurons, i.e., neurons that respond to movement detected by the contralateral eye, located in the anterior medial cluster of the pretectum, as reported before (Kubo et al., 2014). Ipsilateral monocular DS neurons, which were present in the much larger dataset of Kubo et al. (2014), are missing in our FuGIMA dataset (Figure S2E). We suspect that this discrepancy is rooted in the different transgenic lines used (*HuC:GCaMP5G* by Kubo et al., 2014 and *Gal4^{S101t} × UAS:FuGIMA* in this study, respectively).

We hypothesized that at least a subset of the translation-selective pretectal cells might be projection neurons (PPNs), which convey information to the premotor centers that drive the OMR. Activity in the reticular formation and the tegmentum has been shown to be correlated with forward swimming and/or turning behavior (Chen et al., 2018; Naumann et al., 2016; Portugues et al., 2014; Vladimirov et al., 2018). Another potential recipient of optic-flow-related information from the pretectum is the cerebellum. Previous work described cerebellar tuning to whole-field motion in cerebellar granule and Purkinje cells (Knogler et al., 2017; Matsui et al., 2014). Purkinje cells in the medial part of the cerebellum were active during OMR, whereas the lateral part was active during the OKR (Matsui et al., 2014). We interrogated a single-neuron atlas (Kunst et al., 2019) to search for PPNs whose cell bodies reside in the optic-flow-responsive region. Most PPNs from this dataset send axons to either of two targets, the reticular formation or the cerebellum. In addition, many PPN axons form collateral branches in the hypothalamus, thalamus, raphe, pretectum, and tegmentum. A mutually exclusive innervation of cerebellum and reticular formation by pretectal efferents has also been reported for adult zebrafish (Yáñez

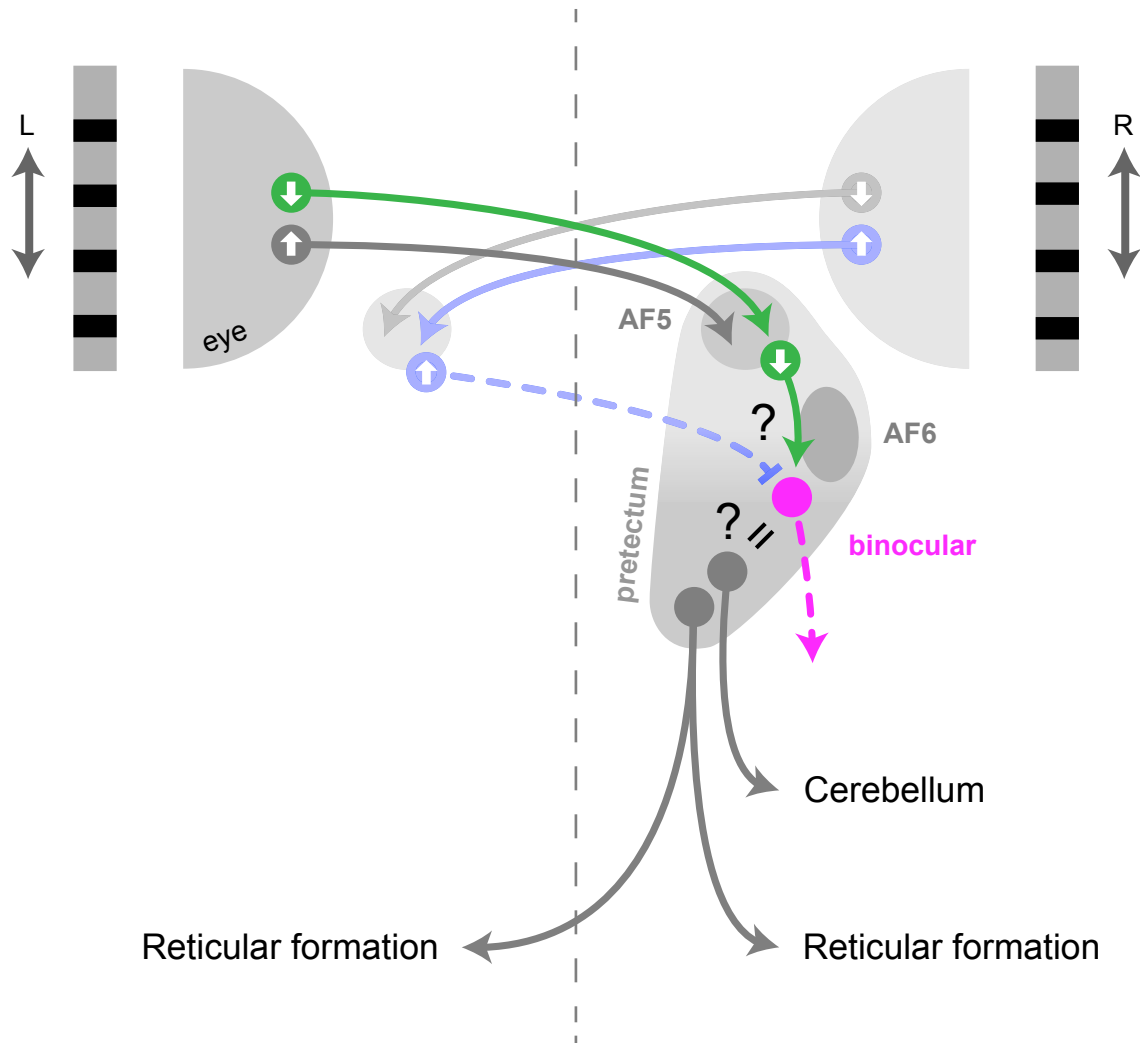


Figure 7. Model for the Optic-Flow-Processing Pathway

The majority of pretectal DS-RGCs terminate in AF5, where they likely synapse onto simple monocular DS neurons. Monocular DS neurons project to a neuropil region within the pretectum, close to the dorsal edge of AF6, where they overlap with translation-selective neurons. Binocularity can be established via inhibition by predicted commissural monocular DS neurons. Information about translational optic flow is transmitted by mutually exclusive populations of pretectal projection neurons to premotor centers either in the cerebellum or in the reticular formation, together evoking directed optomotor responses.

et al., 2018). The PPNs that we describe here are not characterized functionally. However, 10 out of 38 PPNs arborize in AF6, 8, or 9, which some of the FuGIMA-reconstructed neurons also innervate, suggesting that a subset, if not all, of the PPNs correspond to optic-flow-responsive cells that we analyzed with FuGIMA. Binocular integration depends on interhemispheric transfer of DS information (Kubo et al., 2014; Naumann et al., 2016). Interestingly, when we scanned the single-cell atlas anterior to the FuGIMA volume, we discovered a population of commissural neurons in the pretectum that might subserve this function (unpublished data). Commissural neurons projecting to the contralateral pretectum have been described in adult zebrafish (Yáñez et al., 2018).

In conclusion, our results identify a cell-resolved retina-pretectum-hindbrain pathway of the optic flow computation underlying the OMR. A combination of functional and anatomical approaches can offer a unique opportunity to gain new insights

into neural circuits that cannot be obtained by a single approach alone. Our circuit model provides a blueprint for the identification of synaptic connectivity and circuit mechanisms underlying optic flow processing in the vertebrate brain.

STAR★METHODS

Detailed methods are provided in the online version of this paper and include the following:

- KEY RESOURCES TABLE
- CONTACT FOR REAGENT AND RESOURCE SHARING
- EXPERIMENTAL MODEL AND SUBJECT DETAILS
 - Animal care and transgenic zebrafish
 - Line establishment
- METHOD DETAILS

- RGC axons and pretectal neuropil functional imaging
- Pixelwise calcium imaging analysis (RGCs)
- Image registration for RGC and pretectal neuropil
- Segmentation of AFs and 3D rendering
- Lipophilic Dye labeling
- Functional imaging and analysis (FuGIMA dataset)
- Photoactivation of paGFP and z stack acquisition
- Tracing of FuGIMA neurons and consolidation
- Image registration of FuGIMA data
- Integration of RGC and FuGIMA datasets
- Complementation with the single-neuron atlas
- **QUANTIFICATION AND STATISTICAL ANALYSIS**
- **DATA AND SOFTWARE AVAILABILITY**

SUPPLEMENTAL INFORMATION

Supplemental Information can be found online at <https://doi.org/10.1016/j.neuron.2019.04.018>.

A video abstract is available at <https://doi.org/10.1016/j.neuron.2019.04.018#mmc8>.

ACKNOWLEDGMENTS

We thank Irene Arnold-Ammer for plasmid construction, Estuardo Robles for advice on the annotations of RGC arborization fields, Marco Dal Maschio for assistance with 2p microscopy, Thomas Helmbrecht and Vilim Štíh for writing code enabling fast regressor-based analysis of functional imaging time series, Michael Kunst for advice on image registration with ANTs and sharing of the single-neuron database prior to publication, Nouwar Mokayes for programming, Aristides B. Arrenberg and agency Prudenter Agas for illustrations of the visual stimulation setup, the entire Baier lab for constructive feedback throughout the project, the Max Planck Computing and Data Facility in Garching for processing the image registration, and the staff of the MPIN fish facility for outstanding fish care. Funding was provided by the Max Planck Society (all authors) and the DFG Priority Programme “Computational Connectomics” (SPP 2041; F.K.).

AUTHOR CONTRIBUTIONS

H.B. and F.K. conceived the project. A.K. performed FuGIMA experiments, generated the *UAS:FuGIMA* and *UAS:FuGIMA-C3PA* transgenic lines, and performed anatomical registrations and complementation analyses. Y.W. performed the imaging on RGC terminal responses and analyzed the direction-selective responses in RGCs. F.K. generated the *UAS:sgCaMP6s* transgenic line. A.K., Y.W., and F.K. annotated arborization fields. A.K., Y.W., H.B., and F.K. wrote the manuscript.

DECLARATION OF INTERESTS

The authors declare no competing interests.

Received: December 21, 2018

Revised: February 17, 2019

Accepted: April 10, 2019

Published: May 27, 2019

REFERENCES

- Ahrens, M.B., Orger, M.B., Robson, D.N., Li, J.M., and Keller, P.J. (2013). Whole-brain functional imaging at cellular resolution using light-sheet microscopy. *Nat. Methods* *10*, 413–420.
- Arrenberg, A.B., Del Bene, F., and Baier, H. (2009). Optical control of zebrafish behavior with halorhodopsin. *Proc. Natl. Acad. Sci. USA* *106*, 17968–17973.
- Avants, B.B., Epstein, C.L., Grossman, M., and Gee, J.C. (2008). Symmetric diffeomorphic image registration with cross-correlation: evaluating automated labeling of elderly and neurodegenerative brain. *Med. Image Anal.* *12*, 26–41.
- Avants, B.B., Yushkevich, P., Pluta, J., Minkoff, D., Korczykowski, M., Detre, J., and Gee, J.C. (2010). The optimal template effect in hippocampus studies of diseased populations. *Neuroimage* *49*, 2457–2466.
- Avants, B.B., Tustison, N.J., Song, G., Cook, P.A., Klein, A., and Gee, J.C. (2011). A reproducible evaluation of ANTs similarity metric performance in brain image registration. *Neuroimage* *54*, 2033–2044.
- Baier, H. (2000). Zebrafish on the move: towards a behavior-genetic analysis of vertebrate vision. *Curr. Opin. Neurobiol.* *10*, 451–455.
- Barlow, H.B., and Hill, R.M. (1963). Selective sensitivity to direction of movement in ganglion cells of the rabbit retina. *Science* *139*, 412–414.
- Biot, E., Crowell, E., Höfte, H., Maurin, Y., Vernhettes, S., and Andrey, P. (2008). A new filter for spot extraction in N-dimensional biological imaging. In *Fifth IEEE International Symposium on Biomedical Imaging (ISBI'08) (From Nano to Macro (IEEE))*, pp. 975–978.
- Burrill, J.D., and Easter, S.S., Jr. (1994). Development of the retinofugal projections in the embryonic and larval zebrafish (*Brachydanio rerio*). *J. Comp. Neurol.* *346*, 583–600.
- Cazin, L., Precht, W., and Lannou, J. (1980). Pathways mediating optokinetic responses of vestibular nucleus neurons in the rat. *Pflügers Arch.* *384*, 19–29.
- Chen, X., Mu, Y., Hu, Y., Kuan, A.T., Nikitchenko, M., Randlett, O., Chen, A.B., Gavornik, J.P., Sompolinsky, H., Engert, F., and Ahrens, M.B. (2018). Brainwide organization of neuronal activity and convergent sensorimotor transformations in larval zebrafish. *Neuron* *100*, 876–890.e5.
- Dal Maschio, M., Donovan, J.C., Helmbrecht, T.O., and Baier, H. (2017). Linking neurons to network function and behavior by two-photon holographic optogenetics and volumetric imaging. *Neuron* *94*, 774–789.e5.
- Del Bene, F., Wyart, C., Robles, E., Tran, A., Looger, L., Scott, E.K., Isacoff, E.Y., and Baier, H. (2010). Filtering of visual information in the tectum by an identified neural circuit. *Science* *330*, 669–673.
- Dhande, O.S., and Huberman, A.D. (2014). Retinal ganglion cell maps in the brain: implications for visual processing. *Curr. Opin. Neurobiol.* *24*, 133–142.
- Distel, M., Hocking, J.C., Volkmann, K., and Köster, R.W. (2010). The centrosome neither persistently leads migration nor determines the site of axonogenesis in migrating neurons in vivo. *J. Cell Biol.* *191*, 875–890.
- Dreosti, E., Odermatt, B., Dorostkar, M.M., and Lagnado, L. (2009). A genetically encoded reporter of synaptic activity in vivo. *Nat. Methods* *6*, 883–889.
- Dunn, T.W., Gebhardt, C., Naumann, E.A., Riegler, C., Ahrens, M.B., Engert, F., and Del Bene, F. (2016). Neural circuits underlying visually evoked escapes in larval zebrafish. *Neuron* *89*, 613–628.
- Feng, L., Zhao, T., and Kim, J. (2015). neuTube 1.0: a new design for efficient neuron reconstruction software based on the SWC format. *eNeuro* *2*, ENEURO.0049-14.2014.
- Förster, D., Kramer, A., Baier, H., and Kubo, F. (2018). Optogenetic precision toolkit to reveal form, function and connectivity of single neurons. *Methods* *150*, 42–48.
- Freeman, J., Vladimirov, N., Kawashima, T., Mu, Y., Sofroniew, N.J., Bennett, D.V., Rosen, J., Yang, C.T., Looger, L.L., and Ahrens, M.B. (2014). Mapping brain activity at scale with cluster computing. *Nat. Methods* *11*, 941–950.
- Fujimoto, E., Gaynes, B., Brimley, C.J., Chien, C.B., and Bonkowsky, J.L. (2011). Gal80 intersectional regulation of cell-type specific expression in vertebrates. *Dev. Dyn.* *240*, 2324–2334.
- Gabriel, J.P., Trivedi, C.A., Maurer, C.M., Ryu, S., and Bollmann, J.H. (2012). Layer-specific targeting of direction-selective neurons in the zebrafish optic tectum. *Neuron* *76*, 1147–1160.
- Gebhardt, C., Baier, H., and Del Bene, F. (2013). Direction selectivity in the visual system of the zebrafish larva. *Front. Neural Circuits* *7*, 111.
- Giovannucci, A., Friedrich, J., Gunn, P., Kalfon, J., Brown, B.L., Koay, S.A., Taxisidis, J., Najafi, F., Gauthier, J.L., Zhou, P., et al. (2019). CalmAn: an open source tool for scalable calcium imaging data analysis. *eLife* *8*, e38173.

- Heap, L.A., Goh, C.C., Kassahn, K.S., and Scott, E.K. (2013). Cerebellar output in zebrafish: an analysis of spatial patterns and topography in eurydendroid cell projections. *Front. Neural Circuits* 7, 53.
- Helmbrecht, T.O., dal Maschio, M., Donovan, J.C., Koutsouli, S., and Baier, H. (2018). Topography of a visuomotor transformation. *Neuron* 100, 1429–1445.e4.
- Jefferis, G.S.X.E., and Manton, J.D. (2014). NeuroAnatomy Toolbox v1.5.2 (ZENODO).
- Kaifosh, P., Zaremba, J.D., Danielson, N.B., and Losonczy, A. (2014). SIMA: Python software for analysis of dynamic fluorescence imaging data. *Front. Neuroinform.* 8, 80.
- Knogler, L.D., Markov, D.A., Dragomir, E.I., Štih, V., and Portugues, R. (2017). Sensorimotor representations in cerebellar granule cells in larval zebrafish are dense, spatially organized, and non-temporally patterned. *Curr. Biol.* 27, 1288–1302.
- Kubo, F., Hablitzel, B., Dal Maschio, M., Driever, W., Baier, H., and Arrenberg, A.B. (2014). Functional architecture of an optic flow-responsive area that drives horizontal eye movements in zebrafish. *Neuron* 81, 1344–1359.
- Kunst, M., Laurell, E., Mokayes, N., Kramer, A., Kubo, F., Fernandes, A.M., Förster, D., Dal Maschio, M., and Baier, H. (2019). A cellular-resolution atlas of the larval zebrafish brain. *Neuron* 103, this issue, 21–38.
- Longair, M., and Jefferis, G.S. (2006). Name landmarks and register. Fiji plugin. https://imagej.net/name_landmarks_and_register.
- Longair, M.H., Baker, D.A., and Armstrong, J.D. (2011). Simple Neurite Tracer: open source software for reconstruction, visualization and analysis of neuronal processes. *Bioinformatics* 27, 2453–2454.
- Lowe, A.S., Nikolaou, N., Hunter, P.R., Thompson, I.D., and Meyer, M.P. (2013). A systems-based dissection of retinal inputs to the zebrafish tectum reveals different rules for different functional classes during development. *J. Neurosci.* 33, 13946–13956.
- Marquart, G.D., Tabor, K.M., Horstick, E.J., Brown, M., Geoca, A.K., Polys, N.F., Nogare, D.D., and Burgess, H.A. (2017). High-precision registration between zebrafish brain atlases using symmetric diffeomorphic normalization. *Gigascience* 6, 1–15.
- Masseck, O.A., and Hoffmann, K.P. (2009a). Comparative neurobiology of the optokinetic reflex. *Ann. N Y Acad. Sci.* 1164, 430–439.
- Masseck, O.A., and Hoffmann, K.P. (2009b). Question of reference frames: visual direction-selective neurons in the accessory optic system of goldfish. *J. Neurophysiol.* 102, 2781–2789.
- Matsui, H., Namikawa, K., Babaryka, A., and Köster, R.W. (2014). Functional regionalization of the teleost cerebellum analyzed in vivo. *Proc. Natl. Acad. Sci. USA* 111, 11846–11851.
- Mazurek, M., Kager, M., and Van Hooser, S.D. (2014). Robust quantification of orientation selectivity and direction selectivity. *Front. Neural Circuits* 8, 92.
- Meyer, M.P., and Smith, S.J. (2006). Evidence from in vivo imaging that synaptogenesis guides the growth and branching of axonal arbors by two distinct mechanisms. *J. Neurosci.* 26, 3604–3614.
- Naumann, E.A., Fitzgerald, J.E., Dunn, T.W., Rihel, J., Sompolinsky, H., and Engert, F. (2016). From whole-brain data to functional circuit models: the zebrafish optomotor response. *Cell* 167, 947–960.e20.
- Neuhauss, S.C., Biehmaier, O., Seeliger, M.W., Das, T., Kohler, K., Harris, W.A., and Baier, H. (1999). Genetic disorders of vision revealed by a behavioral screen of 400 essential loci in zebrafish. *J. Neurosci.* 19, 8603–8615.
- Nikolaou, N., Lowe, A.S., Walker, A.S., Abbas, F., Hunter, P.R., Thompson, I.D., and Meyer, M.P. (2012). Parametric functional maps of visual inputs to the tectum. *Neuron* 76, 317–324.
- Orger, M.B., Smear, M.C., Anstis, S.M., and Baier, H. (2000). Perception of Fourier and non-Fourier motion by larval zebrafish. *Nat. Neurosci.* 3, 1128–1133.
- Orger, M.B., Gahtan, E., Muto, A., Page-McCaw, P., Smear, M.C., and Baier, H. (2004). Behavioral screening assays in zebrafish. *Methods Cell Biol.* 77, 53–68.
- Orger, M.B., Kampff, A.R., Severi, K.E., Bollmann, J.H., and Engert, F. (2008). Control of visually guided behavior by distinct populations of spinal projection neurons. *Nat. Neurosci.* 11, 327–333.
- Paquet, D., Bhat, R., Sydow, A., Mandelkow, E.M., Berg, S., Hellberg, S., Fäiting, J., Distel, M., Köster, R.W., Schmid, B., and Haass, C. (2009). A zebrafish model of tauopathy allows in vivo imaging of neuronal cell death and drug evaluation. *J. Clin. Invest.* 119, 1382–1395.
- Patterson, G.H., and Lippincott-Schwartz, J. (2002). A photoactivatable GFP for selective photolabeling of proteins and cells. *Science* 297, 1873–1877.
- Pittman, A.J., Law, M.Y., and Chien, C.B. (2008). Pathfinding in a large vertebrate axon tract: isotopic interactions guide retinotectal axons at multiple choice points. *Development* 135, 2865–2871.
- Pnevmatikakis, E.A., and Giovannucci, A. (2017). NoRMCorre: an online algorithm for piecewise rigid motion correction of calcium imaging data. *J. Neurosci. Methods* 297, 83–94.
- Pologruto, T.A., Sabatini, B.L., and Svoboda, K. (2003). ScanImage: flexible software for operating laser scanning microscopes. *Biomed. Eng. Online* 2, 13.
- Portugues, R., and Engert, F. (2009). The neural basis of visual behaviors in the larval zebrafish. *Curr. Opin. Neurobiol.* 19, 644–647.
- Portugues, R., Feierstein, C.E., Engert, F., and Orger, M.B. (2014). Whole-brain activity maps reveal stereotyped, distributed networks for visuomotor behavior. *Neuron* 81, 1328–1343.
- Rinner, O., Rick, J.M., and Neuhauss, S.C. (2005). Contrast sensitivity, spatial and temporal tuning of the larval zebrafish optokinetic response. *Invest. Ophthalmol. Vis. Sci.* 46, 137–142.
- Robles, E., Laurell, E., and Baier, H. (2014). The retinal projectome reveals brain-area-specific visual representations generated by ganglion cell diversity. *Curr. Biol.* 24, 2085–2096.
- Ruta, V., Datta, S.R., Vasconcelos, M.L., Freeland, J., Looger, L.L., and Axel, R. (2010). A dimorphic pheromone circuit in *Drosophila* from sensory input to descending output. *Nature* 468, 686–690.
- Sabbah, S., Gemmer, J.A., Bhatia-Lin, A., Manoff, G., Castro, G., Siegel, J.K., Jeffery, N., and Berson, D.M. (2017). A retinal code for motion along the gravitational and body axes. *Nature* 546, 492–497.
- Schiff, D., Cohen, B., and Raphan, T. (1988). Nystagmus induced by stimulation of the nucleus of the optic tract in the monkey. *Exp. Brain Res.* 70, 1–14.
- Schindelin, J., Arganda-Carreras, I., Frise, E., Kaynig, V., Longair, M., Pietzsch, T., Preibisch, S., Rueden, C., Saalfeld, S., Schmid, B., et al. (2012). Fiji: an open-source platform for biological-image analysis. *Nat. Methods* 9, 676–682.
- Schneider, C.A., Rasband, W.S., and Eliceiri, K.W. (2012). NIH Image to ImageJ: 25 years of image analysis. *Nat. Methods* 9, 671–675.
- Scott, E.K., Mason, L., Arrenberg, A.B., Ziv, L., Gosse, N.J., Xiao, T., Chi, N.C., Asakawa, K., Kawakami, K., and Baier, H. (2007). Targeting neural circuitry in zebrafish using GAL4 enhancer trapping. *Nat. Methods* 4, 323–326.
- Semmelhack, J.L., Donovan, J.C., Thiele, T.R., Kuehn, E., Laurell, E., and Baier, H. (2014). A dedicated visual pathway for prey detection in larval zebrafish. *eLife* 3, e04878.
- Stuermer, C.A. (1988). Retinotopic organization of the developing retinotectal projection in the zebrafish embryo. *J. Neurosci.* 8, 4513–4530.
- Temizer, I., Donovan, J.C., Baier, H., and Semmelhack, J.L. (2015). A visual pathway for looming-evoked escape in larval zebrafish. *Curr. Biol.* 25, 1823–1834.
- Vishwanathan, A., Daie, K., Ramirez, A.D., Lichtman, J.W., Aksay, E.R.F., and Seung, H.S. (2017). Electron microscopic reconstruction of functionally identified cells in a neural integrator. *Curr. Biol.* 27, 2137–2147.e3.
- Vladimirov, N., Wang, C., Höckendorf, B., Pujala, A., Tanimoto, M., Mu, Y., Yang, C.T., Wittenbach, J.D., Freeman, J., Preibisch, S., et al. (2018). Brain-wide circuit interrogation at the cellular level guided by online analysis of neuronal function. *Nat. Methods* 15, 1117–1125.
- Wang, K., Hinz, J., Haikala, V., Reiff, D.F., and Arrenberg, A.B. (2019). Selective processing of all rotational and translational optic flow directions in the zebrafish pretectum and tectum. *BMC Biol.* 17, 29.

- Westerfield, M. (2007). *The Zebrafish Book. A Guide for the Laboratory Use of Zebrafish (Danio rerio), Fifth Edition* (Eugene: Univ. of Oregon Press).
- Wylie, D.R., Bischof, W.F., and Frost, B.J. (1998). Common reference frame for neural coding of translational and rotational optic flow. *Nature* 392, 278–282.
- Yáñez, J., Suárez, T., Quelle, A., Folgueira, M., and Anadón, R. (2018). Neural connections of the pretectum in zebrafish (*Danio rerio*). *J. Comp. Neurol.* 526, 1017–1040.
- Zhang, B.B., Yao, Y.Y., Zhang, H.F., Kawakami, K., and Du, J.L. (2017). Left habenula mediates light-preference behavior in zebrafish via an asymmetrical visual pathway. *Neuron* 93, 914–928.e4.

STAR★METHODS

KEY RESOURCES TABLE

REAGENT or RESOURCE	SOURCE	IDENTIFIER
Chemicals, Peptides, and Recombinant Proteins		
Alpha-Bungarotoxin	Invitrogen	B1601
Dil (1,1'-Diiododecyl-3,3',3'-Tetramethylindocarbocyanine Perchlorate)	Invitrogen	D3911
Tricaine	Sigma-Aldrich	MS-222
Experimental Models: Organisms/Strains		
Zebrafish <i>Tg(atox7:Gal4-VP16)s1992t, a. k. a. ath5:Gal4</i>	Del Bene et al., 2010	ZFIN ID: ZDB-FISH-150901-27082
Zebrafish <i>Tg(elavl3:lyn-tagRFP)mpn404, a. k. a. HuC:lyn-tagRFP</i>	Dal Maschio et al., 2017	ZFIN ID: ZDB-ALT-170731-38
Zebrafish <i>Tg(elavl3:GCaMP6s)a4598</i>	Ahrens et al., 2013	ZFIN ID: ZDB-FISH-150901-22335
<i>Tg(elavl3:Has.H2B-GCaMP6s)jf5</i> aka HuC:H2B-GCaMP6s	Freeman et al., 2014	ZFIN ID: ZDB-FISH-170711-1
Zebrafish <i>Et(E1b:Gal4-VP16)s1101t</i>	Scott et al., 2007	ZFIN ID: ZDB-FISH-150901-5255
Zebrafish <i>Tg(isl2b:Gal4-VP16, myl7:TagRFP)zc65</i>	Fujimoto et al., 2011	ZFIN ID: ZDB-FISH-150901-13523
Zebrafish <i>Tg(UAS:mCherry)s1984t</i>	Heap et al., 2013	ZFIN ID: ZDB-FISH-150901-14417
Zebrafish <i>Tg(UAS:syn-GFP) a. k. a. UAS:sypGFP</i>	Heap et al., 2013	ZFIN ID: ZDB-FISH-150901-21811
Zebrafish <i>Tg(UAS:Dendra-kras)s1998t</i>	Arrenberg et al., 2009	ZFIN ID: ZDB-ALT-110808-3
Zebrafish <i>Tg(UAS:syGCaMP6s)mpn156</i>	This paper	NA
Zebrafish <i>Tg(UAS-Janus:nlsGCaMP6s,PA-GFP)mpn161, a.k.a. UAS:FuGIMA</i>	This paper	NA
Zebrafish <i>Tg(UAS-Janus:nlsGCaMP6s,C3PA-GFP)mpn162, a.k.a. UAS:FuGIMA-C3PA</i>	This paper	NA
Software and Algorithms		
ImageJ/Fiji	Schindelin et al., 2012	https://fiji.sc/
Simple Neurite Tracer (Fiji plugin)	Longair et al., 2011	https://imagej.net/Simple_Neurite_Tracer
Attenuation Correction (Fiji plugin)	Biot et al., 2008	http://imagejdocu.tudor.lu/doku.php?id=plugin:stacks:attenuation_correction:start
Name Landmarks and Register (Fiji plugin)	Longair and Jefferis, 2006	https://imagej.net/Name_Landmarks_and_Register
NeuTube	Feng et al., 2015	https://www.neutracing.com/
Advanced Normalization Tools (ANTs)	Avants et al., 2008 ; Avants et al., 2011 ; Avants et al., 2010	http://stnava.github.io/ANTs/
RStudio Version 1.0.143	RStudio	https://www.rstudio.com/
Python 2.7	Python.org	https://www.python.org
Python 3	Python.org	https://www.python.org
Amira	Thermo Fisher Scientific	https://www.thermofisher.com/global/en/home/industrial/electron-microscopy/electron-microscopy-instruments-workflow-solutions/3d-visualization-analysis-software/amira-life-sciences-biomedical.html
Imaris	Bitplane	https://imaris.oxinst.com
FFmpeg		https://ffmpeg.org/
CalmAn (Calcium Imaging Analysis toolbox)	Giovannucci et al., 2019 ; Pnevmatikakis and Giovannucci, 2017	https://github.com/flatironinstitute/CalmAn
R package nat (NeuroAnatomy Toolbox)	Jefferis and Manton, 2014	http://jefferis.github.io/nat/
R package rgl	Daniel Adler, Duncan Murdoch and others	https://cran.r-project.org/web/packages/rgl/index.html

(Continued on next page)

Continued

REAGENT or RESOURCE	SOURCE	IDENTIFIER
Other		
Confocal microscope LSM 700, with a 20x/1.0 NA water-dipping objective	Carl Zeiss	https://www.zeiss.com/microscopy/int/home.html?vaURL=www.zeiss.com/microscopy
Movable object two-photon microscope with a 20x water-dipping objective (Olympus, NA 1.0)	Sutter Instruments/ Olympus	https://www.sutter.com/ / https://www.olympus-lifescience.com/de/
Femtonics 3DRC two-photon microscope, with 16x or 20x water-dipping objective	Femtonics	http://femtonics.eu/
Tracings, brain area annotations, and standard brain	Single-neuron atlas of Kunst et al., 2019	https://fishatlas.neuro.mpg.de/zebrafishatlas/

CONTACT FOR REAGENT AND RESOURCE SHARING

Further information and requests for resources and reagents should be directed to and will be fulfilled by the Lead Contact, Fumi Kubo (fumikubo@nig.ac.jp).

EXPERIMENTAL MODEL AND SUBJECT DETAILS**Animal care and transgenic zebrafish**

Adult and larval zebrafish (*Danio rerio*) were housed and handled according to standard procedures (Westerfield, 2007). Animal experiments were performed according to regulations of the Max Planck Society and the regional government of Upper Bavaria (Regierung von Oberbayern; approved protocols: ROB-55.2Vet-2532.Vet_02-16-31 and 55.2-1-54-2532-101-2012). We used the following previously described transgenic lines: *HuC:GCaMP5G (Tg(elavl3:GCaMP5G)a4598)*; *Tg(isl2b:Gal4-VP16)z65*; *Tg(atoh7:Gal4-VP16)s1992t*; *Tg(UAS:mCherry)s1984t*; *Tg(UAS:Dendra-kras)s1998t*; *Tg(UAS:sypGFP)*; *Et(E1b:Gal4-VP16)s1101t (= Gal4^{s1101t})*, *HuC:lyn-tagRFP (Tg(elavl3:lyn-tagRFP)mpn404)*; *Tg(elavl3:H2B-GCaMP6s)*. Transgenic fish were kept in either a TL or TLN (nacre) background and larvae lacking trunk pigmentation (outcrossed to TLN, nacre) were used in the experiment. Zebrafish larvae were raised in Danieau's solution until day 5 or 6 post-fertilization (dpf). As sex determination has not yet taken place in larvae, we used future males and females indiscriminately.

Line establishment

To generate the *UAS:syGCaMP6s* plasmid, the synaptophysin coding sequence (Meyer and Smith, 2006) was fused with *GCaMP6s* and inserted into a pTol2-14xUAS vector. *Tg(UAS:syGCaMP6s)mpn156* transgenic fish were generated using the standard Tol2 transposon system.

To co-express nls-*GCaMP6s* and either paGFP (for *UAS:FuGIMA*) or C3PA-GFP (for *UAS:FuGIMA-C3PA*), we fused nls-*GCaMP6s* and either paGFP (Patterson and Lippincott-Schwartz, 2002) or C3PA-GFP (Ruta et al., 2010) to the two sides of a bidirectional 14x UAS sequence (Janus-UAS; Distel et al., 2010; Paquet et al., 2009) in a Tol2 vector harboring a transgenesis marker ("bleeding heart," *cmic2:mCherry*). The transgenic lines *Tg(UAS:paGFP,nlsGCaMP6s)mpn161* and *Tg(UAS:C3PA-GFP,nlsGCaMP6s)mpn162* were generated in the background of *Gal4^{s1101t}* using the standard Tol2 transposon system. Most FuGIMA experiments were conducted in the F2 and F3 generations of the *UAS:FuGIMA* line, which showed considerable variegation and silencing of the transgene expression. Of the 58 FuGIMA tracings, three were performed with *UAS:FuGIMA-C3PA*, *Gal4^{s1101t}* or *HuC:Gal4*. These neurons belong to the monocular direction-selective response type class and do not intersect with AF5.

METHOD DETAILS**RGC axons and pretectal neuropil functional imaging**

Calcium imaging of RGC terminals was performed in triple transgenic zebrafish larvae expressing *syGCaMP6s* and *mCherry* in RGCs (*Tg(isl2b:Gal4-VP16)z65*, *Tg(UAS:syGCaMP6s)mpn156*, *Tg(UAS:mCherry)s1984t*) between 5 and 6 dpf. Larvae were mounted in 2% low-melting agarose with the dorsal side up. The fish were positioned in the center of a dish with a diameter of 3 cm. Larvae were intraspinally injected with α -bungarotoxin (2 mg/mL α -bungarotoxin (Invitrogen, B1601), FastRed 10% v/v, 1x Danieau's solution). A moveable objective microscope (MOM, Sutter Instruments) was used to record *GCaMP* signals (920 nm, 10-20 mW after the objective) with a 20x objective (Olympus, NA 1.0). ScanImage software (Pologruto et al., 2003) was used for image acquisition. We typically recorded one of two volumes per fish, each covering AF10 or AF4, AF5 and AF6 volume. For recording of AF10, ca. 20 z-planes were imaged with the z-step size of 4 μ m. For recording of AF4, 5 and 6, ca. 25 z-planes were imaged with the z-step size of 3 μ m. For each z-plane, images were acquired with a spatial resolution of 256x256 pixels (pixel size of 0.33 μ m for AF10 and 0.19 μ m for AF 4, 5 and 6) at a frame rate of 2.38 Hz. Since the average diameter of a presynaptic bouton in zebrafish RGCs

is $\sim 0.8 \mu\text{m}$ (Meyer and Smith, 2006), the physical lateral dimensions of pixels are below that of a typical presynaptic bouton. Sinusoidal grating stimuli were generated by custom written scripts using PsychoPy and presented onto a screen positioned either below or on the side of the fish using a digital light processing (DLP) projector (DLP LightCrafter 4500), using the red channel only, which allowed simultaneous visual stimulation and detection of green fluorescence. The visual stimuli consisted of whole-field luminance change (lowest luminance \rightarrow highest luminance \rightarrow lowest luminance) followed by gratings moving in 12 equally spaced angular directions presented in a random order. For each presentation of a different direction, the gratings initially stayed stationary for 10 s, in motion for 5 s, and back to stationary for 5 s, and this process was repeated for all grating presentations. The total length of the visual stimulus protocol was about 5 min. For the projection from the side of the fish, spatial and temporal frequency of the gratings was 0.06 cycle/degree and 1.8 Hz, respectively. The projected image filled a visual field of approximately 120° in azimuth and $\pm 35^\circ$ in elevation. For the projection from below the fish, gratings were designed as described in the recent study (Naumann et al., 2016). Briefly, the gratings of the spatial period of 1 cm moving at 10 mm/sec were presented onto a 12 cm x 12 cm screen. In contrast to this recent study, the complete screen area was covered by the grating (no stimulus omission directly below the fish).

Calcium imaging of pretectal neuropil was performed in *HuC:GCaMP5G* fish between 5 and 6 dpf. A volume centered around the pretectal neuropil was imaged with the z-step size of $5 \mu\text{m}$. For each z-plane, images were acquired with a spatial resolution of 512×512 pixels (pixel size of $0.19 \mu\text{m}$) at a frame rate of 2.38 Hz. The visual stimulus was presented from below the fish, as described above.

Pixelwise calcium imaging analysis (RGCs)

Raw time series of two-photon recordings were first corrected for motion artifacts by a hidden Markov model (HMM)-based algorithm using the SIMA toolkit (Kaifosh et al., 2014) and then processed by a uniform filter for noise removal. For each pixel in the filtered motion corrected recordings, its fluorescence time series was divided into 14 phases based on the visual stimuli. These 14 phases consisted of 1 ON phase (whole-field luminance increase), 1 OFF phase (whole-field luminance decrease), and 12 motion phases. The normalized signal intensity changes ($\Delta F/F_0$) were calculated for each phase, and they were tested for correlation with the stimulus time series convolved with a kernel with syGGCaMP6s kinetics ($\tau_{\text{decay}} = 1.2$ s). Pixels were considered motion responsive, if 1) their Pearson correlation coefficients were above the threshold of 0.35 in no less than 2 motion phases and 2) their t-scores (the coefficient from linear regression divided by error) in at least one motion phase were above noise threshold of 1.3. For each motion responsive pixel, we generated a response profile which consisted of the integral response over motion presentation for 12 directions.

To identify DS and OS populations, we plotted the response profiles as vectors in direction and orientation space, and we calculated the vector sum. The angle of the vector sum represents the preferred direction or orientation, and the normalized length of the vector sum (L_{dir} and L_{ori} as calculated below) represents the degree of selectivity. This has been shown to be a robust method to quantify direction and orientation selectivity (Mazurek et al., 2014).

$$L_{\text{dir}} = \left| \frac{\sum_k R(\theta_k) \exp(i\theta_k)}{\sum_k R(\theta_k)} \right|$$

$$L_{\text{ori}} = \left| \frac{\sum_k R(\theta_k) \exp(2i\theta_k)}{\sum_k R(\theta_k)} \right|$$

θ_k represents a direction of motion, and $R(\theta_k)$ is the integral response during the motion phase in the direction of θ_k . An empirical threshold of 0.4 was set for L_{ori} and 0.5 for L_{dir} . Pixels that surpassed the threshold were considered DS or OS. If a pixel was classified as both DS and OS, that pixel was regarded as DS, for which we have set a more stringent threshold. This ensured that DS and OS pixels are mutually exclusive. These thresholded, binary DS and OS pixels were color coded according to their preferred direction or orientation and plotted on top of the anatomical references, which are the mean images of the motion-corrected time series. To generate histograms of preferred direction (Figure 4), we first obtained the distribution of the preferred direction of DS pixels for each individual fish. The total number of DS pixels was normalized across different fish, and then the average of the normalized distribution was plotted. To compare our data with the previously published result of distribution of preferred directions of DS-RGC terminals (Figure 4D), we selected 3 planes (separated by $4 \mu\text{m}$) in the dorsal part of AF10 (approximately 30 - $45 \mu\text{m}$ from the dorsal surface of the tectum). The luminance response was determined independently of the response to motion stimuli (Figure S6). Pixels were deemed luminance responsive, if they showed activity correlated with changes in light intensity (Pearson correlation coefficient $>$ empirically derived threshold 0.45). The activity of ON pixels increases when luminance rises, while that of OFF pixels increases when luminance drops. ON-OFF pixels show an increase in activity when luminance rises and drops. For a pixel to be regarded as luminance responsive, mutually exclusive criteria were used: i.e., ON if $\text{ON} > 0.45$ and $\text{OFF} < 0.45$, and OFF if $\text{ON} < 0.45$ and $\text{OFF} > 0.45$, and ON-OFF if $\text{ON} > 0.45$ and $\text{OFF} > 0.45$.

Image registration for RGC and pretectal neuropil

After calcium imaging, we acquired anatomical z stacks of the same fish (*isl2b:Gal4, UAS:syGGCaMP6s, UAS:mCherry*). We first obtained small stacks (256×256 pixels) with the two-photon microscope, using syGGCaMP6s and covering the functionally imaged

volume (either AF10 or AF4, AF5 and AF6, or both in a few cases). Additionally, one overview stack with a higher resolution (1024x1024 pixels) was taken at the confocal microscope (LSM700, Carl Zeiss, Jena, Germany) with a 20x objective (W Plan-Apochromat 20x/1.0, Carl Zeiss, NA 1.0) with a z-step size of 1 μm and using both syGCaMP6s and mCherry channels.

In order to visualize the DS and OS RGC terminals imaged in multiple fish and compare them with the *HuC:GCaMP5G* expression pattern, we developed a three-step registration procedure (Figure S5A): 1) the mean image of the motion corrected time series were manually aligned (custom written Python script) onto the two-photon anatomical z stack using the syGCaMP6s signal as reference. As such, we registered the functional information to the anatomical z stacks. To circumvent changes of pixel values and thereby changes of DS/OS information caused by the image registration, we binned functional data according to preferred direction/orientation. Namely, we created 12 separate channels, with each channel corresponding to one of the 12 bins of preferred directions. 2) the two-photon anatomical z stacks were registered to the confocal stack of the same fish using syGCaMP6s as the reference channel. To facilitate gross alignment between the stacks, we pre-aligned the z stacks according to manual landmark selection using the plugin “Name Landmarks and Register” (by Mark Longair and Greg Jefferis) in Fiji (Schindelin et al., 2012; Schneider et al., 2012). The stacks were then precisely registered by the image registration library ANTs (Advanced Normalization Tools) (Avants et al., 2008; Avants et al., 2011; Avants et al., 2010) using syGCaMP6s signal as a reference for registration. The parameters for the command `antsRegistration` recently applied to zebrafish live images (Marquart et al., 2017) were used, except for variation of the initial transform parameter and the application of a mask. This mask was drawn in Fiji with the plugin segmentation editor (by Johannes Schindelin, Francois Kuzstos and Benjamin Schmid) and restricted the search for corresponding pixels to the area containing RGC terminals. 3) The resulting stack was then registered to the template (RGC standard brain) which was generated from six different stacks (*isl2b:Gal4, UAS:mCherry*) using the command `antsMultivariateTemplateConstruction2` in ANTs. Using the mCherry signal as a reference channel, we applied the same settings as for the previous round of ANTs registration (but without mask). Therefore, for each step of registration, the previous template stack served as the pattern to be registered. If a pitch difference between the experimental fish and the template was greater than $\pm 5^\circ$ (as calculated from the transformation information), DS and OS bins were recalculated accordingly before applying image registration. After anatomical stacks underwent registration, functional stacks containing DS/OS information were treated as additional channels and subjected to the same transformations using the command `antsApplyTransforms` (Marquart et al., 2017). As DS/OS depicting pixels were broadened due to registration, we applied a threshold of a pixel intensity value 50 to eliminate the smearing effect of the registration (custom Python script). This threshold was determined visually to display the same spatial extent of DS/OS information in the template volume as in the original two-photon frames. To visualize the *isl2b* template in the context of the *HuC:GCaMP5G* expression pattern, we registered a single *isl2b:Gal4, UAS:mCherry, HuC:GCaMP5G* fish to the template via the mCherry channel. For registering DS neuropil signals imaged in *HuC:GCaMP5G* fish (N = 6 fish), the same image registration protocol was applied except that 1) pre-alignment of the two-photon anatomical z stacks using manual landmark selection was skipped (during step 2 of the registration protocol) and 2) the confocal anatomical stacks of the functionally imaged fish were registered to our reference brain via the previously aligned *HuC:GCaMP5G* pattern.

Segmentation of AFs and 3D rendering

Segmentation of AFs was performed based on presynaptic puncta signals in *atoh7:Gal4, UAS:sypGFP* fish after they had been registered to the RGC standard brain using ANTs. AFs were manually segmented using published anatomical information about AFs (Burrill and Easter, 1994; Robles et al., 2014). Note that our segmentation of AFs relied only on anatomical features, without referring to functional maps of RGC terminals. We noted some variability of SypGFP localization patterns across different individual fish, especially at the boundary between AF5 and AF6. To account for this individual fish differences, 3 fish were segmented by 3 annotators each, and average of the 9 annotations was used to generate a consensus mask for AF4, AF5 and AF6. To quantify the number of DS pixels in different AFs, we used original calcium time series before anatomical registration to avoid the smearing effect (thereby leading to changes in the absolute number of pixels of each RGC puncta) caused by the registration. To count DS pixels in the original calcium time series in each AF, we either drew masks of AFs directly on the original calcium time series (with the aid of anatomical stacks) or back-transformed our consensus AF masks (drawn on the registered image volume) to the original calcium time series using inverse transformation. To determine the proportion of DS pixels relative to the entire number of pixels in AFs, we first quantified the pixel counts in AF5 and AF6 using the synaptic puncta signals of 9 anatomical stacks obtained from *isl2b:Gal4, UAS:sypGFP* fish. Subsequently, the number of DS pixels was divided by the average pixel counts in each AF to derive the percentage of DS pixels per total number of pixels in each AF. 3D rendering of registered image stacks was performed using Imaris software. Autofluorescence of the skin and eyes was removed by applying 3D masks and the volumes corresponding to AFs were highlighted in Imaris. Movies were prepared using Imaris and Fiji.

Lipophilic Dye labeling

6 day old *isl2b:Gal4, UAS:Dendra-kras* transgenic larvae were fixed in 4% paraformaldehyde in PBS for 1 hr at 4°C. 1% solutions of Dil in chloroform were pressure injected between the lens and the retina to visualize all axonal projections. Fluorescent images were acquired one day after the injection.

Functional imaging and analysis (FuGIMA dataset)

Larvae were mounted in agarose (LMP-agarose, 1.5% w/v in Danieau's solution), and intraspinally injected with alpha-bungarotoxin (2 mg/mL α -bungarotoxin (Invitrogen, B1601), FastRed 10% v/v, 1x Danieau's solution) before the experiment to abolish movements. During injection, larvae were under anesthesia with tricaine (0.02%, MS-222, Sigma-Aldrich) and the tricaine was washed out after injection. We used a two-photon microscope (Femtonics 3DRC microscope, Femtonics, Tuzlo, Hungary) for functional imaging as well as acquisition of z stacks. The visual stimuli were presented to the fish using a custom-built red LED arena as reported previously (Kubo et al., 2014; four flat panels covering 360° around the fish; no grating presentation in ~30° in front of the fish). In each experiment session, gratings moved horizontally in eight phases (3 s each at spatial frequency of 0.033 cycles/degree and temporal frequency of 2 cycles/sec, interspersed with 10 s stationary gratings, Figure S2A). Four of the eight phases are monocular, four are binocular: 1) left nasalward, 2) left temporalward, 3) right temporalward, 4) right nasalward, 5) backward, 6) forward, 7) clockwise, 8) counterclockwise. The sequence of eight phases was repeated three times. During visual stimulation, GCaMP fluorescence was imaged at about 3 Hz using the laser tuned to 920 nm (0.5 × 0.5 μ m/pixel, ca. 15 mW after the objective, imaging region of about 90 × 98 μ m). Response types of recorded neurons were identified using a custom written python script (regressor based, near-online analysis: approx. 2 minutes run time). First, traces of the three repetitions were averaged. Second, the averaged time series of each pixel were correlated to 256 regressors (visual stimulus time series convolved with nls-GCaMP6s kernel, tau = 3 s, tau determined visually to resemble the fluorescence trace), and the best-correlated regressor was determined for each pixel (threshold of Pearson's correlation coefficient > 0.3). For each regressor-of-interest (e.g., monocular DS and translation-selective response types), we generated a map of correlated pixels overlaid on the mean $\Delta F/F_0$ image (Figure 1E), based on which cells of interest were chosen. The selected cells of interest were further manually inspected for variability in response across repetitions, baseline fluorescence (indicator of transgene expression level), and accessibility for photoactivation (separation from neighboring neurons).

To improve display of fluorescence traces, functional imaging time series were motion corrected with CalmAn (Giovannucci et al., 2019; Pnevmatikakis and Giovannucci, 2017). We extracted average brightness from ROIs centered on the cell of interest (using Fiji), and calculated $\Delta F/F_0$ with F_0 being the mean of the 10th percentile. For neurons of the monocular DS and translation selective type, we plotted the mean trace of three repetitions, grouped by response type. For non-motion-selective neurons we in addition plotted the variance over three stimulus repetitions of the trial (SEM). Regressor traces were manually overlaid with corresponding fluorescence traces.

Photoactivation of paGFP and z stack acquisition

Photoactivation of paGFP in selected cells of interest was performed according to a detailed published protocol (Förster et al., 2018). Briefly, a ROI of about 0.8 × 0.8 μ m (0.2 × 0.2 μ m/pixel, 4 × 4 pixels) was placed in the center of the nucleus in 3D. Initially, paGFP was photoactivated with trial pulses of 200 ms (one and three pulses, laser wavelength 750 nm, ca. 10 - 17 mW after the objective, 1 Hz). If no neighboring cells were photoactivated, the ROI was re-centered and the first full cycle of photoactivation was delivered (40 × 200 ms, 1 Hz, Figure 1F). In cases of residual movement of the fish, tricaine was added before photoactivation. The whole protocol consisted of 15 cycles, with typically five minutes intervals between two activation cycles. However, in the dataset containing 58 neurons, 3 were photoactivated with less than 5 cycles and 11 with 5-10 cycles of photoactivation. Typically, paGFP fluorescence intensity in the photoactivated soma rapidly increased with the first photoactivation cycle, reaching the maximum after several cycles of photoactivation, suggesting that the maximum level of the photoactivation is achieved after several cycles of photoactivation (Figure S1C). To control progress of diffusion, z stacks capturing both green and red fluorescence (1020 nm, 1 μ m z-step) were typically acquired every five cycles, as well as a high resolution stack after the last activation period.

We quantified the degree of photoactivation by calculating the normalized fluorescence change after each cycle of photoactivation (mean of n = 5 neurons in 3 fish). An experiment was terminated, if 1) a directly neighboring neuron was also photoactivated, 2) fluorescence in the neurite did not strongly increase after the first cycle of photoactivation, or 3) the sample drifted. Furthermore, as the pretectum is located directly ventral to the tectum, we photoactivated few neurons resembling tectal neurons' morphology (neurite targeting the tectal neuropil, perpendicular branching in the neuropil layers), which were excluded. Two-photon and confocal microscopy offer different advantages: while two-photon microscopy achieves superior resolution in deeper tissue, it typically does not allow to image close to the eye pigment epithelium (due to photomultiplier tube (PMT) saturation). As confocal microscopy does not show this restriction, we acquired a large z stack at the confocal microscope (LSM 700, Carl Zeiss, Jena, Germany 20x/1.0 NA, water-dipping objective) in addition to the two-photon z stack.

To exclude the possibility that tracing quality underlies differential neurite trajectories of different response types, we manually sorted z stacks into four groups according to their image quality and compared tracings between groups. We did not find systematic differences in tracing length or overall morphology among the four groups (Figure S4C). Furthermore, all four groups contained tracings of all three response classes. Translation-selective neurons were even slightly overrepresented in the "best" image group. It is thus unlikely that we overlooked particular features, such as AF5 targeting, of translation-selective neurons.

Tracing of FuGIMA neurons and consolidation

Neurons were semi-manually traced from the confocal and two-photon z stacks using the Fiji plugin Simple Neurite Tracer (Longair et al., 2011) or the software neuTube (Feng et al., 2015) (Figure 1G). Neurons were traced in both confocal and two-photon z stacks, if available, as the two imaging modalities complement one another (see above). Finally, we merged the tracings of the same neuron

after co-registration (see section Image registration of FuGIMA data below) using a custom written python code. For merging, node locations of two tracings were compared and corresponding nodes were identified based on a maximal distance between them (defined by an empirically chosen tolerance factor). Residual nodes were then added to the merged tracing (OR operation). To assess the labeling distance of paGFP, we photoactivated a neuron co-expressing a membrane-tagged red fluorescent protein and FuGIMA. Briefly, we injected the plasmid *pTol2-UAS:tdTomato-CAAX* into embryos (*Gal4^{S1101t}, UAS:FuGIMA*) at the two to four cell stage and selected larvae with sparse expression of tdTomato. We applied the full photoactivation protocol on a spinal cord neuron co-expressing FuGIMA and tdTomato-CAAX. While tdTomato in the soma was considerably photo-bleached, it colocalized with paGFP in the neurite. Neurons highlighted with paGFP can be followed over 200 μm , as shown in a spinal cord neuron co-expressing tdTomato-CAAX (Figures S1A and S1B).

Image registration of FuGIMA data

The basis of comparisons across fish is their registration to a standard brain. We established the FuGIMA standard brain using the ANTs from four z stacks of four live fish expressing *HuC:lyn-tagRFP*, *HuC:H2B-GCaMP6s* (imaged at the confocal microscope). The FuGIMA standard brain is centered on the pretectum of the right hemisphere and extends $311.2 \times 311.2 \times 161 \mu\text{m}$ (x/y/z direction, $0.69 \times 0.69 \times 1 \mu\text{m}$ voxel size). To compare tracings from different experimental fish in one volume, z stacks were registered to the standard brain (overlay of three registered example z stacks: Figure 1H, registration workflow: Figure S1D). As preparation, the *HuC:lyn-tagRFP* channel was corrected for depth-dependent decrease of brightness (Fiji plugin Attenuation Correction (Biot et al., 2008)). If the experimental z stack was centered on the contralateral hemisphere, the z stack was flipped and rotated prior to registration using Fiji. Z stacks were registered to the standard brain using the software ANTs (Avants et al., 2008; Avants et al., 2011; Avants et al., 2010) and based on the common reference labeling pattern of *HuC:lyn-tagRFP*. We used the parameters recently determined for live samples (Marquart et al., 2017). Tracings (.swc files) were co-registered using the command ANTsApplyTransformsToPoints contained in the package ANTsR using R. If both confocal and two-photon-stacks were available, two-photon-stacks were registered to the confocal stack of the same fish and confocal stacks were registered to the FuGIMA standard brain. In the case of insufficient registration precision (visually determined), we either altered parameter *r* to change search initialization or applied a mask to restrict the search area. Search masks (binary .tiff files) were drawn manually or derived from previous rounds of registration. To verify the accuracy of our registration, we annotated eleven anatomical landmarks in the standard brain and individual z stacks ($n = 8$ z stacks from 6 fish for LM 1–9 and 11, $n = 6$ z stacks from 4 fish for LM 10). After co-registration into the standard brain, we calculated the distance between the landmark of the standard brain and the individual brains using R. The deviations of the landmark positions of the registered fish from those of the standard brain were on average $6.7 \pm 2.8 \mu\text{m}$ (STD, 11 landmarks, 4 or 6 z stacks from 6 fish, Figure S1E).

To facilitate comparison of tracing results across datasets, we described the x,y-position of FuGIMA neuron somata relative to a previously defined coordinate system origin (as in Kubo et al., 2014). For this, we extracted soma coordinates from .swc files, subtracted the origin coordinates (intersection of planes connecting the anterior tips of the AF9 containing neuropil, the midline, and the plane just dorsal to the anterior tips of AF9), and transformed the coordinates (45° rotation between the RGC and FuGIMA standard brain volumes). Soma locations (relative to the origin) were plotted in histograms (bin size = $16 \mu\text{m}$, visually determined).

To combine visualization of neuronal tracings with landmark annotations, the latter were transformed to surfaces. For this, registered z stacks were binarized, if necessary manually smoothed (both using Fiji), and surface renderings were produced using the software Amira (Thermo Fisher Scientific/FEI, smoothing: unconstrained smoothing, extent = 5). Neuronal tracings and landmark surfaces were plotted using R with the packages rgl (Adler, Murdoch, and others) and NeuroAnatomy Toolbox package (Jefferis and Manton, 2014). For the accompanying videos, FuGIMA tracings were smoothed. The video was assembled using Fiji, then converted and compressed with the software FFmpeg.

Integration of RGC and FuGIMA datasets

We had generated consensus AF masks in the RGC standard brain (see section Segmentation of AFs and 3D rendering above). To transfer these masks into the FuGIMA volume, we applied a two-step registration process (Figure S3A): 1) we registered the RGC standard brain (based on *isl2b:Gal4, UAS:mCherry*) to individual “bridge”-z stacks of fish expressing *isl2b:Gal4, UAS:GFP, HuC:lyn-tagRFP* ($n = 7$ z stacks from 4 fish), 2) then we registered the “bridge”-z stacks to the FuGIMA standard brain (based on *HuC:lyn-tagRFP*). As we observed slight differences in the localization of co-registered AF masks, we applied a kernel-density estimation (KDE) to the collection of binarized z stacks. After normalizing the maximum pixel intensity to 100, the stack was thresholded (pixel values = 25, 50, 75, and 90) and surfaces were generated. We utilized the KDE = 50% mask for further analysis of tracing intersections with AFs.

To compare FuGIMA tracings with functional information (z stacks), we first registered the functional imaging datasets (DS in RGC terminals and all neurons) to the FuGIMA standard brain. Streaks of DS pixels were found in the region of the eye pigment in the pan-neuronal DS stack, resulting from noise due to PMT saturation. We removed those pixels with a mask. To convert .swc files of tracings to rastered data (z stacks) we applied a custom-written Fiji macro script. Resulting pixelated tracings were smoothed in Fiji to improve the impression of continuous neurites for display.

Complementation with the single-neuron atlas

To compare FuGIMA neurons with a single-neuron atlas (Kunst et al., 2019), we registered the FuGIMA dataset to the standard brain of this single-neuron atlas. The single-neuron atlas standard brain is based on the synapsin pattern (antibody staining, fixed samples) and contains several registered expression patterns to enable registration of external datasets based on those patterns (e.g., fixed *HuC:lyn-tagRFP*). To register the FuGIMA standard brain (acquired live, a sub-volume of the fish brain) into the single-neuron atlas volume (fixed, whole-brain), we employed registration in three steps as follows: 1) FuGIMA volume to a sub-volume of the live *HuC:lyn-tagRFP* standard brain (at this time not yet registered to the single-neuron atlas), 2) extension to the full live standard brain volume, 3) live standard brain to fixed *HuC:lyn-tagRFP* standard brain. Co-registration of FuGIMA tracings (.swc files) and landmark annotations (.tiff stacks), followed by surface rendering of landmarks allowed to visualize both datasets together. We searched among 1743 tracings from the web-interface of the single neuron atlas for tracings complementing the FuGIMA tracings (Pretectal projection neurons, PPNs) (<https://fishatlas.neuro.mpg.de/zebrafishatlas/>, download: 25. Oct. 2018, combined results of searches in different brain regions). To define the search volume for PPNs (FuGIMA VOI), we dilated FuGIMA somata and merged patches in the binary .tiff stack (distance surface to soma approx. 10 μm (x/y) and 11 μm (z), in the FuGIMA standard volume). After co-registration of the FuGIMA VOI to the single-neuron atlas volume, we identified PPNs with somata in the FuGIMA VOI (custom written python script). For the innervation analysis, we retrieved the number of tips per PPN for all 78 brain region annotations and one additional area “contralateral hemisphere.” To focus on the most prominently targeted areas, we depicted areas with > 5 intersecting PPNs, omitting similar annotations i.e., only “cerebellum,” no additional “corpus cerebelli,” and included all annotated AFs intersecting with PPNs. For visualization, we ordered the list starting with the contralateral hemisphere, then in the order of the number of intersections.

QUANTIFICATION AND STATISTICAL ANALYSIS

The statistical information is provided in each of the sections above.

The analyzed number of zebrafish and brains is indicated in the main text and figure legends. Error bars correspond to SEM unless stated otherwise.

DATA AND SOFTWARE AVAILABILITY

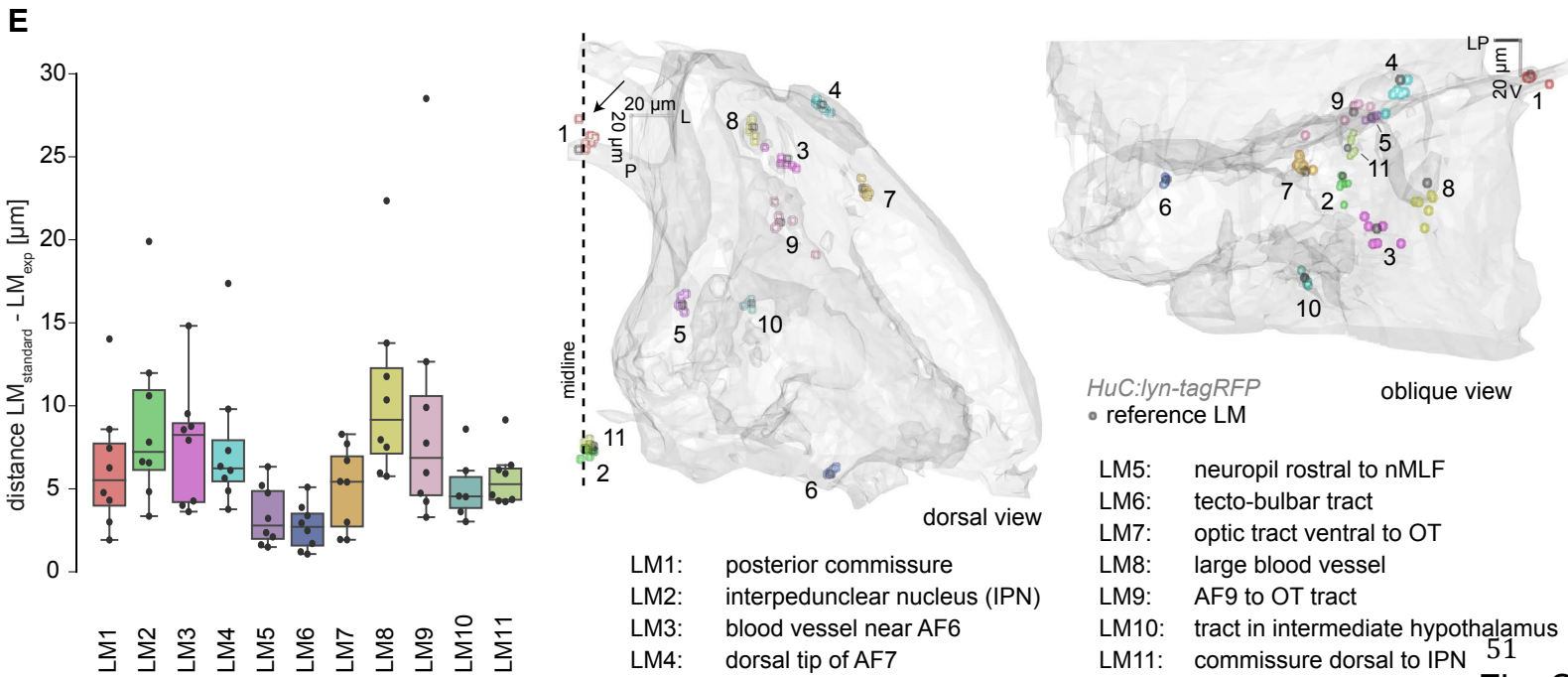
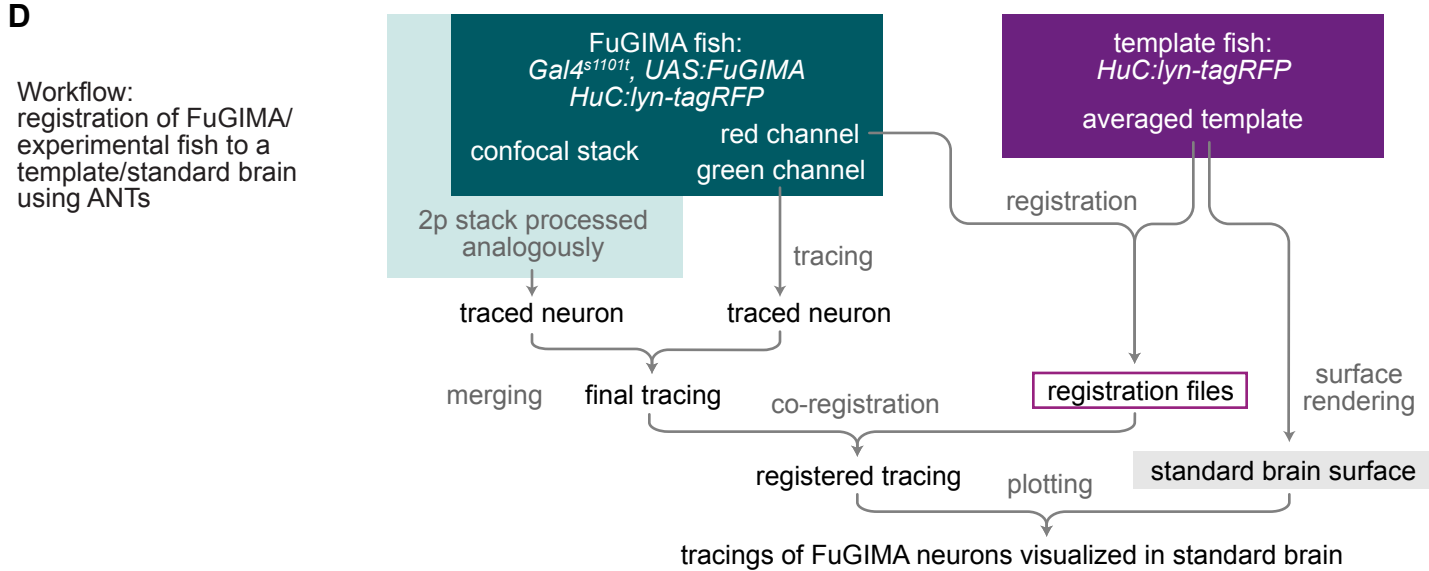
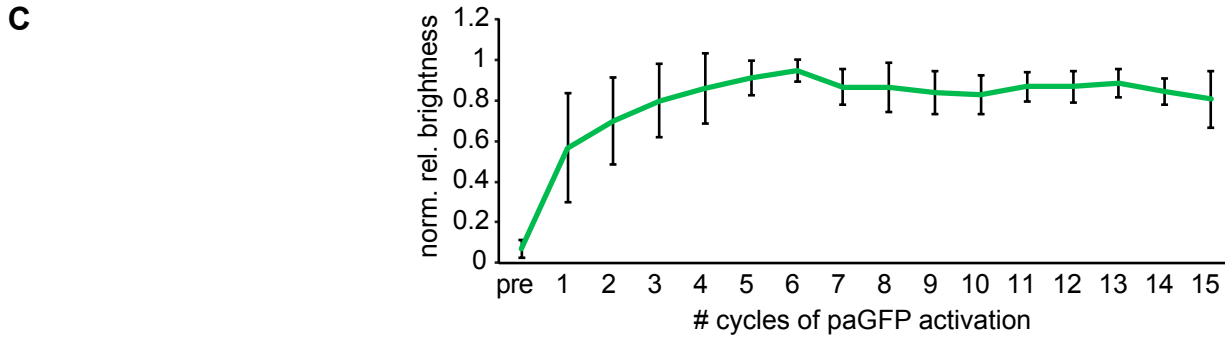
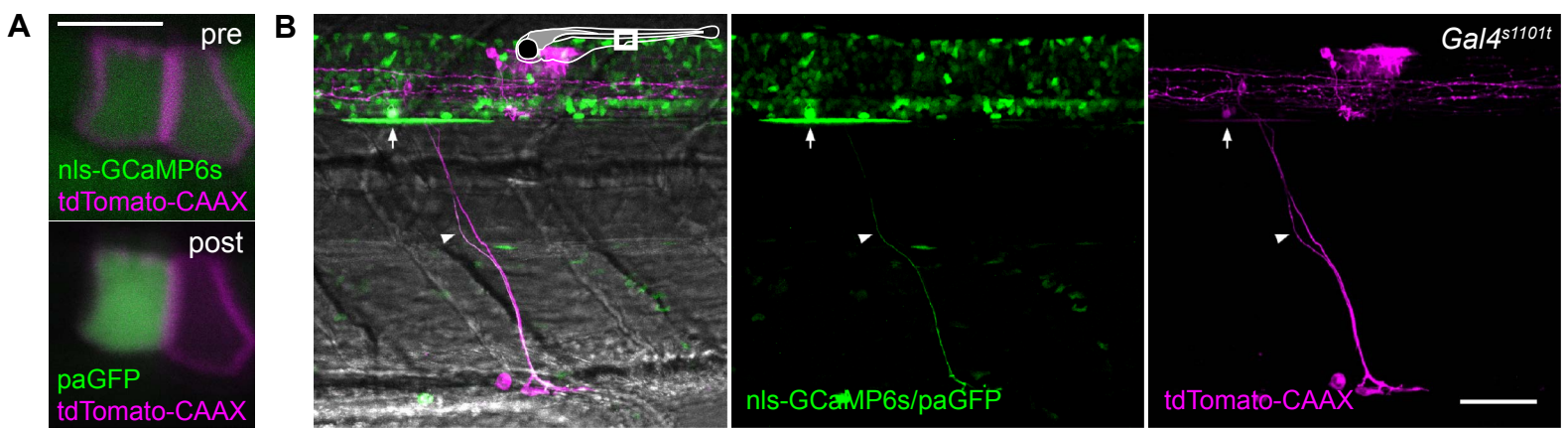
Data and software will be made available upon request.

Neuron, Volume 103

Supplemental Information

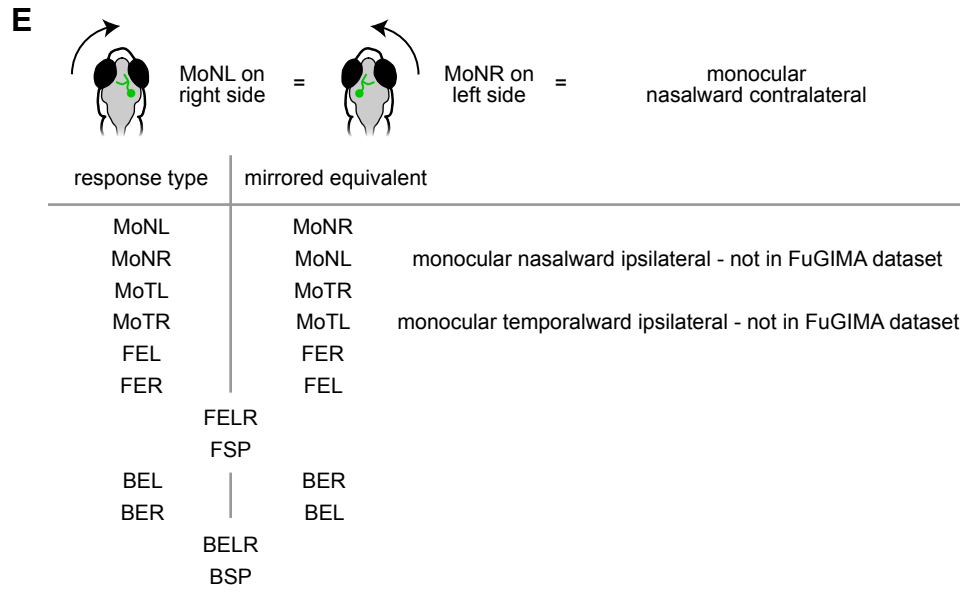
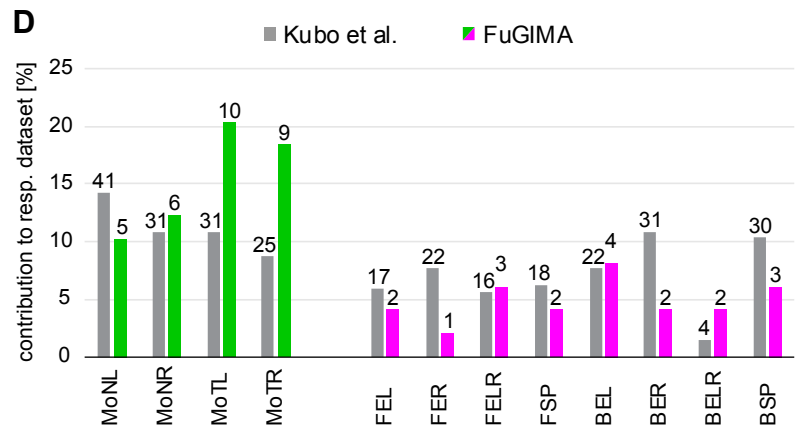
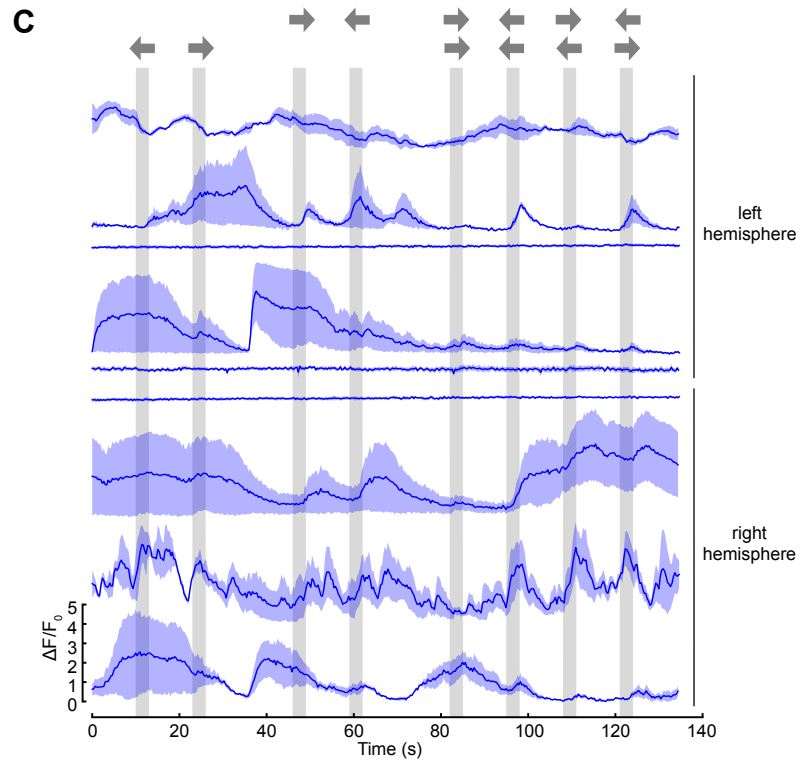
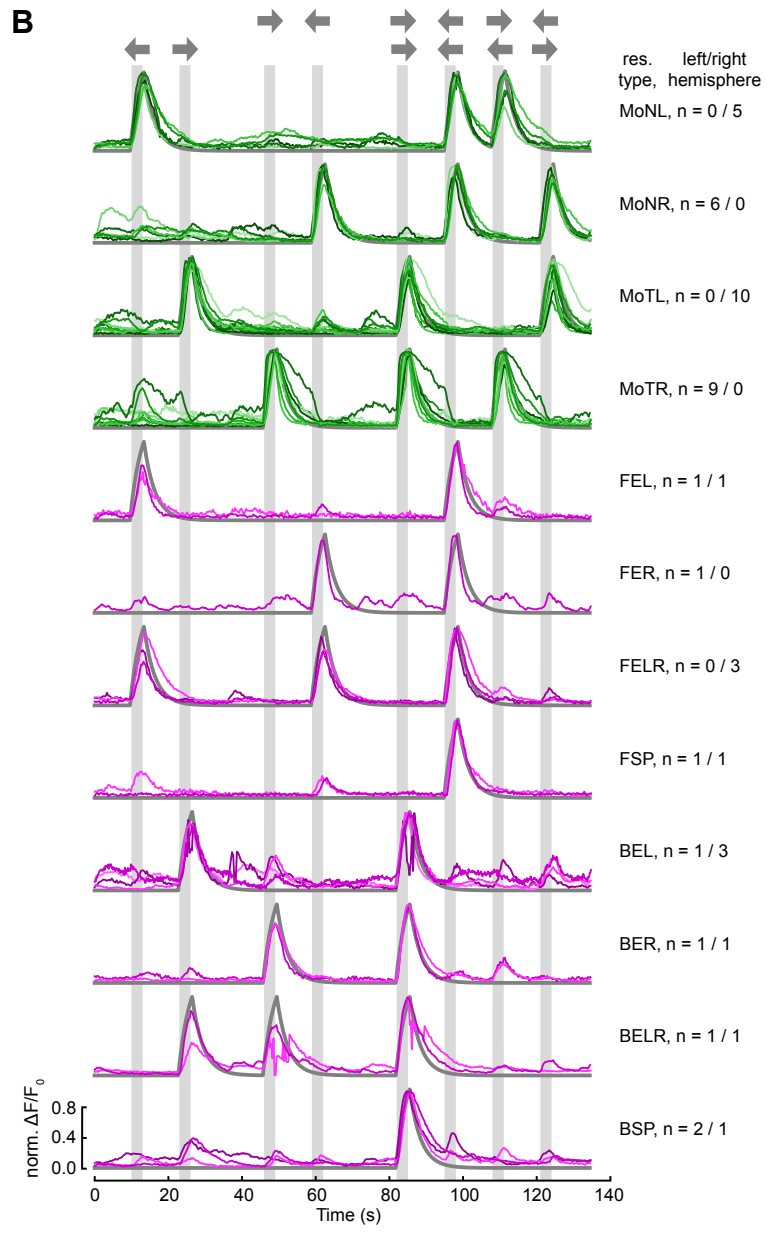
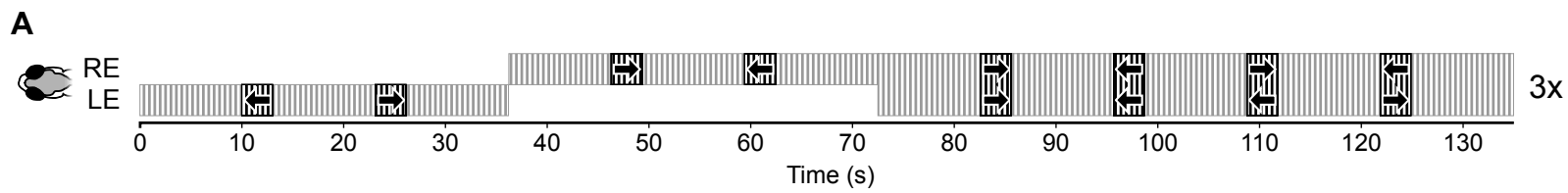
**Neuronal Architecture of a Visual Center
that Processes Optic Flow**

Anna Kramer, Yunmin Wu, Herwig Baier, and Fumi Kubo



Supplementary Figure S1 (related to Figure 1). Characterization of paGFP activation in single cells, registration procedure of tracings and alignment precision of landmarks.

(A) Application of the FuGIMA photoactivation protocol in a single spinal cord neuron co-expressing *UAS:FuGIMA* and *UAS:tdTomato-CAAX* (driver: *Gal4^{s1101t}*). Photoactivation in a single spinal cord neuron, pre- and post-photoactivation with a single activation cycle (brightness/contrast adapted separately). **(B)** Lateral views of the tail with the photoactivated neuron extending from the spinal cord after full photoactivation protocol of 15 cycles. (Inset: rectangle on fish schematic indicates the field of view. Green: nls-GCaMP6s/paGFP, magenta: tdTomato-CAAX, white arrow: soma of photoactivated neuron, arrowhead: filled neurite). **(C)** Time course of paGFP brightness in the soma over the course of 15 cycles of photoactivation (n = 5 pretectal neurons in 3 fish, mean +/- STD). **(D)** Workflow of image registration enabling visualization of FuGIMA neurons in the standard brain. Experimental z stacks are split into two separately processed channels. Neurons are traced in the nls-GCaMP6s/paGFP channel and tracings of neurons imaged at both the two-photon (2p) and the confocal microscope are merged. In parallel, the reference marker channel (*HuC:lyn-tagRFP*) is registered to the standard brain (averaged *HuC:lyn-tagRFP*). The resulting registration files are applied to tracings (co-registration), enabling their visualization within the volume of the standard brain. **(E)** Quantification of distances between the location of landmarks in the standard brain and in the registered experimental fish. Left: combined box plot and swarm plot (middle horizontal line: median, horizontal box outlines: first and third quartile, whiskers: last points included in 1.5 * interquartile range from the respective quartile), right: 3D rendering of landmarks in the standard brain (gray surface: reference marker *HuC:lyn-tagRFP*, dark gray: landmark position in standard brain, colors: registered landmarks from experimental fish, n = 8 z stacks from 6 fish for LM 1 – 9 and 11, n = 6 z stacks from 4 fish for LM 10, middle: dorsal view, black arrow: viewing direction for lateral view, shown on the right, LM, landmark). Scale bar: 5 μ m in (A), 50 μ m in (B).



Supplementary Figure S2 (related to Figures 1 and 2). Visual stimulus protocol, functional imaging time series of all FuGIMA neurons and comparison of response type sampling with Kubo *et al.* (2014). **(A)** During functional imaging, fish are presented with the following whole-field motion stimulus, consisting of eight motion phases with three repetitions (same order): Horizontally moving gratings (3 s each, black arrows) are presented in four monocular phases (left nasalward, left temporalward, right temporalward, right nasalward), followed by four binocular phases (backward, forward, clockwise and counter-clockwise) and interspersed by the presentation of stationary gratings (gray, 10 s) (RE: right eye, LE: left eye). **(B)** Normalized fluorescence traces of motion-sensitive pretectal FuGIMA neurons grouped according to their response type, numbers indicate occurrence in FuGIMA dataset and hemisphere of origin. **(C)** Fluorescence traces of non-motion-sensitive pretectal FuGIMA neurons and hemisphere of origin (blue line: average over three repetitions, light blue: SEM). **(D)** Comparison of response type frequency between Kubo *et al.* (2014) (number of cells per fish) and this work (total number of cells in the dataset). Proportions of response type are normalized to the total number of neurons across the investigated motion-sensitive response types (four monocular DS and eight translation-selective), absolute number of neurons are indicated on top of each bars. **(E)** FuGIMA neurons were imaged in both left and right hemispheres. Mirroring leads to a change in response type name as indicated.

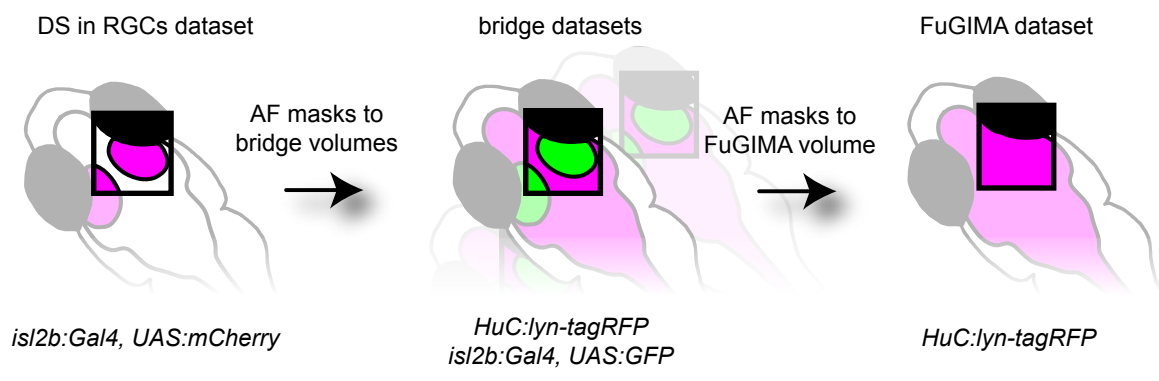
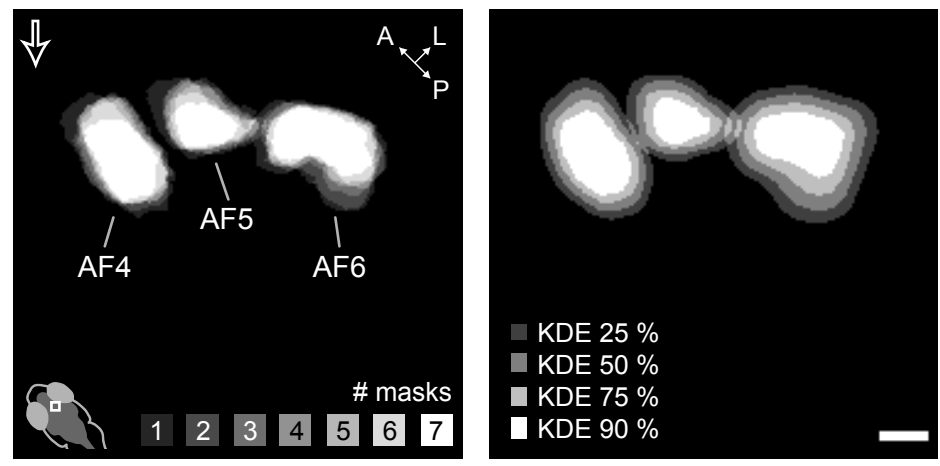
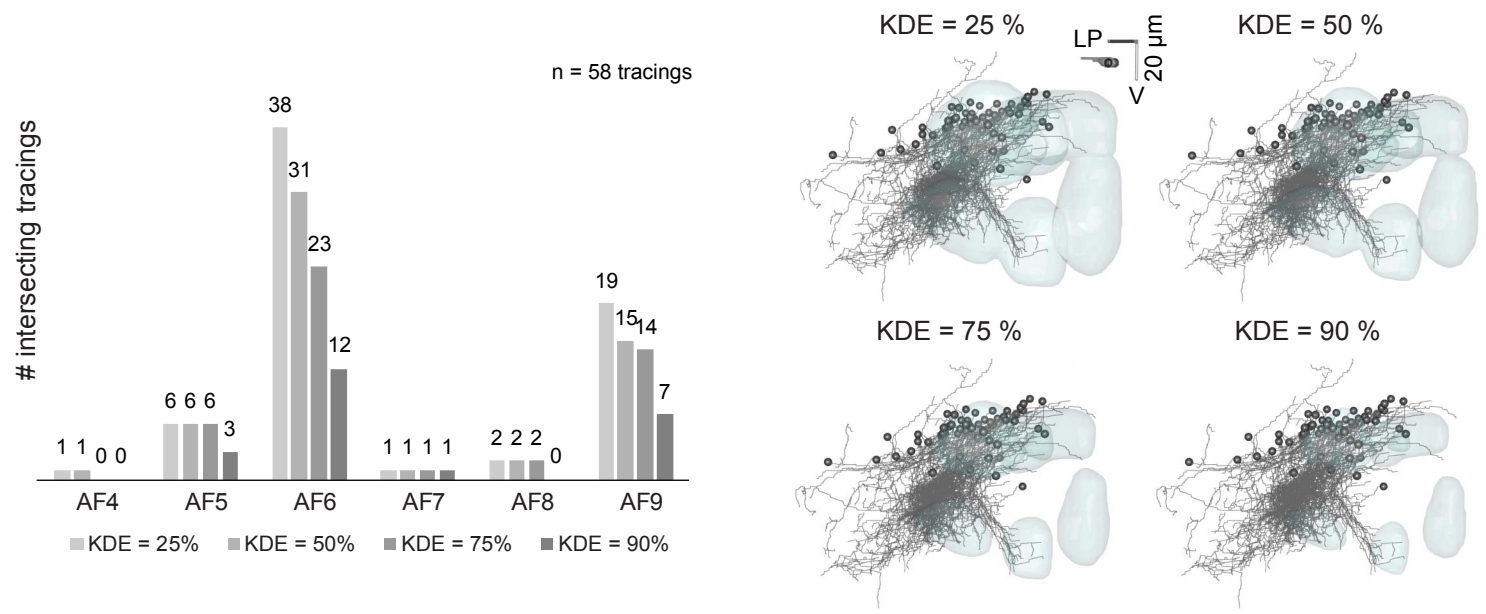
A**B****C**

Fig. S3

Supplementary Figure S3 (related to Figure 2). Establishment of arborization field approximation boundaries and effect of boundary stringency on intersections with FuGIMA tracings. **(A)** Schematic illustrating registration of AF masks from the RGC standard volume via bridging z stacks (derived from multiple fish) to the FuGIMA reference brain. **(B)** Generation of approximation boundaries of AFs based on a kernel-density estimation (KDE) over registered AF masks (underlying Figure 2C). Left: Overlap of registered AF masks (n = 7 bridging z stacks, from 4 fish, open arrow: direction of oblique view), right: KDE of registered masks, thresholded to 25, 50, 75, and 90 %. **(C)** Quantification of intersections of FuGIMA tracings with AF boundaries of various stringency (KDE=25, 50, 75, and 90%). Right: 3D renderings of AF boundaries of various stringency and the full FuGIMA dataset (oblique view). Scale bar: 20 μm in (B).

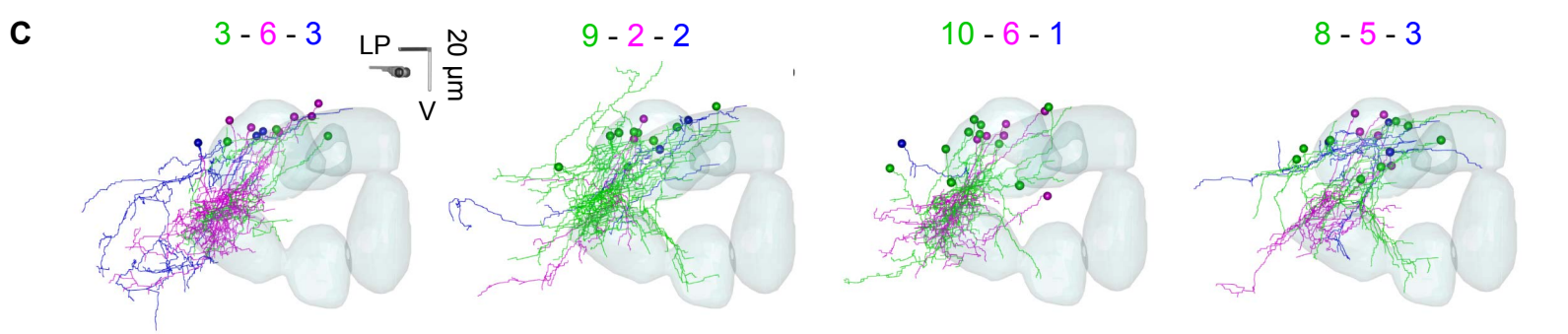
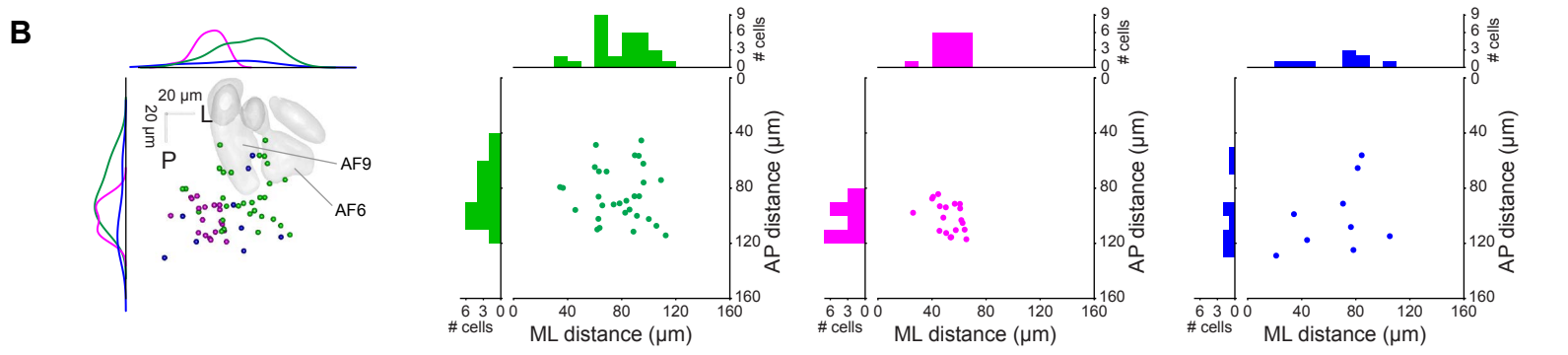
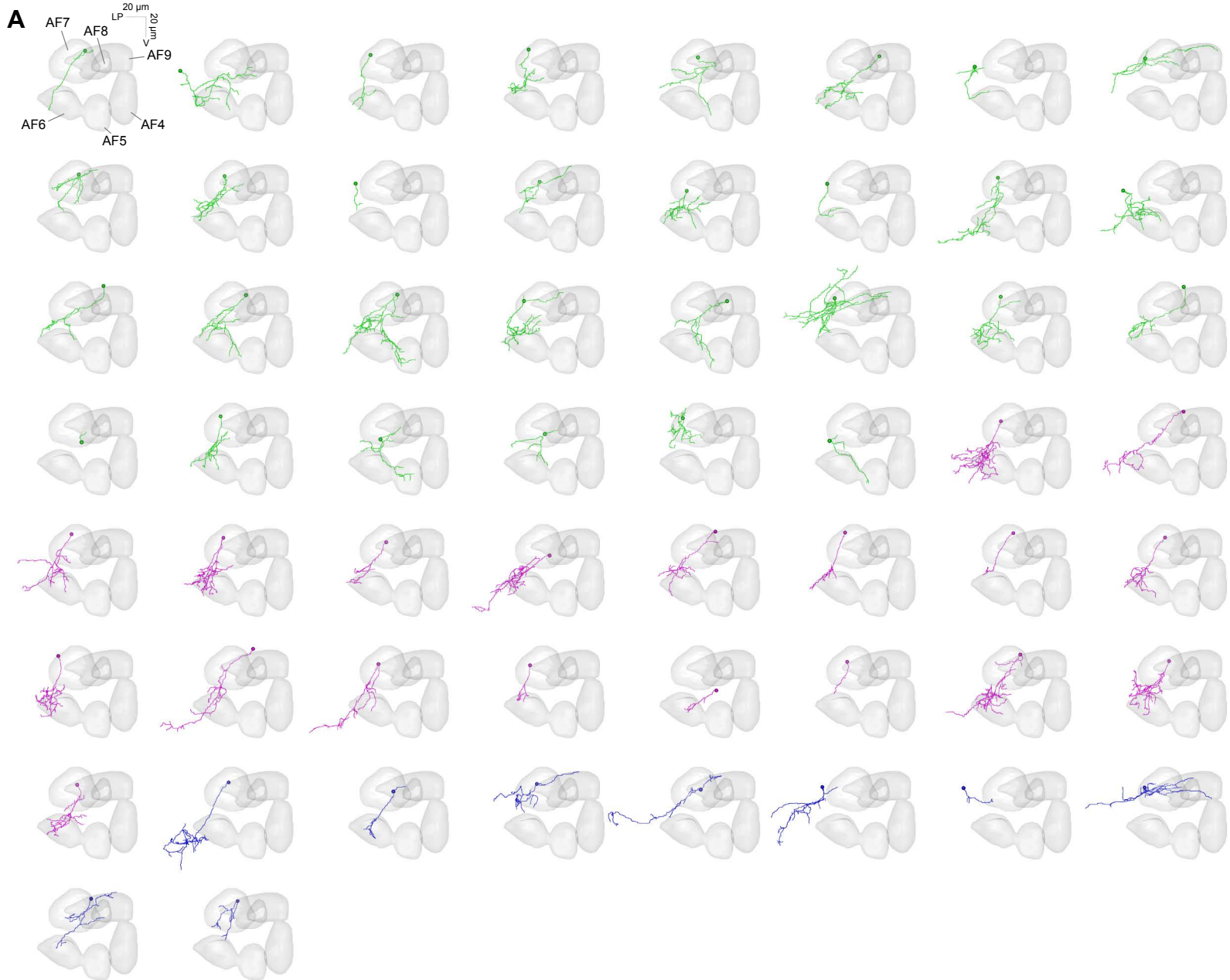
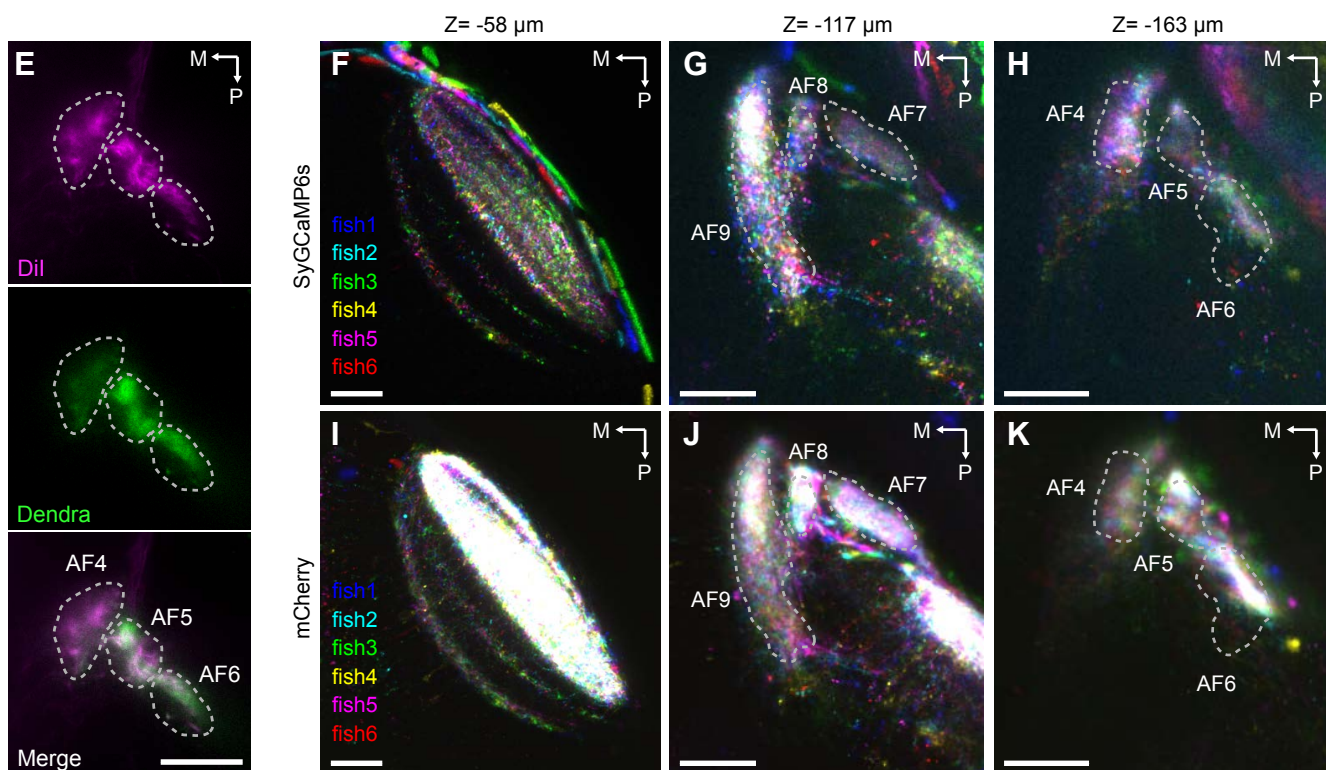
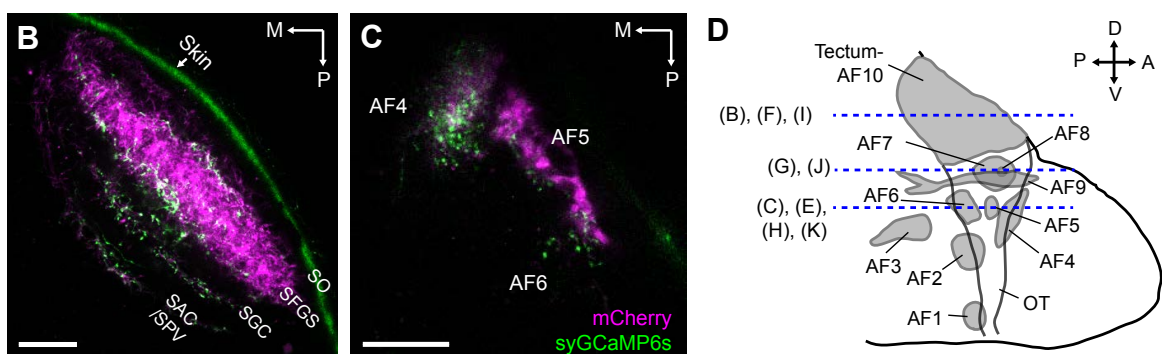
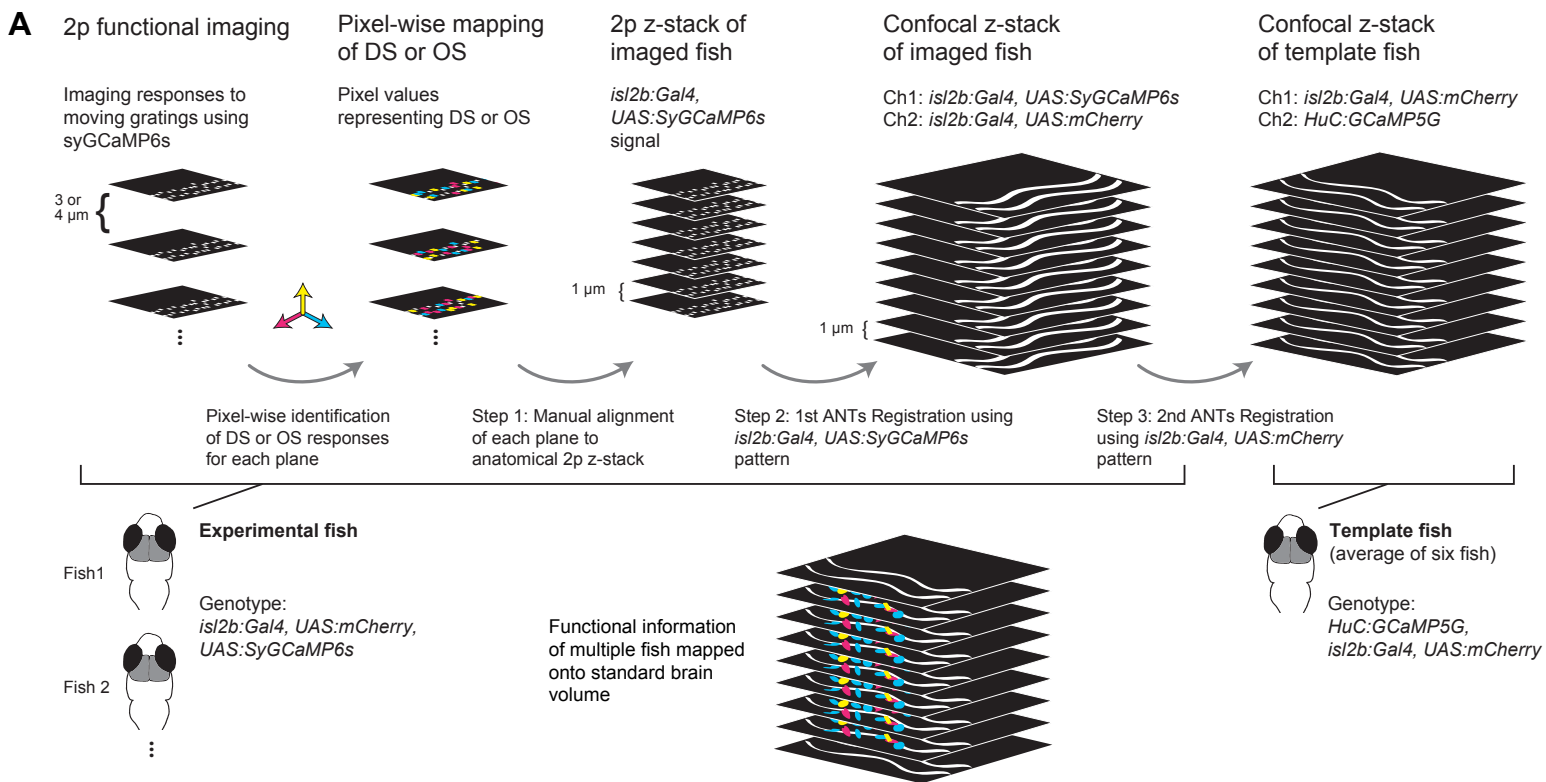


Fig. S4 57

Supplementary Figure S4 (related to Figure 2). Morphology of all FuGIMA neurons, soma locations regarding response class and split of dataset according to z stack quality.

(A) Individual FuGIMA neurons plotted together with AF masks (KDE=50%), tracings color-coded according to response class (green: monocular DS, magenta: translation-selective, blue: non-motion-sensitive, color-code as in Figure 1C, oblique view). **(B)** Soma location of FuGIMA neurons color-coded according to their response class. (Left) Montage of 3D rendering of FuGIMA somata with surfaces of AFs 4-9 and KDE for ML and AP distributions. (Right) Plot of soma location with histogram of ML and AP distribution (separated by response class). ML: medial-lateral, AP: anterior-posterior, distance measured from the origin as defined in Kubo et al., 2014. **(C)** Split of FuGIMA dataset into four categories according to image quality of the z stack (“best” to “worst”, manual annotation). For each category, the tracings of each class are color-coded as in (A), and the number of each class is stated on top. All four categories contain tracing of all response classes, with relatively more translation and non-motion-sensitive tracings emanating from the best quality z stacks.



Supplementary Figure S5 (related to Figure 3). Image registration work flow to generate a 3D map of direction-selectivity, characterization of *isl2b:Gal4, UAS:syGCaMP6s* expression and overlay from image registration. (A) Schematic workflow for registering functional responses with anatomical structures. For clarity, only 3 preferred directions are represented here. See STAR Methods for details. **(B, C)** Subcellular localization of syGCaMP6s in the tectum/AF10 (B) and AF4, AF5 and AF6 (C) in *isl2b:Gal4, UAS:syGCaMP6s, UAS:mCherry* fish. Note that syGCaMP6s expression exhibits punctate signals in RGC terminals, in contrast to uniform mCherry signals in *en passant* RGC axon bundles. SO, *stratum opticum*; SFGS, *stratum fibrosum et griseum superficiale*; SGC, *stratum griseum centrale*; SAC, *stratum album centrale*. **(D)** Schematic illustration of AFs (modified from Burrill and Easter (1994)). Blue dotted lines indicate approximate z-planes shown in other panels of this figure. OT, optic tract. **(E)** Lipophilic dye Dil injection of the RGC axons in *isl2b:Gal4, UAS:Dendra-kras* fish. Note that the *isl2b:Gal4* line labels most of RGCs projecting to AF4, AF5 and AF6. **(F-K)** Overlay of 6 different transgenic fish (*isl2b:Gal4, UAS:syGCaMP6s, UAS:mCherry*) that have been registered into a reference system (RGC standard brain based on *isl2b:Gal4, UAS:mCherry*). Z-position indicates the distance from the dorsal most surface of AF10. Note that both syGCaMP6s (F-H) and mCherry (I-K) patterns from 6 fish occupy conserved space in the registered volume. A, anterior; P, posterior; D, dorsal; V, ventral, M, medial. Scale bars represent 30 μ m.

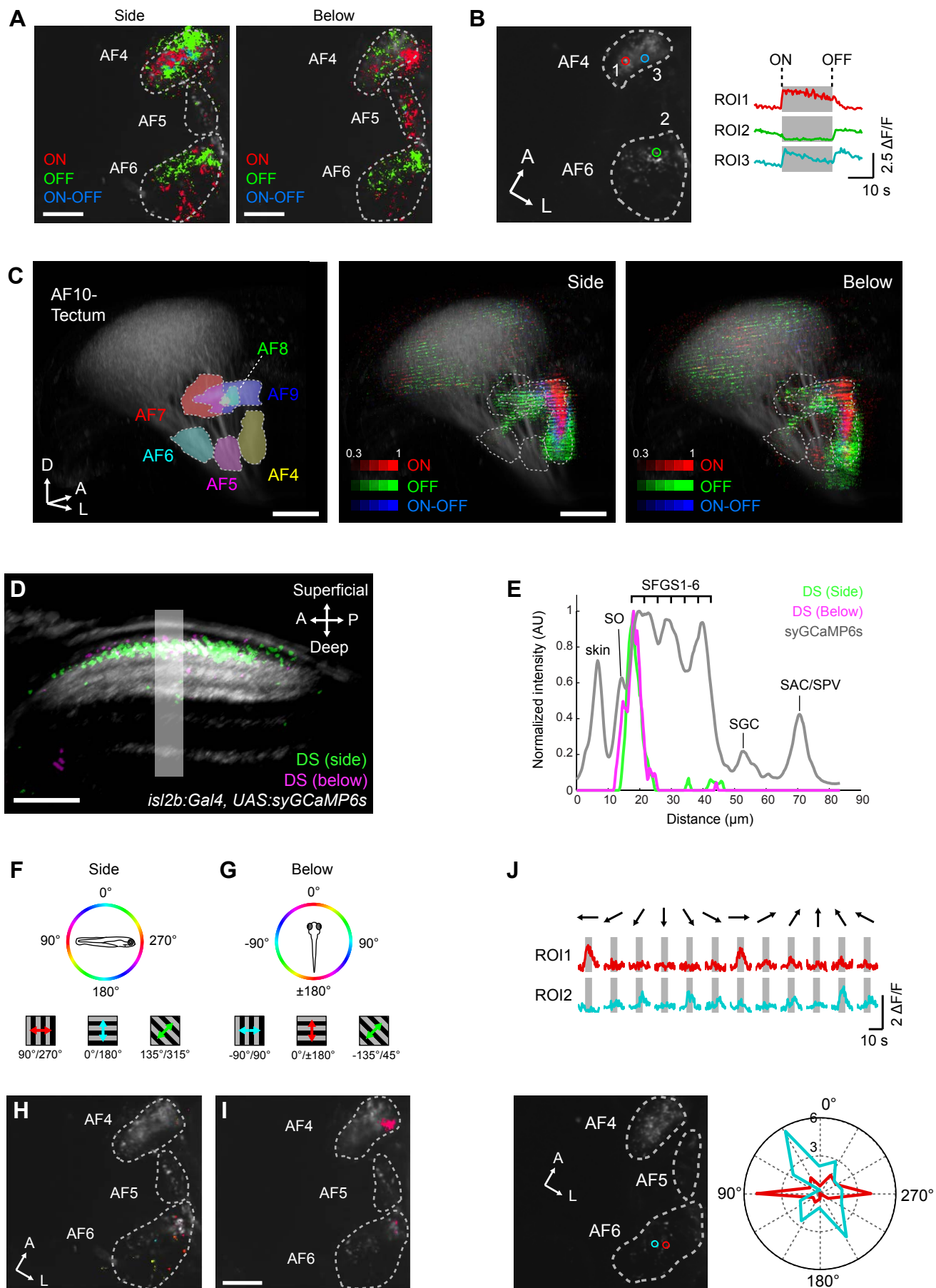
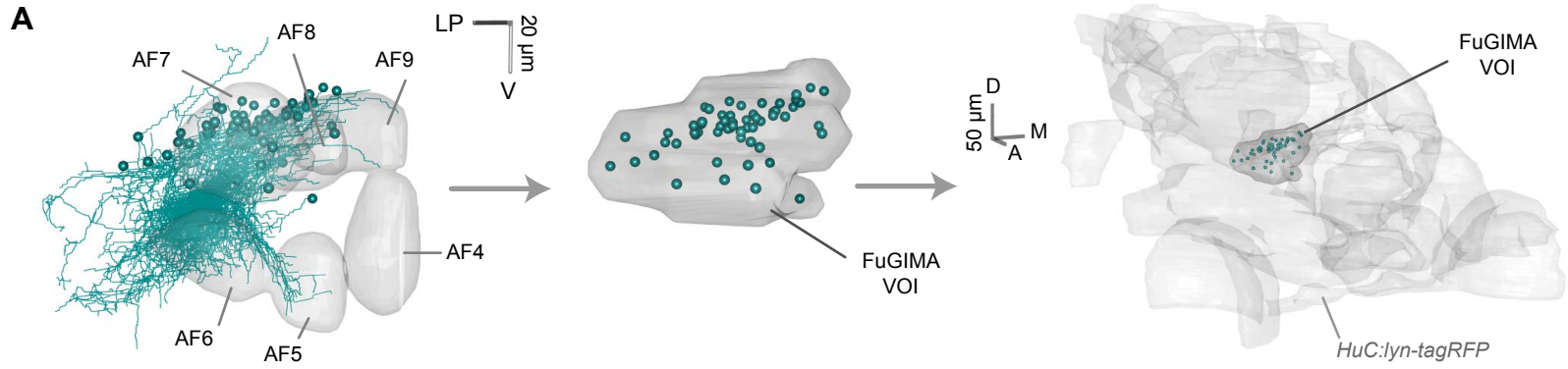


Fig. S6

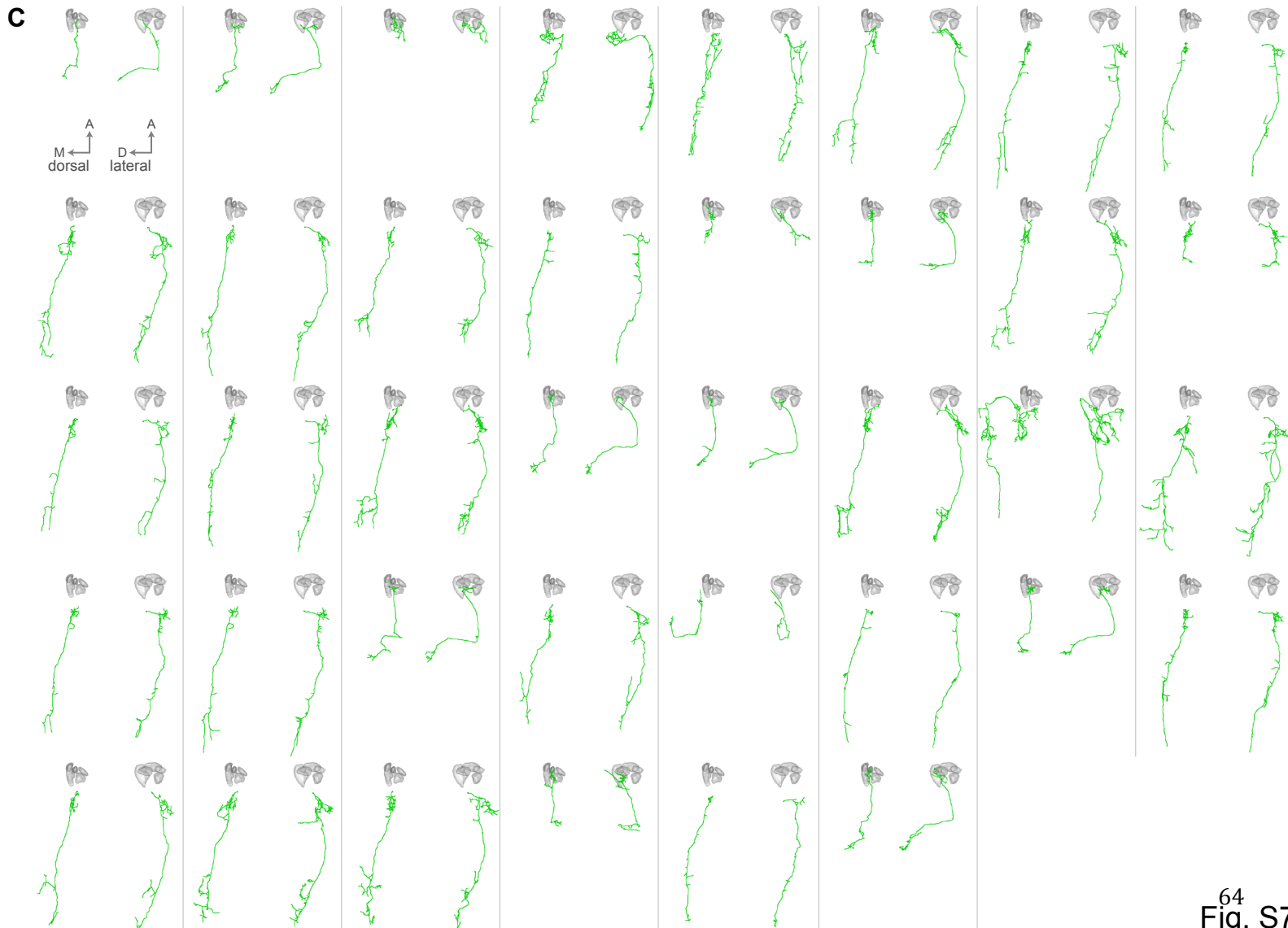
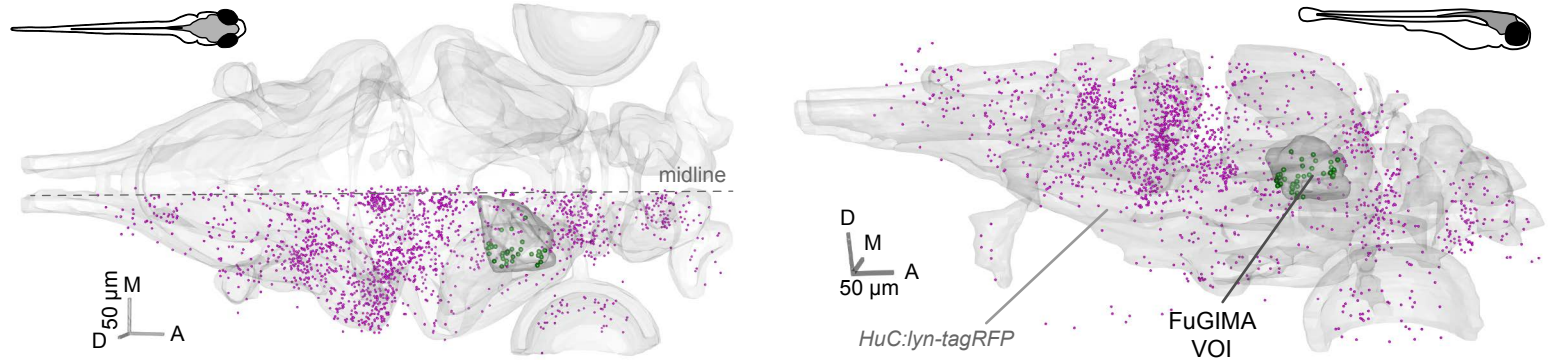
Supplementary Figure S6 (related to Figure 3). Mapping of orientation-selectivity, direction-selectivity, and luminance responses in RGC terminals. (A) Response profile to luminance changes in AF 4, 5, and 6 presented from the side or below. Pixels are color coded according to the mutually exclusive luminance response types: pixels responsive to increase in luminance (ON), decrease in luminance, and both increase and decrease in luminance (ON-OFF). **(B)** Representative luminance response in AF4 and 6. Visual stimuli were presented from the side. ROIs correspond to synaptic puncta marked in the right panel. Note that AF5 is not contained in this optical plane. In (A) and (B), functional pixels are plotted on top of the mean image of syGCaMP6s (gray). **(C)** 3D representation of luminance response in RGC terminals. (Left) 3D model of AFs (as Figure 2B). For side presented 3D map, both AF10 and AF 4, 5, and 6 volumes are pooled from 6 functionally imaged volumes. For underneath presented 3D map, both AF10 and AF 4, 5, and 6 volumes are pooled from 7 functionally imaged volumes. The intensity of pixels corresponds to the frequency of a particular pixel to be luminance responsive across all imaged fish. Note that AF4 and AF9 contain highly luminance responsive RGC terminals and AF5 is weakly ON responsive (right panel). **(D)** Localization of DS pixels in tectal sublaminae. After registration into the RGC reference brain, DS pixels identified by the side (green) and below (magenta) presentations of visual stimuli were overlaid to the average image of *isl2b:Gal4, UAS:syGCaMP6s* signals of the same registered volume. DS pixels tuned to forward motion are plotted here for both side and below stimulus presentations. The volume was sliced obliquely to reveal laminar structure along the superficial-deep axis within the tectal neuropil. **(E)** Intensity plot along region indicated by a box shown in (D). Note that DS pixels for both stimulus positions (side, below) occupy SFGS1. **(F, G)** Color scheme of orientation space for motion presented from the side (F) and below (G). **(H, I)** Orientation selectivity (OS) in AF4, AF5 and AF6. The motion was presented from the side (H) and below (I). The color code is shown in (F, G). OS pixels are plotted on top of the mean image of syGCaMP6s (gray). **(J)** Representative responses of OS-RGC terminals in AF6. Visual stimuli were presented from the side. ROIs correspond to synaptic puncta

marked by the two circular ROIs in the bottom left image. Polar plot (bottom right) is derived from the $\Delta F/F$ traces shown above. A, anterior; P, posterior; D, dorsal, L, lateral. SO, *stratum opticum*; SFGS, *stratum fibrosum et griseum superficiale*; SGC, *stratum griseum centrale*; SAC, *stratum album centrale*. Scale bars: 10 μm (A, I), 30 μm (D) and 50 μm (C).



FuGIMA VOI: surface encompassing somata of FuGIMA neurons (n = 58)

B search in single-neuron atlas:
 • somata in FuGIMA VOI (n = 38), • somata outside of FuGIMA VOI (n = 1705)



Supplementary Figure S7 (related to Figure 6). Search strategy to complement FuGIMA tracings with a single-neuron atlas and results. (A) Definition of the FuGIMA “volume-of-interest” (FuGIMA VOI), the search area to find neurons complementing FuGIMA neurons (pretectal projection neuron (PPNs)) in a single-neuron atlas. The surface encompasses the somata of all FuGIMA neurons (n = 58 neurons) and is registered to the volume of a single-neuron atlas (Kunst et al. (2019), this issue of *Neuron*). **(B)** 3D rendering of the single-neuron atlas standard brain (*HuC:lyn-tagRFP*, Kunst et al. (2019), this issue of *Neuron*) and all somata from this single-neuron atlas, color-coded according to position within (green, n = 38, pretectal projection neurons, PPNs) or outside of the FuGIMA VOI (magenta, n = 1705, out of 1743 tracings in the atlas) (left: dorsal view, right: lateral view). **(C)** Individual tracings of PPNs, plotted with AFs 4 – 9; two plots per neuron: dorsal view (left) and lateral view (right), respectively.

2.2 An Essential Circuit Node for Motion-Induced Behavior Identified by an Optical Illusion

Yunmin Wu, Marco Dal Maschio, Herwig Baier, Fumi Kubo

The manuscript “An Essential Circuit Node for Motion-Induced Behavior Identified by an Optical Illusion” is in preparation for submission.

Author contributions:

Y.W., H.B., and F.K. conceived the project. **Y.W.** performed behavior, functional imaging, optogenetics, and ablation experiments. **Y.W.** designed and implemented the analysis for the behavior data. **Y.W.** and M.D.M. designed the analysis pipeline for functional imaging and wrote the custom python scripts. **Y.W.**, M.D.M., H.B., and F.K. wrote the manuscript.

Title: An Essential Circuit Node for Motion-Induced Behavior Identified by an Optical Illusion

Authors: Yunmin Wu¹, Marco Dal Maschio^{1,2}, Fumi Kubo^{1,3*}, Herwig Baier¹

Affiliations:

5 ¹Max Planck Institute of Neurobiology, Department Genes-Circuits-Behavior, Am Klopferspitz 18, 82152 Martinsried, Germany

²Department of Biomedical Sciences, University of Padua, Via 8 Febbraio 1848, 2, 35122 Padova, Italy

10 ³National Institute of Genetics, Center for Frontier Research, 1111 Yata, Mishima, Shizuoka, 411-8540, Japan

*Correspondence to: fumikubo@nig.ac.jp (F.K.)

Abstract (100-125 words):

15 Optical illusions have long been used in human psychophysics to infer general mechanisms of neural processing, such as lateral inhibition in the retina and pattern completion by the visual cortex. Here we use the motion aftereffect, which causes the well-known 'waterfall illusion', together with cellular-resolution functional imaging and region-specific optogenetic manipulations in zebrafish larva, to identify neurons whose activity induces the optokinetic reflex. Remarkably, these neurons represent merely a small fraction of the entire population of direction-selective cells, are clustered in a pretectal area, and are both necessary and sufficient to drive optokinetic eye
20 movements. Thus, the illusion-based paradigm allowed us to pinpoint key circuit elements of global motion processing in the brain of a vertebrate.

One Sentence Summary (125 characters): Functional imaging during illusory motion identifies a subset of direction selective neurons that evoke optokinetic behavior.

25

Main Text:

Sensory perception, cognition and action arise by the activity of populations of interconnected neurons across the brain. Generally, researchers can rely on a large toolbox of experimental and analytical approaches to identify such activity patterns and to formulate models of underlying circuit mechanisms (1, 2). However, in many cases, it remains a challenge to distill causal relationships from the correlative information for a given behavior due to the abundance of responsive neurons and their widespread distribution. For example, recent whole-brain imaging studies in larval zebrafish demonstrated widespread activation of neurons responding to horizontal motion of a visual scene (3, 4). The large number (in the thousands) and scattered distribution of direction-selective (DS) neurons has been taken as evidence for distributed network activity in even simple motion-evoked behaviors (3). An alternative interpretation of these results argues that the stream of behavior-causing activity is in fact limited to a 'labeled line' of a few, sequentially connected areas. In this view, the majority of co-active neurons outside of this central stream might process unrelated (e.g. local motion computation), corollary or feedback information. Disentangling correlation from causation would require necessity and sufficiency experiments on each of the candidate neuronal subsets – a daunting task given the sheer number of testable combinations.

To narrow down the neurons responsible for global motion perception in zebrafish, we took advantage of a classical optical illusion called motion aftereffect (MAE). MAE describes the phenomenon in which, after a prolonged exposure to a visual scene moving in one direction (e.g. a waterfall), stationary objects (e.g. the rocks near the waterfall) appear to drift in the opposite direction. The existence of MAE has been documented in invertebrates (5) and vertebrates (6–8), including zebrafish (9). Given the unique scenario of motion perception in the absence of visual motion, we hypothesized that DS neurons that are active during MAE might play a causal role in global motion perception. If so, MAE responsiveness can be used as a signature to tag neurons that sit within the core stream of global motion processing.

Normally, a presentation of motion in the visual scene (e.g. the conditioning phase, Fig. 1B) elicits an optokinetic reflex (OKR), which consists of cycles of slow phase eye movements in the motion direction, interspersed by reset saccades in the opposite direction (10). Interestingly, after prolonged motion stimulation in the conditioning phase, the fish frequently (91.6% under optimal condition) showed reversed OKR-like behavior instead of undirected spontaneous eye movements,

suggesting they perceive motion opposite to the conditioning motion (the test phase; Fig. 1B). Similar to MAE in human (11, 12), this OKR-like behavior in zebrafish exhibited lower velocity and smaller amplitudes compared to the OKR to real motion (fig. S1).

5 By systematically varying the duration (2, 3, 4, 5, 6, and 7 min) and the speed (5, 15, and 30 °/s) of the conditioning motion, we determined the best stimulus conditions to induce MAE in our assay (fig. S1A). Similar to a previous study (9), induction of MAE depended on the duration of the conditioning motion and saturated for durations of 5 min and longer, while the speed in the range tested had negligible effect (fig. S2). Thus, we chose a conditioning phase of 5 min at 30°/s for further experiments.

10 To identify the brain area(s) required for MAE, we used GtACR2, an optogenetic silencer, to disrupt the activity of candidate areas (Fig. 1C, fig. S3D-G). We separately targeted retinal ganglion cell (RGC) axons, tectum, and pretectum with tissue-specific transgenic drivers (Fig. 1D) and quantified the eye movements using an ‘OKR index’ (OKR index = #CW saccades over 60s - #CCW saccades over 60s.). When blue light was turned on in the test phase, fish in which either RGC axons or
15 tectum were silenced still showed MAE (Fig. 1, E and F), suggesting that neurons in these areas are dispensable for MAE. In contrast, MAE was diminished in pretectum-silenced fish, suggesting that the pretectum is required for the OKR-like behavior in the test phase (Fig. 1G).

A widely accepted hypothesis attributes MAE to an imbalance between oppositely tuned direction selective (DS) neurons after motion adaptation (13). To determine the source of motion adaptation,
20 we inhibited the tectum and the pretectum in the conditioning phase. MAE was significantly reduced for both tectum- and pretectum-silenced fish, suggesting that motion adaptation in both areas contributed to MAE (Fig. 1, H and I). Notably, the OKR in the conditioning phase was severely impaired in the pretectum-silenced fish. In some cases, OKR behavior was replaced by spontaneous eye movements despite the presence of motion stimuli (fig. S3H). We ruled out the
25 effect of blue light stimulation by exposing non-expressing clutchmates to the same visual stimuli and light stimulation (Fig. 1, J and K). The fact that silencing of pretectal activity strongly affected the OKR to both real and illusory motion suggests that MAE arises from motion-processing circuits in the pretectum.

To test this scenario, we searched for neural correlates of MAE by performing calcium imaging in
30 brains expressing a nuclear-localized calcium indicator (n=10, Fig. 2B). We performed volumetric

calcium imaging at cellular resolution focusing on the tectum, the pretectum and surrounding areas (Fig. 2, B and C). The visual stimulus consisted of the pre-phase, the conditioning phase, and the test phase as in the behavior assay (Fig. 2A). We began by presenting short periods of clockwise (CW) and counterclockwise (CCW) motion to probe the direction selectivity of neurons. After the MAE stimulus protocol, we then exposed the fish to a series of motion phases, which included monocular and binocular optic flow patterns (Fig 2H).

To identify prominent response types, we employed unsupervised hierarchical clustering based on vectors of coefficients that represent how a cell responded during real and illusory motion perception (fig. S4). This approach divided motion-responsive neurons into 11 clusters, of which 5 represented DS neurons (Fig. 2, D and E). Conditioning-motion tuned (CMT) neurons, i.e. neurons with their preferred direction aligned with the conditioning direction, were divided into two subtypes, C5 and C6 (Fig. 2G). Compared to C5, C6 neurons adapted more rapidly ($\tau_{C5} = 90s$, $\tau_{C6} = 39s$) and their activity dropped more by the end of the conditioning phase ($decrease_{C5} = 54.0\%$, $decrease_{C6} = 87.9\%$). On the other hand, opposing motion tuned (OMT) neurons, whose preferred direction is opposite to the conditioning motion but same as the expected illusory motion, were classified into three subtypes, namely C2, C3 and C4, which differ in their activity during the test phase (Fig. 2F). Remarkably, despite the presence of OKR-like behavior, 47.3% of the OMT neurons (C4) stayed inactive throughout the test phase. In contrast, C2 and C3 neurons were active in the test phase, but with different temporal dynamics. C2 neurons showed a fast onset in the test phase ($\tau_{C2} = 5.4s$), while C3 showed a slow onset ($\tau_{C3} = 17.2s$). A shorter conditioning phase, insufficient to induce MAE, also did not induce activity of C2 and C3 in the test phase (fig. S5), suggesting they are the neural correlates of MAE.

Interestingly, most MAE-correlated neurons (C2 and C3) received monocular input, mainly from the contralateral eye (Fig. 2I, fig. S6). Note that the neurons tuned to temporal motion in the contralateral eye were more enriched in "fast" MAE neurons (C2), whereas the neurons tuned to nasal motion in the contralateral eye were more enriched in "slow" MAE neurons (C3) (Fig. 2I). On the other hand, neurons with rotation-selective response, which involves binocular computation (14), were overrepresented in non-MAE neurons (Fig. 2J).

To find out if there exists a spatial segregation of MAE-correlated neurons, we registered the coordinates of each functionally identified neuron into a single standard brain (fig. S7-8), which

also holds the previously annotated contours of various brain areas (Fig. 3A)(15). This registration procedure allows a high-resolution anatomical annotation of functionally identified neurons. MAE-correlated neurons were found mostly in visual areas, e.g. tectum and pretectum, but also in motor/premotor areas, e.g. cerebellum (Fig. 3B and fig. S9). Notably, the pretectum contained the largest proportion of MAE-correlated neurons (Fig. 3C).

Interestingly, DS neurons of different functional subtypes appear to concentrate in largely non-overlapping spatial hotspots. MAE-correlated neurons (C2 and C3) formed symmetrical hotspots in the ventral-lateral pretectum, coincident with the migrated pretectal region M1 (16) (Fig. 3, D and E, cyan). Within this hotspot, C2 neurons are located more dorsally than C3 neurons (Fig 3, G and H). On the other hand, non-MAE DS neurons (C4) also form their own spatial hotspot close to the midline (Fig. 3F, green). These neurons, given their location and tuning, are most likely neurons in the previously identified posterior-dorsal cluster (PDC) (Fig. 3I, fig. S10, D-F)(14).

MAE-correlated neurons in the pretectum might play an essential and specific role in driving the OKR. To test this hypothesis, we unilaterally photoablated small groups of MAE-correlated neurons in the pretectal hotspot (typically 6-12 individual neurons; CCW tuned cells in left hemisphere or CW tuned cells in right hemisphere; Fig. 4, A and B, fig. S11A). After overnight recovery, the fish were tested for their behavioral response to four monocular motion phases (i.e. LN, LT, RN, and RT) (Fig. 4C), because almost all DS neurons in this hotspot are monocular and receive contralateral input (Fig. 3, G and H). The ablation of the MAE-correlated neurons in the pretectal hotspot resulted in a specific impairment of the OKR to nasal motion presented to the contralateral eye, but not to nasal motion in the ipsilateral eye or temporal motion both in the contra- and ipsilateral eyes (n=7, Fig. 4, D and E). There was no significant effect, when non-MAE DS pretectal neurons were ablated or when neurons unresponsive to motion in the vicinity of the hotspot were ablated (n=4 for each control condition; Fig. 4, F to H; fig. S11, B to D). Together, these results suggest that MAE-correlated neurons in the pretectal hotspot are required to induce OKR.

We asked further if these pretectal MAE-correlated neurons were also sufficient to drive OKR. To answer this question, we locally activated neurons in the hotspot using transgenic fish that expressed channelrhodopsin in the pretectum (Fig. 4I). Strikingly, unilateral laser stimulation targeted at ventral-lateral pretectum induced OKR (Fig. 4J). The optogenetically induced OKR

was more prominent and robust in the eye contralateral to the illumination (Fig. 4K). Same light intensity caused no detectable change in spontaneous eye movements in non-expressing clutchmates (Fig. 4K, fig. S12, D and E). We conclude that a pretectal hotspot is a necessary and sufficient station in the global motion-processing stream that evokes OKR behavior.

5 In summary, our experiments granted us an opportunity to pinpoint a cluster of behaviorally relevant DS neurons, which could not have been straightforwardly identified by imaging of responses to real global motion (3, 4, 14). Our finding that many DS neurons stayed quiet during the OKR-like behavior elicited by MAE implies that neurons of the same direction selectivity might be engaged in separate pathways dedicated to different behavioral goals. It is yet to be found
10 out what behaviors the non-MAE neurons contribute to and how connectivity of MAE and no-MAE neurons differs. The pretectal sub-circuit identified here in a small vertebrate brain may constitute a neural substrate for the MAE parallel to the one ascribed to visual cortex in primates (17–19). More generally, we show here that imaging of neuronal responses to an optical illusion in zebrafish provide an inroad into the neuronal mechanisms of visual processing, complementing
15 the electrophysiology and functional brain imaging studies in human and non-human primates by offering brain-wide and cellular resolution.

References:

1. S. Panzeri, C. D. Harvey, E. Piasini, P. E. Latham, T. Fellin, Cracking the Neural Code for Sensory Perception by Combining Statistics, Intervention, and Behavior. *Neuron*. **93**, 491–507 (2017).
- 5 2. M. Dal Maschio, J. C. Donovan, T. O. Helmbrecht, H. Baier, Linking Neurons to Network Function and Behavior by Two-Photon Holographic Optogenetics and Volumetric Imaging. *Neuron*. **94**, 774-789.e5 (2017).
3. E. A. Naumann, J. E. Fitzgerald, T. W. Dunn, J. Rihel, H. Sompolinsky, F. Engert, From
10 Whole-Brain Data to Functional Circuit Models: The Zebrafish Optomotor Response. *Cell*.
167, 947-960.e20 (2016).
4. R. Portugues, C. E. Feierstein, F. Engert, M. B. Orger, Whole-Brain Activity Maps Reveal Stereotyped, Distributed Networks for Visuomotor Behavior. *Neuron*. **81**, 1328–1343 (2014).
5. M. V. Srinivasan, D. R. Dvorak, The waterfall illusion in an insect visual system. *Vision Research*. **19**, 1435–1437 (1979).
- 15 6. H. B. Barlow, R. M. Hill, Evidence for a Physiological Explanation of the Waterfall Phenomenon and Figural After-effects. *Nature*. **200**, 1345 (1963).
7. T. R. Scott, D. A. Powell, Measurement of a Visual Motion Aftereffect in the Rhesus Monkey. *Science*. **140**, 57–59 (1963).
8. J. M. Samonds, S. Lieberman, N. J. Priebe, Motion Discrimination and the Motion Aftereffect
20 in Mouse Vision. *eNeuro*. **5** (2018), doi:10.1523/ENEURO.0065-18.2018.
9. V. Pérez-Schuster, A. Kulkarni, M. Nouvian, S. A. Romano, K. Lygdas, A. Jouary, M. Dipoppa, T. Pietri, M. Haudrechy, V. Candat, J. Boulanger-Weill, V. Hakim, G. Sumbre, Sustained Rhythmic Brain Activity Underlies Visual Motion Perception in Zebrafish. *Cell Reports*. **17**, 1098–1112 (2016).

10. S. S. Easter, G. N. Nicola, The development of eye movements in the zebrafish (*Danio rerio*). *Dev Psychobiol.* **31**, 267–276 (1997).
11. D. I. Braun, L. Pracejus, K. R. Gegenfurtner, Motion aftereffect elicits smooth pursuit eye movements. *Journal of Vision.* **6**, 671–684 (2006).
- 5 12. J. L. Gardner, S. N. Tokiyama, S. G. Lisberger, A Population Decoding Framework for Motion Aftereffects on Smooth Pursuit Eye Movements. *J. Neurosci.* **24**, 9035–9048 (2004).
13. N. S. Sutherland, Figural After-Effects and Apparent Size. *Quarterly Journal of Experimental Psychology.* **13**, 222–228 (1961).
14. F. Kubo, B. Hablitzel, M. Dal Maschio, W. Driever, H. Baier, A. B. Arrenberg, Functional
10 Architecture of an Optic Flow-Responsive Area that Drives Horizontal Eye Movements in Zebrafish. *Neuron.* **81**, 1344–1359 (2014).
15. M. Kunst, E. Laurell, N. Mokayes, A. Kramer, F. Kubo, A. M. Fernandes, D. Förster, M. D. Maschio, H. Baier, A Cellular-Resolution Atlas of the Larval Zebrafish Brain. *Neuron.* **103**, 21-38.e5 (2019).
- 15 16. T. Mueller, M. F. Wullimann, BrdU-, neuroD (nrd)- and Hu-studies reveal unusual non-ventricular neurogenesis in the postembryonic zebrafish forebrain. *Mechanisms of Development.* **117**, 123–135 (2002).
17. R. B. H. Tootell, J. B. Reppas, A. M. Dale, R. B. Look, M. I. Sereno, R. Malach, T. J. Brady, B. R. Rosen, Visual motion aftereffect in human cortical area MT revealed by functional
20 magnetic resonance imaging. *Nature.* **375**, 139–141 (1995).
18. H. Hautzel, J. G. Taylor, B. J. Krause, N. Schmitz, L. Tellmann, K. Ziemons, N. J. Shah, H. Herzog, H. W. Müller-Gärtner, The motion aftereffect: more than area V5/MT? Evidence from 15O-butanol PET studies. *Brain Res.* **892**, 281–292 (2001).
19. J. C. Culham, S. P. Dukelow, T. Vilis, F. A. Hassard, J. S. Gati, R. S. Menon, M. A. Goodale,
25 Recovery of fMRI activation in motion area MT following storage of the motion aftereffect. *J. Neurophysiol.* **81**, 388–393 (1999).

Materials and Methods

Animal care and transgenic zebrafish

Adult and larval zebrafish (*Danio rerio*) were housed and handled according to standard procedures (Westerfield, 2007). All animal experiments were performed under the regulations of the Max Planck Society and the regional government of Upper Bavaria. We used the following transgenic lines: Tg(isl2b:Gal4-VP16)zc65 and Tg(UAS:syGCaMP6s)mpn156; Tg(elavl3:lyn-tagRFP)mpn404; Tg(elavl3:H2B-GCaMP6s); Tg(UAS:GCaMP6s)mpn101; Tg(Vglut2a:Gal4); Tg(gad1b:Gal4VP16)mpn155; Tg(Gal4s1026t); Tg(UAS-E1b:Ntr-mCherry)c264; Tg(UAS:Cr.ChR2_H134R-mCherry); Tg(SAGFF(LF)81C), kindly provided by Koichi Kawakami (National Institute of Genetics, Japan); Tg(UAS:GtACR2:eYFP)sq212, generously provided by Suresh Jesuthasan (Nanyang Technological University, Singapore). Transgenic fish were kept in either a TL or TLN (nacre) background and larvae lacking trunk pigmentation (outcrossed to TLN, nacre) were used in the experiment. Zebrafish larvae were raised in Danieau's solution on a 14/10h light/dark cycle until day 5 or 6 post-fertilization (dpf) with the exception of optogenetic silencer expressing larvae, which were raised in the dark. There was no gender bias in experiment subjects, since sex determination has not yet occurred at this stage.

MAE behavior assay and optogenetic stimulations

5 or 6 dpf zebrafish larvae were embedded in 2% low melting point agarose at the center of 35mm diameter dish. To allow free eye movements, the agarose in the vicinity of the eyes was carefully removed. Afterwards, individual larvae were placed in the center of a visual arena made of 4 miniature LCD screens (height, 6cm; width, 8cm), which displayed either stationary or moving sinusoidal gratings with spatial frequency of 0.066 cycle/°. The visual stimulation protocol in the MAE behavior assay consisted of three phases: 1) the pre-phase, in which stationary grating was presented for 5 min, 2) the conditioning phase, in which unidirectional rotating gratings were presented for a set period of time, and 3) the test phase, in which stationary grating was presented again for 5 min. To find out the stimulus determinants of MAE, we tested different durations (2, 3, 4, 5, 6, 7 min) and speeds (5, 15, 30°/s) in the conditioning phase. The direction of motion in the conditioning phase was randomized to be either CW or CCW in each trial, and each larva went through only one trial to avoid cumulative effect of motion conditioning. Concurrent with visual stimulation, eye movements of the fish were recorded at 15Hz using a CCD video camera (Allied

Vision Technology) mounted upon a dissecting scope. For behavior experiments with optogenetic stimulation, the conditioning phase was fixed to 5min at 30°/s, and the fish was illuminated by 850nm infrared LED to avoid the contamination of optogenetic illumination, which was filtered out by an IR filter (Thorlabs absorptive filter, ND=1.0). A 200um (for perturbation with GtACR2) or a 50um (for activation with ChR2) light fiber delivering 473nm laser (Omicron Lighthub) was placed right on top of the fish targeting desired brain area. For optogenetic silencing, the laser was turned on in either the conditioning phase or the test phase using custom python script. Although GtACR2 has been shown to have both activating and inactivating effects depending on the subcellular locations of activation (1), bilaterally activating GtACR2 in an entire population of the RGCs, the tectum, or the pretectum perturbed OKR to the expected extent (2, 3), suggesting that GtACR2 acted as a silencer under these conditions (fig. S3, D to G)(4). To rule out the effect of genotype, we tested all lines we used with the same visual stimuli without optogenetic illumination (fig. S3, A to C). All the MAE behavioral assay was conducted between 10am and 7pm.

15 Ocular tracking and analysis

From the recorded videos, the angle of both eyes in reference to the midline was extracted using either a custom python script or the Eyetracker program in LabVIEW (as described in Kubo et al. 2014). We focused on saccades in the eye angle time series, which serve as a reliable readout of motion perception in zebrafish larvae: in motion the eyes of a fish almost exclusively saccade in the opposite direction of the motion, whereas in still the eyes of the fish saccade in both CW and CCW directions. To automatically detect saccades, we looked for positive and negative peaks in the first derivative of the eye angle time series using “peak detector” – a python script developed by Marcos Duarte (<https://github.com/demotu/BMC>). The location of the peaks represents saccade time points, and the sign of the peaks represents the saccade direction. To compare between individuals and across experiment conditions, we calculated an OKR index based on the number of saccades to quantify motion perception in zebrafish larvae:

$$\text{OKR index} = \# \text{saccades in CCW direction over 60s} - \# \text{saccades in CW direction over 60s}$$

The 60s time window to calculate the OKR index slides with a step size of 10s. The OKR index is 1) positive, when a fish sees CW motion, 2) negative, when a fish sees CCW motion, and 3) around zero, when a fish is presented with no motion. The sign of the OKR index was reversed for fish

conditioned with CW motion, so that they could be directly compared to fish conditioned with CCW motion, and the OKR index in the conditioning phase is always negative.

Two-Photon calcium imaging

5 2P calcium imaging was performed on 5 or 6dpf Tg(elavl3:H2B-GCaMP6s), Tg(elavl3:lyn-tagRFP)mpn404 double-transgenic zebrafish larvae immobilized in 2% agarose. The visual stimuli were presented to the fish by a custom-built 360° red LED-arena (660 nm Kubo et al., 2014). The LED-arena displayed gratings with spatial frequency of 0.033 cycles/° and temporal frequency of 1Hz when moving. We presented 3 different visual stimulus protocols to each fish. The first
10 protocol consists of 8 motion phases in pseudorandom order repeated for 3 times. These 8 phases includes 4 binocular motion: 1) clockwise (CW), 2) counterclockwise (CCW), 3) forward (FW), 4) backward (BW), and 4 monocular motion: 5) left-eye nasal (LN), 6) left-eye temporal (LT), 7) right-eye nasal (RN), 8) right-eye temporal (RT). Each motion phase lasted for 5s and was followed by a 30s interval of stationary gratings. An additional 30s interval was installed whenever
15 luminance change occurred. This protocol was used to probe the ocular selectivity and rotation selectivity of a neuron. The second protocol has 4 sequential components: 1) 8min of stationary gratings to identify the baseline of neurons without motion stimulation, 2) 2 rounds of alternating CW and CCW motion for 5s with 30s interval to determine the direction selectivity of neurons (the direction opposite to the conditioning motion always came first), 3) 5min of rotating gratings
20 in either CW or CCW direction to induce MAE (the conditioning phase), and 4) 3 min of stationary gratings in which the fish supposedly experienced illusory motion (the test phase). This protocol was used to probe the response of different neural populations during MAE. The third protocol was the same as the second except that the conditioning phase was shortened to 1min. Behaviorally there was no response to illusory motion under this condition, therefore this protocol served as a
25 control to verify if a neuron was truly the neural correlates of MAE. Concurrent with visual stimulation, we performed volumetric imaging of the brain using Femtonics 3DRC microscope (Femtonics, Tuzlo, Hungary) coupled with electrically tunable lens (Optotune, EL-10-30-Ci-IR-LD-MV) and a 16x objective (Nikon CFI70, NA 0.8, WD 3.0mm). This enabled us to simultaneously image 10 planes of 419.6 um by 234 um with 14-16 um intervals at 1Hz. The pixel
30 size (0.9 um/pixel) was sufficient for single cell resolution, given the diameter of zebrafish neurons

is about 5 μm . We presented each visual stimulus protocol twice in order to cover our volume of interest at 7-8 μm intervals.

Data analysis for 2P calcium imaging

5 The recordings from volumetric imaging was first deinterleaved by a custom-written python script. Then for the time series of each plane, we used CaImAn (DOI: [10.7554/eLife.38173](https://doi.org/10.7554/eLife.38173)) for motion correction and ROI extraction (~22,000 ROIs per fish out of 20 planes). To narrow down to motion responsive ROIs, we performed two linear-regression-based analyses on the fluorescence time series from extracted ROIs. Briefly, we created 3 motion regressors (CW, CCW, and CW+CCW),
10 which are times series of zeros (when there is no motion) and ones (when the corresponding visual motion is on) convolved by a kernel of H2B-GCaMP6s dynamics ($\tau_{\text{H2B-GCaMP6s}} = 7\text{s}$). These regressors model the expected response of a neuron to a stimulus. For each ROI, we correlated the time series during the short motion part in protocol 2 to the 3 motion regressors in the corresponding time window. Moreover, we fitted the time series in the same period with regressor
15 CW and CCW using the linear model module from sklearn. The ROIs, whose absolute value of correlation coefficients surpassed the threshold 0.4 and whose coefficient of determination (R^2) from fitting surpassed 0.2, were then inspected individually. Overlapping ROIs and ROIs of multiple neurons (10-20% of all ROIs) were detected semi-automatically and corrected manually. From these curated ROI masks of single neurons (fig. S4A), we re-extracted dF/F_0 time series and
20 repeated the regression based analysis. Only ROIs with robust motion response, namely those that surpassed a higher threshold ($|\text{correlation coefficient}|_{\text{max}} > 0.45$, $R^2 > 0.25$) in all three protocols were considered in further analysis.

To parameterize the response to both real and illusory motion, we performed regression based analysis in two time windows using 6 real motion regressors and 6 illusory motion regressors (fig.
25 S4B). These 6 real motion regressors correspond to the three short motion regressors (CW, CCW, and CW+CCW) as described and their reverse, and the 6 illusory motion regressors corresponds to neural activity lasting for 5s, 35s, 65s, 95s, 125s, 155s starting from the beginning of the test phase. To find out the prominent response types in the motion responsive neurons, we performed hierarchical clustering using the 12-parameter matrix as input. We experimentally defined 14 as
30 the cut-off distance in the dendrogram, which yielded 11 distinct clusters.

Quantification of the eye- and optic-flow-pattern-specificity

To quantify the eye- and optic-flow-pattern-specificity of the DS neurons, we focused on their response to the first visual stimulus protocol, which contains 8 motion phases. With the coefficient derived from linear fitting using the linear model module from sklearn, we calculated the average response of each neuron to these 8 motion phases.

To quantify if a neuron responds selectively to rotational motion, we calculated a rotation selectivity index:

$$\text{Rotation selectivity index} = \frac{\text{Response to Rotation. max} - \text{Response to Translation. max}}{(\text{Response to Rotation, Response to Translation}). \text{max}}$$

This index is 0 if a neuron responds equally to rotational and translational motion, 1 if a neuron only respond to rotational motion, and -1 if a neuron only respond to translational motion.

To quantify from which eye a neuron receives its input, we calculated an ocular selectivity index:

$$\text{Ocular selectivity index} = \frac{\text{Response to Right Eye. max} - \text{Response to Left Eye. max}}{(\text{Response to Right Eye, Response to Left Eye}). \text{max}}$$

This index is 0 if a neuron responds equally to motion presented to both eyes, 1 if a neuron only respond to motion presented to the right eye, and -1 if a neuron only respond to motion presented to the left eye.

We categorized DS neurons with rotation selectivity index > 0.5 as rotation selective complex cells. In the remaining DS neurons, we categorized neurons with ocular selectivity index < -0.4 or > 0.4 as monocular simple cells. Based on the location of their cell bodies and their directional tuning, these monocular cells were further divided into subgroups tuned to contralateral nasal (Contra-N), contralateral temporal (Contra-T), ipsilateral nasal (Ipsi-N), and ipsilateral temporal (Ipsi-T) motion. We categorized neurons with $|\text{ocular selectivity index}| < 0.4$ and $|\text{rotation selectivity index}| < 0.5$ as binocular simple cells.

Z stacks acquisition and image registration

For each functionally imaged fish, we acquired a local z-stack of the imaged volume (374.4*374.4 mm², mostly captured at 720 * 720 pixels, 1 um in z, green channel only) with the 2P microscope (Femtonics 3DRC), plus an overview z-stack of the whole brain (640.17*640.17 mm², mostly captured at 1024 pixels * 1024 pixels, 1 um in z, green channel at 488 nm, red channel at 543 nm) with a confocal microscope (Carl Zeiss LSM-700). Before acquisition of the z-stacks, the fish were

treated with tricaine (0.02 %, MS-222, Sigma-Aldrich) to avoid any movement artifacts. To visualize ROIs from different fish in the same standard brain framework, we developed a 3-step registration strategy based on the image registration library ANTs (Advanced Normalization Tools): (1) with custom python script, we mapped the average time series of the imaged planes onto the 2P z-stack. (2) using the command “antsRegistration” in ANTs, we registered the 2P local z-stack onto the confocal overview z-stack of the same fish using elavl3:H2B-GCaMP6s as the reference channel. To facilitate precise registration, we specified a manually defined target region as the guiding mask; (3) using the same ANTs command again (without the guiding mask), we registered the confocal z-stack of each individual fish onto the standard brain using elavl3:lyn-tagRFP as the reference channel (fig. S7A). The generation of the standard brain and the parameters used for ANTs registration has been described in detail in Kunst et al (5). With the transformation files generated from this 3-step registration process, we applied the “antsApplyTransformsToPoints” command to convert the spatial coordinates of each ROI centroids from the 2P z-stack framework to the standard brain framework. For anatomical characterization, we employed the masks of annotated areas established by Kunst et al. in the framework of fixed brain tissue. To make use of these masks in the framework of our standard brain, we used the same “antsRegistration” command to register the fixed brain to our live standard brain using elavl3:lyn-tagRFP as the reference channel. The masks of anatomical areas were coregistered and then thresholded (pixels with intensity < 70 were deemed background) to eliminate the smearing effect of registration. A custom Python script based on Mayavi library was used to visualize cell body locations and anatomical masks in 3D.

Laser targeted ablation

At 5dpf, Tg(elavl3:H2B-GCaMP6s) zebrafish larvae were mounted in 2.0% agarose. We selected 2-3 planes spaced by 10 um in ventral pretectum/dorsal thalamus to perform single-plane functional imaging (Femtonics). To locate DS neurons and identify how they respond to MAE, we presented the fish with protocol(2) using the LED-arena. With a custom python script, we identified in near-online fashion DS neurons with MAE response in the spatial hotspot (5-10 cells per fish), and we ablated these neurons by scanning a small region (4 pixels by 8 pixels) in the center of the target neuron with high power laser (80-100 mW at 800 nm). For one round of ablation, the laser was delivered three times for 0.2s separated by 6s intervals. Multiple rounds of

ablation were carried out until a hole was visible on the cell body and the target cell lost its DS response completely. For the control experiments, non-MAE DS neurons (8-11 cells per fish) or non-motion-responsive neurons in the vicinity of the pretectal hotspot were ablated instead. The ablated fish were freed from the agarose after ablation and left to recover overnight. At 6 dpf, the ablated fish were mounted again with 2% agarose. First, they were reimaged with a simple protocol of alternating CW and CCW motion to confirm effective ablation. Then we removed the agarose surrounding the eyes of the fish, and they were tested for their response to monocular motion stimulation. The visual stimulation consisted of 1 min of stationary gratings followed by 1 min of moving gratings presented monocularly (90° in azimuth, $f_{\text{spatial}} = 0.066$ cycle/ $^\circ$, $f_{\text{temporal}} = 2\text{Hz}$). The 4 monocular motions (LN, LT, RN, and RT) were shown in random order. A piece of black matt metal sheet was put next to the unstimulated eye to avoid reflection from the side of the plastic dish. The eye movements of the fish were recorded and analyzed as described in the section of ocular tracking and analysis.

15 Quantification and Statistical Analysis

All analyses and visualizations were performed with custom-written code in Python, using NumPy, Scipy, Matplotlib, Seaborn, Pandas, Scikit-image, Mayavi, Bokeh and Scikit-learn libraries (Hunter, 2007; McKinney, 2011; Oliphant, 2007; Pedregosa and Varoquaux, 2011; Perez and Granger, 2007; van der Walt et al., 2011, 2014). All statistical details are described in the figure captions, including the exact values of n, what n represents, the definition of center and dispersion, and the statistical tests used.

Fig. 1. Pretectum plays an indispensable role for both veridical and illusory motion detection

(A) Setup for the MAE assay. (B) Eye movements of a zebrafish larvae in response to the visual stimulus. Gray shading, continuous motion. Blue, right eye; Red, left eye. Orange line marks when MAE took place. (C) Schematics of bilateral optogenetic stimulation with a 200um optic fiber. (D) Transgenic lines used to express GtACR2 selectively in RGCs (Islet2b:Gal4), tectum (SAGFF(LF)81C), and pretectum (Gal4 s1026t). (E-G) Mean OKR index (shaded area: mean \pm SEM) of fish with RGCs, tectum and pretectum silenced in the test phase. (H, I) Mean OKR index (shaded area: mean \pm SEM) of fish with tectum and pretectum silenced in the conditioning phase. (J, K) OKR index in the 1st minute of the test phase for tectum and pretectum silenced fish. OFF, no blue illumination; Test ON, blue illumination in the test phase; Cond On, blue illumination in the conditioning phase. Each gray line represents the responses of one fish. * for $P < 0.05$, ** for $P < 0.01$, *** for $P < 0.001$.

Fig. 2. Functional imaging identifies subpopulations of direction-selective neurons that are active during MAE.

(A) Visual stimulus protocol for MAE. (B) Expression pattern of elav3:H2B-GCaMP6s in 5-6dpf larvae. Rectangular box represents the imaging volume. (C) Example planes from volumetric imaging with single-neuron ROIs circled in yellow. (D) 11 clusters identified by hierarchical clustering. Euclidean Distance reflects the similarity between two ROIs. Yellow and blue squares highlight the opposing motion tuned (OMT) and conditioning motion tuned (CMT) populations, respectively. (E) Averaged $\Delta F/F_0$ time series (shaded area: mean \pm SEM) for each cluster. Blue areas represent motion in same direction as the conditioning phase, and red represent motion in reversed direction to the conditioning phase. (F, G) Cluster composition for OMT and CMT neurons. (H) Visual stimulus protocol to probe the ocular input and the rotation selectivity of a neuron. (I) Ocular selectivity and direction preference in monocular OMT neurons per cluster. (J) Rotation selectivity of OMT neurons per cluster. A, anterior; D, dorsal; P, posterior; V, ventral.

Fig. 3. MAE neural correlates are clustered in a spatial hotspot in the pretectum

(A) Previously annotated anatomical masks registered onto the standard brain. (B) Anatomical distribution of OMT neurons in comparison to all DS neurons in the imaged volume. (C)

Percentage of OMT neurons per cluster in various brain areas. (D-F) Spatial distribution of OMT neurons per cluster. Top left, top view; top right, side view from the right; bottom frontal view. Relative density is calculated as the number of neighbors belonging to the same cluster in a radius of 20um, normalized by the highest density per cluster. Cyan dashed line encircles the MAE hotspot; green dashed line encircles the non-MAE hotspot. (G-I) Spatial distribution and tuning of OMT neurons within the MAE and non-MAE hotspots. Frontal view of the region marked by black dashed line in (D-F). The dashed line represents the midline. Contra, contralateral; Ipsi, ipsilateral; N, nasal; T, temporal; Bi, binocular; Rot-sel, rotation selective.

Fig. 4. The pretectal hotspot is not only required but also sufficient to drive OKR

10 (A) Time course of imaging, ablation and behavioral test. (B) MAE neural correlates in the pretectal hotspot before (left) and after (right) the ablation. Scale bar, 20um. (C) Monocular motion stimuli used for the behavioral test. (D) Example responses to the monocular motion stimuli from a fish with 9 CW tuned MAE neural correlates in the right hemisphere ablated. L, left eye; R, right eye. N, nasal direction; T: temporal direction. (E-H) OKR index in response to four monocular motion stimuli for fish with MAE-correlated neurons ablated, non-MAE DS neurons ablated, non-motion neurons in the hotspot ablated, and no ablation, respectively. Ipsi and contra represent motion presented to the eye ipsilateral and contralateral to the ablation side, respectively. (I) Schematics of unilateral optogenetic activation of the pretectal hotspot with channelrhodopsin (Tg(s1026t:gal4; UAS:ChR2-mCherry)) using a 50um optic fiber. (J) Example of optogenetically induced OKR in the absence of visual motion by targeting the pretectal hotspot in the left hemisphere as illustrated in (I). Blue line, right eye; red line, left eye. (K) OKR index of the left eye (red) and the right eye (blue) in response to left and right pretectal hotspot activation. Nil represents no illumination. Colored lines represent ChR2(+) fish, and gray lines represent ChR2(-) fish. The solid line in (E-H, K) showed averaged response with error bars of SEM, whereas each fainter line represents the response of individual fish. Asterisks indicate statistical significance from paired (E-H) and unpaired t test (K): *P < 0.05, **P < 0.01, ***P < 0.001.

Fig. S1. Characteristics of the MAE in larval zebrafish

(A) 18 versions of the conditioning phase of various durations and speeds to identify the optimal MAE stimulus protocol. (B-C) Initial speed of slow-phase eye movements during real and illusory motion. R^2 indicates the goodness of fit for the linear model.

5 **Fig. S2. MAE depends on the duration, but not the speed, of the conditioning phase**

(A-F) Comparison of the averaged OKR index for larvae undergone different conditioning speeds presented for the same duration. (G-I) Comparison of the averaged OKR index for larvae undergone the same conditioning speed presented for different durations. For (A-I), the shaded area represents mean \pm SEM, and the orange arrowheads mark the occurrence of MAE. Color of each line corresponds to the panel shown in Fig. S1A. (J) The OKR index of the first minute in the test phase for all 18 conditions (n = 6 fish for each condition). Ctl refers to the control, which is the OKR index of the last minute of the pre-phase. (n = 6 fish for each condition). Asterisks indicate statistical significance: *P < 0.05, **P < 0.01, ***P < 0.001 for unpaired t test.

Fig. S3. Controls for optogenetic inhibition of the RGCs, the tectum, and the pretectum

15 (A-C) Mean OKR index (shaded area: mean \pm SEM) of *isl2b:Gal4*, *81C:Gal4*, and *s1026t:Gal4* transgenic fish in response to the MAE stimulus protocol without blue light illumination. The light gray areas indicate the conditioning phase. Colored lines represent the GtACR2 expressers, and gray represent GtACR2 non-expressing clutchmates. (D) Example OKR response during motion presentation with RGC inhibition. The light blue line indicates when the blue light illumination
20 was present. Top, response of a GtACR2 expresser; bottom, response of a GtACR2 non-expressing clutchmate. (E-G) OKR index during motion presentation for the RGC-, the tectum- and the pretectum-silenced fish. OFF, no light stimulation; ON, blue light illumination. Each grey line represents the response of one fish to all light conditions. Asterisks indicate statistical significance: *P < 0.05, **P < 0.01, ***P < 0.001, paired t test was used for the same fish under different light
25 conditions, and unpaired t test for different fish under the same light condition. (H) Example response of fish with pretectal inhibition in the conditioning phase. The light gray area indicates

the conditioning phase. The light blue line on top indicates when the blue light illumination was present. Blue line, right eye; red line, left eye.

Fig. S4. Generation of response profile for motion responsive neurons

(A) Example imaged plane. Top, ROIs extracted by CaImAn. Bottom, ROIs in the same plane after filtering away non-motion-responsive ROIs and manual curation to remove overlapping ROIs and ROIs of multiple neurons. (B) 12 regressors and their applicable time windows (marked by dashed boxes) to parameterize the response of each ROI to real and illusory motion.

Fig. S5. Comparison of neural activity per cluster with the conditioning phase of 5min and 1min

Averaged $\Delta F/F_0$ time series (shaded area: mean \pm SEM) for each cluster is plotted on top of the heatmaps of $\Delta F/F_0$ time series for individual neurons. In the plots for averaged $\Delta F/F_0$ time series, the blue areas represent motion in same direction as the conditioning phase, and the red areas represent motion in reversed direction to the conditioning phase. In the heatmaps, one horizontal line represents the response of one neuron. Left, response to a 5min conditioning phase; right, response to a 1min conditioning phase. The left and right heatmaps are sorted in the same order.

Fig. S6. Rotation selectivity and ocular selectivity of CMT and OMT neurons

(A) Density histogram of the rotation selectivity for the CMT neurons (C5&C6). (B) Ocular selectivity and direction preference of monocular CMT neurons per cluster. (C, D) Density histogram of the ocular selectivity for the OMT neurons (C2, C3&C4) and the CMT neurons (C5&C6).

Fig. S7. Registration scheme to the standard brain

(A) Registration pipeline using ANTs. Yellow dots represent the positions of the motion responsive neurons on this example z plane before and after the registration procedures. (B) Overlay of 7 different functionally imaged fish (elav3:H2B-GCaMP6s) that have been registered into the standard brain framework. 3D side-view on the left shows the location of the two selected example z planes. A, anterior; D, dorsal. Scale bars represent 50 μm .

Fig. S8. Spatial distribution of DS and non-DS motion responsive neurons per cluster

For each panel, top left, top view; top right, side view from the right; bottom, frontal view. Relative density is calculated as the number of neighbors belonging to the same cluster in a radius of 20 μm , normalized by the highest density per cluster.

5 **Fig. S9. Anatomical distribution of motion responsive neurons**

(A) Normalized anatomical composition per cluster. (B) Composition of clusters per anatomical area.

Fig. S10. Anatomical identity of the MAE and the non-MAE hotspots

10 (A) MAE neurons (C2&C3) in the MAE hotspot overlaid with the expression patterns of *vglut2a:dsRed* and *gad1b:EGFP* registered to the standard brain. (B-C) Zoom-in views of the dashed line enclosed area in (A) with the *vglut2a:dsRed* pattern only in (B) and the *gad1b:EGFP* expression pattern only in (C). (D) Non-MAE motion responsive neurons (C4) in the non-MAE hotspot on top of the *isl1:EGFP* and the *chatA:GFP* expression patterns registered to the standard brain. (E) Zoom-in view of the dashed line enclosed area in (D). (F) Neurite projection of the
15 neurons found in the single cell atlas (5) with their cell bodies located in the C4 non-MAE hotspot. The search was done using a manually defined mask of the C4 non-MAE hotspot. Scale bars, 50 μm .

Fig. S11. Example of laser targeted ablation and subsequent monocular OKR response

20 (A) MAE neural correlates in the MAE hotspot targeted for laser ablation. Top, location of the 4 out of 8 ablated neurons in this example fish; Bottom, $\Delta F/F_0$ time series in response of the MAE stimulus protocol for all the ablated neurons. (B-D) Example responses to the monocular motion stimuli from fish with non-MAE neurons ablated in the right hemisphere (B), non-motion neurons ablated in the right hemisphere (C), and without ablation (D). Colored areas represent the periods of monocular motion presentation. L, left eye; R, right eye. N, nasal direction; T: temporal
25 direction. RH, ablation in the right hemisphere.

Fig. S12. Optogenetic activation of the pretectal hotspot

(A) Schematics of unilateral optogenetic activation of channelrhodopsin (*Tg(s1026t:gal4; UAS:ChR2-mCherry)*) in the pretectal hotspot using a 50 μm optic fiber. (B) Image of a zebrafish

larva under the setup in (A). (C) Example response of induced OKR in the absence of visual motion by focal activation of the pretectal hotspot in the right hemisphere as illustrated in (A). Blue line, right eye; red line, left eye. (D, E) OKR index of the right eye and the left eye with focal blue light illumination. The result of the ChR2 expressing larvae is in (D) and that of the non-expressing larvae in (E). LPt, illumination in the left ventral lateral pretectum; RPt, illumination in the right ventral lateral pretectum. One dot represents the result from one trial (each fish undergone five trials per side of optogenetic stimulation). Asterisks indicate statistical significance: *P < 0.05, **P < 0.01, ***P < 0.001, paired t test was used for the left eye and right eye response of the same fish, and unpaired t test was used for the rest.

10 **Fig. S13. Minimal circuit model for MAE**

The minimal circuit model of MAE consists of three layers, which could be in principle implemented by the RGCs, the pretectum, and the oculomotor nuclei (OMN) plus the abducens nuclei (ABD), respectively. Each circle represents a subpopulation of DS neurons that share neurotransmitter identity, directional tuning and response to MAE. The arrow within the circle indicates the preferred direction of the corresponding DS population. E, excitatory neurons; I, inhibitory neurons. Circle cap, excitatory synapse; bar cap, inhibitory synapse. Orange highlights the essential wiring that gives rise to the response of MAE neural correlates. Grey highlights the non-MAE neurons, whose contribution to the OKR-like behavior is negligible (dashed line).

20

Figure 1

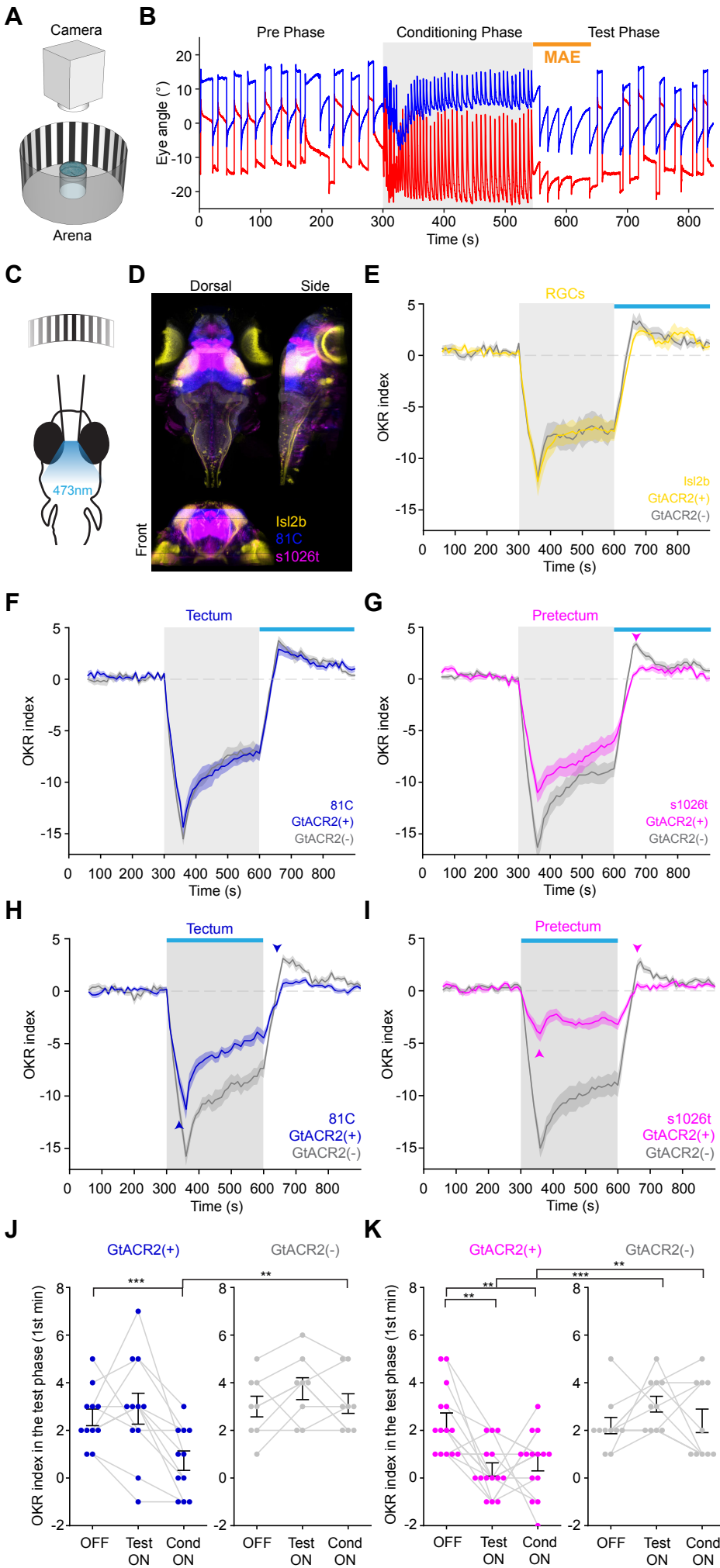


Figure 2

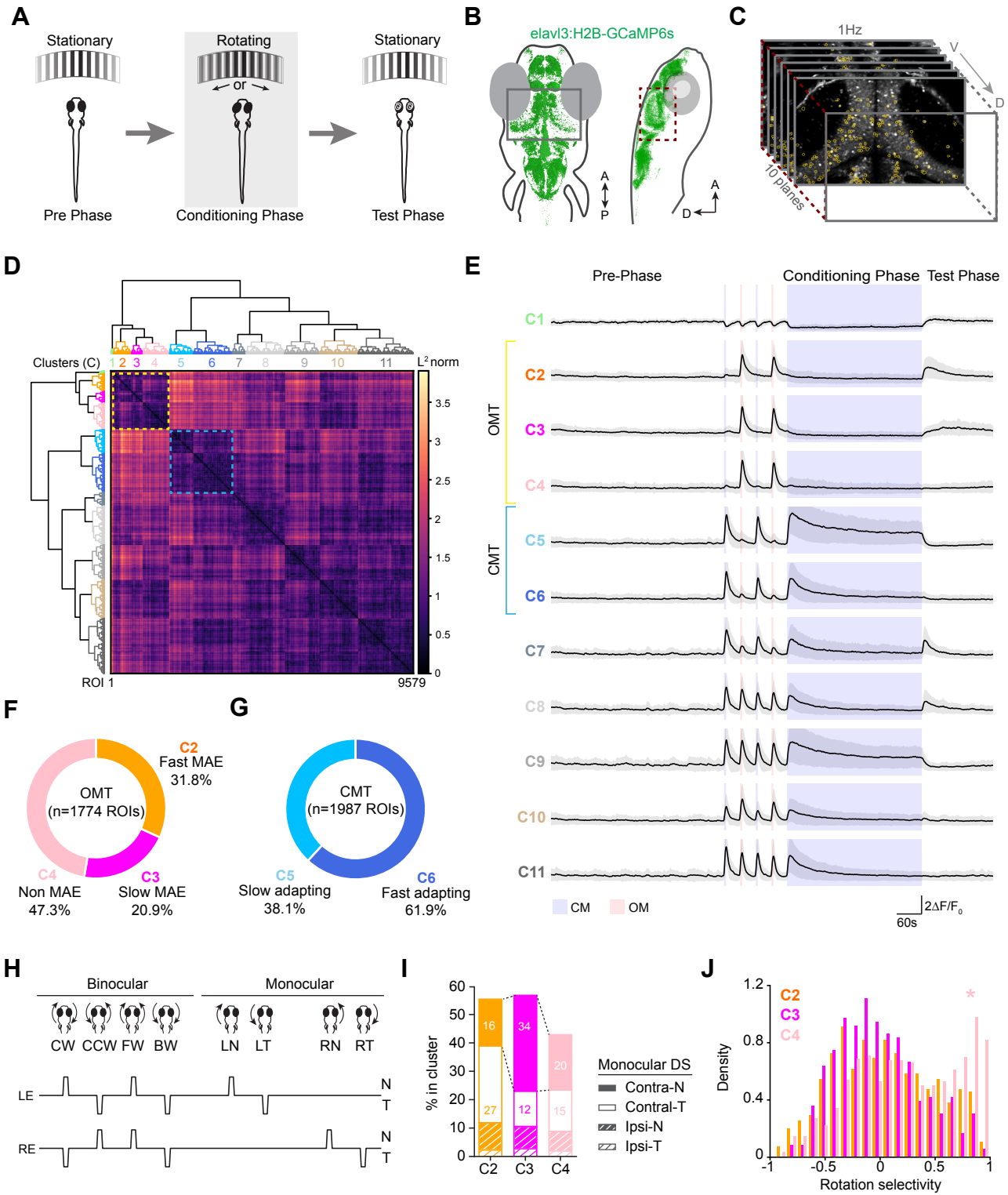


Figure 3

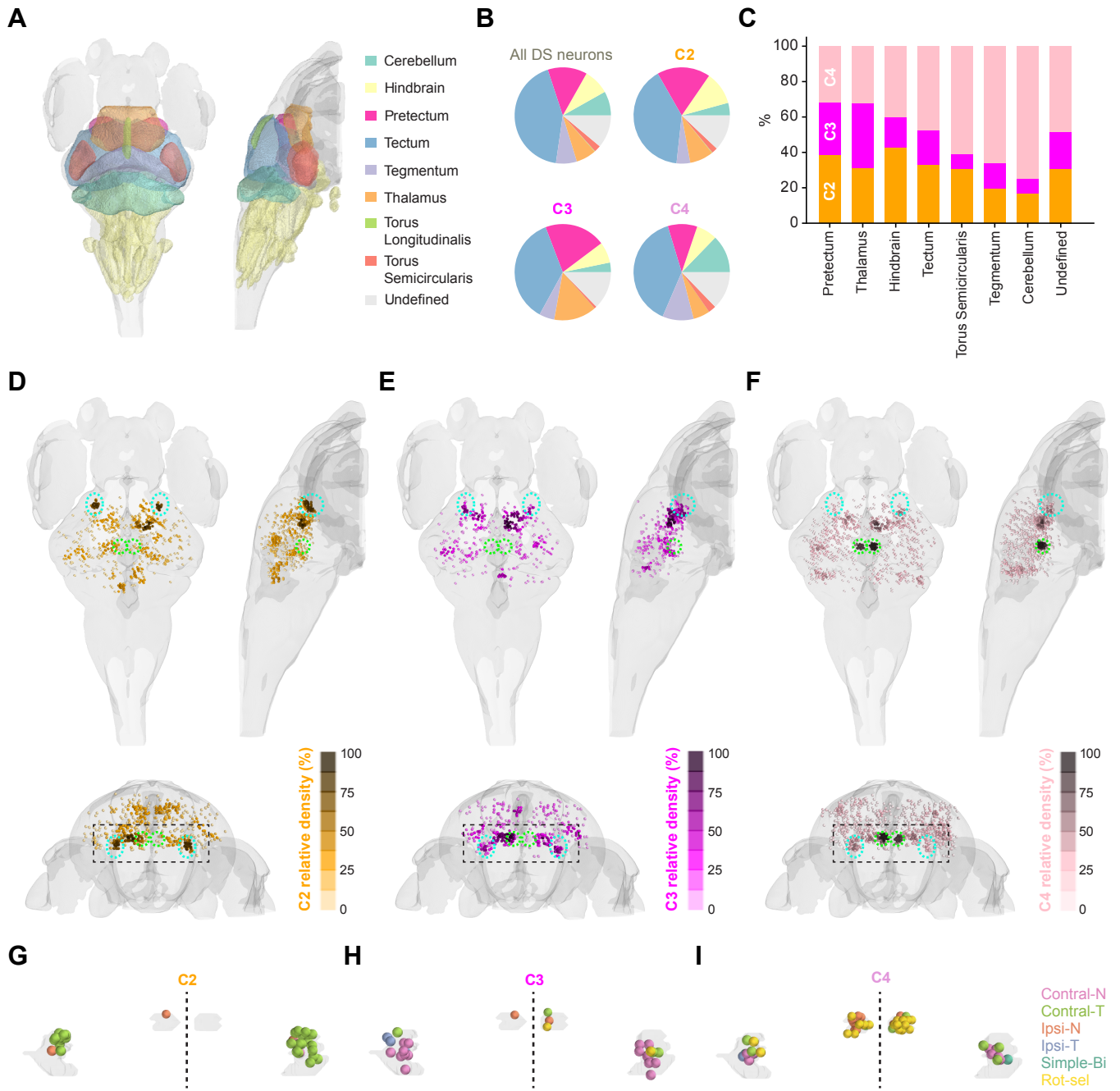
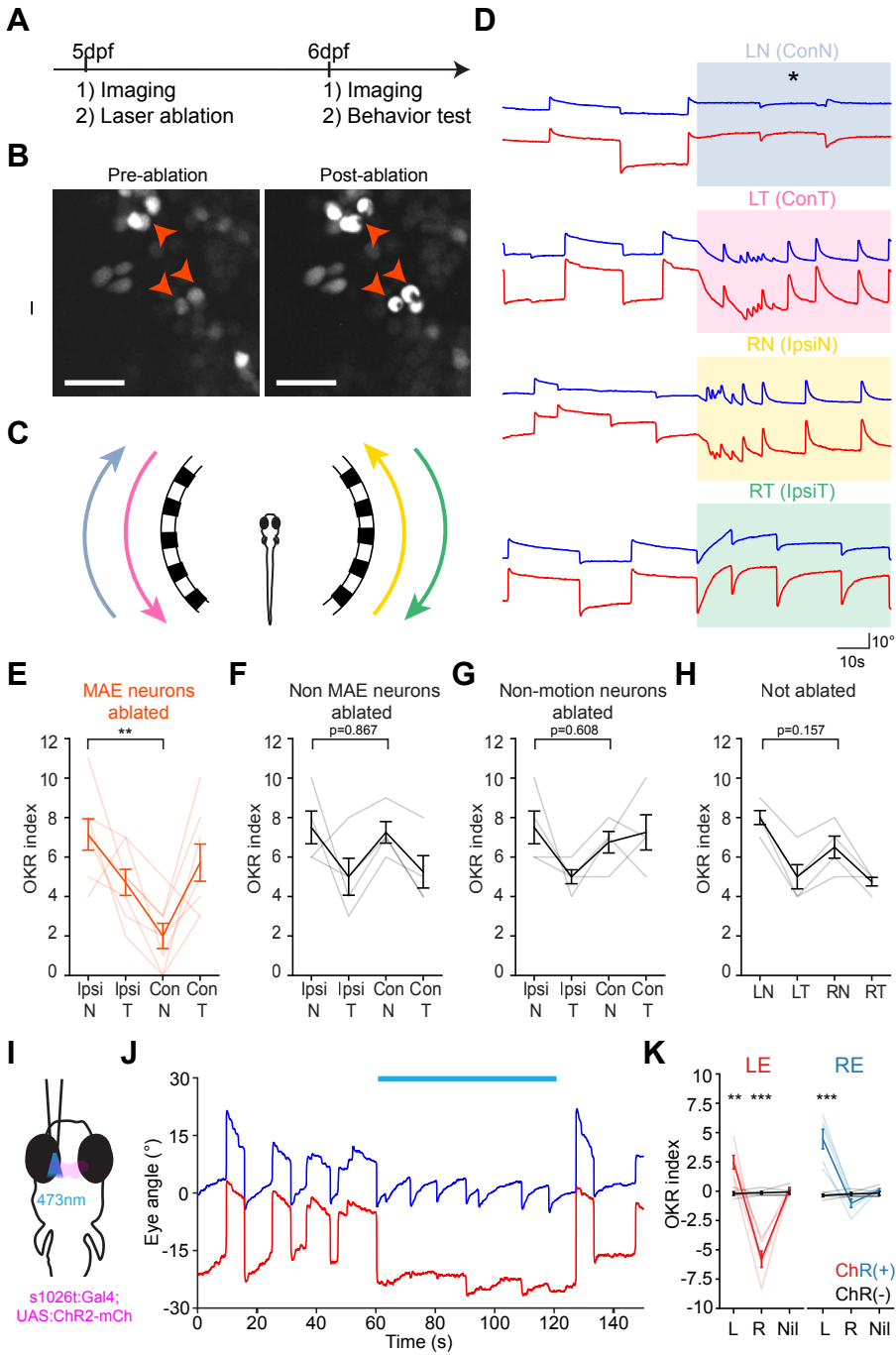
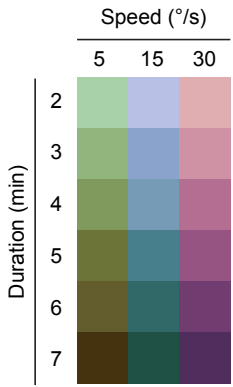


Figure 4

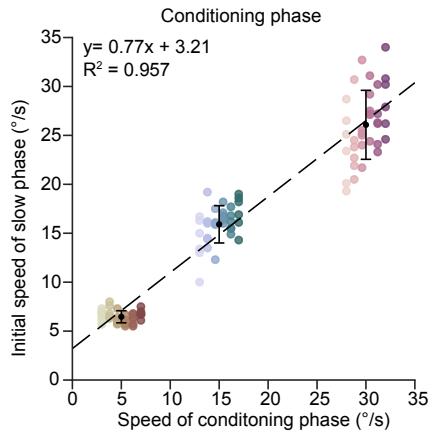


Supplementary Figure 1

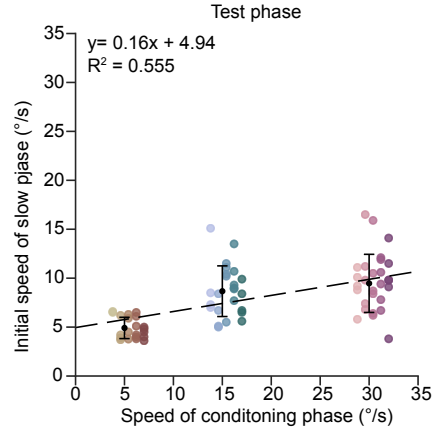
A



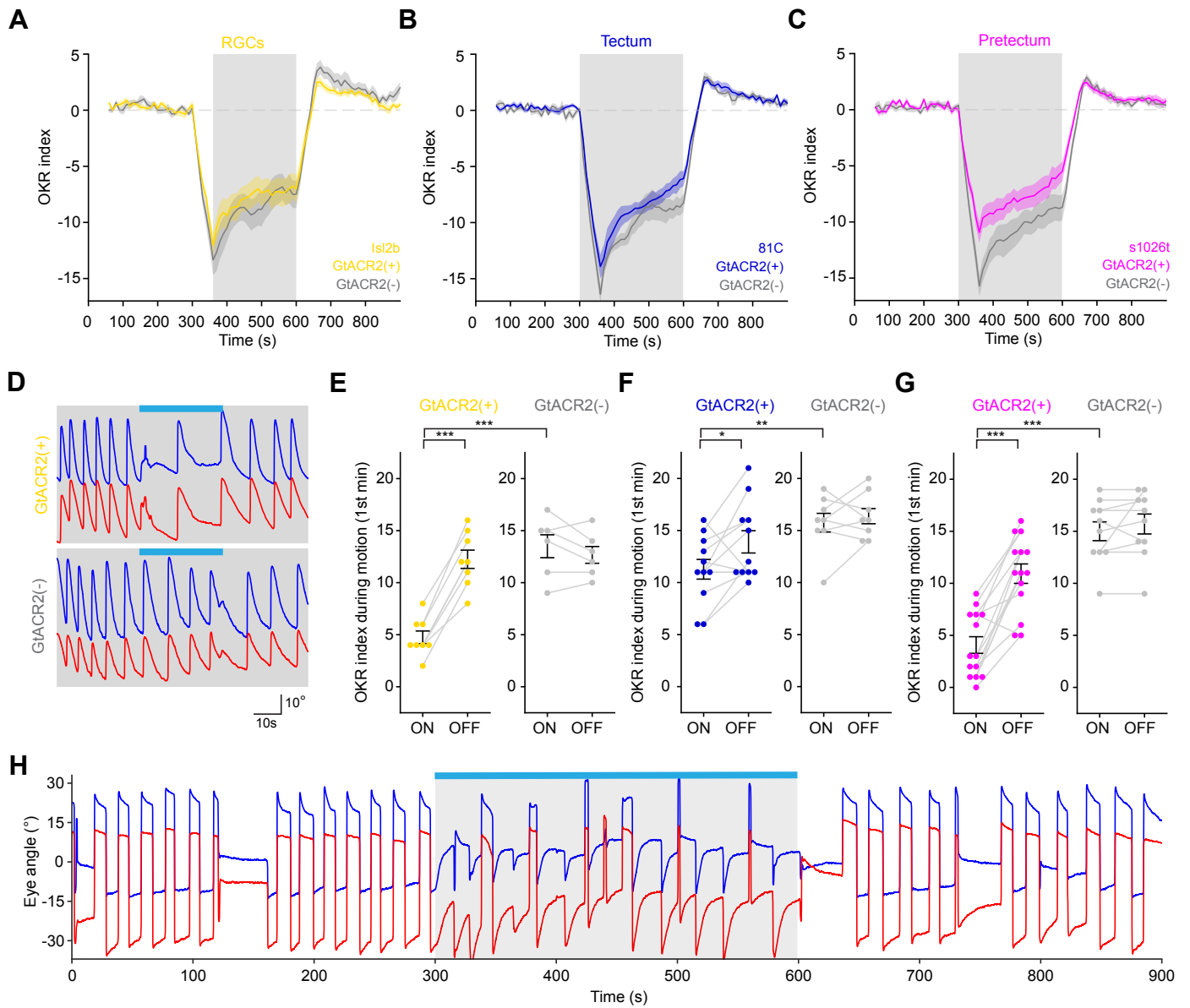
B



C

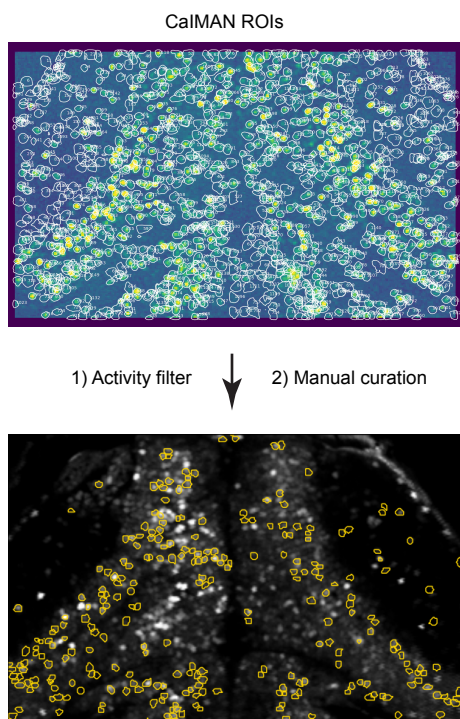


Supplementary Figure 3

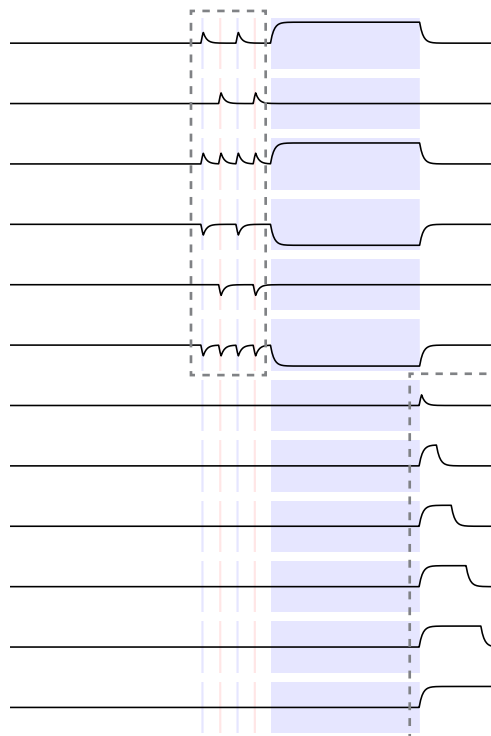


Supplementary Figure 4

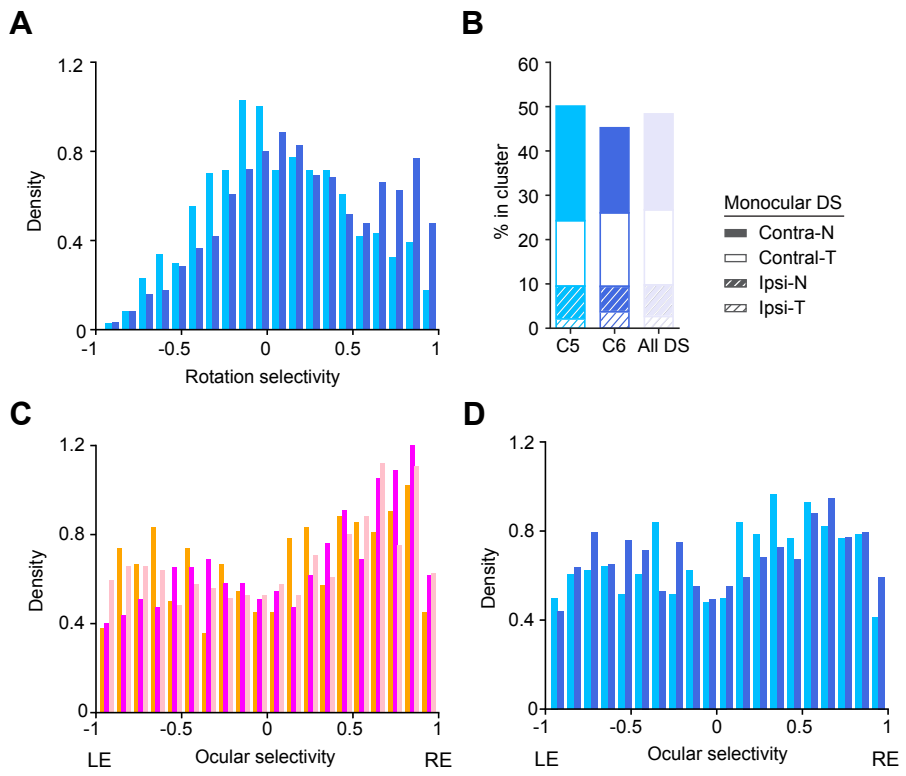
A



B

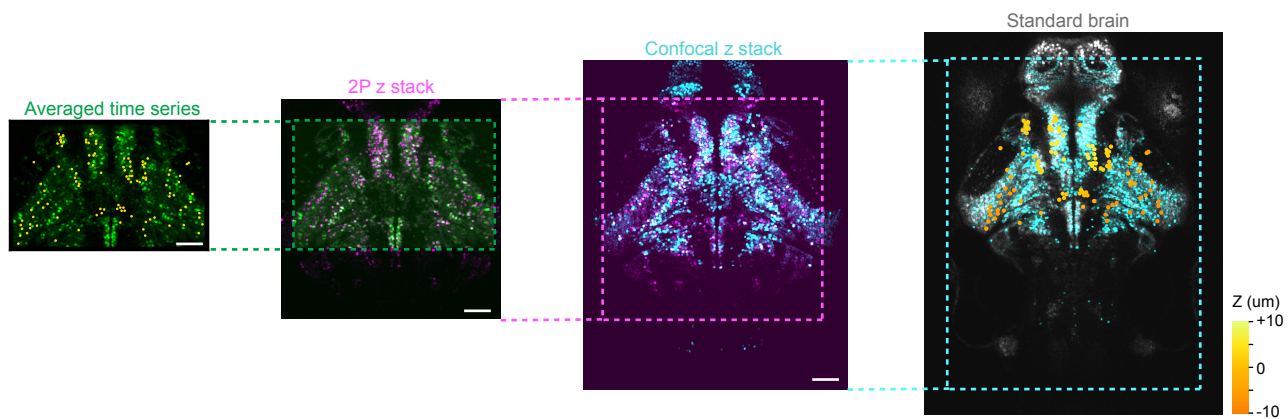


Supplementary Figure 6

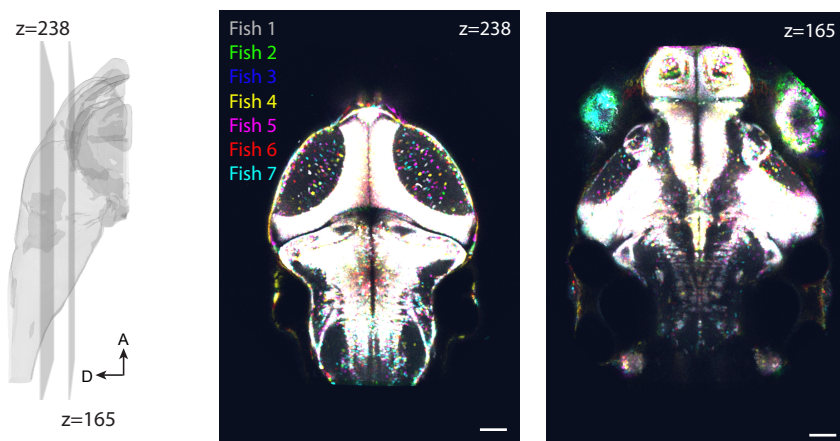


Supplementary Figure 7

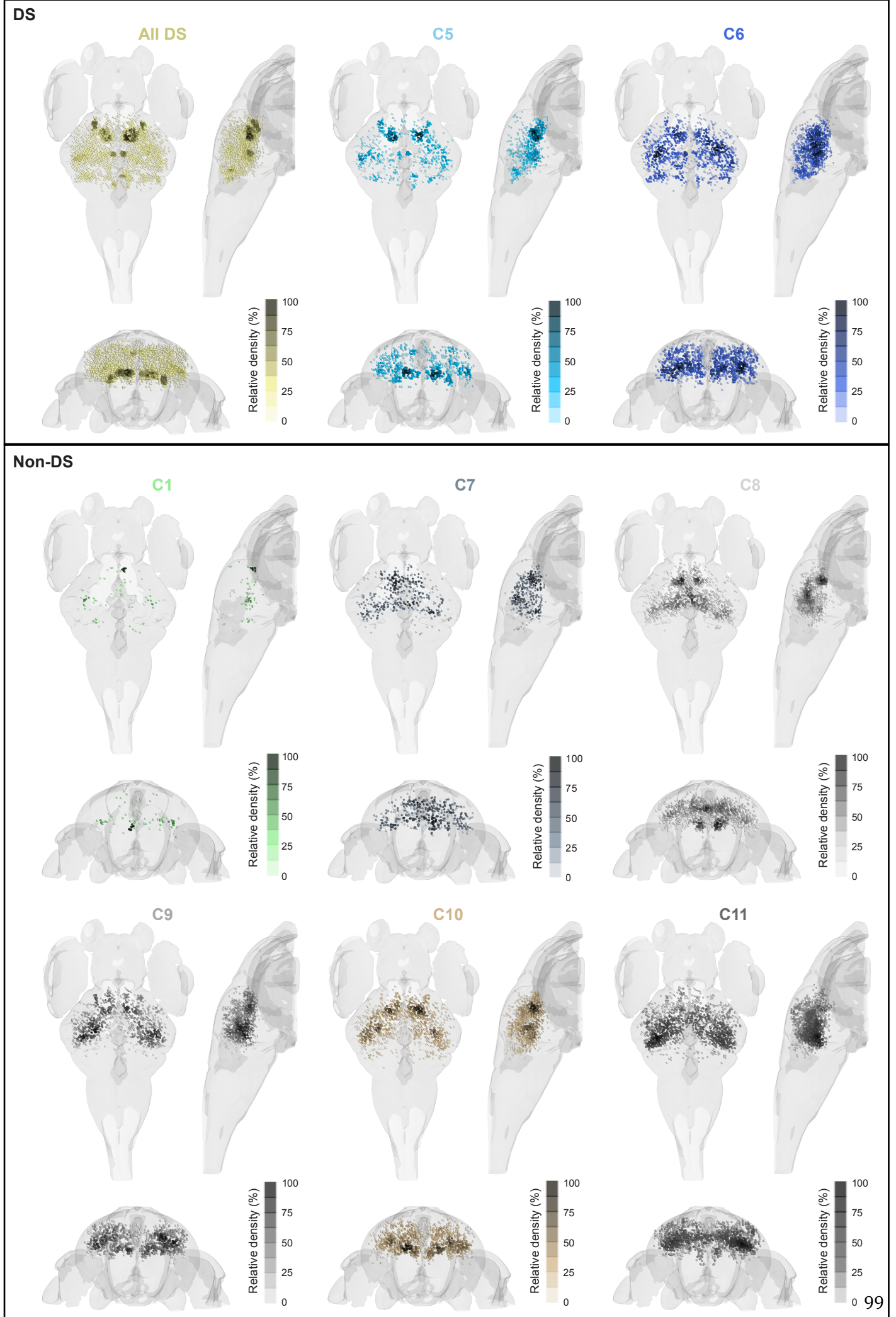
A



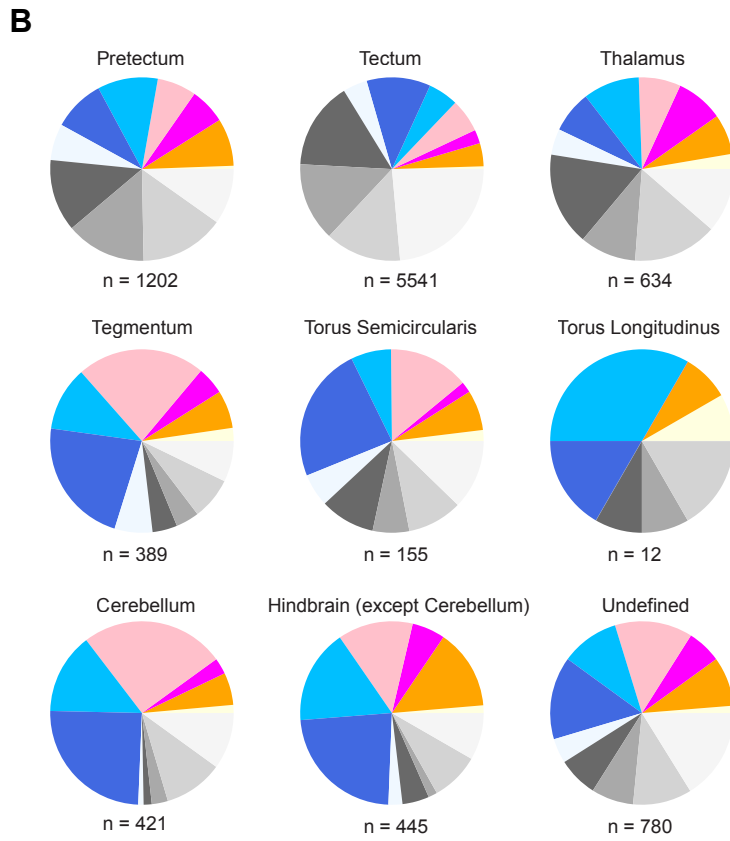
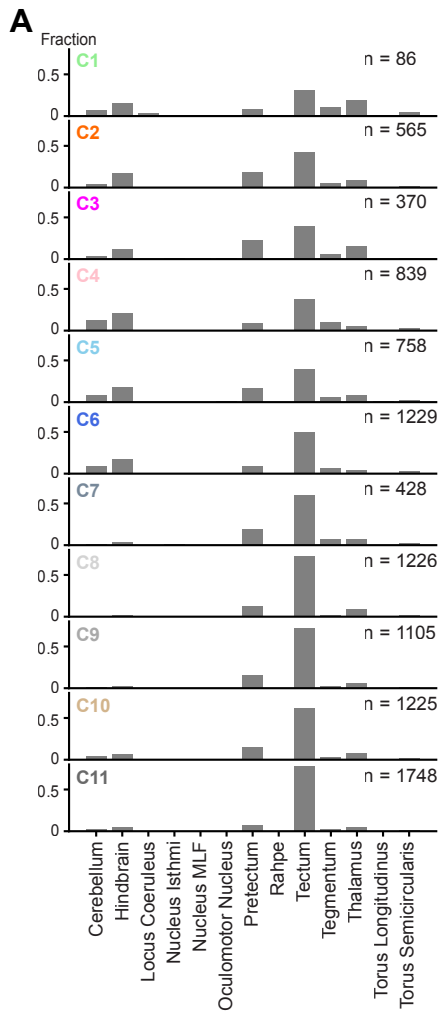
B



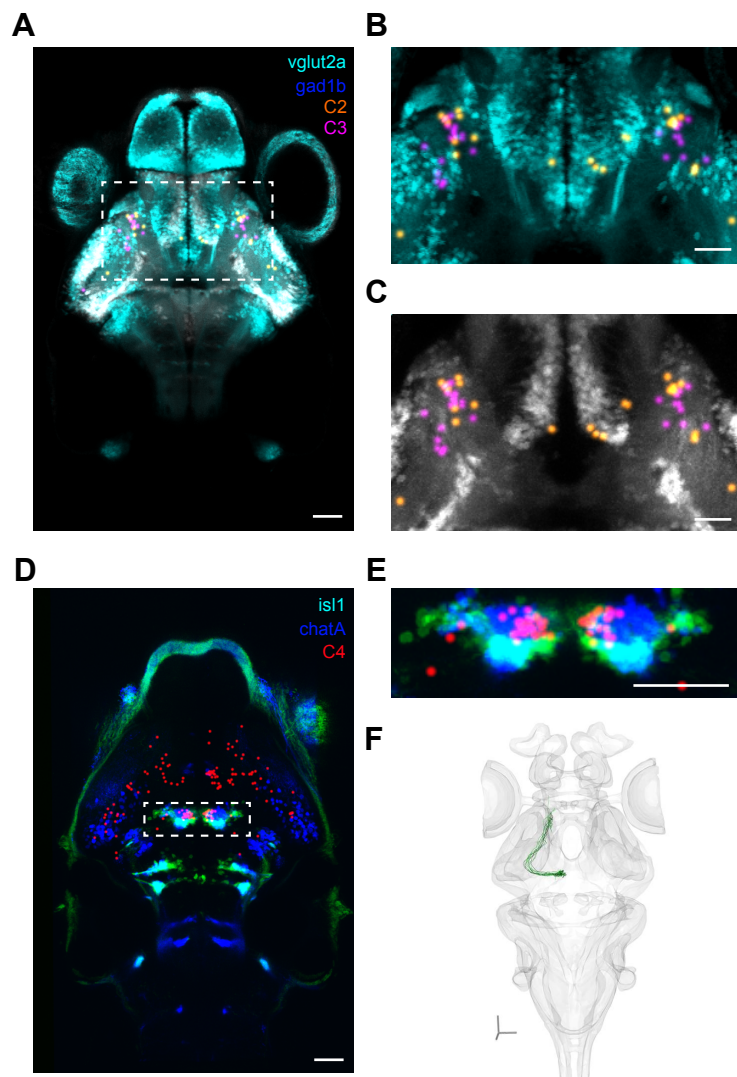
Supplementary Figure 8



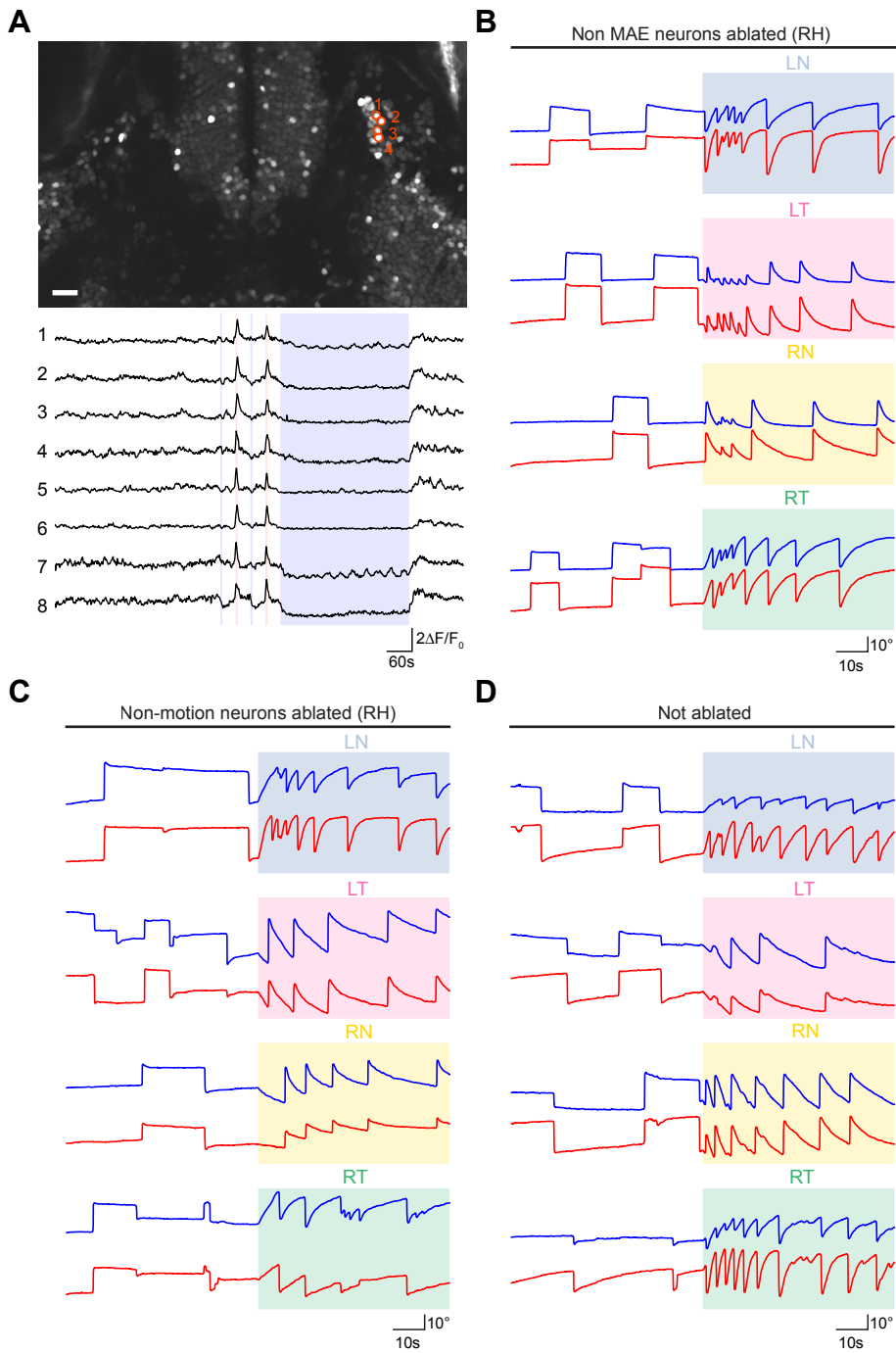
Supplementary Figure 9



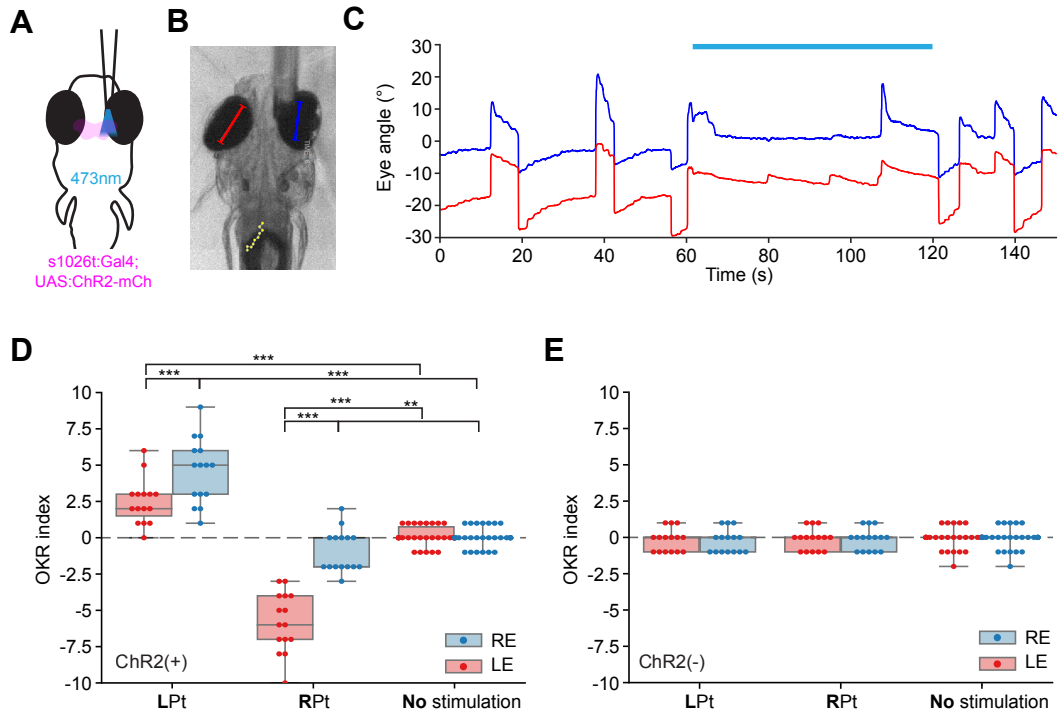
Supplementary Figure 10



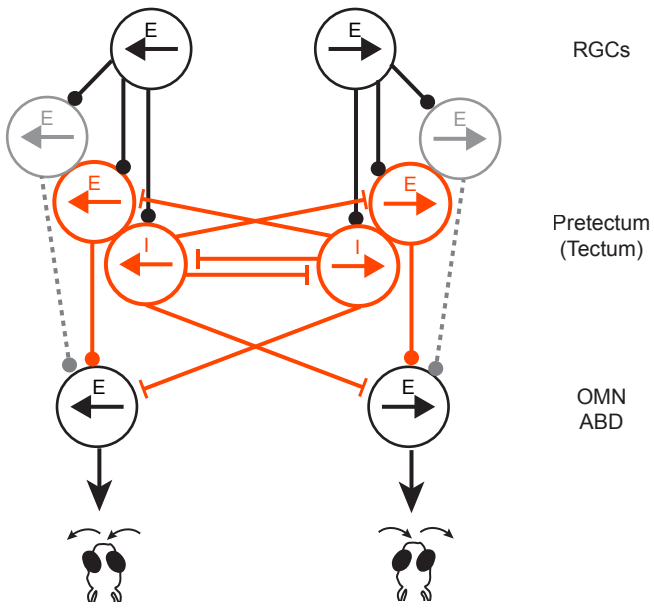
Supplementary Figure 11



Supplementary Figure 12



Supplementary Figure 13



3. DISCUSSION

The two studies in this thesis took two different angles to further dissect the neural basis of visual motion processing. The first study focused on sensory encoding. By systematically sampling RGC projections to AFs, it revealed how the motion information was conveyed from the retina to the brain. The second study concerned the behavioral relevance of neurons with similar sensory tuning. Guided by MAE, it uncovered a potential further division of labor in the vast DS neural population to serve in distinct functionally specialized pathways. Taken together, the work presented in this thesis not only identified key components in the motion processing circuit, but it also shed light on the computational mechanisms and the organizational principles of the circuit.

3.1 Direction selectivity in zebrafish RGCs

RGCs with direction-selective response are not unique to larval zebrafish. Initially discovered in rabbits (Barlow and Hill, 1963b; Barlow et al., 1964), DS RGCs were well characterized in vertebrate animal models (Weng et al., 2005). In mice, where DS RGCs were most extensively studied, DS RGCs can be further divided into two subtypes, i.e. the On-Off and the On DS RGCs, based on their response to bright and dark contrasts. The On-Off DS RGCs have bistratified dendritic arbors in the On and the Off sublamina of the inner plexiform layer (IPL) (Amthor et al., 1984; Famiglietti, 1992), whereas the ON DS RGCs have monostatified dendritic arbors in the On sublamina (Amthor et al., 1984; Famiglietti, 1992; He and Masland, 1998). In the IPL, the DS RGCs synapse with starburst amacrine cells (SACs), which grant them direction selectivity (Briggman et al., 2011; Taylor et al., 2000). In particular, On DS RGCs project exclusively to AOS and prefer slower motion, which implicates their role in mediating the optokinetic response (Berson, 2008; Kay et al., 2011).

In comparison, in larval zebrafish, RGCs that innervate in AF5, AF6 and/or AF10, where DS response was identified, could be On, Off, or On-Off based on their dendritic stratification in the IPL (Robles et al., 2014). The optokinetic behavior is most likely mediated by the On and On-Off DS RGCs in larval zebrafish, since a mutant with normal Off responses but abnormal On-Off and On responses could not perform OKR (Emran et al., 2007). Just like in mammals, the direction selectivity in zebrafish RGCs most likely stems from the SACs, although direct evidence is still missing.

Interestingly, my results demonstrated that the directional tunings in AF5 and AF10 were very similar, which could be explained by the DS RGCs that form collaterals in both AFs. Such DS RGCs were indeed identified in my pilot experiments of functional imaging in stochastically labeled single RGCs (unpublished). With this organization, the same motion information was conveyed to two retinorecipient areas, which could serve to fulfill distinct behavioral goals. One possibility is that the pretectal pathway via AF5 leads to global motion induced behaviors like OKR, whereas the tectal pathway via AF10 provides background subtraction for other visually guided behaviors e.g. object motion detection.

3.2 MAE in an animal without a cortex

Larval zebrafish lack an extended telencephalon and cortex (Parker et al., 2013). The finding that they were also affected by MAE challenges the cortical origin of MAE (Kohn and Movshon, 2004; Tootell et al., 1995; Van Wezel and Britten, 2002). One possible explanation is that the MAE in larval zebrafish and human represents two different behaviors controlled by two visual pathways. In primates, there exist two parallel pathways for motion processing: one in the cortical areas and the other in the subcortical areas. The divergence of motion processing occurs at the level of RGCs. A substantial number of RGCs that project to the LGN to relay information to the cortex also form branching axons in the midbrain (Guillery, 2003). Since the midbrain contains motor and premotor centers concerned with bodily movements, the subcortical pathway could underlie the vision-to-action transformation; since the cortex is involved in cognitive processes, the cortical pathway could underlie the vision-to-perception transformation. The MAE in primates, as measured by self-reported motion perception, is most likely governed by the vision-to-perception pathway. In contrast, the MAE in larval zebrafish, as measured by eye movements, probably relies on the vision-to-action pathway.

This hypothesis can potentially explain the difference in the time course of MAE between larval zebrafish and human. Namely, on one hand, a much longer conditioning motion was required to induce MAE in larval zebrafish (~3 min for zebrafish as opposed to 0.5 - 1 min for human), which could emerge from a higher activation threshold in the vision-to-action pathway. On the other hand, the duration of MAE was significantly longer in larval zebrafish (~1min for zebrafish as opposed to ~10s for human), implying that distinct neural populations of different temporal dynamics might underlie the MAE in the two species. Given the limited access to the midbrain, the vision-to-action pathway might

have been overlooked in the studies of MAE in primates. The possibility to study MAE in larval zebrafish opens up a window to this less studied vision-to-action pathway.

3.3 Neural mechanism of MAE

Our working hypothesis for MAE is the “opponent process” model by Barlow and Hill, which is a two-layer model that computes the difference between oppositely tuned motion sensors (Figure 4)(Barlow and Hill, 1963a). After motion adaptation, the imbalance in oppositely tuned motion sensors results in an increase in activity in the downstream comparator cells, which give rise to MAE. Based on the direction of the conditioning motion, DS neurons can be divided into conditioning motion tuned (CMT) and opposing motion tuned (OMT) populations depending on their preferred directions. The preferred direction of the CMT neurons aligned with the conditioning motion, whereas the preferred direction of the OMT neurons is opposite to the conditioning motion.

3.3.1 CMT neurons

As expected, the CMT neurons in my study, namely the DS neurons whose preferred direction aligned with the conditioning motion, exhibited decreasing activity in the course of the conditioning phase. Similar adaptation over prolonged motion stimulation has been reported in the RGCs, V1, and V5 neurons by means of electrophysiology and fMRI studies (Barlow and Hill, 1963a; Giaschi et al., 1993; Marlin et al., 1988; Van Wezel and Britten, 2002). Interestingly, my clustering analysis unveiled a variation in adaptation rate in different DS subpopulations. The variation could stem from the input, the firing property of the cells per se, or both. Generally, our data showed that the neurons further down the motion processing pathways seemed to adapt more compared to the ones at earlier stages of processing. For instance, the neurons in the tectum and the pretectum adapted more than the RGCs (Figure 14). This observation is in agreement with a previous study in cats, which reported a slower adaptation rate in the LGN compared to that in the V1 (Sanchez-Vives et al., 2000). Furthermore, within each anatomical area, there existed CMT neurons of different adaptation rates. The functional implication of such organization is yet to be determined.

Unexpectedly, after prolonged motion stimulation, we did not observe a significant suppression of baseline activity in the CMT neurons, which was reported in the

electrophysiology recordings of RGCs (Barlow and Hill, 1963a). This discrepancy could be due to the limitation of our method calcium imaging, which only reflects the change of firing rate in a certain dynamic range. Therefore, the decrease of an originally low baseline might not be detected, if it fell below the range of detection.

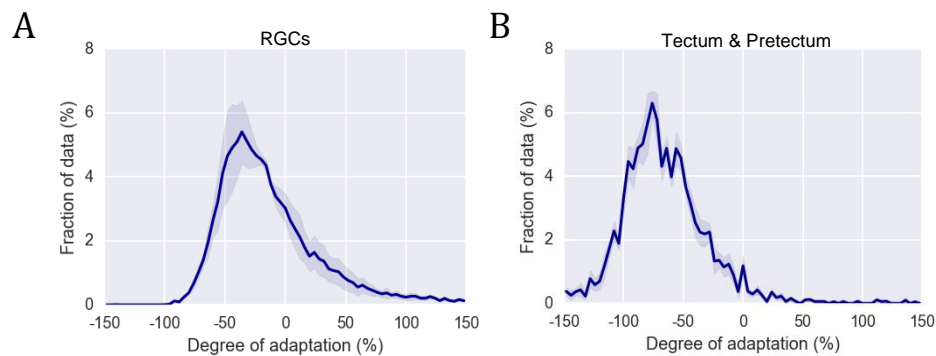


Figure 14. Degree of adaptation at different levels of visual motion processing. (A) Degree of adaptation in the RGCs. (B) Degree of adaptation in the tectum and pretectum. Degree of adaptation is calculated as the difference in activity between the end and the beginning of the conditioning phase divided by that in the beginning of the conditioning phase. It is plotted in the form of normalized histogram.

3.3.2 OMT neurons

On the other hand, some of the OMT neurons, namely the DS neurons tuned to the opposite direction of the conditioning motion, showed increase in activity in the test phase. Notably, most of these neurons also showed motion opponent response, meaning that their activity was suppressed below the baseline when motion in their null direction was presented. Such response profile suggests that they could be the comparator cells in the “opponent process” model, which computes the difference in activity of oppositely tuned motion sensors by combining excitatory input from sensors tuned to one direction and inhibitory input from sensors tuned to the opposite (Figure 4). The fact we found both excitatory and inhibitory neurons in the DS population further supports the “opponent process” model (unpublished).

Interestingly, MAE-correlated neurons could be further categorized based on their temporal dynamics during MAE, which has not been documented before. One subtype (C2) showed a rather fast and transient response, while the other (C3) displayed a slow and sustained response. The two subtypes also differed in terms of their tuning. The former (C2) was more enriched with monocular neurons tuned to the temporal direction in the contralateral eye, while the latter (C3) was more enriched with monocular neurons

tuned to the nasal direction in the contralateral eye. One possible explanation to this could be the asymmetry in the tuning of DS RGCs, which are predominantly selective to the nasal direction in larval zebrafish (Kramer et al., 2019; Nikolaou et al., 2012). Thus, nasal motion could result in stronger inhibition and consequently a more striking rebound in the downstream temporal motion tuned comparator cells. Further study is necessary to reveal the neural computation that underlies these two subtypes of MAE-correlated neurons, and furthermore, how they contribute to the illusory motion perception.

An unexpected result in the functional imaging study of MAE is that the rotation selective complex cells, namely the neurons that were binocular and responded more strongly to rotational motion than translational motion, were more enriched in the non-MAE DS neurons, suggesting that they were not responsible for the OKR-like behavior during MAE. Instead, this result implies a monocular organization of the optokinetic circuit. In principle, the OKR could be driven solely by monocular neurons.

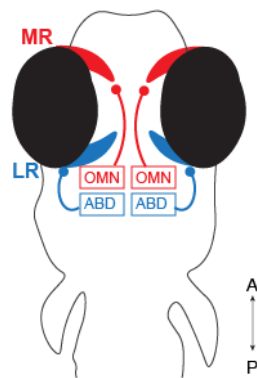


Figure 15. Schematics of the motor nuclei and the extraocular muscles for horizontal eye movements. The motoneurons in the oculomotor nuclei (OMN) and the abducens nuclei (ABD) innervate ipsilateral medial rectus (MR) and lateral rectus (LR) respectively. A, anterior; P, posterior. (Adapted from Schoonheim et al., 2010).

More surprisingly, the rotation selective non-MAE DS neurons also include the ones located in the oculomotor nuclei (OMN), which controls extraocular eye muscles in larval zebrafish together with the trochlear and the abducens (ABD) nuclei (Greaney et al., 2017). In particular, motoneurons in the OMN innervate the ipsilateral medial and inferior rectus (MR, IR), the inferior oblique (IO) and contralateral superior rectus (SR); those in the trochlear nuclei control the contralateral superior oblique (SO); and those in the abducens nuclei drive the ipsilateral lateral rectus (LR) muscle. This organization of

muscle innervation from the extraocular motor nuclei is highly conserved across vertebrate species (Büttner-Ennever, 2006). The nasal/temporal eye movement concerned in the MAE study is driven by the MR and the LR, which are innervated by OMN and ABD respectively (Figure 15)(Schoonheim et al., 2010).

3.3.1 Neural implementation of the “opponent process” model

By functional imaging, we have identified the potential neural implementations of all the proposed components in the “opponent process” model. Theoretically, MAE in larval zebrafish could arise from a three-layer minimal circuit, with the RGCs as the DS motion sensors, the pretectal neurons as the comparator cells, and the OMN and the ABD neurons as the actuator cells to drive eye movements (Figure 16). Since all RGCs are excitatory, inhibitory interneurons are necessary to provide inhibitory input to the comparator cells in the pretectum.

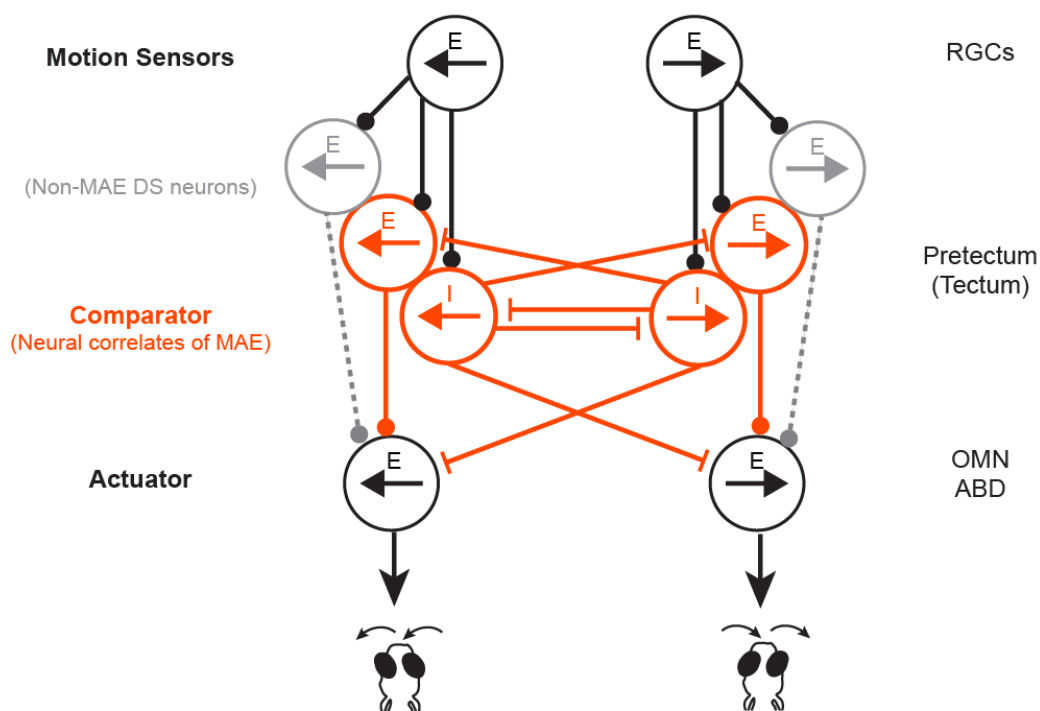


Figure 16. Minimal circuit model of MAE. Each circle represents a subpopulation of DS neurons that share neurotransmitter identity, directional tuning and response to MAE. The arrow within the circle indicates the preferred direction of the corresponding DS population. E, excitatory neurons; I, inhibitory neurons. Circle cap, excitatory synapse; bar cap, inhibitory synapse. Orange highlights the opponent processing that gives rise to the response of MAE correlated neurons. Grey highlights the non-MAE neurons, whose contribution to OKR is negligible (dashed line).

The lack of activity in the OMN prompted a bold hypothesis that the OKR-like activity during MAE could be driven by inhibition instead of activation of the extraocular motoneurons (Figure 15&16). While at rest, the extraocular muscles keep a constant tone

to resist passive stretch and maintain the position of the eyes. Normally, when a real motion is present in visual scene e.g. in the CW direction, it activates the motoneurons in the OMN in the left hemisphere and the ABD in the right hemisphere, which in turn contracts the MR in the left eye and the LR in the right eye. This generates conjugated rotational eye movement in the CW direction. In contrast, during MAE, if the OMN in the right hemisphere and the ABD in the left hemisphere are inhibited, meaning the LR in the left eye and the MR in the right eye are relaxed, the same conjugated rotational eye movement in the CW direction can be generated. Given the dynamic range of inhibition is much smaller than activation in most neurons, it is expected that eye movements driven by inhibition are less pronounced compared to those driven by activation.

This hypothesis is supported by behavioral evidence and potential neural basis. Just as predicted, we found that the OKR-like behavior during MAE was less pronounced compared to the normal OKR in the conditioning phase. The initial speed of the slow phase was lower during MAE, and the saccades were less frequent. Aside from the behavioral evidence, we also identified a substantial number of GABAergic MAE-correlated neurons (Figure 17). These neurons could potentially realize the inhibition to OMN and ABD to relax the eye muscles. Confirmation of this hypothesis awaits further connectivity and electrophysiology evidence.

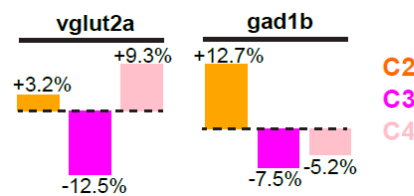


Figure 17. Cluster compositions of glutamatergic and GABAergic OMT neurons compared to the pan-neuronal dataset. Left, glutamatergic neurons labeled by *vglut2a:Gal4*. Right, GABAergic neurons labeled by *gad1b:Gal4*.

3.4 Role of the pretectum in OKR

Consistent with the past studies in larval zebrafish (Kubo et al., 2014; Naumann et al., 2016; Portugues et al., 2014; Wang et al., 2019), we observed a substantial number of DS neurons in the pretectum. The majority of them were monocular, and mostly responding to motion presented to the contralateral eye. In addition, our optogenetic silencing of the pretectum resulted in similar impairment in OKR as previously reported (Kubo et al., 2014). Unlike in mammals, which encode different motion directions in separate nuclei in the accessory optic system, teleost fish have only one pretectal nucleus that undertakes

the functions of the whole accessory optic system (Masseck and Hoffmann, 2009a). It encodes both horizontal (temporal and nasal) and vertical (up and down) motion directions (Klar and Hoffmann, 2002; Masseck and Hoffmann, 2009b; Wang et al., 2019). Therefore, broad pretectal silencing in larval zebrafish would impair OKR to both CW and CCW motion, just as shown in our result. Together, our results emphasize the crucial role of the pretectum in larval zebrafish for global motion induced OKR.

Furthermore, guided by MAE, we were able to sift through the broad DS population in the pretectum and home in on a focal hotspot, which, we showed for the first time, was both required and sufficient to drive OKR behavior. This ventral lateral hotspot may correspond to the migrated region of pretectum (M1), which grows into the superficial pretectal region in adult zebrafish (Mueller and Wullimann, 2002). The superficial pretectal region is not only involved in primary visual circuits, but also in higher order visual and multisensory circuits (Wullimann, 1997). A recent study in larval zebrafish reported that neurons in M1 also responded to vestibular stimulation (Favre-Bulle et al., 2018), suggesting a potential multimodal nature of M1 neurons. In free moving animals, the OKR often works in conjunction with the vestibulo-ocular reflexes (VOR) to ensure image stabilization during self-motion and environmental drifts. Thus, M1 could serve as a hub, which integrates visual and vestibular information and generates proper motor commands to drive behaviors like eye movements.

In many species including teleosts, there exist direct pretectal projections to the oculomotor complex (Büttner-Ennever et al., 1996; Clarke et al., 2003). This implicates that the pretectal neurons could directly drive the motor neurons innervating the extraocular muscles to elicit OKR behavior. Apart from this, pretectal neurons in fish also project to premotor areas including the cerebellum, the reticular formation, the inferior olive and the vestibular nuclei, which can further modulate the behavior (Kramer et al., 2019; Masseck and Hoffmann, 2009a).

3.5 Role of the tectum in OKR

Although a big proportion of the tectal neurons were also DS, our results suggest that the tectum does not drive OKR directly, but rather facilitates it. Compared to the outcome of tectal ablation (Pérez-Schuster et al., 2016; Roeser and Baier, 2003), optogenetic inhibition of the tectum resulted in a similar reduction of saccade frequency at motion

onset. However, we did not observe diminished adaptation over prolonged motion stimulation, which could be explained by decreasing efficiency of optogenetic inhibition over time. Interestingly, the decreased adaptation in the tectum weakened the OKR-like behavior during MAE, suggesting that neural adaptation in the tectum contributed to MAE. One possibility is that tectal DS neurons function as the motion sensors in the “opponent process” model, whose adaptation and subsequent suppression in the baseline give rise to the response of the comparator cells, presumably the pretectal MAE-correlated neurons. The presence of descending tectal efferents in the pretectum, especially in the M1 region, is consistent with such a role (Wullimann, 1997). Alternatively, the tectum can also mediate OKR behavior via other premotor areas (e.g. reticular formation) (Wullimann, 1997).

3.6 Dedicated motion processing pathways

To achieve optimal wiring and efficient processing, the brain has evolved to have segregated pathways to process different features of the visual scene in parallel. This is best demonstrated by a neurological disorder called cerebral akinetopsia. Patients who suffer from this disorder can not perceive motion despite having normal color and form vision (Zihl and Heywood, 2015). This indicates that there exist dedicated motion processing pathways in the brain that are separated from the pathways for other visual features.

In larval zebrafish, the dedicated motion processing pathway begins in the retina. Although the cell bodies of DS RGCs presumably tile the retina, their axons relay the motion information mainly to AF5 and the superficial layers of SFGS in AF10. The cellular and molecular mechanisms underlying this specific innervation pattern are still elusive. Axon guidance molecule Slit has been shown to speed up the innervation of DS RGCs in AF10, although it is not required to establish the right synaptic connections (Nikolaou and Meyer, 2015).

Downstream of RGCs, a substantial number of DS neurons were identified in the larval zebrafish brain, especially in the tectum, the pretectum, and the hindbrain. While some neurons simply inherit the DS response from RGCs, some others develop new complex responses, including motion opponent response, preference to a new motion direction, and selectivity to binocular optic-flow patterns (Kubo et al., 2014; Naumann et al., 2016;

Wang et al., 2019). A common feature shared by many brain regions is that there exist many neurons of similar tunings (Dhawale et al., 2010; Holy, 2010; Panzeri et al., 2017; Puchalla et al., 2005). Interestingly, the ablation of some DS neurons in the pretectum disrupted OKR behavior, while some others not. This suggests that the motion processing pathway further diverges into functionally specialized pathways that serve different behavioral goals.

The work in this thesis has singled out some of the DS neurons involved in the pathway that drives OKR behavior. Surprisingly, the ablation of only 6-12 neurons was enough to disrupt OKR. This result implies sparse coding in the optokinetic circuit, which is probably the most efficient way to elicit a simple reflexive behavior like OKR. On the other hand, this result also inspires new research on the functional roles of the DS neurons, especially the ones not required for OKR. In addition to image stabilization on the retina, many other behaviors rely on the detection of global motion, e.g. background subtraction during object motion detection. The neural underpinnings of these more complex global motion guided behaviors are yet to be determined.

3.7 Conclusions and outlook

The larval zebrafish brain, with its genetic and optical accessibility, serves as an excellent platform to study the neural underpinnings of perception and behavior. Taking advantage of the larval zebrafish brain, I ascertained that the processing of motion is already segregated in the RGCs. AF5, in addition to AF10, serves as the major venue to relay directional information from the retina to the brain. Furthermore, I showed, for the first time, the neural substrates of MAE in the pretectum with single cell resolution. These neurons had two distinct kinetics during MAE, which have not been described before. Meanwhile, I also demonstrated the utility of an optical illusion as a powerful circuit breaking tool. Using the response to the MAE stimulus as an additional criterion, I was able to classify the DS neurons beyond their DS tuning profile. Most importantly, focusing on the MAE-correlated neurons, I identified an essential component in the optokinetic circuit, which is not only required but also sufficient to drive OKR behavior. In summary, with a highly resourceful platform and a unique illusory perspective, this thesis advanced the understanding of the neural basis of visual motion processing in larval zebrafish.

However, several open questions remain to be addressed to fully illuminate the neural circuit for visual motion processing. One of them is the local circuit that implements motion opponency, which gives rise to the response of the MAE-correlated neurons. Given that motion opponent responses are not prominent in the RGCs, the opponent processing is most likely carried downstream (e.g. in the pretectum). We have identified neurons with the required DS response and the neurotransmitter identity to implement motion opponency, although it is still unknown whether these neurons are wired according to the “opponent processing” model. Another issue that was not addressed in this thesis is the downstream target of the essential node in the optokinetic circuit. The neurons there are sufficient to drive the OKR behavior, but whether they directly innervate motor neurons in the extraocular nuclei remains to be elucidated.

As alluded by the open questions, a deeper understanding of the neural basis of visual motion processing calls for functional information in combination with detailed synaptic circuitry. One strategy is to use FuGIMA (function-guided inducible morphological analysis), which allows us to visualize the neurites of a chosen neuron after determining its functional identity (Förster et al., 2018; Kramer et al., 2019). However, currently this method is unsuited to reveal long-range projections or direct synaptic contacts, and the number of neurons that can be labeled distinguishably in one brain is limited. An alternative strategy is to use dense electron microscopic reconstructions (e.g. serial blockface EM), which could potentially reveal the complete connectome of the larval zebrafish brain (Hildebrand et al., 2017). Nevertheless, a robust method to combine functional imaging results with EM reconstruction in the same brain is yet to be developed. For now, the combination of function and synaptic wiring persists as a challenge in circuit neuroscience. However, I firmly believe that, with technological advances in tools and methods, we will soon overcome this barrier and obtain a full picture of the neural basis of visual motion processing in larval zebrafish.

4. REFERENCES

- Abbas, F., Triplett, M.A., Goodhill, G.J., and Meyer, M.P. (2017). A Three-Layer Network Model of Direction Selective Circuits in the Optic Tectum. *Front. Neural Circuits* 11.
- Abdeljalil, J., Hamid, M., Abdel-mouttalib, O., Stéphane, R., Raymond, R., Johan, A., José, S., Pierre, C., and Serge, P. (2005). The optomotor response: A robust first-line visual screening method for mice. *Vision Research* 45, 1439–1446.
- Addams, R. (1834). LI. *An account of a peculiar optical phænomenon seen after having looked at a moving body*. The London, Edinburgh, and Dublin Philosophical Magazine and Journal of Science 5, 373–374.
- Ahrens, M.B., Orger, M.B., Robson, D.N., Li, J.M., and Keller, P.J. (2013). Whole-brain functional imaging at cellular resolution using light-sheet microscopy. *Nat. Methods* 10, 413–420.
- Amthor, F.R., Oyster, C.W., and Takahashi, E.S. (1984). Morphology of on-off direction-selective ganglion cells in the rabbit retina. *Brain Research* 298, 187–190.
- Antal, A., Nitsche, M.A., Kruse, W., Kincses, T.Z., Hoffmann, K.-P., and Paulus, W. (2004). Direct current stimulation over V5 enhances visuomotor coordination by improving motion perception in humans. *J Cogn Neurosci* 16, 521–527.
- Antinucci, P., Folgueira, M., and Bianco, I.H. (2019). A pretectal command system controls hunting behaviour. *BioRxiv*.
- Aristotle (350AD). *Parva naturalia* (in aedibus B. G. Teubneri).
- Arrenberg, A.B., Del Bene, F., and Baier, H. (2009). Optical control of zebrafish behavior with halorhodopsin. *Proc. Natl. Acad. Sci. U.S.A.* 106, 17968–17973.
- Asakawa, K., Suster, M.L., Mizusawa, K., Nagayoshi, S., Kotani, T., Urasaki, A., Kishimoto, Y., Hibi, M., and Kawakami, K. (2008). Genetic dissection of neural circuits by Tol2 transposon-mediated Gal4 gene and enhancer trapping in zebrafish. *Proc. Natl. Acad. Sci. U.S.A.* 105, 1255–1260.
- Avants, B.B., Tustison, N.J., Song, G., Cook, P.A., Klein, A., and Gee, J.C. (2011). A reproducible evaluation of ANTs similarity metric performance in brain image registration. *Neuroimage* 54, 2033–2044.
- Baier, H. (2000). Zebrafish on the move: towards a behavior-genetic analysis of vertebrate vision. *Curr. Opin. Neurobiol.* 10, 451–455.
- Baier, H. (2013). Synaptic Laminae in the Visual System: Molecular Mechanisms Forming Layers of Perception. *Annual Review of Cell and Developmental Biology* 29, 385–416.
- Balciunas, D., Davidson, A.E., Sivasubbu, S., Hermanson, S.B., Welle, Z., and Ekker, S.C. (2004). Enhancer trapping in zebrafish using the Sleeping Beauty transposon. *BMC Genomics* 5, 62.

- Barker, A.J., and Baier, H. (2015). Sensorimotor Decision Making in the Zebrafish Tectum. *Curr. Biol.* *25*, 2804–2814.
- Barlow, H.B., and Hill, R.M. (1963a). Evidence for a Physiological Explanation of the Waterfall Phenomenon and Figural After-effects. *Nature* *200*, 1345.
- Barlow, H.B., and Hill, R.M. (1963b). Selective Sensitivity to Direction of Movement in Ganglion Cells of the Rabbit Retina. *Science* *139*, 412–412.
- Barlow, H., Hill, R., and Levick, W. (1964). Retinal Ganglion Cells Responding Selectively to Direction + Speed of Image Motion in Rabbit. *J. Physiol.-London* *173*, 377-.
- Bavelier, D., Brozinsky, C., Tomann, A., Mitchell, T., Neville, H., and Liu, G. (2001). Impact of Early Deafness and Early Exposure to Sign Language on the Cerebral Organization for Motion Processing. *J. Neurosci.* *21*, 8931–8942.
- Beck, J.C., Gilland, E., Tank, D.W., and Baker, R. (2004). Quantifying the ontogeny of optokinetic and vestibuloocular behaviors in zebrafish, medaka, and goldfish. *J. Neurophysiol.* *92*, 3546–3561.
- Berger, C.C., and Ehrsson, H.H. (2016). Auditory Motion Elicits a Visual Motion Aftereffect. *Front Neurosci* *10*, 559.
- Berson, D.M. (2008). 1.25 - Retinal Ganglion Cell Types and Their Central Projections. In *The Senses: A Comprehensive Reference*, R.H. Masland, T.D. Albright, T.D. Albright, R.H. Masland, P. Dallos, D. Oertel, S. Firestein, G.K. Beauchamp, M. Catherine Bushnell, A.I. Basbaum, et al., eds. (New York: Academic Press), pp. 491–519.
- Bex, P.J., Metha, A.B., and Makous, W. (1999). Enhanced motion aftereffect for complex motions. *Vision Research* *39*, 2229–2238.
- Bianco, I.H., and Engert, F. (2015). Visuomotor transformations underlying hunting behavior in zebrafish. *Curr. Biol.* *25*, 831–846.
- Bilotta, J., and Saszik, S. (2001). The zebrafish as a model visual system. *Int. J. Dev. Neurosci.* *19*, 621–629.
- Blumhagen, F., Zhu, P., Shum, J., Schärer, Y.-P.Z., Yaksi, E., Deisseroth, K., and Friedrich, R.W. (2011). Neuronal filtering of multiplexed odour representations. *Nature* *479*, 493–498.
- Born, R.T., and Bradley, D.C. (2005). STRUCTURE AND FUNCTION OF VISUAL AREA MT. *Annual Review of Neuroscience* *28*, 157–189.
- Bowditch, H.P. and G.S.H. (1881). OPTICAL ILLUSIONS OF MOTION. (*Journal of Physiology*).
- Boyden, E.S., Zhang, F., Bamberg, E., Nagel, G., and Deisseroth, K. (2005). Millisecond-timescale, genetically targeted optical control of neural activity. *Nature Neuroscience* *8*, 1263–1268.

- Braun, D.I., Pracejus, L., and Gegenfurtner, K.R. (2006). Motion aftereffect elicits smooth pursuit eye movements. *Journal of Vision* 6, 671–684.
- Briggman, K.L., Helmstaedter, M., and Denk, W. (2011). Wiring specificity in the direction-selectivity circuit of the retina. *Nature* 471, 183–188.
- Brockerhoff, S.E., Hurley, J.B., Janssen-Bienhold, U., Neuhaus, S.C., Driever, W., and Dowling, J.E. (1995). A behavioral screen for isolating zebrafish mutants with visual system defects. *Proc Natl Acad Sci U S A* 92, 10545–10549.
- Broerse, J., Dodwell, P.C., and Ehrenstein, W.H. (1994). Experiments on the Afterimages of Stimulus Change (Dvořák 1870): A Translation with Commentary. *Perception* 23, 1135–1144.
- Bundschuh, S.T., Zhu, P., Schäfer, Y.-P.Z., and Friedrich, R.W. (2012). Dopaminergic modulation of mitral cells and odor responses in the zebrafish olfactory bulb. *J. Neurosci.* 32, 6830–6840.
- Burrill, J.D., and Easter, S.S. (1994). Development of the retinofugal projections in the embryonic and larval zebrafish (*Brachydanio rerio*). *J. Comp. Neurol.* 346, 583–600.
- Büttner-Ennever, J.A. (2006). The extraocular motor nuclei: organization and functional neuroanatomy. In *Progress in Brain Research*, J.A. Büttner-Ennever, ed. (Elsevier), pp. 95–125.
- Büttner-Ennever, J.A., Cohen, B., Horn, A.K., and Reisine, H. (1996). Pretectal projections to the oculomotor complex of the monkey and their role in eye movements. *J. Comp. Neurol.* 366, 348–359.
- Chen, X., Mu, Y., Hu, Y., Kuan, A.T., Nikitchenko, M., Randlett, O., Chen, A.B., Gavornik, J.P., Sompolinsky, H., Engert, F., et al. (2018). Brain-wide Organization of Neuronal Activity and Convergent Sensorimotor Transformations in Larval Zebrafish. *Neuron* 100, 876–890.e5.
- Cheng, R.-K., Krishnan, S., and Jesuthasan, S. (2016). Activation and inhibition of tph2 serotonergic neurons operate in tandem to influence larval zebrafish preference for light over darkness. *Sci Rep* 6, 20788.
- Cheng, R.-K., Krishnan, S., Lin, Q., Kibat, C., and Jesuthasan, S. (2017). Characterization of a thalamic nucleus mediating habenula responses to changes in ambient illumination. *BMC Biology* 15, 104.
- Clarke, R.J., Blanks, R.H.I., and Giolli, R.A. (2003). Midbrain connections of the olivary pretectal nucleus in the marmoset (*Callithrix jacchus*): implications for the pupil light reflex pathway. *Anat. Embryol.* 207, 149–155.
- Coltheart, M. (1971). Visual feature-analyzers and aftereffects of tilt and curvature. *Psychological Review* 78, 114–121.
- Curran, W., and Benton, C.P. (2006). Test stimulus characteristics determine the perceived speed of the dynamic motion aftereffect. *Vision Research* 46, 3284–3290.

- Dal Maschio, M., Donovan, J.C., Helmbrecht, T.O., and Baier, H. (2017). Linking Neurons to Network Function and Behavior by Two-Photon Holographic Optogenetics and Volumetric Imaging. *Neuron* *94*, 774-789.e5.
- Davison, J.M., Akitake, C.M., Goll, M.G., Rhee, J.M., Gosse, N., Baier, H., Halpern, M.E., Leach, S.D., and Parsons, M.J. (2007). Transactivation from Gal4-VP16 transgenic insertions for tissue-specific cell labeling and ablation in zebrafish. *Dev. Biol.* *304*, 811–824.
- Dhawale, A.K., Hagiwara, A., Bhalla, U.S., Murthy, V.N., and Albeanu, D.F. (2010). Non-redundant odor coding by sister mitral cells revealed by light addressable glomeruli in the mouse. *Nat. Neurosci.* *13*, 1404–1412.
- Douglass, A.D., Kraves, S., Deisseroth, K., Schier, A.F., and Engert, F. (2008). Escape Behavior Elicited by Single, Channelrhodopsin-2-Evoked Spikes in Zebrafish Somatosensory Neurons. *Curr Biol* *18*, 1133–1137.
- Drysdale, A.E. (1975). The movement after-effect and eye movements. *Vision Research* *15*, 1171.
- Dunn, T.W., Gebhardt, C., Naumann, E.A., Riegler, C., Ahrens, M.B., Engert, F., and Del Bene, F. (2016). Neural Circuits Underlying Visually Evoked Escapes in Larval Zebrafish. *Neuron* *89*, 613–628.
- Eagleman, D.M. (2001). Visual illusions and neurobiology. *Nature Reviews Neuroscience* *2*, 920–926.
- Easter, S.S., and Nicola, G.N. (1996). The development of vision in the zebrafish (*Danio rerio*). *Dev. Biol.* *180*, 646–663.
- Easter, S.S., and Nicola, G.N. (1997). The development of eye movements in the zebrafish (*Danio rerio*). *Dev Psychobiol* *31*, 267–276.
- Ellingsen, S., Laplante, M.A., König, M., Kikuta, H., Furmanek, T., Hoivik, E.A., and Becker, T.S. (2005). Large-scale enhancer detection in the zebrafish genome. *Development* *132*, 3799–3811.
- Elstrott, J., Anishchenko, A., Greschner, M., Sher, A., Litke, A.M., Chichilnisky, E.J., and Feller, M.B. (2008). Direction selectivity in the retina is established independent of visual experience and cholinergic retinal waves. *Neuron* *58*, 499–506.
- Emran, F., Rihel, J., Adolph, A.R., Wong, K.Y., Kraves, S., and Dowling, J.E. (2007). OFF ganglion cells cannot drive the optokinetic reflex in zebrafish. *PNAS* *104*, 19126–19131.
- Famiglietti, E.V. (1992). Dendritic co-stratification of ON and ON-OFF directionally selective ganglion cells with starburst amacrine cells in rabbit retina. *J. Comp. Neurol.* *324*, 322–335.
- Favre-Bulle, I.A., Vanwalleghem, G., Taylor, M.A., Rubinsztein-Dunlop, H., and Scott, E.K. (2018). Cellular-Resolution Imaging of Vestibular Processing across the Larval Zebrafish Brain. *Current Biology* *28*, 3711-3722.e3.

- Filosa, A., Barker, A.J., Dal Maschio, M., and Baier, H. (2016). Feeding State Modulates Behavioral Choice and Processing of Prey Stimuli in the Zebrafish Tectum. *Neuron* 90, 596–608.
- Fischer, J.A., Giniger, E., Maniatis, T., and Ptashne, M. (1988). GAL4 activates transcription in *Drosophila*. *Nature* 332, 853–856.
- Förster, D., Kramer, A., Baier, H., and Kubo, F. (2018). Optogenetic precision toolkit to reveal form, function and connectivity of single neurons. *Methods* 150, 42–48.
- Gabriel, J.P., Trivedi, C.A., Maurer, C.M., Ryu, S., and Bollmann, J.H. (2012). Layer-specific targeting of direction-selective neurons in the zebrafish optic tectum. *Neuron* 76, 1147–1160.
- Gandhi, T., Kali, A., Ganesh, S., and Sinha, P. (2015). Immediate susceptibility to visual illusions after sight onset. *Curr Biol* 25, R358–R359.
- Gardner, J.L., Tokiyama, S.N., and Lisberger, S.G. (2004). A Population Decoding Framework for Motion Aftereffects on Smooth Pursuit Eye Movements. *J. Neurosci.* 24, 9035–9048.
- Gebhardt, C., Baier, H., and Del Bene, F. (2013). Direction selectivity in the visual system of the zebrafish larva. *Front Neural Circuits* 7, 111.
- Giaschi, D., Douglas, R., Marlin, S., and Cynader, M. (1993). The time course of direction-selective adaptation in simple and complex cells in cat striate cortex. *J. Neurophysiol.* 70, 2024–2034.
- Gibson, J.J., and Radner, M. (1937). Adaptation, after-effect and contrast in the perception of tilted lines. I. Quantitative studies. *Journal of Experimental Psychology* 20, 453–467.
- Giolli, R.A., Blanks, R.H.I., and Lui, F. (2006). The accessory optic system: basic organization with an update on connectivity, neurochemistry, and function. In *Progress in Brain Research*, (Elsevier), pp. 407–440.
- Glasser, D.M., Tsui, J.M.G., Pack, C.C., and Tadin, D. (2011). Perceptual and neural consequences of rapid motion adaptation. *PNAS* 108, E1080–E1088.
- Gomez-Villa, A., Martin, A., Vazquez-Corral, J., and Bertalmio, M. (2019). Convolutional Neural Networks Can Be Deceived by Visual Illusions. 9.
- Gonçalves, P.J., Arrenberg, A.B., Hablitzel, B., Baier, H., and Machens, C.K. (2014). Optogenetic perturbations reveal the dynamics of an oculomotor integrator. *Front Neural Circuits* 8.
- Govorunova, E.G., Sineshchekov, O.A., Janz, R., Liu, X., and Spudich, J.L. (2015). NEUROSCIENCE. Natural light-gated anion channels: A family of microbial rhodopsins for advanced optogenetics. *Science* 349, 647–650.
- Gradinaru, V., Thompson, K.R., and Deisseroth, K. (2008). eNpHR: a *Natronomonas* halorhodopsin enhanced for optogenetic applications. *Brain Cell Biol* 36, 129–139.

- Grama, A., and Engert, F. (2012). Direction selectivity in the larval zebrafish tectum is mediated by asymmetric inhibition. *Front Neural Circuits* 6, 59.
- Greaney, M.R., Privorotskiy, A.E., D'Elia, K.P., and Schoppik, D. (2017). Extraocular motoneuron pools develop along a dorsoventral axis in zebrafish, *Danio rerio*. *J Comp Neurol* 525, 65–78.
- Grewe, B.F., Voigt, F.F., Hoff, M. van 't, and Helmchen, F. (2011). Fast two-layer two-photon imaging of neuronal cell populations using an electrically tunable lens. *Biomed. Opt. Express*, BOE 2, 2035–2046.
- Guarente, L., Yocum, R.R., and Gifford, P. (1982). A GAL10-CYC1 hybrid yeast promoter identifies the GAL4 regulatory region as an upstream site. *Proc. Natl. Acad. Sci. U.S.A.* 79, 7410–7414.
- Guillery, R.W. (2003). Branching Thalamic Afferents Link Action and Perception. *Journal of Neurophysiology* 90, 539–548.
- Haffenden, A.M., Schiff, K.C., and Goodale, M.A. (2001). The dissociation between perception and action in the Ebbinghaus illusion: Nonillusory effects of pictorial cues on grasp. *Current Biology* 11, 177–181.
- Hammond, P., Mouat, G.S., and Smith, A.T. (1985). Motion after-effects in cat striate cortex elicited by moving gratings. *Exp Brain Res* 60, 411–416.
- Hammond, P., Mouat, G.S., and Smith, A.T. (1988). Neural correlates of motion after-effects in cat striate cortical neurones: monocular adaptation. *Exp Brain Res* 72, 1–20.
- Han, X., and Boyden, E.S. (2007). Multiple-color optical activation, silencing, and desynchronization of neural activity, with single-spike temporal resolution. *PLoS ONE* 2, e299.
- Harris, J. (1994). The duration of the movement aftereffect as an index of psychiatric illness. *Perception* 23, 1145–1153.
- Hartley, K.O., Nutt, S.L., and Amaya, E. (2002). Targeted gene expression in transgenic *Xenopus* using the binary Gal4-UAS system. *PNAS* 99, 1377–1382.
- Hautzel, H., Taylor, J.G., Krause, B.J., Schmitz, N., Tellmann, L., Ziemons, K., Shah, N.J., Herzog, H., and Müller-Gärtner, H.W. (2001). The motion aftereffect: more than area V5/MT? Evidence from 15O-butanol PET studies. *Brain Res.* 892, 281–292.
- He, S., and Masland, R.H. (1998). ON direction-selective ganglion cells in the rabbit retina: dendritic morphology and pattern of fasciculation. *Vis. Neurosci.* 15, 369–375.
- He, S., Cohen, E.R., and Hu, X. (1998). Close correlation between activity in brain area MT/V5 and the perception of a visual motion aftereffect. *Current Biology* 8, 1215–1218.
- Heap, L.A.L., Vanwalleghem, G., Thompson, A.W., Favre-Bulle, I.A., and Scott, E.K. (2018). Luminance Changes Drive Directional Startle through a Thalamic Pathway. *Neuron* 99, 293-301.e4.

- Helmbrecht, T.O., dal Maschio, M., Donovan, J.C., Koutsouli, S., and Baier, H. (2018). Topography of a Visuomotor Transformation. *Neuron* 100, 1429-1445.e4.
- Henriques, P.M., Rahman, N., Jackson, S.E., and Bianco, I.H. (2019). Nucleus Isthmi Is Required to Sustain Target Pursuit during Visually Guided Prey-Catching. *Curr Biol* 29, 1771-1786.e5.
- Hernandez, O., Papagiakoumou, E., Tanese, D., Fidelin, K., Wyart, C., and Emiliani, V. (2016). Three-dimensional spatiotemporal focusing of holographic patterns. *Nat Commun* 7, 11928.
- von der Heydt, R., Hännny, P., and Adorjani, C. (1978). Movement aftereffects in the visual cortex. *Archives Italiennes de Biologie* 116, 248–254.
- Hildebrand, D.G.C., Cicconet, M., Torres, R.M., Choi, W., Quan, T.M., Moon, J., Wetzel, A.W., Scott Champion, A., Graham, B.J., Randlett, O., et al. (2017). Whole-brain serial-section electron microscopy in larval zebrafish. *Nature* 545, 345–349.
- Hoffman, D.D. (2005). Visual illusions and perception. 2005 McGraw-Hill Yearbook of Science and Technology 7.
- Hogendoorn, H., and Verstraten, F.A.J. (2013). Decoding the motion aftereffect in human visual cortex. *NeuroImage* 82, 426–432.
- Holy, T.E. (2010). “Yes! We’re all individuals!”: redundancy in neuronal circuits. *Nat Neurosci* 13, 1306–1307.
- Hubel, D.H., and Wiesel, T.N. (1959). Receptive fields of single neurones in the cat’s striate cortex. *J Physiol* 148, 574–591.
- Hubel, D.H., and Wiesel, T.N. (1962). Receptive fields, binocular interaction and functional architecture in the cat’s visual cortex. *J. Physiol. (Lond.)* 160, 106–154.
- Huk, A.C., Ress, D., and Heeger, D.J. (2001). Neuronal basis of the motion aftereffect reconsidered. *Neuron* 32, 161–172.
- Hunter, P.R., Lowe, A.S., Thompson, I.D., and Meyer, M.P. (2013). Emergent properties of the optic tectum revealed by population analysis of direction and orientation selectivity. *J. Neurosci.* 33, 13940–13945.
- Iwashita, M., Kanai, R., Funabiki, K., Matsuda, K., and Hirano, T. (2001). Dynamic properties, interactions and adaptive modifications of vestibulo-ocular reflex and optokinetic response in mice. *Neurosci. Res.* 39, 299–311.
- Kawakami, K. (2005). Transposon tools and methods in zebrafish. *Developmental Dynamics* 234, 244–254.
- Kawakami, K., and Shima, A. (1999). Identification of the Tol2 transposase of the medaka fish *Oryzias latipes* that catalyzes excision of a nonautonomous Tol2 element in zebrafish *Danio rerio*. *Gene* 240, 239–244.

- Kawakami, K., Koga, A., Hori, H., and Shima, A. (1998). Excision of the Tol2 transposable element of the medaka fish, *Oryzias latipes*, in zebrafish, *Danio rerio*. *Gene* 225, 17–22.
- Kawakami, K., Shima, A., and Kawakami, N. (2000). Identification of a functional transposase of the Tol2 element, an Ac-like element from the Japanese medaka fish, and its transposition in the zebrafish germ lineage. *PNAS* 97, 11403–11408.
- Kawakami, K., Takeda, H., Kawakami, N., Kobayashi, M., Matsuda, N., and Mishina, M. (2004). A Transposon-Mediated Gene Trap Approach Identifies Developmentally Regulated Genes in Zebrafish. *Developmental Cell* 7, 133–144.
- Kawashima, T., Zwart, M.F., Yang, C.-T., Mensh, B.D., and Ahrens, M.B. (2016). The Serotonergic System Tracks the Outcomes of Actions to Mediate Short-Term Motor Learning. *Cell* 167, 933–946.e20.
- Kay, J.N., De la Huerta, I., Kim, I.-J., Zhang, Y., Yamagata, M., Chu, M.W., Meister, M., and Sanes, J.R. (2011). Retinal ganglion cells with distinct directional preferences differ in molecular identity, structure, and central projections. *J. Neurosci.* 31, 7753–7762.
- Kimura, Y., Satou, C., Fujioka, S., Shoji, W., Umeda, K., Ishizuka, T., Yawo, H., and Higashijima, S. (2013). Hindbrain V2a neurons in the excitation of spinal locomotor circuits during zebrafish swimming. *Curr. Biol.* 23, 843–849.
- Kinoshita, M., and Ito, E. (2006). Roles of periventricular neurons in retinotectal transmission in the optic tectum. *Prog. Neurobiol.* 79, 112–121.
- Klar, M., and Hoffmann, K.-P. (2002). Visual direction-selective neurons in the pretectum of the rainbow trout. *Brain Res. Bull.* 57, 431–433.
- Kohn, A., and Movshon, J.A. (2004). Adaptation changes the direction tuning of macaque MT neurons. *Nature Neuroscience* 7, 764.
- Konkle, T., Wang, Q., Hayward, V., and Moore, C.I. (2009). Motion aftereffects transfer between touch and vision. *Curr. Biol.* 19, 745–750.
- Köster, R.W., and Fraser, S.E. (2001). Tracing transgene expression in living zebrafish embryos. *Dev. Biol.* 233, 329–346.
- Kramer, A., Wu, Y., Baier, H., and Kubo, F. (2019). Neuronal Architecture of a Visual Center that Processes Optic Flow. *Neuron* 103, 118–132.e7.
- Kubo, F., Hablitzel, B., Dal Maschio, M., Driever, W., Baier, H., and Arrenberg, A.B. (2014). Functional Architecture of an Optic Flow-Responsive Area that Drives Horizontal Eye Movements in Zebrafish. *Neuron* 81, 1344–1359.
- Kumar, M., Kishore, S., Nasenbeny, J., McLean, D.L., and Kozorovitskiy, Y. (2018). Integrated one- and two-photon scanned oblique plane illumination (SOPi) microscopy for rapid volumetric imaging. *Opt Express* 26, 13027–13041.

- Kunst, M., Laurell, E., Mokayes, N., Kramer, A., Kubo, F., Fernandes, A.M., Förster, D., Maschio, M.D., and Baier, H. (2019). A Cellular-Resolution Atlas of the Larval Zebrafish Brain. *Neuron* 103, 21-38.e5.
- Lauterbur, P.C. (1973). Image Formation by Induced Local Interactions: Examples Employing Nuclear Magnetic Resonance. *Nature* 242, 190.
- Lin, M.Z., and Schnitzer, M.J. (2016). Genetically encoded indicators of neuronal activity. *Nat. Neurosci.* 19, 1142–1153.
- Ling, G., and Gerard, R.W. (1949). The normal membrane potential of frog sartorius fibers. *Journal of Cellular and Comparative Physiology* 34, 383–396.
- Loomis, J.M. (1972). The photopigment bleaching hypothesis of complementary after-images: a psychophysical test. *Vision Res.* 12, 1587–1594.
- Lowe, A.S., Nikolaou, N., Hunter, P.R., Thompson, I.D., and Meyer, M.P. (2013). A Systems-Based Dissection of Retinal Inputs to the Zebrafish Tectum Reveals Different Rules for Different Functional Classes during Development. *J. Neurosci.* 33, 13946–13956.
- Lucretius De Rerum Natura (Harvard University Press).
- Maffei, L., and Fiorentini, A. (1973). The visual cortex as a spatial frequency analyser. *Vision Res.* 13, 1255–1267.
- Malyshev, A.Y., Roshchin, M.V., Smirnova, G.R., Dolgikh, D.A., Balaban, P.M., and Ostrovsky, M.A. (2017). Chloride conducting light activated channel GtACR2 can produce both cessation of firing and generation of action potentials in cortical neurons in response to light. *Neurosci. Lett.* 640, 76–80.
- Marlin, S.G., Hasan, S.J., and Cynader, M.S. (1988). Direction-selective adaptation in simple and complex cells in cat striate cortex. *J. Neurophysiol.* 59, 1314–1330.
- Marquart, G.D., Tabor, K.M., Brown, M., Strykowski, J.L., Varshney, G.K., LaFave, M.C., Mueller, T., Burgess, S.M., Higashijima, S., and Burgess, H.A. (2015). A 3D Searchable Database of Transgenic Zebrafish Gal4 and Cre Lines for Functional Neuroanatomy Studies. *Front Neural Circuits* 9.
- Marquart, G.D., Tabor, K.M., Horstick, E.J., Brown, M., Geoca, A.K., Polys, N.F., Nogare, D.D., and Burgess, H.A. (2017). High-precision registration between zebrafish brain atlases using symmetric diffeomorphic normalization. *Gigascience* 6, 1–15.
- Masseck, O.A., and Hoffmann, K.-P. (2008). Responses to Moving Visual Stimuli in Pretectal Neurons of the Small-Spotted Dogfish (*Scyliorhinus canicula*). *Journal of Neurophysiology* 99, 200–207.
- Masseck, O.A., and Hoffmann, K.-P. (2009a). Comparative Neurobiology of the Optokinetic Reflex. *Annals of the New York Academy of Sciences* 1164, 430–439.

- Masseck, O.A., and Hoffmann, K.-P. (2009b). Question of Reference Frames: Visual Direction-Selective Neurons in the Accessory Optic System of Goldfish. *Journal of Neurophysiology* *102*, 2781–2789.
- Mather, G., Verstraten, F., and Anstis, S. (1998). *The Motion Aftereffect: A Modern Perspective* (The MIT Press).
- Maunsell, J.H.R., and Van Essen, D.C. (1983). Functional properties of neurons in middle temporal visual area of the macaque monkey. I. Selectivity for stimulus direction, speed, and orientation. *Journal of Neurophysiology* *49*, 1127–1147.
- Mély, D.A., Linsley, D., and Serre, T. (20180920). Complementary surrounds explain diverse contextual phenomena across visual modalities. *Psychological Review* *125*, 769.
- Meng, X., Mazzoni, P., and Qian, N. (2006). Cross-fixation transfer of motion aftereffects with expansion motion. *Vision Research* *46*, 3681–3689.
- Mitchell, D.E., and Ware, C. (1974). Interocular transfer of a visual after-effect in normal and stereoblind humans. *J. Physiol. (Lond.)* *236*, 707–721.
- Mohamed, G.A., Cheng, R.-K., Ho, J., Krishnan, S., Mohammad, F., Claridge-Chang, A., and Jesuthasan, S. (2017). Optical inhibition of larval zebrafish behaviour with anion channelrhodopsins. *BMC Biol.* *15*, 103.
- Monesson-Olson, B.D., Browning-Kamins, J., Aziz-Bose, R., Kreines, F., and Trapani, J.G. (2014). Optical stimulation of zebrafish hair cells expressing channelrhodopsin-2. *PLoS ONE* *9*, e96641.
- Movshon, J.A., Chambers, B.E., and Blakemore, C. (1972). Interocular transfer in normal humans, and those who lack stereopsis. *Perception* *1*, 483–490.
- Mueller, T., and Wullimann, M.F. (2002). BrdU-, neuroD (nrd)- and Hu-studies reveal unusual non-ventricular neurogenesis in the postembryonic zebrafish forebrain. *Mechanisms of Development* *117*, 123–135.
- Muto, A., Orger, M.B., Wehman, A.M., Smear, M.C., Kay, J.N., Page-McCaw, P.S., Gahtan, E., Xiao, T., Nevin, L.M., Gosse, N.J., et al. (2005). Forward Genetic Analysis of Visual Behavior in Zebrafish. *PLoS Genet* *1*.
- Muto, A., Lal, P., Ailani, D., Abe, G., Itoh, M., and Kawakami, K. (2017). Activation of the hypothalamic feeding centre upon visual prey detection. *Nat Commun* *8*.
- Mutter, M., Swietek, N., and Münch, T.A. (2014). Salvaging Ruins: Reverting Blind Retinas into Functional Visual Sensors. In *Photoswitching Proteins: Methods and Protocols*, S. Cambridge, ed. (New York, NY: Springer New York), pp. 149–160.
- Nagel, G., Szellas, T., Huhn, W., Kateriya, S., Adeishvili, N., Berthold, P., Ollig, D., Hegemann, P., and Bamberg, E. (2003). Channelrhodopsin-2, a directly light-gated cation-selective membrane channel. *PNAS* *100*, 13940–13945.

- Najafian, M., Alerasool, N., and Moshtaghian, J. (2014). The effect of motion aftereffect on optomotor response in larva and adult zebrafish. *Neuroscience Letters* 559, 179–183.
- Nakai, J., Ohkura, M., and Imoto, K. (2001). A high signal-to-noise Ca²⁺ probe composed of a single green fluorescent protein. *Nature Biotechnology* 19, 137.
- Naumann, E.A., Fitzgerald, J.E., Dunn, T.W., Rihel, J., Sompolinsky, H., and Engert, F. (2016). From Whole-Brain Data to Functional Circuit Models: The Zebrafish Optomotor Response. *Cell* 167, 947-960.e20.
- Neuhauss, S.C.F. (2003). Behavioral genetic approaches to visual system development and function in zebrafish. *Journal of Neurobiology* 54, 148–160.
- Neuhauss, S., Biehlmaier, O., W Seeliger, M., Das, T., Kohler, K., William, H., and Baier, H. (1999). Genetic Disorders of Vision Revealed by a Behavioral Screen of 400 Essential Loci in Zebrafish. *The Journal of Neuroscience: The Official Journal of the Society for Neuroscience* 19, 8603–8615.
- Nevin, L.M., Robles, E., Baier, H., and Scott, E.K. (2010). Focusing on optic tectum circuitry through the lens of genetics. *BMC Biology* 8, 126.
- Nikolaou, N., and Meyer, M.P. (2015). Lamination Speeds the Functional Development of Visual Circuits. *Neuron* 88, 999–1013.
- Nikolaou, N., Lowe, A.S., Walker, A.S., Abbas, F., Hunter, P.R., Thompson, I.D., and Meyer, M.P. (2012). Parametric functional maps of visual inputs to the tectum. *Neuron* 76, 317–324.
- Nishida, S., and Sato, T. (1995). Motion aftereffect with flickering test patterns reveals higher stages of motion processing. *Vision Research* 35, 477–490.
- Nishida, S., Ashida, H., and Sato, T. (1994). Complete interocular transfer of motion aftereffect with flickering test. *Vision Res.* 34, 2707–2716.
- Nöbauer, T., Skocek, O., Pernía-Andrade, A.J., Weilguny, L., Traub, F.M., Molodtsov, M.I., and Vaziri, A. (2017). Video rate volumetric Ca²⁺ imaging across cortex using seeded iterative demixing (SID) microscopy. *Nature Methods* 14, 811–818.
- Ogura, E., Okuda, Y., Kondoh, H., and Kamachi, Y. (2009). Adaptation of GAL4 activators for GAL4 enhancer trapping in zebrafish. *Dev. Dyn.* 238, 641–655.
- O’leary, A., and McMahon, M. (1991). Adaptation to form distortion of a familiar shape. *Perception & Psychophysics* 49, 328–332.
- Orger, M.B. (2016). The Cellular Organization of Zebrafish Visuomotor Circuits. *Current Biology* 26, R377–R385.
- Ornitz, D.M., Moreadith, R.W., and Leder, P. (1991). Binary system for regulating transgene expression in mice: targeting int-2 gene expression with yeast GAL4/UAS control elements. *PNAS* 88, 698–702.

- Panzeri, S., Harvey, C.D., Piasini, E., Latham, P.E., and Fellin, T. (2017). Cracking the Neural Code for Sensory Perception by Combining Statistics, Intervention, and Behavior. *Neuron* 93, 491–507.
- Papagiakoumou, E., Anselmi, F., Bègue, A., de Sars, V., Glückstad, J., Isacoff, E.Y., and Emiliani, V. (2010). Scanless two-photon excitation of channelrhodopsin-2. *Nature Methods* 7, 848–854.
- Parinov, S., Kondrichin, I., Korzh, V., and Emelyanov, A. (2004). Tol2 transposon-mediated enhancer trap to identify developmentally regulated zebrafish genes in vivo. *Dev. Dyn.* 231, 449–459.
- Parker, M.O., Brock, A.J., Walton, R.T., and Brennan, C.H. (2013). The role of zebrafish (*Danio rerio*) in dissecting the genetics and neural circuits of executive function. *Front. Neural Circuits* 7.
- Pasik, P., Pasik, T., and Valciukas, J.A. (1972). Quantitative studies on optokinetic nystagmus in the monkey. *Bibl Ophthalmol* 82, 317–326.
- Pérez-Schuster, V., Kulkarni, A., Nouvian, M., Romano, S.A., Lygdas, K., Jouary, A., Dipoppa, M., Pietri, T., Haudrechy, M., Candat, V., et al. (2016). Sustained Rhythmic Brain Activity Underlies Visual Motion Perception in Zebrafish. *Cell Reports* 17, 1098–1112.
- Portugues, R., and Engert, F. (2009). The neural basis of visual behaviors in the larval zebrafish. *Current Opinion in Neurobiology* 19, 644–647.
- Portugues, R., Severi, K.E., Wyart, C., and Ahrens, M.B. (2013). Optogenetics in a transparent animal: circuit function in the larval zebrafish. *Curr. Opin. Neurobiol.* 23, 119–126.
- Portugues, R., Feierstein, C.E., Engert, F., and Orger, M.B. (2014). Whole-Brain Activity Maps Reveal Stereotyped, Distributed Networks for Visuomotor Behavior. *Neuron* 81, 1328–1343.
- Puchalla, J.L., Schneidman, E., Harris, R.A., and Berry, M.J. (2005). Redundancy in the population code of the retina. *Neuron* 46, 493–504.
- Purkinje, E. (1820). Beiträge zur näheren Kenntniss des Schwindels aus heautognostischen Daten. 79–125.
- Quirin, S., Vladimirov, N., Yang, C.-T., Peterka, D.S., Yuste, R., and Ahrens, M.B. (2016). Calcium imaging of neural circuits with extended depth-of-field light-sheet microscopy. *Opt Lett* 41, 855–858.
- Randlett, O., Wee, C.L., Naumann, E.A., Nnaemeka, O., Schoppik, D., Fitzgerald, J.E., Portugues, R., Lacoste, A.M.B., Riegler, C., Engert, F., et al. (2015). Whole-brain activity mapping onto a zebrafish brain atlas. *Nat. Methods* 12, 1039–1046.
- Raymond, J.E. (1993). Complete interocular transfer of motion adaptation effects on motion coherence thresholds. *Vision Res.* 33, 1865–1870.

- Reichardt, W.E. (1969). Movement perception in insects. *Processing of Optical Data by Organisms and by Machines* 465–493.
- Rickgauer, J.P., and Tank, D.W. (2009). Two-photon excitation of channelrhodopsin-2 at saturation. *PNAS* *106*, 15025–15030.
- Rinner, O., Rick, J.M., and Neuhauss, S.C.F. (2005). Contrast sensitivity, spatial and temporal tuning of the larval zebrafish optokinetic response. *Invest. Ophthalmol. Vis. Sci.* *46*, 137–142.
- Robles, E., Laurell, E., and Baier, H. (2014). The Retinal Projectome Reveals Brain-Area-Specific Visual Representations Generated by Ganglion Cell Diversity. *Current Biology* *24*, 2085–2096.
- Roeser, T., and Baier, H. (2003). Visuomotor Behaviors in Larval Zebrafish after GFP-Guided Laser Ablation of the Optic Tectum. *J. Neurosci.* *23*, 3726–3734.
- Rohlfing, T., and Maurer, C.R. (2003). Nonrigid image registration in shared-memory multiprocessor environments with application to brains, breasts, and bees. *IEEE Transactions on Information Technology in Biomedicine* *7*, 16–25.
- Sadowski, I., Ma, J., Triezenberg, S., and Ptashne, M. (1988). GAL4-VP16 is an unusually potent transcriptional activator. *Nature* *335*, 563–564.
- Samonds, J.M., Lieberman, S., and Priebe, N.J. (2018). Motion Discrimination and the Motion Aftereffect in Mouse Vision. *Eneuro* *5*, ENEURO.0065-18.2018.
- Sanchez-Vives, M.V., Nowak, L.G., and McCormick, D.A. (2000). Membrane mechanisms underlying contrast adaptation in cat area 17 in vivo. *J. Neurosci.* *20*, 4267–4285.
- Scheer, N., and Campos-Ortega, J.A. (1999). Use of the Gal4-UAS technique for targeted gene expression in the zebrafish. *Mechanisms of Development* *80*, 153–158.
- Schiffman, H.R., and Thompson, J.G. (1977). The role of converging lines on the perception of vertical lines: A Ponzo illusion variant. *Acta Psychologica* *41*, 461–466.
- Schiller, P.H., and Carvey, C.E. (2005). The Hermann Grid Illusion Revisited. *Perception* *34*, 1375–1397.
- Schoonheim, P.J., Arrenberg, A.B., Del Bene, F., and Baier, H. (2010). Optogenetic localization and genetic perturbation of saccade-generating neurons in zebrafish. *J. Neurosci.* *30*, 7111–7120.
- Scott, E.K., and Baier, H. (2009). The cellular architecture of the larval zebrafish tectum, as revealed by gal4 enhancer trap lines. *Front Neural Circuits* *3*, 13.
- Scott, T.R., and Milligan, W.L. (1970). The Psychophysical Study of Visual Motion Aftereffect Rate in Monkeys. In *Animal Psychophysics: The Design and Conduct of Sensory Experiments*, W.C. Stebbins, ed. (Boston, MA: Springer US), pp. 341–361.

- Scott, E.K., Mason, L., Arrenberg, A.B., Ziv, L., Gosse, N.J., Xiao, T., Chi, N.C., Asakawa, K., Kawakami, K., and Baier, H. (2007). Targeting neural circuitry in zebrafish using GAL4 enhancer trapping. *Nat. Methods* 4, 323–326.
- Seidman, S.H., Leigh, R.J., and Thomas, C.W. (1992). Eye movements during motion after-effect. *Vision Res.* 32, 167–171.
- Sekuler, R.W., and Ganz, L. (1963). Aftereffect of Seen Motion with a Stabilized Retinal Image. *Science* 139, 419–419.
- Semmelhack, J.L., Donovan, J.C., Thiele, T.R., Kuehn, E., Laurell, E., and Baier, H. (2014). A dedicated visual pathway for prey detection in larval zebrafish. *Elife* 3.
- Simpson, J.I. (1984). The accessory optic system. *Annual Review of Neuroscience VOL. 7*, 13–41.
- Singh, P., and Shepherd, A.J. (2016). Enhanced Motion Aftereffects in Migraine Are Related to Contrast Sensitivity: Implications for Models of Differences in Precortical/Cortical Function. *Invest. Ophthalmol. Vis. Sci.* 57, 1228–1234.
- Spigel, I.M. (1962). Contour absence as a critical factor in the inhibition of the decay of a movement aftereffect. *The Journal of Psychology: Interdisciplinary and Applied* 54, 221–228.
- Springer, A.M., Easter, S.S., and Agranoff, B.W. (1977). The role of the optic tectum in various visually mediated behaviors of goldfish. *Brain Research* 128, 393–404.
- Srinivasan, M.V., and Dvorak, D.R. (1979). The waterfall illusion in an insect visual system. *Vision Research* 19, 1435–1437.
- Stewart, L., Battelli, L., Walsh, V., and Cowey, A. (1999). Motion perception and perceptual learning studied by magnetic stimulation. *Electroencephalogr Clin Neurophysiol Suppl* 51, 334–350.
- Sun, L.O., Brady, C.M., Cahill, H., Al-Khindi, T., Sakuta, H., Dhande, O.S., Noda, M., Huberman, A.D., Nathans, J., and Kolodkin, A.L. (2015). Functional Assembly of Accessory Optic System Circuitry Critical for Compensatory Eye Movements. *Neuron* 86, 971–984.
- Sun, W., Deng, Q., Levick, W.R., and He, S. (2006). ON direction-selective ganglion cells in the mouse retina. *J. Physiol.-London* 576, 197–202.
- Sutherland, N.S. (1961). Figural After-Effects and Apparent Size. *Quarterly Journal of Experimental Psychology* 13, 222–228.
- Tan, N.G.A., Wu, W., and Seifalian, A.M. (2015). Optogenetics: lights, camera, action! A ray of light, a shadow unmasked. In *Applications of Nanoscience in Photomedicine*, (Elsevier), pp. 185–203.
- Tarnutzer, A.A., and Straumann, D. (2018). Nystagmus. *Curr. Opin. Neurol.* 31, 74–80.

- Taylor, J.G., Schmitz, N., Ziemons, K., Grosse-Ruyken, M.L., Gruber, O., Mueller-Gaertner, H.W., and Shah, N.J. (2000). The network of brain areas involved in the motion aftereffect. *Neuroimage* *11*, 257–270.
- Temizer, I., Donovan, J.C., Baier, H., and Semmelhack, J.L. (2015). A Visual Pathway for Looming-Evoked Escape in Larval Zebrafish. *Curr. Biol.* *25*, 1823–1834.
- Théoret, H., Kobayashi, M., Ganis, G., Di Capua, P., and Pascual-Leone, A. (2002). Repetitive transcranial magnetic stimulation of human area MT/V5 disrupts perception and storage of the motion aftereffect. *Neuropsychologia* *40*, 2280–2287.
- Thompson, P., and Wright, J. (1994). The Role of Intervening Patterns in the Storage of the Movement Aftereffect. *Perception* *23*, 1233–1240.
- Tomsic, D. (2016). Visual motion processing subserving behavior in crabs. *Current Opinion in Neurobiology* *41*, 113–121.
- Tootell, R.B.H., Reppas, J.B., Dale, A.M., Look, R.B., Sereno, M.I., Malach, R., Brady, T.J., and Rosen, B.R. (1995). Visual motion aftereffect in human cortical area MT revealed by functional magnetic resonance imaging. *Nature* *375*, 139–141.
- Tsai, P.S., and Kleinfeld, D. (2009). In Vivo Two-Photon Laser Scanning Microscopy with Concurrent Plasma-Mediated Ablation Principles and Hardware Realization. In *In Vivo Optical Imaging of Brain Function*, R.D. Frostig, ed. (Boca Raton (FL): CRC Press/Taylor & Francis), p.
- Umeda, K., Ishizuka, T., Yawo, H., and Shoji, W. (2016). Position- and quantity-dependent responses in zebrafish turning behavior. *Sci Rep* *6*, 27888.
- Van Wezel, R.J.A., and Britten, K.H. (2002). Motion Adaptation in Area MT. *Journal of Neurophysiology* *88*, 3469–3476.
- Vanwallegem, G.C., Ahrens, M.B., and Scott, E.K. (2018). Integrative whole-brain neuroscience in larval zebrafish. *Current Opinion in Neurobiology* *50*, 136–145.
- Vautin, R.G., and Berkley, M.A. (1977). Responses of single cells in cat visual cortex to prolonged stimulus movement: neural correlates of visual aftereffects. *Journal of Neurophysiology* *40*, 1051–1065.
- Vladimirov, N., Wang, C., Höckendorf, B., Pujala, A., Tanimoto, M., Mu, Y., Yang, C.-T., Wittenbach, J.D., Freeman, J., Preibisch, S., et al. (2018). Brain-wide circuit interrogation at the cellular level guided by online analysis of neuronal function. *Nature Methods* *15*, 1117.
- Wade, N.J., Swanston, M.T., and de Weert, C.M. (1993). On interocular transfer of motion aftereffects. *Perception* *22*, 1365–1380.
- Wallman, J. (1993). Subcortical optokinetic mechanisms. *Rev Oculomot Res* *5*, 321–342.

- Wang, K., Hinz, J., Haikala, V., Reiff, D.F., and Arrenberg, A.B. (2019). Selective processing of all rotational and translational optic flow directions in the zebrafish pretectum and tectum. *BMC Biol.* 17, 29.
- Watamaniuk, S.N.J., and Heinen, S.J. (2007). Storage of an oculomotor motion aftereffect. *Vision Research* 47, 466–473.
- Watanabe, E., Kitaoka, A., Sakamoto, K., Yasugi, M., and Tanaka, K. (2018). Illusory Motion Reproduced by Deep Neural Networks Trained for Prediction. *Front. Psychol.* 9.
- Weng, S.J., Sun, W.Z., and He, S.G. (2005). Identification of ON-OFF direction-selective ganglion cells in the mouse retina. *J. Physiol.-London* 562, 915–923.
- Wiegert, J.S., Mahn, M., Prigge, M., Printz, Y., and Yizhar, O. (2017). Silencing Neurons: Tools, Applications, and Experimental Constraints. *Neuron* 95, 504–529.
- Wilson, H.R., Ferrera, V.P., and Yo, C. (1992). A psychophysically motivated model for two-dimensional motion perception. *Vis. Neurosci.* 9, 79–97.
- Wohlgemuth, A. (1911). On the After-Effect of Seen Movement. (*Brit. J. of Psychol., Monog. Suppl. No. 1.*) (Oxford, England: Univ. Press).
- Wullimann, M.F. (1997). *The Physiology of Fishes* (New York, NY: CRC Press).
- Xiao, Q., and Güntürkün, O. (2008). Do pigeons perceive the motion aftereffect? A behavioral study. *Behav. Brain Res.* 187, 327–333.
- Yakushin, S.B., Gizzi, M., Reisine, H., Raphan, T., Büttner-Ennever, J., and Cohen, B. (2000). Functions of the nucleus of the optic tract (NOT). *Exp Brain Res* 131, 433–447.
- Yáñez, J., Suárez, T., Quelle, A., Folgueira, M., and Anadón, R. (2018). Neural connections of the pretectum in zebrafish (*Danio rerio*).
- Yin, C., Li, X., and Du, J. (2019). Optic tectal superficial interneurons detect motion in larval zebrafish. *Protein Cell* 10, 238–248.
- Zaidi, Q., Ennis, R., Cao, D., and Lee, B. (2012). Neural locus of color afterimages. *Curr. Biol.* 22, 220–224.
- Zeki, S.M. (1974). Functional organization of a visual area in the posterior bank of the superior temporal sulcus of the rhesus monkey. *The Journal of Physiology* 236, 549–573.
- Zhang, B.-B., Yao, Y.-Y., Zhang, H.-F., Kawakami, K., and Du, J.-L. (2017). Left Habenula Mediates Light-Preference Behavior in Zebrafish via an Asymmetrical Visual Pathway. *Neuron* 93, 914-928.e4.
- Zhang, F., Wang, L.-P., Brauner, M., Liewald, J.F., Kay, K., Watzke, N., Wood, P.G., Bamberg, E., Nagel, G., Gottschalk, A., et al. (2007). Multimodal fast optical interrogation of neural circuitry. *Nature* 446, 633–639.

Zihl, J., and Heywood, C.A. (2015). The contribution of LM to the neuroscience of movement vision. *Front Integr Neurosci* 9.

ACKNOWLEDGMENT

I would like to thank my supervisors Herwig and Fumi for giving me the opportunity to explore cool illusions in larval zebrafish. The independence they granted me in the pursuit of my thesis projects, and the support and encouragement they gave me to present my work at national and international conferences made me a confident scientist today. Special thanks to Fumi for her support and patient supervision all along. Although she moved to Japan in 2018, I never felt far away from her with our regular skype meetings and frequent email communications.

My thesis project would not be possible without the open and supporting environment created by the whole Baier lab. I am especially grateful to Anna for the wonderful collaboration on the AF project, Marco for his valuable advice on two-photon microscopes and data analysis, Miguel for his constant support and feedback and the lively environment in our office, Thomas for sharing code and helping me jumpstart with python, Irene for all the supports with molecular cloning, Michael for his help with the brain atlas, Johannes for his advice on the manuscripts, and Duncan for all the fruitful scientific discussions. As my colleague Anna put it: the Baier lab is like a village. For everything you need, there is a specialist: a butcher, a baker, a carpenter, you name it. They are not only the best at what they do, but they are also always willing to lend a helping hand. This unique ecosystem taught me not to shy away from asking for help, and moreover, always be generous whenever my experience or knowledge could be helpful to others. This lesson I will carry on for life.

I also sincerely appreciate the input from my TAC members Axel Borst and Thomas Euler. They not only offered constructive suggestions regarding my thesis projects, but they also cared about my personal development. I am deeply grateful to Thomas, who always took the time to travel from Tübingen to Munich to attend my TAC meetings.

Finally yet importantly, I want to say thank you to all my friends and family, who offered me great accompany, especially on those not so rosy days. The biggest thanks to Hendrik, who stood by me through all the ups and downs along this journey.

APPENDIX 1: CURRICULUM VITAE

Yunmin Wu

Am Klopferspitz 18,

82152 Martinsried, Germany

Email: yunminwu@neuro.mpg.de

Further Educations

- Since 2015 **Max Planck Institute of Neurobiology**, Munich, Germany
- PhD candidate, IMPRS & GSN graduate program
 - Supervised by Prof. Dr. Herwig Baier & Dr. Fumi Kubo, Department Genes-Circuits-Behavior
- 2014 - **Graduate School of Neuroscience - LMU**, Munich, Germany
- 2015
- Fast-track program: one-year intensive program in systemic neurosciences for students starting PhD without a master degree
- 2013 **École Polytechnique Fédérale de Lausanne**, Lausanne, Switzerland
- One-semester exchange student
 - Life sciences and technologies section
- 2010 - **The Hong Kong University of Science and Technology**, Hong Kong
- 2014
- Bachelor of Science (First Class Honor)
 - Major in Biochemistry, minor in Bioengineering

Awards and Achievements

- 2019 Young Investigator Award at the European Retina Meeting
- 2018 Best talk at 23rd IMPRS seminar
- 2016 Scholarship from Helmsley Charitable Trust for advanced training at Marine Biological Laboratory, University of Chicago
- 2016 Best poster at 20th IMPRS seminar
- 2014 Gold medal award of RedBird Award Program, HKUST
- 2013 & 2014 Academic Excellence award, HKUST
- 2012 HKSAR Government Scholarship Fund - Reaching Out Award
- 2011 - 2014 Dean's list, HKUST
- 2011 - 2014 Scholarship Scheme for Continuing Undergraduates, HKUST
- 2011 Best presentation at Asian Jamboree - iGEM Competition 2011

Research Experience

- Jun - Jul 2016 **Summer course “Neural systems and behavior” - Marine Biology Lab**
- Actively participated in an 8-week discovery-based intensive course in neuroscience
 - Designed and executed novel pilot projects on multiple species
- Sep 2013 - May 2014 **Final Year Project - HKUST**
- Studied the effect of GSK-3 inhibitor lithium chloride on the level of survival motor neuron protein in cell culture
 - Supervised by Prof. Benjamin H. Peng
- Jul - Aug 2013 **Summer internship - PDN, University of Cambridge**
- Investigated the retinal stem cell fate determination in larval zebrafish with advanced imaging;
 - Examined the effect of light entrained circadian cycle on retinal development
 - Supervised by Prof. William A. Harris
- Jan - Aug 2012 **Undergraduate Research Opportunity (internship) - HKUST**
- Conducted a two-semester research project on PICK1 protein and Parkinson’s disease
 - Supervised by Prof. Jun Xia
- Nov 2010 - Nov 2011 **iGEM Competition 2011, project “E.trojan” - HKUST&MIT**
- Genetically engineered *E. Coli* to disrupt indole quorum-sensing for improving the effectiveness of antibiotics
 - Supervised by Prof. King-Lau Chow

Conferences

- 2019 European Retina Meeting, Helsinki, Finland - Poster & Quickfire Talk
- 2018 Champalimaud Research Symposium: Quantitative approaches to Behavior and Neural Systems, Lisbon, Portugal - Poster
- 2018 SPP1926 3rd Annual Meeting, Bonn, Germany - Poster
- 2018 < interact > 2018 symposium, Munich, Germany - Poster
- 2017 International Workshop on Zebrafish Neural Circuits and Behavior, Maryland, USA - Poster
- 2017 SFN annual meeting, Washington D.C., USA
- 2016 < interact > 2016 symposium, Munich, Germany - Organizer
- 2016 4th Imaging Structure and Function in the Zebrafish Brain Conference, Munich, Germany - Poster

APPENDIX 2: PUBLICATIONS

1. Wan, Y., Almeida, A. D., Rulands, S., Chalour, N., Muresan, L., **Wu, Y.**, et al. (2016). The ciliary marginal zone of the zebrafish retina: clonal and time-lapse analysis of a continuously growing tissue. *Development* 143, 1099–1107.
2. Kramer, A., **Wu, Y.**, Baier, H., and Kubo, F. (2019). Neuronal Architecture of a Visual Center that Processes Optic Flow. *Neuron* 103, 118-132.e7.
3. **Wu, Y.**, Dal Maschio, M., Kubo, F., and Baier, H. (2019) An Essential Circuit Node for Motion-Induced Behavior Identified by an Optical Illusion. (In preparation)

APPENDIX 3: AFFIDAVIT

Hiermit versichere ich an Eides statt, dass ich die vorliegende Dissertation “Neural Basis of Visual Motion Perception: An Illusory Perspective“ selbstständig angefertigt habe, mich außer der angegebenen keiner weiteren Hilfsmittel bedient und alle Erkenntnisse, die aus dem Schrifttum ganz oder annähernd übernommen sind, als solche kenntlich gemacht und nach ihrer Herkunft unter Bezeichnung der Fundstelle einzeln nachgewiesen habe.

I hereby confirm that the dissertation “Neural Basis of Visual Motion Perception: An Illusory Perspective” is the result of my own work and that I have only used sources or materials listed and specified in the dissertation.

Munich, Oct 1st, 2019

.....
Yunmin Wu

APPENDIX 4: DECLARATION OF AUTHOR CONTRIBUTIONS

The author contributions to the publication “Neuronal Architecture of a Visual Center that Processes Optic Flow” by Anna Kramer, Yunmin Wu, Herwig Baier, and Fumi Kubo published in *Neuron*, 3 Jul 2019, Volume 103, Issue 1, Page 118-132.e7 were as follows: H.B. and F.K. conceived the project. A.K. performed FuGIMA experiments, generated the UAS:FuGIMA and UAS:FuGIMA-C3PA transgenic lines, and performed anatomical registrations and complementation analyses. Y.W. performed the imaging on RGC terminal responses and analyzed the direction-selective responses in RGCs. F.K. generated the UAS:syGCaMP6s transgenic line. A.K., Y.W., and F.K. annotated arborization fields. A.K., Y.W., H.B., and F.K. wrote the manuscript.

The author contributions to the manuscript “An Essential Circuit Node for Motion-Induced Behavior Identified by an Optical Illusion” by Yunmin Wu, Marco Dal Maschio, Fumi Kubo, and Herwig Baier were as follows: Y.W., H.B., and F.K. conceived the project. Y.W. performed behavior, functional imaging, optogenetics, and ablation experiments. Y.W. designed and implemented the analysis for the behavior data. Y.W. and M.D.M. designed the analysis pipeline for functional imaging and wrote the custom python scripts. Y.W., M.D.M., H.B., and F.K. wrote the manuscript.

I hereby certify that the information above is true and accurate.

Munich, Oct 1st, 2019

.....
Herwig Baier

.....
Yunmin Wu